2008-04-01

# Ocular Aberrations Wavefront Sensor in Clinical Application

Matthew Sheehan
*Technological University Dublin*

# Ocular Aberrations
# Wavefront Sensor In Clinical Application

Matthew Sheehan B App Sc (Optometry)

Submitted in partial fulfilment of the requirements
for the degree of Master of Philosophy

Supervisors: Dr Veronica O'Dwyer, Prof. Chris Dainty,
Dr Vincent Toal, and Dr Brenda McGrath

Dublin Institute of Technology - School of Physics

Submitted April 2008

## Abstract

A versatile Hartmann-Shack (HS) wavefront sensor (WFS) was designed and constructed. Its advantages include simultaneous pupil centre determination, off-axis capability, realtime data displays, and efficient lenslet sampling orientation. The instrument is compact and transportable, making it convenient for use in a clinical setting. Subject alignment is achieved by the use of a parallel channel that is recombined with the sensing channel to simultaneously image the external eye and the HS spots onto a single charge coupled device (CCD). The pupil centre is determined using this image of the eye, rather than the HS spots. Off-axis measurements are possible throughout an unobstructed 10 degree field of view. User-friendly software was developed to provide the clinician with data displays at 10 Hertz and above. The optical design includes a rotated lenslet array which increases the dynamic range in those meridians where astigmatism is most typically expected in the eye. Telecentric re-imaging of the HS spots increases the system's robustness to CCD misalignment.

Our experimental WFS was used in two experiments. The first experiment examined agreement between the experimental WFS and the ZyWave (a commercially avaliable WFS) for monochromatic aberrations measured on 21 normal eyes. The second experiment investigated the variation of monochromatic aberrations over the central visual field. Measurements were performed on 60 normal eyes and the data was used to produce a statistical model of population distributions of Zernike coefficients. It is hoped this data will aid future designs for ocular multi-conjugate adaptive optics systems endeavouring to achieve wide-field high resolution retinal images.

## Declaration

I certify that this thesis which I now submit for examination for the award of Master of Philosophy, is entirely my own work and has not being taken from the work of others save and to the extent that such work has been cited and acknowledged within the text of my work.

This thesis was prepared according to the regulations for post graduate study by research of the Dublin Institute of Technology and has not been submitted in whole or in part for an award in any other Institution or University.

The work reported on in this thesis conforms to the principals and requirements of the Institute's guidelines for ethics in research.

The Institute has permission to keep, to lend or to copy this thesis in whole or in part, on condition that any such use of the material of the thesis be duly acknowledged.

Signature

Matthew Thomas Sheehan

Date

4th April 2008

## Acknowledgements

Thanks very much to my two principal supervisors: Prof. Chris Dainty and Dr Veronica O'Dwyer. Two very clever scientists, and also very friendly and genuinely excellent people to work with. This work has relied heavily on their advice and instruction.

The Applied Optics group at NUIG – everyone, thank you. Especially Sasha.

Optometry at DIT – lecturers, staff, and students - thank you. Especially John.

To my supervisors; Prof Chris Dainty, Dr Veronica O'Dwyer, Dr Vincent Toal, and Dr Brenda McGrath – thank you

This research is funded by a Science Foundation Ireland grant No. SFI/01/PI.2/B039C and Dublin Institute of Technology.

## Abbreviations list

Adaptive optics (AO)

Charge coupled device (CCD)

Commission Internationale de l'Eclairage (CIE)

Contrast sensitivity function (CSF)

Diopters spherical (DS)

Diopters cylindrical (DC)

Full width half maximum (FWHM)

Graphical user interface (GUI)

Hartmann-Shack (HS)

Laser *in situ* keratomileusis (LASIK)

Light emitting diode (LED)

Modulation transfer function (MTF)

Multi-conjugate adaptive optics (MCAO)

Optical Society of America (OSA)

Point spread function (PSF)

Region of interest (ROI)

Root mean square (RMS)

Retinal pigmented epithelium (RPE)

Signal to noise ratio (SNR)

Super luminous diode (SLD)

Short wavelength cones (SWC)

Wavefront sensor (WFS)

## Table of contents

**CHAPTER FOUR**

## Optical system components



**CHAPTER FIVE**

## Software development and functions

# Table of figures

## Chapter One

## Chapter Two

## Chapter Three



## Chapter Four

## Chapter Five



## Chapter Six

## Chapter Seven



## Chapter Eight

# List of tables

# CHAPTER ONE

## Introduction to optics, aberrations and Hartmann's test

This chapter introduces some fundamental concepts regarding light and defines important parameters that will be used throughout this thesis. Geometrical optics and image formation are briefly discussed before outlining aberration theory, Zernike polynomials, and providing a background to Hartmann's test.

### 1.1 Models of light

Physical entities such as light can be modelled to help understand their interactions and to predict behaviour. In some circumstances light displays a particle (corpuscular) nature and is best described as a stream of discrete bundles of energy: photons (fig. 1.1a).

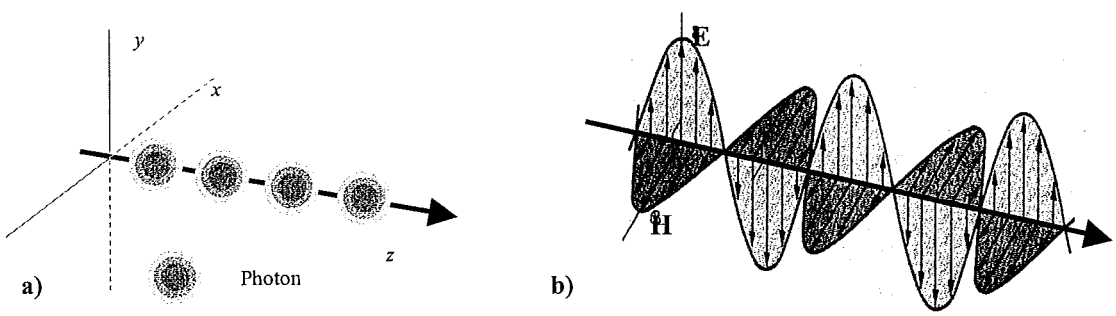


**Figure 1.1 a) The photon model of light and b) the electromagnetic wave model of light (adapted from Alonso and Finn 1992).**

This model is associated with quantum theory, which states that electromagnetic energy is quantised according to Planck's equation,

$$E = h\nu, \tag{1.1}$$

where $E$ is the energy of a photon, $\nu$ is the frequency of light, and $h$ is Planck's constant. In other circumstances light is better described as a propagating transverse disturbance: a wave model (fig. 1.1b). The wave equation is a partial differential equation relating

the dynamics and statics of small displacements of the medium and whose solution may be a propagating disturbance (Lipson *et al.* 1995). The general scalar wave equation is

$$\nabla^2 U = \frac{1}{c^2}\frac{\partial^2 U}{\partial t^2} \quad , \tag{1.2}$$

where $U$ is the optical field, $c$ is the speed of light, and t is time. The general scalar wave equation is a simplification of Maxwell's equations (Lipson *et al.* 1995).

Wave theory is necessary to describe diffraction (bending of light at the edge of an aperture) and interference (the additive nature of component light fields). The vectorial nature of the transverse electromagnetic wave is important in describing polarisation phenomena and when considering anisotropic media (media whose properties are directionally dependant). The photoelectric effect (the liberation of electrons from a metal when photons of a certain energy are incident upon its surface) underpins the physics of charge couple devices (CCDs) and is an example of where a particle model is more appropriate in describing the properties of light. An unambiguous theoretical explanation of all optical phenomena requires a combination of both quantum theory and Maxwell's electromagnetic theory; quantum electrodynamics (Fowles 1989).

### 1.2 Light as an electromagnetic wave

Visible light comprises only a small band of frequencies, approximately $3.8\text{x}10^{14}$Hz to $7.7\text{x}10^{14}$Hz within a much larger spectrum of electromagnetic radiation (Alonso and Finn 1992) as shown in fig. 1.2.

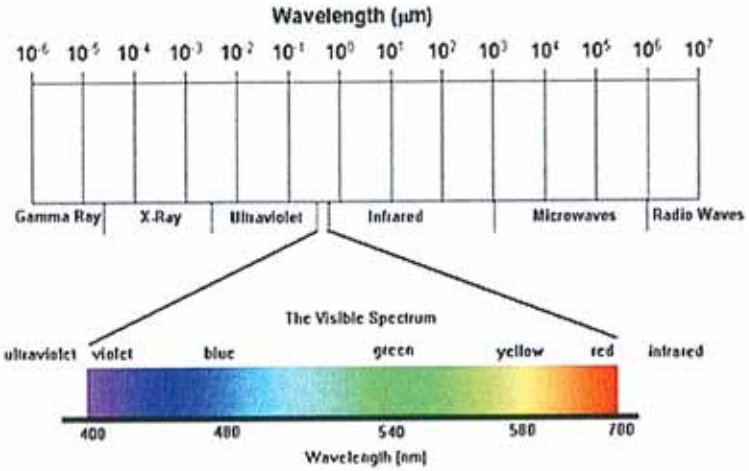


**Figure 1.2 The visible bandwidth of light forms part of the entire electromagnetic spectrum (adapted from Alonso and Finn 1992).**

Light is termed a 'transverse' electromagnetic wave because it propagates through free space in a certain direction while inducing perpendicular electric (**E**) and magnetic (**H**) field vectors in mutually orthogonal transverse planes (fig. 1.1b and fig. 1.3). The Poynting vector ($\prod$) is the cross product of the electric and magnetic fields and specifies the direction and magnitude of the energy flux associated with the light wave according to

$$\prod = \mathbf{E} \times \mathbf{H} \ . \qquad (1.3)$$

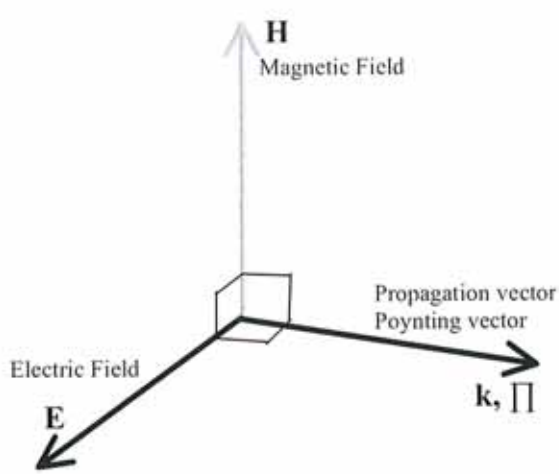


**Figure 1.3 Deposition of vectors in an electromagnetic wave in an isotropic medium (adapted from Lipson *et al.* 1995).**

The electric and magnetic vectors of a light field vary across space and time in a repeating cyclic manner. If an electric (or magnetic) test particle is placed in the path of a light wave, that particle accelerates and undergoes oscillation with each cycle of the wave. The time taken for one complete cycle of the wave to pass through a point in free space is called the period *(T)*. The frequency ($\nu$) of the wave is defined by the number of complete cycles per unit time. The angular frequency ($\omega = 2\pi\nu$) is an associated entity. The distance spanned by one complete cycle of the wave, measured along the direction of propagation and in free space, is the wavelength *($\lambda$)*. The angular wavenumber ($k = 2\pi/\lambda$) is an associated entity as is the propagation vector (**k**), which has the same magnitude as the angular wavenumber *(k)* and the same direction as the Poynting vector in isotropic media (see section 1.4). The phase ($\varphi = \mathbf{k}\cdot\mathbf{r}-\omega t$) of a wave describes exactly what part of the wave cycle is acting upon a given point in space (defined by position vector, **r**) at a given instant of time (t). As light transverses a point in space, the point experiences a continuous phase change cycling between 0 and $2\pi$ radians. The complex amplitude ($U_0$) of the wave is defined by the maximum magnitude of disturbance in the associated optical field. A monochromatic scalar light field propagating through a homogenous, isotropic medium can be approximated by a simple harmonic wave as illustrated in fig. 1.4 and described by

$$U(\mathbf{r}, t) = U_0 \exp\left(i\left(\mathbf{k}\cdot\mathbf{r} - \omega t\right)\right). \qquad (1.4)$$

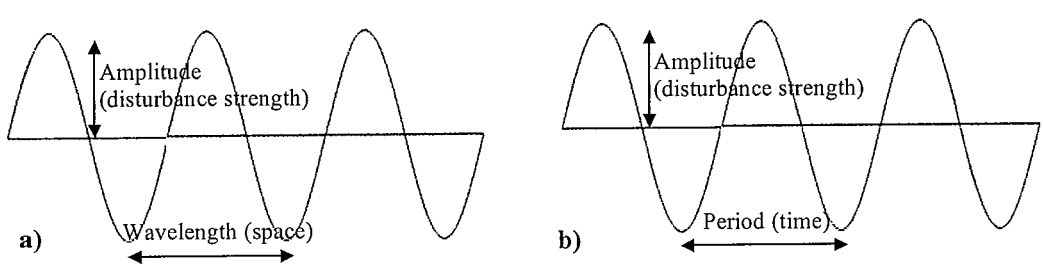


**Figure 1.4 A simple harmonic wave in one dimension of a) space and b) time (adapted from Alonso and Finn 1992).**

Because we perceive light of different frequencies as different colours, a light field composed of only one frequency of light is referred to as monochromatic whereas a light field composed of more than one frequency is referred to as polychromatic or chromatic light. Dispersion of light (the spreading of light into its spectral components) occurs when considering chromatic light in any medium other than free space. This happens because the speed of light in the medium depends on the frequency of the incident light. Equation 1.4 is a non-dispersive wave equation that assumes monochromatic light. Chromatic light gives rise to concepts such as a wave group with an associated group velocity and group frequency. Nearly all objects we observe in the world either emit or reflect chromatic light and thus dispersion and chromatic aberration effects are important considerations for vision.

### 1.3 Detecting light

The speed of light is so great that optical detectors are not capable of determining the phase of a light field directly. Phase is only measurable in a relative context, for example by using a coherent reference light field (such as a laser) in interference phenomena. Optical systems typically use detectors that are sensitive to irradiance ($I$) of light. Irradiance (power per surface area incident on the detector) is the magnitude of the average Poynting flux and is proportional to the square modulus of the amplitude of the electric field ($\mathbf{E}_0$),

$$I = \frac{n}{2\sqrt{(\mu_0/\varepsilon_0)}}\left|\mathbf{E}_0\right|^2 = \frac{\langle \Pi \rangle k}{\mathbf{k}} \quad , \tag{1.5}$$

where $n$ is the refractive index, $\mu_0$ is a constant called the permeability of the vacuum, $\varepsilon_0$ is a constant called the permittivity of the vacuum, and $\mathbf{E}_0$ is the maximum magnitude of disturbance in the electric field.

Light detectors in optical systems (including the human vision system), typically rely on both colour and contrast to distinguish between signals from different objects. An example of contrast is given in fig. 1.5a, which shows a grating pattern with sinusoidal variation in irradiance

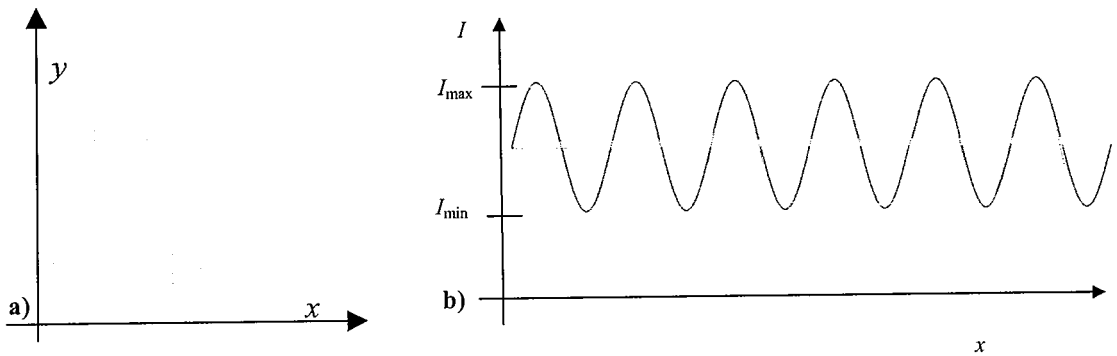


**Figure 1.5 a) An example of a grating pattern with sinusoidal variation in irradiance, and b) the irradiance profile of a line sample taken horizontally through the pattern (adapted from Freeman and Hull 2003).**

Contrast (C) is defined as

$$C = \frac{I_{max} - I_{min}}{I_{max} + I_{min}} \quad , \tag{1.6}$$

where $I_{max}$ is the maximum irradiance value in the profile and $I_{min}$ is the minimum irradiance value in the profile (fig. 1.5b). The eye exhibits a variation in sensitivity to different frequencies as measured under daylight conditions (see fig. 1.6). This leads to a distinction between the radiometric definition of contrast (equation 1.6) and the photometric definition (equation 1.7), which accounts for the photopic spectral sensitivity of the human visual system and is defined by

$$C = \frac{L_{max} - L_{min}}{L_{max} + L_{min}} \quad , \tag{1.7}$$

where $L$ is luminance, and indicates the density of luminous intensity in a given direction. The spectral sensitivity of the human visual system (fig. 1.6) must be

considered when converting wavefront sensor (WFS) measurements typically performed with red or infrared monochromatic sources to meaningful values in the real world (a polychromatic environment). Any conversion of WFS measurements should also consider the chromatic aberration of the eye and compensate for this. Assuming a standard photopic[1] observer as defined by the Commission Internationale de l'Eclairage (CIE) one might choose 555 nm as an appropriate reference wavelength for standardising the reporting of ocular aberrations, but currently there is no accepted agreement in this regard (Thibos *et al.* 2004). If a standard wavelength for reporting ocular aberrations is implemented in the future, suitable conversion models and formulas would be required at least for the defocus term, if not for higher-order aberrations too.

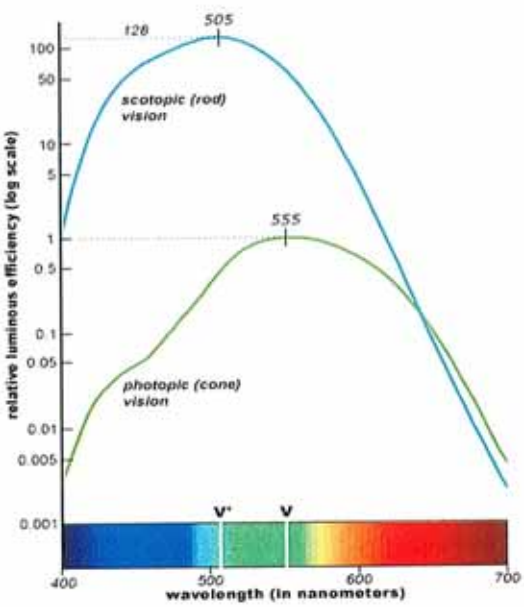


**Figure 1.6 Relative luminous efficiency of equal incident radiant fluxes as a function of wavelength, for the CIE standard photopic and scotopic observer (Commission Internationale de l'Eclairage 1970).**

## 1.4 Optical media and light sources

The properties of light change as it enters a medium. The typical media of significance for optical systems are air, metals, clear fluids, glasses and crystals. Media differ in how

[1] It is sufficient for our purposes to define photopic vision as that measured under normal daylight conditions and scotopic vision as that measured under normal nightlight conditions.

they act on the amplitude, phase, polarisation and speed (or any such combination) of light waves. Most transparent optical media are nonmagnetic (Fowles 1989). The transparency, reflectivity and absorption qualities of an optical medium can be described by the quantum model of electron orbits in the associated atoms of the medium (Born and Wolf 1980). Homogenous media have uniform optical properties in all parts of the medium. Isotropic media are equivalent in all directions in space, and there is no difference between right-handed and left-handed rotation (Lipson *et al.* 1995). A linear medium is one in which the disturbance produced by an applied electric or magnetic field is proportional to that field. Since traditional laboratory light fields (including those used in this work) are several orders of magnitude weaker than interatomic electric fields, their effects are consequentially considered linear (Lipson *et al.* 1995).

Light sources can be categorised in numerous ways, for example, according to the angular subtense (point source or extended source) or emission spectrum (monochromatic or chromatic). Another important categorisation is by coherence. The coherence of light describes the accuracy with which it can be represented by a pure sine wave (Lipson *et al.* 1995). Coherence properties of light waves are a function of both time and space. A point source (e.g. a star) is transversally coherent while an extended source (e.g. the sun) is transversally incoherent. A quasimonochromatic source (e.g. a laser) is temporally coherent while a chromatic source (e.g. an incandescent lamp) is temporally incoherent. Such absolute definitions are not strictly accurate, as most everyday sources of light are *partially* coherent. Coherence of light is an important consideration for wavefront sensing because a coherent source produces an irregular pupil irradiance distribution after reflection from the optically rough retina. This

subsequently produces speckled Hartmann Shack (HS) spots and reduces the accuracy at which their centroids can be estimated, thus contributing to the overall uncertainty of measurements. Angular subtense of the source is another important consideration for HS WFSs because it affects HS spot quality, centroid determination, and dynamic range. Marcos *et al.* (2002) found the polarisation state of the source used in a HS WFS does not significantly alter the ocular aberrations measured, and similar conclusions have been made for measurements regarding other aberrometers (Prieto *et al.* 2002).

### 1.5 Geometrical optics

Geometrical optics provides a simple approach to optical problems based on the idea that light propagates along straight lines (rays) until acted upon at boundaries. Ray angles and distances are calculated to examine the relationships between parameters of interest (e.g. magnification, conjugate positions) in an optical system. The laws of geometrical optics present many conceptual similarities to those of classical mechanics. The most general of which is Fermat's principle, which is analogous to the principle of least action described by Maupertuis in 1746. Although it uses numerous approximations, geometrical optics is very practical at explaining most phenomena we observe from light and often provides reasonably accurate predictions.

The law of rectilinear propagation is an easily observed concept from the geometrical optics approximation. Light appears to travel in a straight path if uninterrupted - a shadow cast by an opaque object exemplifies this[2]. Optical systems are modelled in geometrical optics by 'ray tracing' this straight path of light in sequential steps through the multiple surfaces and elements of an optical system. When illustrating an optical

[2] Wave optics and diffraction theory demonstrate that this is not an entirely accurate statement.

system the rays have arrows to indicate the direction of propagation (and direction of energy in isotropic media). Ray diagrams (fig. 1.7) are typically drawn with rays travelling from left to right and a sign convention is used for all parameters to avoid confusion. A pencil refers to a small group of rays emanating from any point on an extended source or illuminated object. The collection of pencils that pass through the pupil (the limiting aperture of an optical system) is called the beam. Optical elements (e.g. lenses or mirrors) are typically centred along the optical axis which provides a reference for the system.

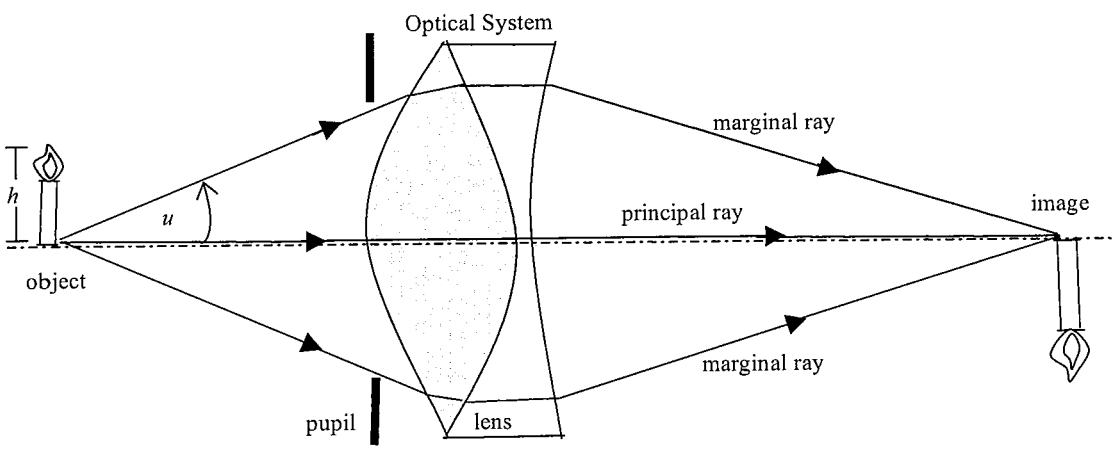


**Figure 1.7 Ray diagram for a simple optical system (adapted from Hecht 1987).**

As light travels through a medium some component of energy is absorbed, however, this is rarely indicated on a ray diagram. When a ray meets a boundary between media, its path may alter direction (fig. 1.8). The component of light that returns back into the original medium is called the reflected ray. The component of light that proceeds into the subsequent medium is called the refracted ray. Specular reflection (fig. 1.9a) describes the reflection at an optically smooth boundary where the angle of reflection is equal to the angle of incidence and a uniform phase change is imparted to the beam. Diffuse reflection (fig. 1.9b) occurs at optically rough surfaces, which impart an irregular phase change to the beam.

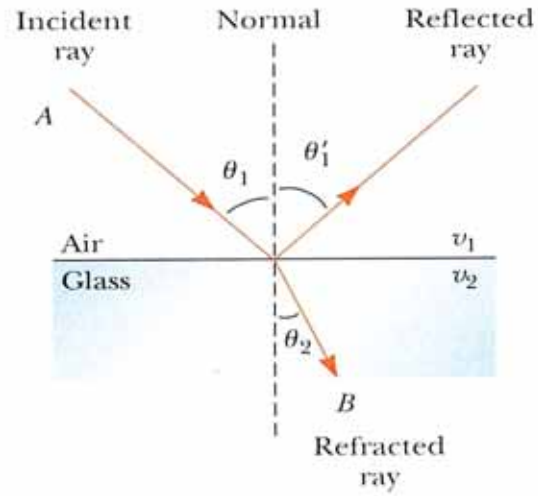


**Figure 1.8 Refraction and reflection at a plane interface (adapted from Serway and Jewett 2004).**

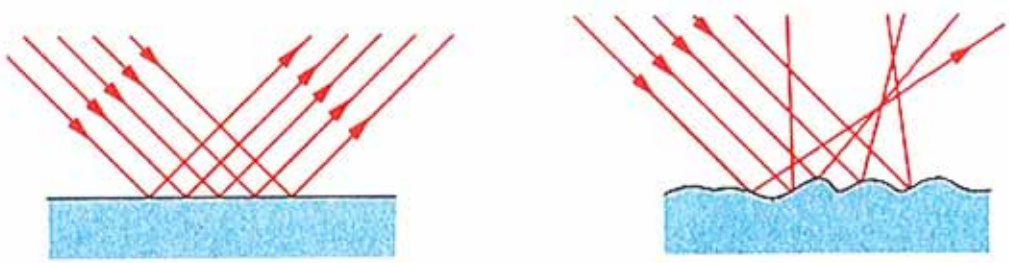

**Figure 1.9 a) Specular reflection and b) diffuse reflection (adapted from Serway and Jewett 2004).**

The speed of light in free space ($c = 2.99792458\times10^8$ m/s) is a fundamental constant. In optical media the speed of light is less than $c$. At a boundary between media, the more optically dense medium will slow the speed of light and its wavelength will decrease. The opposite occurs when light enters a less optically dense medium. The frequency of light remains unchanged at a boundary provided the frame of reference is static. The ratio of the speed of light in free space ($c$) to its speed in an isotropic medium (v) defines the refractive index ($n$) as

$$n = \frac{c}{v} \quad . \tag{1.8}$$

In an optically dense medium (high refractive index), light experiences a 'longer' route, compared to an equal distance in free space. The optical path length *(L)* describes this effect and for a path from A to B, is defined as

$$L = [AB] = \int_A^B n\,ds \quad , \tag{1.9}$$

where *ds* is the differential unit of length

$$ds = \sqrt{dx^2 + dy^2 + dz^2} \quad . \tag{1.10}$$

The optical path length that light experiences as it travels from A to B, through two different refractive indices, is illustrated in fig. 1.10. The optical path length remains constant when the direction of propagation is reversed and the integral in equation 1.9 is examined with swapped end points. This observation gives rise to the principle of reversibility of light – the theory that conjugate points are not dependant on the direction of light.

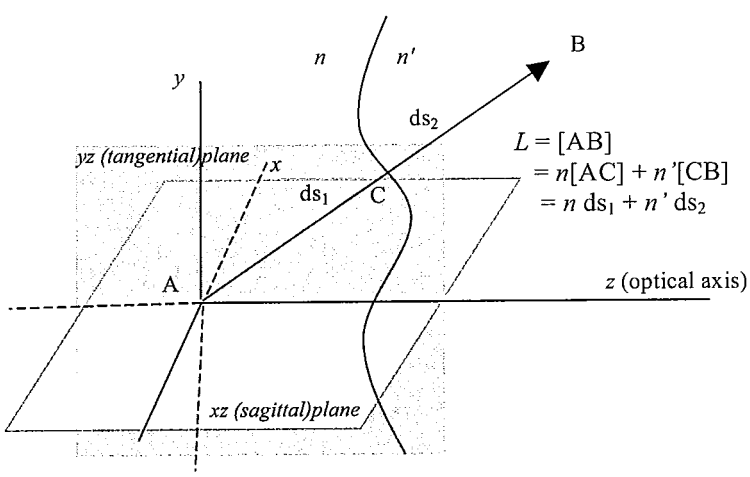


**Figure 1.10 Optical path length for a ray travelling from point A to B, through two refractive indices (adapted from Dainty 2001).**

Fermat's principle is a fundamental concept in geometrical optics. It can be used to derive the law of rectilinear propagation in homogenous media, the reflection law at a boundary, the vectorial refraction law, and the scalar refraction law (Snell's law). It applies to isotropic media and can be summarised as *light will always travel along the stationary path.* Fermat's principle can be used to examine the infinite number of possible paths that light might travel between two points. By setting a small perturbation of the travel time for optical paths from A to B equal to zero, Fermat's principle can then be mathematically expressed as

$$\delta I = \delta \int_A^B f(x, y, z, \frac{\partial x}{\partial t}, \frac{\partial y}{\partial t}, \frac{\partial z}{\partial t}) \partial t = 0 \quad , \tag{1.11}$$

or

$$\delta L = \delta \int_A^B n(x, y, z)\, ds = 0 \quad , \tag{1.12}$$

where δ is a small perturbation of the integral ($I$) describing an infinite number of possible paths that exist for light to travel from point A to B. Fig. 1.11 shows a graphical representation of Fermat's principle and possible solutions to equation 1.12 for three simple optical systems.

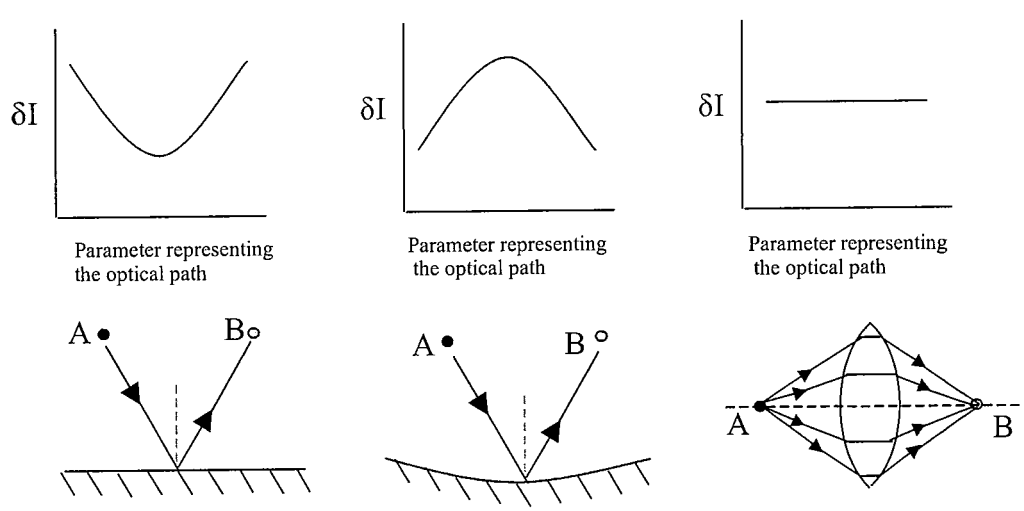


**Figure 1.11 Examples of stationary solutions to optical path length [AB] perturbations. a) plane mirror b) concave mirror c) ideal lens (adapted from Rolland 2006).**

In an ideal optical system there may be a single path or an infinite number of alternative paths that satisfy Fermat's principle at conjugate planes. When the later is true, instead of drawing all of these rays on a diagram, it is common to only draw a few rays that have special significance; the principal ray and the marginal rays (fig. 1.7).

An extremely important consideration in optical design is pupil imagery. The pupil is the limiting aperture within the optical system and its positioning, size and imagery has an overwhelming effect on the imaging quality of an optical system. The optical quality of a system can be drastically improved (or deteriorated) by altering the pupil position and size, which effectively determines which parts of the optical elements are used and which ray is the principal ray. The pupil imagery for the WFS design presented in chapters 3 and 4 is no exception and considerable effort has gone into achieving well-designed pupil imagery.

A wavefront is a surface that connects points on a pencil of rays that have propagated an equal optical path length from a point source (fig. 1.12). As such, a wavefront can be described as a surface of equal time from a point source or as a surface of constant phase (Dainty 2001).

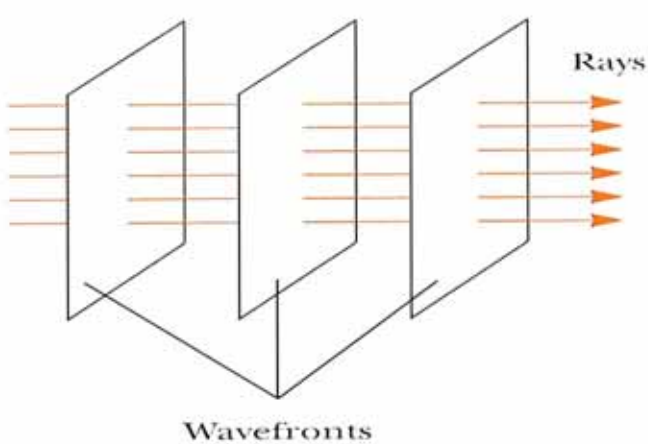


**Figure 1.12 Plane wavefronts associated with collimated rays of light (adapted from Serway and Jewett 2004).**

Malus's theorem considers a pencil of rays in an isotropic medium and their associated wavefronts that have emanated from a point source (fig. 1.13). Such a pencil of rays posses normal congruence, and even after refraction or reflection (typically the pencil of rays are no longer homocentric) the rays and wavefront again form normal congruence (Alonso 1948). Malus's theorem is summarised mathematically as

$$\boldsymbol{T}_W \perp \mathbf{r} \ , \tag{1.13}$$

$$\boldsymbol{T}_W \cdot \mathbf{r} = 0 \ , \tag{1.14}$$

where $T_W$ is a vector tangent to the wavefront and r is a ray vector.

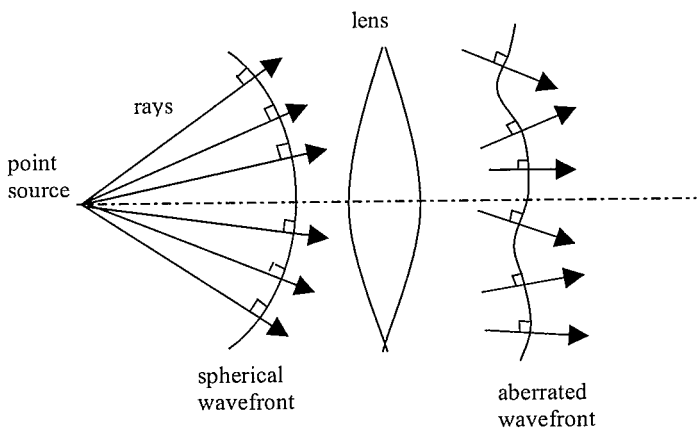


**Figure 1.13 Malus's theorem illustrating normal congruence before and after refraction (adapted from Hecht 1987).**

In about 1650, Huygens introduced a conceptual construction (fig. 1.14) that uses wavelets to predict the propagation of light (Lipson *et al.* 1995). If a wavefront is known at a certain moment, then each point on the wavefront can be treated as a new source of disturbance. Each point can be considered to emit a secondary spherical wavelet (assuming isotropic media) and the wavefront at some time later is the surface which envelopes all of these new disturbances. Figs. 1.12 and 1.14 respectively illustrate the significance of a plane wavefront which retains its shape during

propagation, and a spherical wavefront which emanates from a point source in isotropic homogenous media.

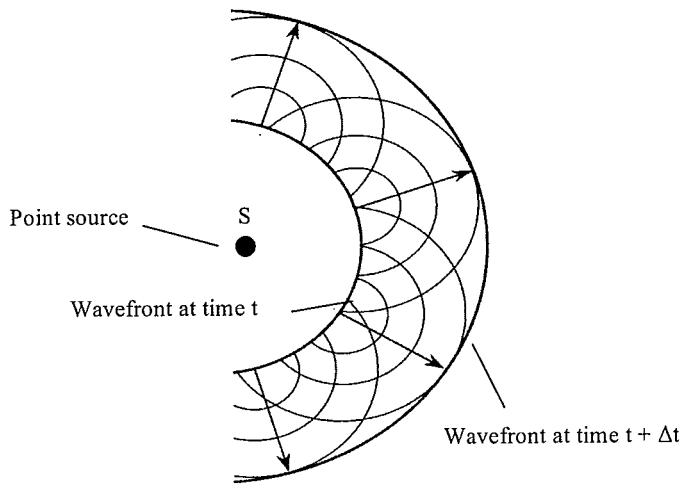


**Figure 1.14 Huygen's construction used to predict the location of a wavefront (adapted from Hecht 1987).**

Nearly all formulas used in geometrical optics are only valid for rays with small angles of incidence at a boundary. This is called the paraxial approximation,

$$\sin\theta = \theta + \frac{\theta^3}{3!} - \frac{\theta^5}{5!} + \frac{\theta^7}{7!} + \ldots\ldots\ldots \approx \theta \ , \tag{1.15}$$

where $\theta$ is the angle of incidence measured in radians. It is often called a first order approximation because the true infinite polynomial equation is approximated by its first term. The same approximation can be applied to truncate the expansion describing a spherical surface to its first term. The paraxial approximation becomes unsatisfactory when considering rays with large angles of incidence. The decision to approximate an expansion to a simpler term can be made using Marechal's condition (or equivalently the Rayleigh criterion), which truncates any terms on a wavefront or surface with a magnitude less than $\lambda/4$ (Dainty 2001). For small aberrations, this is approximately equivalent to a Root Mean Square (RMS) value of $\lambda/14$ or equivalently a Strehl Ratio of

0.8 (see section 1.7). Even a perfectly constructed optical system exhibits aberrations - simply because the paraxial approximation is not valid at all ray angles.

The Lagrange Invariant *(H)* is an important parameter that features in many geometrical optics equations, including those describing Seidel aberrations (see section 1.9). In any optical system, $H$ remains a constant no matter what the optical arrangement and is thus *invariant*. The flux of light through an optical system is proportional to $H^2$. The Lagrange Invariant may be defined as

$$H = nuh \ , \tag{1.16}$$

where $u$ is the marginal ray angle and $h$ is the object height (fig. 1.7). Alternatively, for an object at infinity it may be defined as

$$H = -nh'\eta \ , \tag{1.17}$$

where $\eta$ is the field angle and $h'$ is the ray height at the first principal plane (fig. 1.15).

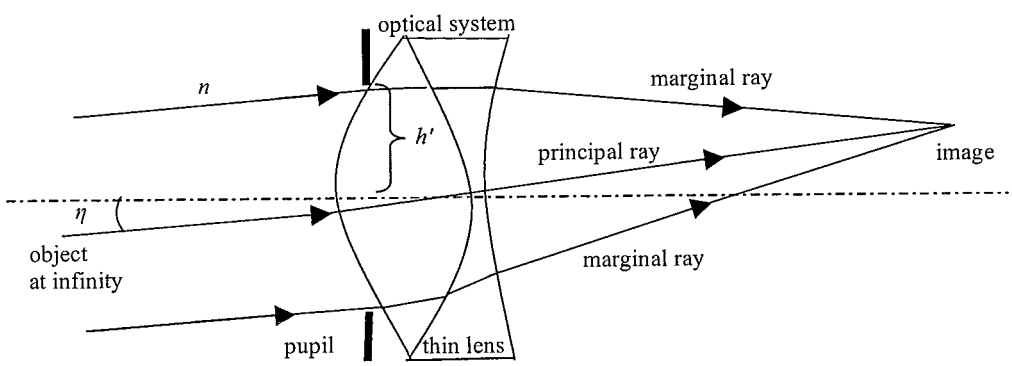


**Figure 1.15 The Lagrange Invariant for an object at infinity and a thin lens (adapted from Dainty 2001).**

## 1.6 Imaging

Optical systems are used to control and manage light for numerous applications, the most common of which is imaging. Propagating light can be thought of as information that is being transported in the form of energy. The information has come from the object of interest which may be a source itself, or an object's surface that light has diffusely reflected off. Information is coded into the amplitude, frequency, polarisation, and phase. To decode the information, optical systems reconstitute the light from the object as an image.

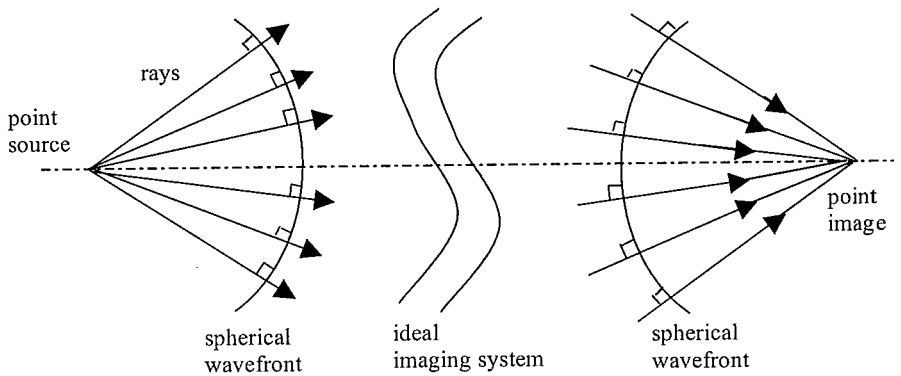


**Figure 1.16 A convex spherical wavefront incident on an ideal imaging system creates a concave spherical wavefront (adapted from Dainty 2001).**

At each field point in object space a pencil of diverging rays emanate with an associated spherical wavefront (assuming homogenous isotropic media). To achieve good imaging these rays must be precisely recombined at the conjugate field point in image space, whether it be virtual or real. In the ideal case the pencil of rays would be associated with a collapsing spherical wavefront (assuming a real image) and all rays would intersect the image point after having travelled an equal optical path length (fig. 1.16). In other words, for each image point, rays are recombining with the same phase relationship they held with each other when first departing the object point. Ideally the optical flux would also be high for all field points, implying that vignetting is well controlled.

There are numerous reasons why real optical systems do not create perfect images; there may be alignment errors, positioning errors, faults in manufacturing, polishing embellishes or any number of design flaws within the system. But even if all these potential defects were removed, the image quality of a real system would still be limited by the effects of three different phenomena; diffraction, scatter and aberrations. Furthermore, psychophysical studies of the visual system must also consider cognition and a multitude of associated neural processes that limit (or in some cases enhance) visual performance, in addition to those that impact on ocular image quality.

Diffraction is a consequence of the wave nature of light and the fact that apertures in an optical system are finite. It describes the bending of light at the edge of an aperture and defines a fundamental limit to the resolution capability of any optical system (discussed further in section 1.7). The consequence of diffraction may be observed in the image plane where a paraxial pencil of light, having passed through the pupil, is not condensed into a single point, but rather is spread into a predictable irradiance pattern (the point spread function) which is dependant upon the wavelength, focal length of the system, and pupil diameter. In a typical human eye, retinal image blur caused by diffraction is negligible when compared to the effects of aberrations for pupil diameters greater than approximately 3mm (Roorda 2005, Salmon *et al.* 1998). This is in similar agreement to Freeman and Hull (2003) (fig. 1.18) who suggests the inflexion point occurs at approximately 4mm diameter. When the pupil diameter is greater than 4.5mm, diffraction has little or no effect on visual acuity, as any image blur induced by diffraction is within the resolving power of the foveal cones (Dave 2004). The minimum angular resolution ($\theta$ min) of a diffraction-limited model eye is illustrated in

fig. 1.17. Assuming a wavelength of 555nm and a pupil diameter of 6mm, $\theta$ min would be approximately 0.4 minutes of arc for the eye.

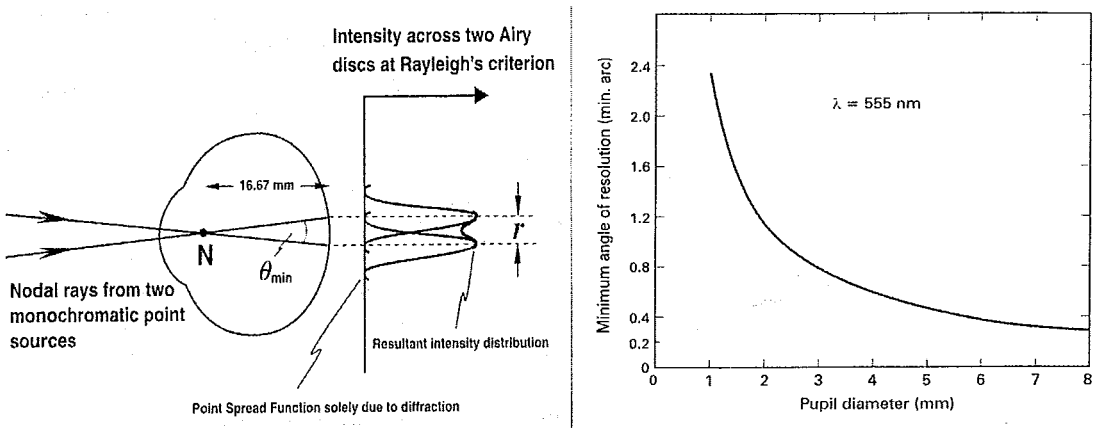


**Figure 1.17 a) The diffraction limit of the human eye (Tunnacliffe 1993) and b) a plot of minimum angle of resolution vs. pupil diameter for a diffraction-limited eye (Freeman and Hull 2003).**

Scatter is the deflection of photons by small particles within an optical medium. Particles are excited by the energy of the photon and then reradiate the portion of the electromagnetic energy that is not absorbed at differing trajectories. This interaction requires various models depending upon the ratio of the particle size to the wavelength of light. In the eye, scatter results in a smeared retinal image and a reduction of contrast, thus degrading the image quality (Cox *et al.* 2003). The eye has numerous features that limit the effects of scatter and they are described throughout chapter two.

Researchers using adaptive optics (AO) to image the retina, in certain experiments may or may not be concerned with the psychophysical effects that result from neural processes. Researchers investigating the potential real world improvements in visual performance from higher-order aberration correction certainly are concerned with these neural processes. This research area is complex and includes considerations such as receptive field status, the Stiles-Crawford effect, adaptation to pre-existing aberrations, photopic and scotopic spectral sensitivity, pupil size control and feedback, and

accommodation control and feedback. The schematic graph in fig. 1.18 shows the resolution ability of the visual system as a function of natural pupil size. It indicates that diffraction is the limiting factor for angular resolution with small pupils, while both aberrations and neural processing factors become the predominant limiting factors for angular resolution with large pupils. Spatial and temporal summation (two key neural processes of the retinal receptive fields) are at a minimum level during photopic conditions when photons are abundant and the natural pupil size is small. The natural pupil size itself is determined by a complex interaction between retinal luminance (typically described by scotopic, mesopic, or photopic viewing conditions), age, accommodation state, natural occurring individual anatomy, and retinal image blur.

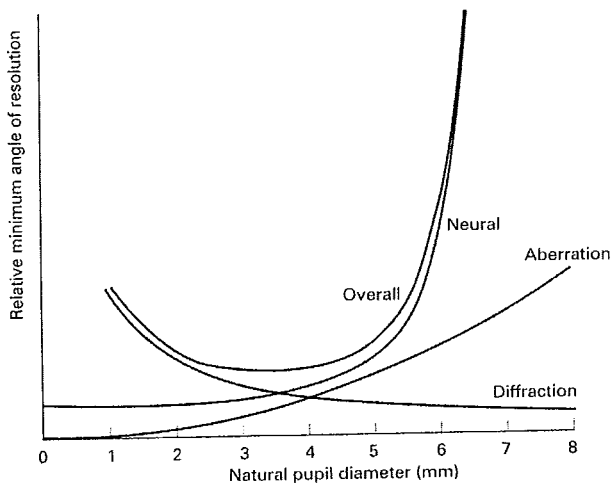


**Figure 1.18 Schematic plot of relative minimum angle of resolution vs. natural pupil diameter (Freeman and Hull 2003).**

Although diffraction, scatter and neural processing are important in the human eye, the principal concern of this work is the ocular aberrations. In real optical systems, rays are displaced from their ideal positions in the image plane as predicted by the paraxial approximation. These ray displacements degrade the image quality and give rise to aberrations (see section 1.8 for a full introduction). Measuring the aberrations of an optical system is only one technique out of many for quantifying optical performance.

## 1.7 Metrics of image quality and the diffraction limit

Linear system theory can be used to describe the action of an optical system $S$ on an object $f(x,y)$ to produce an image $g(x,y)$. A linear system produces an output that is proportional to the sum of the individual inputs, such that

$$g(x,y) = S\{f(x,y)\} \ , \tag{1.18}$$

and satisfies scaling and superposition properties

$$S\left\{\sum_i \alpha_i f_i(x,y)\right\} = \sum_i \alpha_i \, S\{f_i(x,y)\} = \sum_i \alpha_i \, g_i(x,y) \ , \tag{1.19}$$

where $\alpha_i$ represents any scalar value (Goodman 2005). Although objects and images are continuous functions, it is convenient to consider a single point at the object plane (at $(x_1, y_1)$) and how it is realised in the image plane (the point spread function). If this fundamental process is understood then linear system theory describes imaging a more complicated object as simply a repetition of this same process for all points of the object surface, taking into account the differences in positioning coordinates. Representing the object as a linear combination of weighted and displaced delta functions (Brookes 2004) leads to

$$g(x,y) = \int_{-\infty}^{\infty}\int_{-\infty}^{\infty} f(x_1,y_1)\, h(x,y;x_1,y_1)\, dx_1, dy_1 \ , \tag{1.20}$$

where $h$ is the point spread function (PSF). If the system is shift-invariant,

$$h(x,y;x_1,y_1) = h(x-x_1, y-y_1) \ , \tag{1.21}$$

and equation 1.18 then becomes a convolution integral that simplifies to

$$G(u,v) = F(u,v)\, T(u,v) \tag{1.22}$$

in the Fourier domain, where $T$ is the Optical Transfer Function (OTF), which is the Fourier transform of the PSF (Goodman 2005). The PSF represents the irradiance

distribution of a point source imaged by the system. The PSF appears as a 'blob' of light, however if the quality of the optical system is improved this 'blob' reduces in size until it reaches a limit where it can't be any narrower. When this occurs the light energy is highly concentrated and the rays are all intersecting precisely at the same point in image space. Such a system is said to be *diffraction limited* because the diffraction effects of the light wave are now limiting the resolution and the system is free of any measurable aberrations. If an optical system is diffraction limited and the pupil of the system is circular, the distribution of the PSF has a characteristic appearance called the Airy disc (fig.1.19).

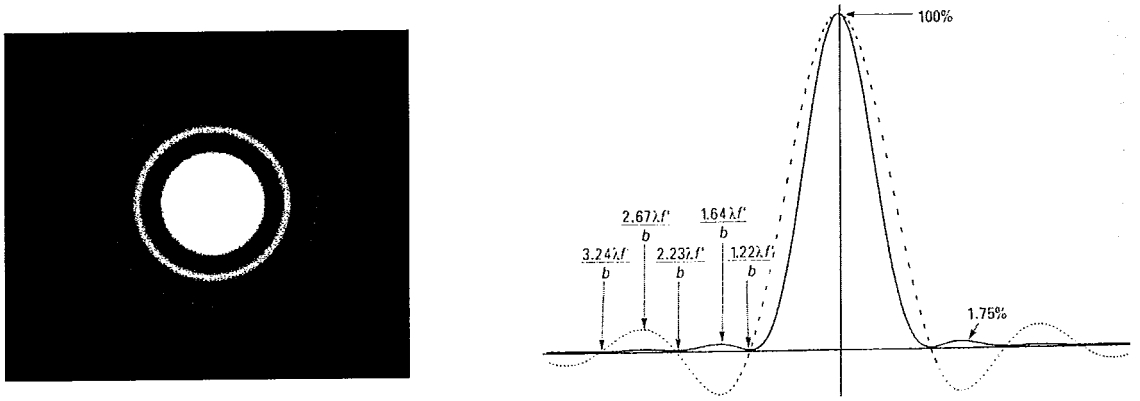


**Figure 1.19 a) Airy disc profile in the *xy* image plane, b) Airy disc profile in *zx* or *zy* image plane. Irradiance (solid line) and amplitude (dashed line) of the Airy disc. Notation indicating 0$^{th}$ order minimum to 2$^{nd}$ order minimum is explained in the text (Freeman and Hull 2003).**

The Airy disc represents a fundamental limit to imaging quality and is given by an approximation called the Fraunhofer far-field diffraction formula, according to

$$U(r) \propto 2\pi \frac{b^2}{4} \frac{J_1(\chi)}{\chi} \quad , \tag{1.23}$$

where $U(r)$ is the amplitude of the light field, r is the transverse distance from the centre of the diffraction pattern ($r = \sqrt{x^2 + y^2}$) in the image plane, $b$ is the pupil diameter of the system, $J_1$ is the first order Bessel function of the first kind, $\chi = \pi br/\lambda f$, and $f$ is the distance from the pupil to the image plane. The irradiance distribution is therefore

$$I(r) \propto \pi^2 \frac{b^4}{16}\left[\frac{2J_1(\chi)}{\chi}\right]^2, \tag{1.24}$$

and solving for the $0^{th}$ order minimum, the first dark ring of the Airy disc occurs at $r = 1.22\lambda f/b$ in the image plane (Fowels 1989).

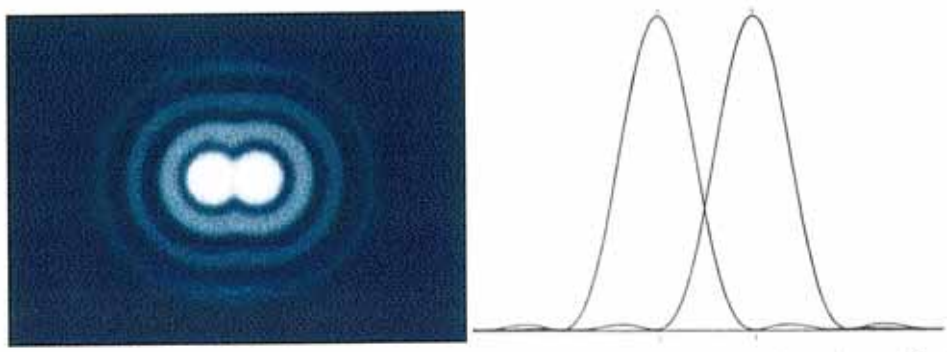

**Figure 1.20 Two point spread functions just resolved by Rayleigh's criterion a) profile in the *xy* image plane, b) irradiance profile in *zx* image plane (adapted from Freeman and Hull 2003).**

The Rayleigh criterion defines the limit of angular resolution occurring when two point sources are separated such that the central maximum of one PSF coincides with the $0^{th}$ order minimum of the fellow point's PSF (fig.1.20).

The Strehl ratio is a metric of image quality and may be defined as the ratio of the maximum of the PSF relative to the maximum of the diffraction-limited PSF for the same system parameters (e.g. wavelength, pupil size). Applying the Rayleigh criterion, a system with a small amount of aberration is considered to be diffraction-limited if the Strehl ratio is greater than 0.8 (Marcos 2003), as approximated by

$$Strehl\ ratio \approx 1 - \left(\frac{2\pi}{\lambda}\right)^2 \cdot wavefront\ variance. \tag{1.25}$$

The modulation transfer function (MTF) of an optical system may be used to describe imaging quality. It represents the image contrast reproduced by the system for a sinusoidal pattern object as a function of spatial frequency (Marcos 2003). The eye has

a 'low-pass' MTF implying that high spatial frequencies contained in an object will not be transmitted by the optics of the eye to the retina. The high frequency cut-off for the normal human eye is approximately 60 cycles per degree (National Research Council 1985). It is important to note that even if a specific spatial frequency is adequately imaged on the retina with sufficient contrast, that frequency is still subject to neural processing throughout the visual pathway and may not necessarily be consciously perceived by the subject. In consideration of the neural processing effects of the visual system, researchers use the contrast sensitivity function (CSF) (fig.1.21). This is a psychophysical function representing the inverse contrast threshold of a sinusoidal grating pattern that is 'just visible' as a function of spatial frequency. A logarithmic scale is normally used due to the large dynamic range of the visual system (National Research Council 1985).

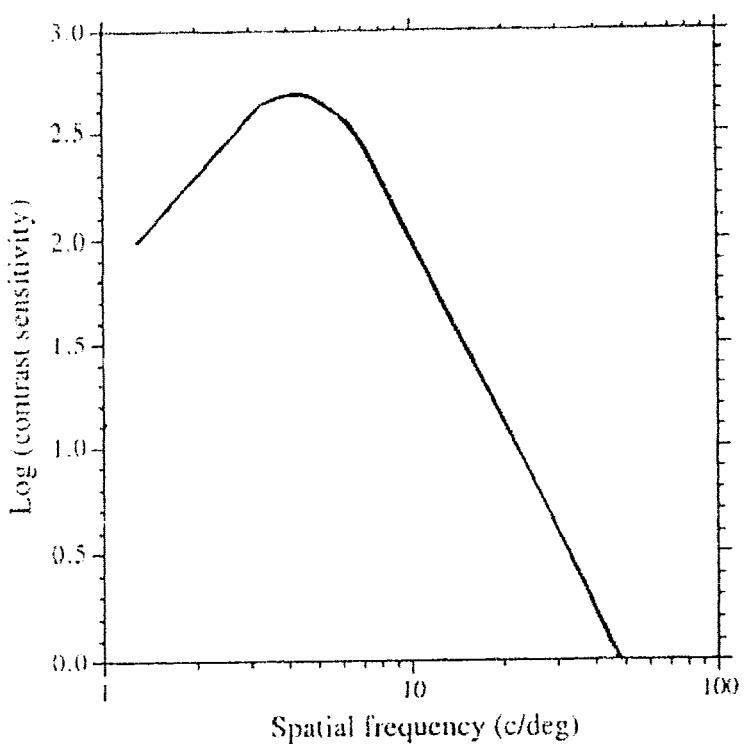


**Figure 1.21 The contrast sensitivity function for a human eye (adapted from Campbell and Green 1965).**

## 1.8 Monochromatic aberration theory

An ideal imaging system maps light from each point in object space to its respective conjugate point in image space as discussed in section 1.6. Optical systems behave ideally in the paraxial approximation, however real systems are typically expected to operate outside this region and image rays that have large angles of incidence. Thus even in the absence of any manufacturing faults, the rays of a real system may be departed from their ideal location. The severity in which a system departs from the paraxial approximation is somewhat represented by the f-number[3] (because some of the parameters that determine the angle of incidence of the marginal ray are the same parameters that determine the f-number). However, the f-number gives no indication of what type of aberrations we might expect in an optical system.

In the image plane the angular deviations of rays from ideal for each particular field point gives rise to transverse and longitudinal aberrations (fig. 1.22). Transverse aberrations are measured as the difference between the ray intersection in the image plane ($xy$) compared to the intersection of the principal ray. Similarly the deviation along the optical axis gives rise to longitudinal aberrations which are measured as the longitudinal difference between the ray intersection with the principal ray compared to the intersection of the principal ray with the image plane.

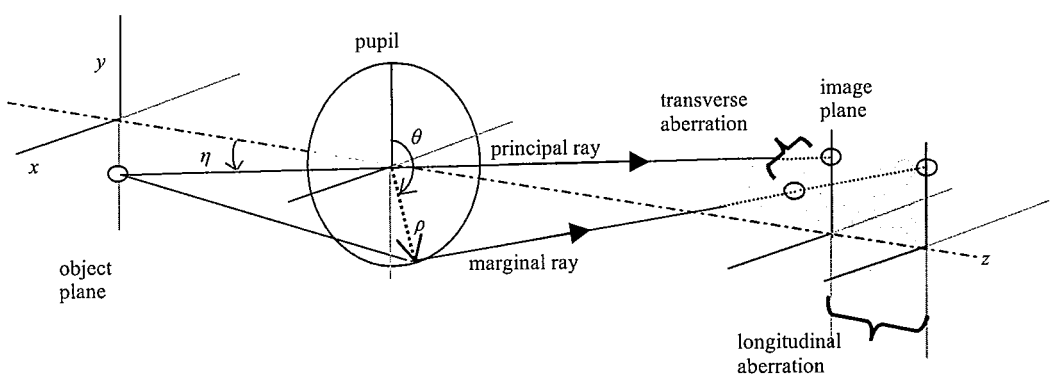


**Figure 1.22 Transverse and longitudinal aberration (adapted from Dainty 2001).**

[3] F-number of an optical system is defined as the focal length divided by entrance pupil diameter.

Aberrations may also be described by their effect in the pupil plane where the phase difference between the wavefront and its ideal counterpart gives rise to the wavefront aberration *(W)*. The wavefront aberration is the optical path length along the optical axis between the aberrated wavefront and the reference wavefront (which is arbitrarily constructed as a sphere or plane surface to suit the particular application) and is dependent upon each point on the wavefront surface ($\theta$, $\rho$) and the field angle ($\eta$) (fig. 1.22). The pupil angle ($\theta$) is measured clockwise from the vertical axis and field points in the object plane are defined along the vertical axis for the following Seidel aberration definitions.

### 1.9 Seidel aberrations

In 1855-56 Ludwig Von Seidel described what are commonly referred to as third order aberrations or Seidel aberrations[4]. This analysis assumes monochromatic light and rotationally symmetric surfaces. The aberration polynomial is derived by considering the contribution of the second term in the sine function identity series ($\theta^3/3!$) that would normally be truncated if using the first order paraxial approximation (Welford 1989). Equivalently, it may be derived from the $\rho^4/8r^3$ term in the binomial expansion for a spherical surface.

When consideration is extended to include off-axis field points, the rotationally symmetric $W(\rho)$ becomes dependent upon a field angle ($\eta$) and pupil angle ($\theta$) components as well as the radial component ($\rho$). To simplify aberration metrics, Seidel coefficients ($S_n$) are usually quoted in reference to the maximum values of $\rho$ and $\eta$ (i.e. for the marginal ray from the field point at the extreme edge of the field). The

[4] For a comprehensive discussion of Seidel aberrations the reader is directed to Welford's book (1989).

normalisation of $\rho$, and $\eta$ makes them dimensionless. The Seidel coefficients have units of length$^{-3}$ and can be transposed to account for a change in the pupil position by calculating the eccentricity of the principal ray.

The aberration polynomial, $W(\rho,\theta,\eta)$, can be arranged and grouped according to the order of the field angle. Neglecting focus and tilt terms, and removing constant terms, the aberration polynomial may be described using $b_n$ coefficients as

$$W(\rho,\theta,\eta) = b_1\rho^4 + b_2\eta\rho^3\cos\theta + b_3\eta^2\rho^2\cos^2\theta + b_4\eta^2\rho^2 + b_5\eta^3\rho\cos\theta \ . \qquad (1.26)$$

This arrangement of terms lends itself to classifying five different aberrations; spherical aberration, coma, off-axis astigmatism, field curvature and distortion. The Seidel arrangement of the aberration polynomial is perhaps more insightful:

$$W(\rho,\theta,\eta) = \frac{1}{8}S_1\rho^4 + \frac{1}{2}S_2\eta\rho^3\cos\theta + \frac{1}{4}(3S_3 + S_4)\eta^2\rho^2\cos^2\theta + \frac{1}{4}(S_3 + S_4)\eta^2\rho^2\sin^2\theta + \frac{1}{2}S_5\eta^3\rho\cos\theta \ . \qquad (1.27)$$

The following definitions of individual Seidel aberrations are defined for a single refracting surface using parameters such as; the Lagrange Invariant ($H$), power ($F$), bending factors ($X$), conjugate factors ($Y$), and various coefficients dependent upon refractive index ($\alpha,\beta,\gamma,\delta,\varepsilon$ and $\xi$). Let us also define the tangential ($yz$) plane and the sagittal ($xz$) plane as shown in fig. 1.10.

Spherical aberration may be defined as

$$W_{spherical} = \frac{1}{8}S_1 = \frac{1}{8}\rho^4F^3(\alpha X^2 + \beta XY + \gamma Y^2 + \delta). \qquad (1.28)$$

It is independent of field angle and is the only Seidel aberration to affect axial images (although it affects off-axis images as well). In the image plane spherical aberration

focuses marginal rays to a different focal length than paraxial rays. Positive notation typically indicates the marginal rays are focussed to intersect the optical axis at a shorter focal length than paraxial rays. This creates a caustic 'funnel and axis' of increased irradiance in the image plane (fig. 1.23). The transverse spherical aberration varies as a function of $\rho^3$ and the longitudinal spherical aberration varies as a function of $\rho^2$ (fig. 1.24). Spherical aberration can be reduced by intentionally defocusing the image plane away from the paraxial focus by a specific amount (dependent upon the criteria used to define 'best focus'), but a single lens can never be completely free of spherical aberration.

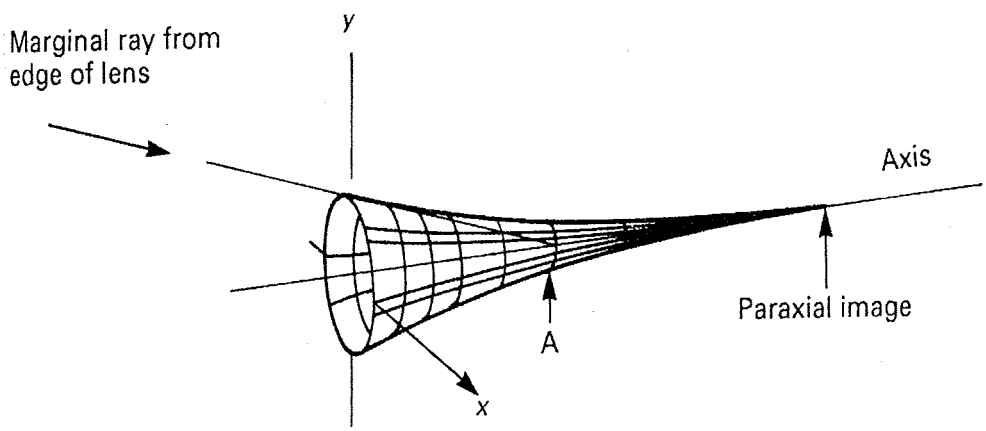


**Figure 1.23 The caustic profile of spherical aberration in the image plane (Freeman and Hull 2003).**

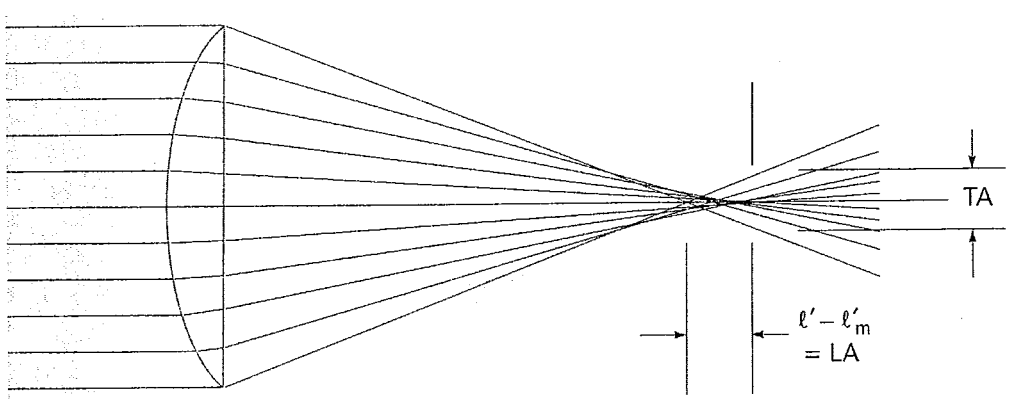


**Figure 1.24 Transverse aberration (TA) and longitudinal aberration (LA) in a lens with spherical aberration (Freeman and Hull 2003).**

Coma may be defined as

$$W_{coma} = \frac{1}{2}S_2 = \frac{1}{2}\rho^2 \cos\theta \; HF^2(\varepsilon X + \xi Y). \tag{1.29}$$

It is due to magnification differences between the centre of the lens and the lens margins. Rays passing through the marginal annulus of the lens have greater magnification than those passing through the centre of the lens. The transverse aberration of coma is circular function on $\rho$ and the field angle also creates a 3:1 differential in the transverse magnification between the tangential and sagittal planes. This produces a comet shaped irradiance distribution in the image plane for an off-axis point source as shown in figs. 1.25a and 1.25b. Because the tangential image is spread over a large area, the sagittal coma appears brighter and the tail of the comet is dull. Coma can be neutralised in the sagittal plane by the *offence against the Abbe sine condition*, (an arrangement that sets the sine of the image ray angle proportional to the sine of the object ray angle). For certain conjugate points, lens bending of a doublet allows the neutralisation of both spherical aberration and coma, thus creating *aplanatic* points.

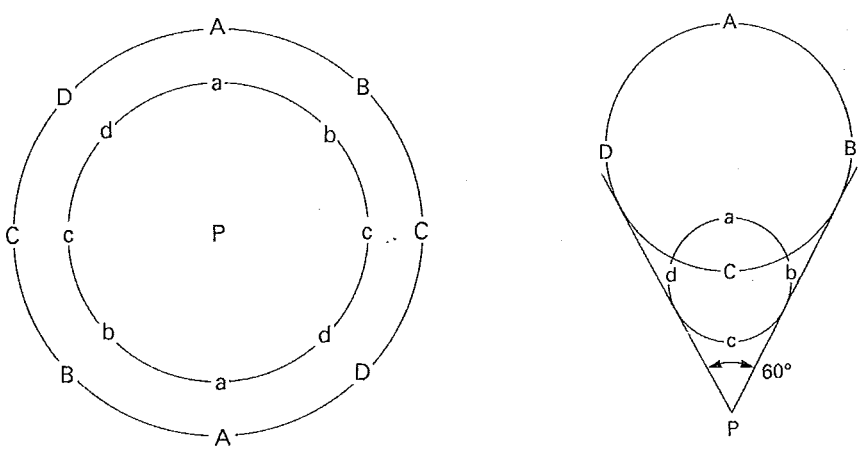


**Figure 1.25 The coma circle in a) the pupil plane and b) the image plane (Freeman and Hull 2003).**

Off axis astigmatism and field curvature are both functions of $\eta^2$ and may be described in combination as in equation 1.27. In reference to fig. 1.26a the tangential ($yz$) plane contains BDE and the sagittal ($xz$) plane contains BAC. Off axis astigmatism and field curvature may be defined as

$$W_{\text{Off axis astigmatism and Field curvature SAGITTAL IMAGE}} = \frac{1}{4}(S_3 + S_4) = \frac{1}{4}\left(H^2F + H^2F/n\right) \qquad (1.30)$$

and

$$W_{\text{Off axis astigmatism and Field curvature TANGENTIALIMAGE}} = \frac{1}{4}(3S_3 + S_4) = \frac{1}{4}\left(3H^2F + H^2F/n\right). \qquad (1.31)$$

Off-axis astigmatism has similar effects as on-axis torroidal astigmatism which may be more familiar to some readers. The effect of considering an off-axis field point is to make the rotationally symmetric lens *appear* toric when observed from that field point. A wavefront from the off-axis point experiences the lens as imparting some arbitrary phase change (that varies from zero at the centre to some positive value at the edge for a positive lens). This phase change occurs over the radius of the lens, but as observed from the off-axis field point (point T in fig. 1.26a) the tangential meridian is foreshortened in comparison to the sagittal meridian of the pupil, thus creating a differential in curvature between the sagittal and tangential meridians of the wavefront.

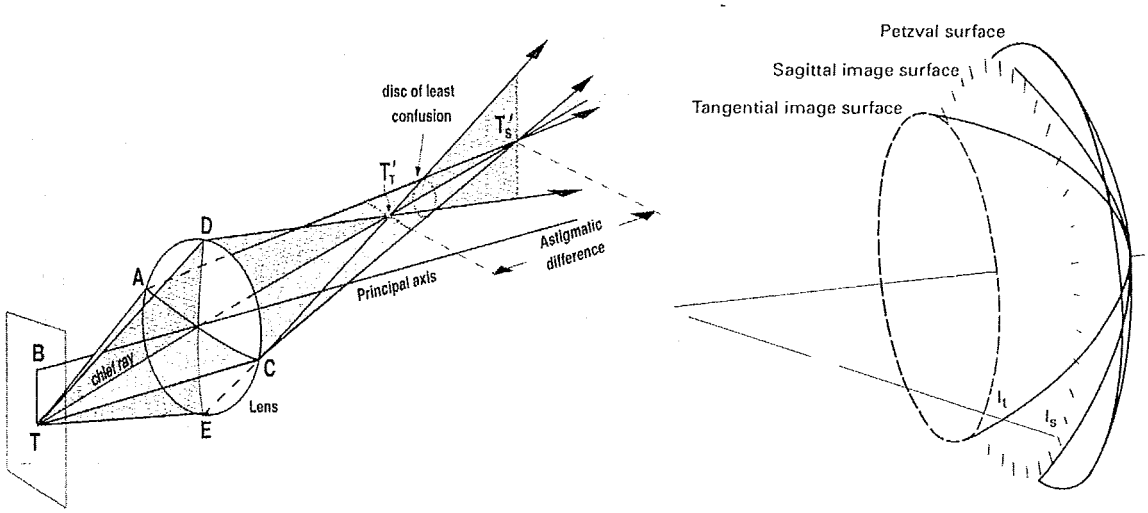


**Figure 1.26 a) Off-axis astigmatism for field point T (Tunnacliffe 1993) and b) sagittal image surface, tangential image surface, and Petzval surface (Freeman and Hull 2003).**

In the image plane this results in a differential in the longitudinal aberration from the Petzval surface (defined below) between the sagittal and tangential meridians as illustrated by the 'cup and saucer' image surfaces (fig. 1.26b). The tangential image surface is always three times further displaced from the Petzval surface than the sagittal image surface. As in torroidal astigmatism, a *circle of least confusion* longitudinally separates two perpendicular line foci images. Although in reality, spherical aberration will cause the 'line' foci to form a short concentric caustic arc in the tangential image surface and a narrow figure eight with radial orientation in the sagittal image surface.

If considered in isolation, field curvature is a variation in the longitudinal position of the image plane (fig. 1.27) as a function of $\eta^2$. The curved image plane that results is called the Petzval surface. Field curvature is independent of lens shape, image conjugates, and pupil position. It can be minimised by modifying the refractive index of lenses used in optical system design.

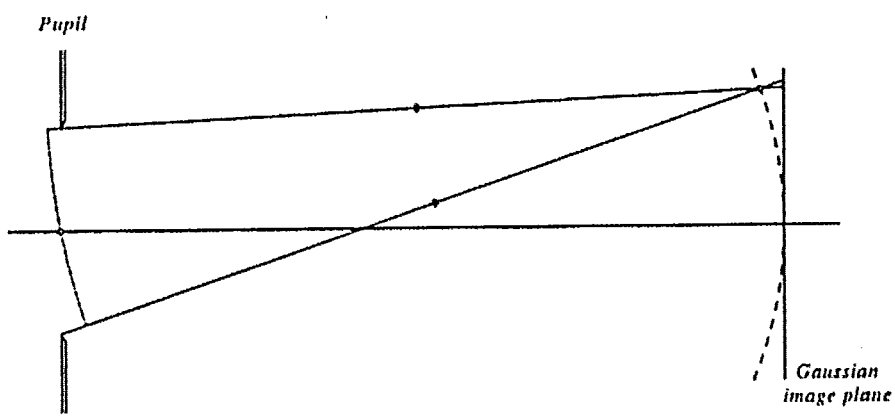


**Figure 1.27 Field curvature and the Petzval surface. Gaussian (paraxial) image plane also shown (Welford 1989).**

Distortion may be defined as

$$W_{distortion} = \frac{1}{2} S_5 \eta^3 \rho \cos\theta \ . \qquad (1.32)$$

It describes the variation in transverse aberration (or equivalently; transverse magnification) for the principal ray as a result of the field angle. Conceptually it may be thought of as a simple tilt for the principal ray. Distortion is normally expressed in terms of percent change from the image size for the corresponding on-axis pencil of rays and is typically described as 'pin cushion' (fig. 1.28b) or 'barrel' (fig. 1.28c) depending on whether the magnification increases or decreases with field angle. It can be minimised by using a symmetrical design with respect to the pupil, as opposed to the asymmetric bending required to neutralise spherical aberration and coma.

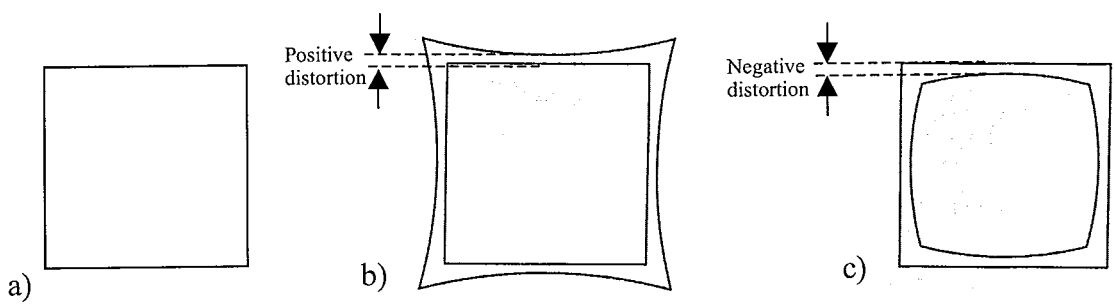


**Figure 1.28 a) Square object, b) the ideal image and the distorted pin-cushion image c) the ideal image and the distorted barrel image (adapted from Welford 1989).**

Optical designers typically manipulate numerous degrees of freedom to balance the aberrations of a system to conform within pre-determined tolerance levels. When describing ocular aberrations, Seidel aberration coefficients are not used because the eye is not a rotationally symmetric system. Additionally, the elements of the eye are aspheric and typically decentred. However, vision scientists do borrow some Seidel terminology and theory because it forms such a fundamental and widely used optical language. The format chosen by the Optical Society of America (OSA) to standardise descriptions of ocular aberrations has its own limitations too (see section 1.11 and 2.22).

## 1.10 Chromatic aberrations

Chromatic aberrations are a consequence of dispersion and they are typically considered separately from monochromatic aberrations. High frequency light undergoes greater refraction at a boundary and the trajectory of these rays depart from those of lower frequency light which undergo less refraction (fig. 1.29). It is sometimes convenient to consider the difference in axial foci for the two extreme frequencies at the ends of the bandwidth under investigation. The difference in foci along the optical axis ($z$) is termed longitudinal chromatic aberration (LCA) while the transverse difference in foci in the image plane ($xy$) is termed transverse chromatic aberration (TCA). The chromatic aberration of a lens can be minimised for a given bandwidth by combining two different media (e.g. glass and flint) into a doublet. Mirrors are not prone to chromatic aberration and provide an important advantage over lenses in this respect.

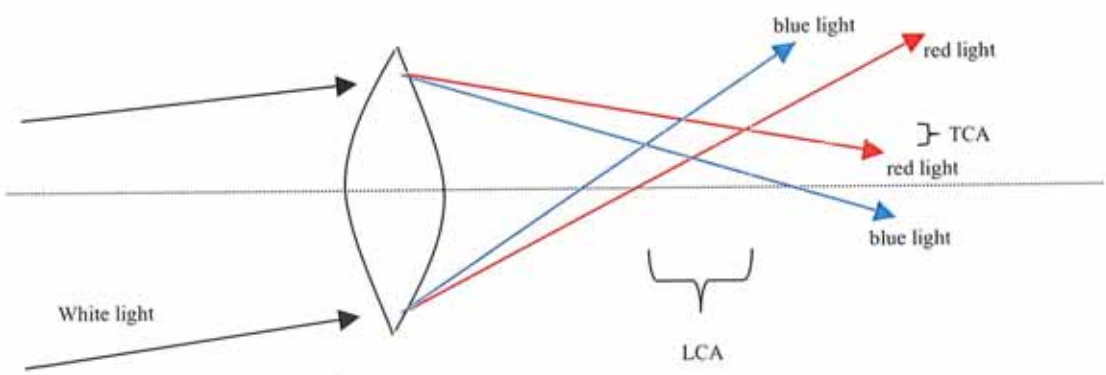


**Figure 1.29 Longitudinal chromatic aberration (LCA) and transverse chromatic aberration (TCA) of a positive lens (adapted Hecht 1987).**

Fig. 1.30 summarises several experimental reports on the typical longitudinal chromatic aberration of the human eye. It is reasonable to assume approximately 2 to 3 dioptres of LCA over the visible spectrum. Howarth *et al.* (1998) concluded that LCA is

independent of age for human adults, however this was a cross-sectional study and this conclusion has been debated by some researchers (Freeman and Hull 2003).

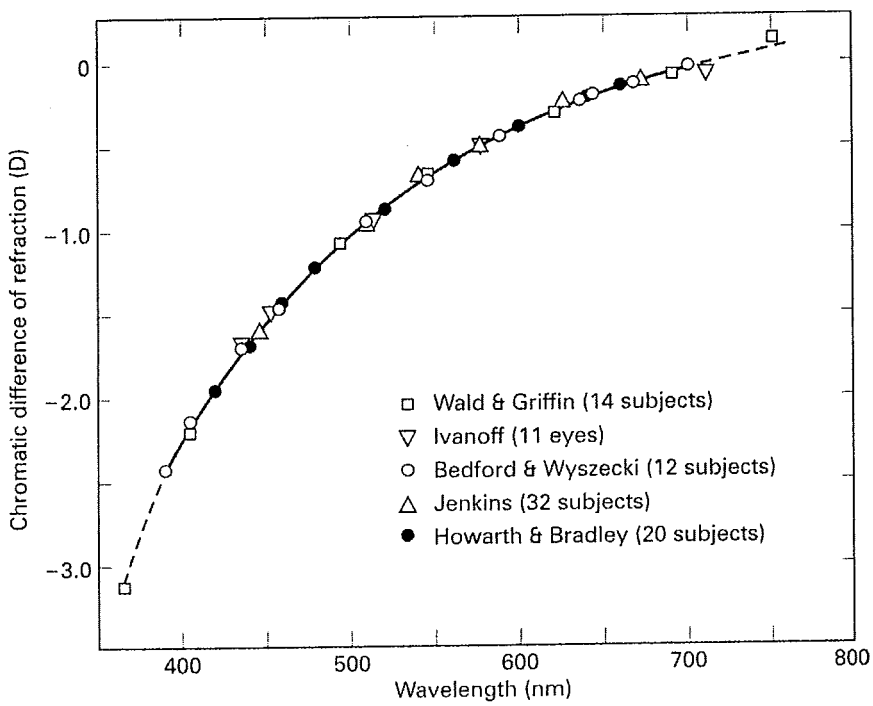


**Figure 1.30 Plot of chromatic difference in refraction vs. wavelength (Freeman and Hull 2003).**

## 1.11 Zernike polynomials

Zernike polynomials ($Z_i$) are a set of polynomials defined over the unit circle and commonly used by the optics community (Noll 1976). In recent years vision scientists have standardised the description of ocular aberrations by using Zernike polynomials (Thibos *et al.* 2000) and these standards are discussed in section 2.22. Zernike polynomials are used because of certain properties they have over the unit radius circle. If a wavefront[5] $W(\rho,\theta)$ is continuous and sufficiently smooth, it may be *completely* described by an infinite series of weighted polynomials (Malacara 1992)

$$W(\rho,\theta)=\sum_{i}^{\infty}\alpha_i Z_i(\rho,\theta), \tag{1.33}$$

where $\alpha_i$ represents the weighting coefficients and the unit circle is constrained by

$$0 \le \rho \le 1 \qquad \text{and} \qquad 0 \le \theta \le 2\pi \ . \tag{1.34}$$

Each Zernike polynomial is orthogonal,

$$\int_0^1 \int_0^{2\pi} Z_i(\rho,\theta) Z_j(\rho,\theta) \rho \, d\rho \, d\theta = \pi \delta_{ij} \ , \tag{1.35}$$

which means that each describes a function that can not be replicated by any linear combination of its fellow polynomials. As such, the fitting variance of any Zernike polynomial term to an arbitrary wavefront is independent of its fellow polynomials. Each Zernike polynomial can be normalised to have a mean of zero and unit variance

$$\frac{\int_0^1 \int_0^{2\pi} Z_i(\rho,\theta) Z_i(\rho,\theta) \rho \, d\rho \, d\theta}{\int_0^1 \int_0^{2\pi} \rho \, d\rho \, d\theta} = 1 \ , \tag{1.36}$$

[5] Defined using right-handed polar coordinates (see section 2.22)

which simplifies total wavefront root mean square (RMS) calculations because the average value for the cross terms then becomes zero (Malacara 1992). In practice, a finite number of polynomials are used to fit the wavefront and equation 1.33 becomes

$$W(\rho,\theta)=\sum_{i}^{n}\alpha_i Z_i(\rho,\theta). \tag{1.37}$$

The Zernike polynomials contain an azimuth component (a trigonometric function) where $m$ is the angular frequency of the azimuth component

$$\begin{cases}\cos m\theta \text{ for } m>0\\ \sin m\theta \text{ for } m<0\\ 1 \quad\quad \text{for } m=0\end{cases}, \tag{1.38}$$

a normalisation component

$$N_n^m=\sqrt{\frac{2(n+1)}{1+\delta_{m0}}}\quad\begin{cases}\delta=1 \text{ for } m=0\\ \delta=0 \text{ for } m\neq 0\end{cases}, \tag{1.39}$$

where $\delta_{m0}$ is the kronecker delta function, and a radial component

$$R_n^m(\rho)=\sum_{s=0}^{\frac{n-|m|}{2}}\frac{(-1)^s(n-s)!}{s!\left(\frac{n+m}{2}-s\right)!\left(\frac{n-m}{2}-s\right)!}\cdot\rho^{n-2s}, \tag{1.40}$$

where $n$ is the radial order. Equations 1.38, 1.39, and 1.40 combine to give the Zernike circle polynomial

$$Z_n^m(\rho,\theta)=N_n^m\ R_n^m(\rho)\cdot\begin{cases}\cos m\theta \text{ for } m>0\\ \sin m\theta \text{ for } m<0\\ 1 \quad\quad \text{for } m=0\end{cases}. \tag{1.41}$$

Values for the radial order $n$ are derived from

$$n = ceiling\left[\frac{-3+\sqrt{9+8(q-1)}}{2}\right], \tag{1.42}$$

where the ceiling function is equivalent to rounding towards positive infinity and $q$ is the polynomial number {q =0,1,2,3,4,5,.....and so on}. Values for the angular frequency $m$ are derived from

$$m = q - \frac{n(n+1)}{2} - 1 . \tag{1.43}$$

Contour maps of the first four orders of Zernike polynomials are shown in fig. 1.31. The plane contour map at the apex of fig. 1.31 represents piston ($0^{th}$ order), which is not a relevant (or measurable) consideration in ocular wavefront sensing. The $2^{nd}$ and $3^{rd}$ rows are contour maps of the $1^{st}$ and $2^{nd}$ order Zernike polynomials. Throughout this thesis, when describing aberrations these functions will be referred to as 'lower-order' aberrations. The $4^{th}$ and $5^{th}$ rows are contour maps representing the $3^{rd}$ and $4^{th}$ order Zernike polynomials. When describing aberrations in this thesis, these functions and all others will be referred to as 'higher-order' aberrations. The WFS constructed as part of this work, fits aberration data to $5^{th}$ order Zernike polynomials.

Table 1.1 lists the first five orders of Zernike polynomials in right-handed polar form and using standard OSA indexing. Some of the functions have been given a descriptive name based on loose similarities the function may share with traditional Seidel aberrations.

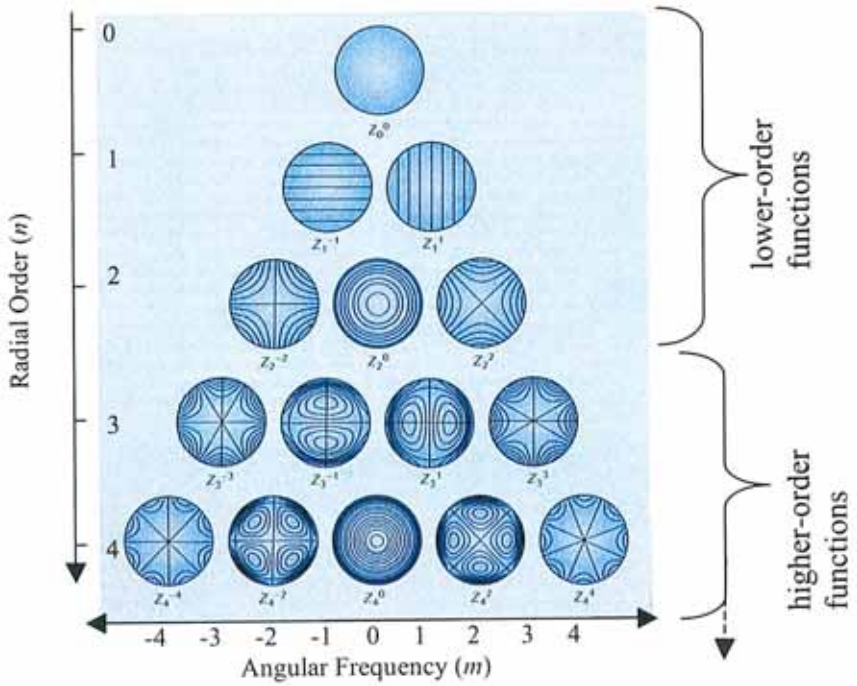


**Figure 1.31 Contour maps showing the wavefront deformation associated with each Zernike polynomial up to 4th order (Charman 2004).**

| $Z_n^m$ | Order (n) | Freq. (m) | Zernike Polynomial | Description |
|---|---|---|---|---|
| $Z_1^{-1}$ | 1 | -1 | $2\rho\sin\theta$ | Tilt about $x$ axis |
| $Z_1^{1}$ | 1 | 1 | $2\rho\cos\theta$ | Tilt about $y$ axis |
| $Z_2^{-2}$ | 2 | -2 | $\sqrt{6}\rho^2\sin 2\theta$ | Astigmatism 45/135 |
| $Z_2^{0}$ | 2 | 0 | $\sqrt{3}(2\rho^2-1)$ | Defocus |
| $Z_2^{2}$ | 2 | 2 | $\sqrt{6}\rho^2\cos 2\theta$ | Astigmatism 0/90 |
| $Z_3^{-3}$ | 3 | -3 | $\sqrt{8}\rho^3\sin 3\theta$ | Trefoil (base on $x$ axis) |
| $Z_3^{-1}$ | 3 | -1 | $\sqrt{8}(3\rho^3-2\rho)\sin\theta$ | Coma along $x$ axis |
| $Z_3^{1}$ | 3 | 1 | $\sqrt{8}(3\rho^3-2\rho)\cos\theta$ | Coma along $y$ axis |
| $Z_3^{3}$ | 3 | 3 | $\sqrt{8}\rho^3\cos 3\theta$ | Trefoil (base on $y$ axis) |
| $Z_4^{-4}$ | 4 | -4 | $\sqrt{10}\rho^4\sin 4\theta$ | |
| $Z_4^{-2}$ | 4 | -2 | $\sqrt{10}(4\rho^4-3\rho^2)\sin 2\theta$ | |
| $Z_4^{0}$ | 4 | 0 | $\sqrt{5}(6\rho^4-6\rho^2+1)$ | Spherical aberration |
| $Z_4^{2}$ | 4 | 2 | $\sqrt{10}(4\rho^4-3\rho^2)\cos 2\theta$ | |
| $Z_4^{4}$ | 4 | 4 | $\sqrt{10}\rho^4\cos 4\theta$ | |
| $Z_5^{-5}$ | 5 | -5 | $\sqrt{12}\rho^5\sin 5\theta$ | |
| $Z_5^{-3}$ | 5 | -3 | $\sqrt{12}(5\rho^5-4\rho^3)\sin 3\theta$ | |
| $Z_5^{-1}$ | 5 | -1 | $\sqrt{12}(10\rho^5-12\rho^3+3\rho)\sin\theta$ | |
| $Z_5^{1}$ | 5 | 1 | $\sqrt{12}(10\rho^5-12\rho^3+3\rho)\cos\theta$ | |
| $Z_5^{3}$ | 5 | 3 | $\sqrt{12}(5\rho^5-4\rho^3)\cos 3\theta$ | |
| $Z_5^{5}$ | 5 | 5 | $\sqrt{12}\rho^5\cos 5\theta$ | |

**Table 1.1 List of Zernike polynomials in right-handed polar form and OSA standard format double indexing scheme.**

## 1.12 Hartmann's test for telescopes

The Hartmann screen test is named after the astronomer Johannes Hartmann (1865 – 1936) who initially designed the test to perform optical metrology on a refracting telescope, although subsequently it has found numerous applications outside of astronomy (Spiricon 2004). The test measures the quality of an optical system and its results are most commonly interpreted using metrics of surface figure, the Hartmann constant, or coefficients of polynomials that describe aberrations (as is the case in this thesis). In the original test (fig 1.32), Hartmann produced a screen of uniformly spaced and uniformly sized holes (subapertures) and placed it over the aperture of the telescope under examination. In this configuration each subaperture allows a pencil of rays to pass through a different region of the entrance pupil of the telescope and be focussed. Photographic plates are exposed at either side of the telescope focus and ray tracing between corresponding spots of each photograph determines exactly where each pencil crosses the optical axis. In the ideal case, pencils of light cross the axis at the same point. In reality Hartmann found the pencils of light were crossing at various points along the optical axis and could thus determine what elements of the telescope required alteration to reduce aberrations and improve imaging (Neal and Schwiegerling 2005).

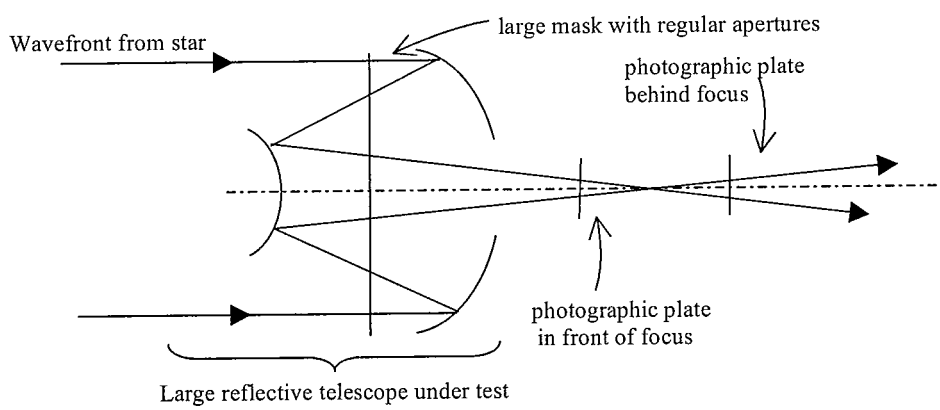


**Figure 1.32 Optical schematic for an early Hartmann test on a reflective telescope. Note: Hartmann initially performed the test on a refractive telescope (adapted from Platt and Shack 2001).**

The physical arrangement of the Hartmann test involves positioning a point source at the centre of curvature of the optical system being examined – thus a plane wavefront is generated in the ideal case. Alternately, to test an afocal system a plane wavefront from an infinitely distant source can be passed through the system under examination. Again, in the ideal case the exiting wavefront would be planar. Today the original Hartmann test is usually modified as schematically shown in fig. 1.33. Instead of examining the focus of each subaperture longitudinally along the optical axis, a lenslet array (an array of extremely small lenses) is placed in a collimated light path (fig. 1.34a) and the transverse shift in focus of each subaperture is examined with respect to its own optical axis. The poor efficiency of the Hartmann aperture screen is improved by the lenslets which increase the signal to noise ratio (SNR) and allows the wavefront to be sensed while simultaneously capturing an image of the science object. In the detector plane CCDs have replaced photographic plates. In the ideal case, a perfectly plane wavefront is incident on the lenslet array and each subaperture focuses a spot of light on the geometric centre of its subfield. Thus the array of spots in the detector plane is uniformly spaced. In the case of an aberrated wavefront (fig. 1.34b), some of the spots of light will be displaced from their ideal position.

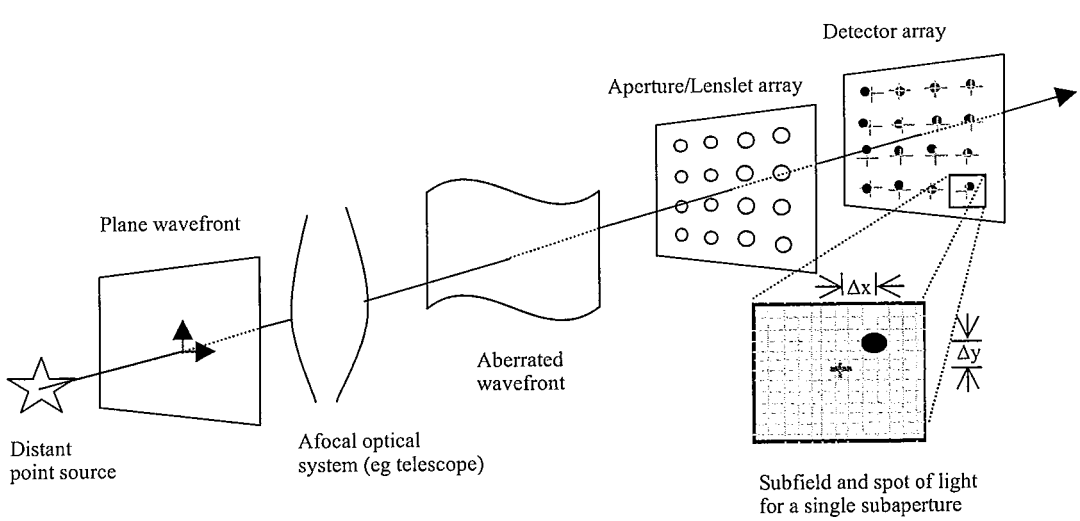


**Figure 1.33 Hartmann's test and Shack's modification (adapted from Spiricon 2004).**

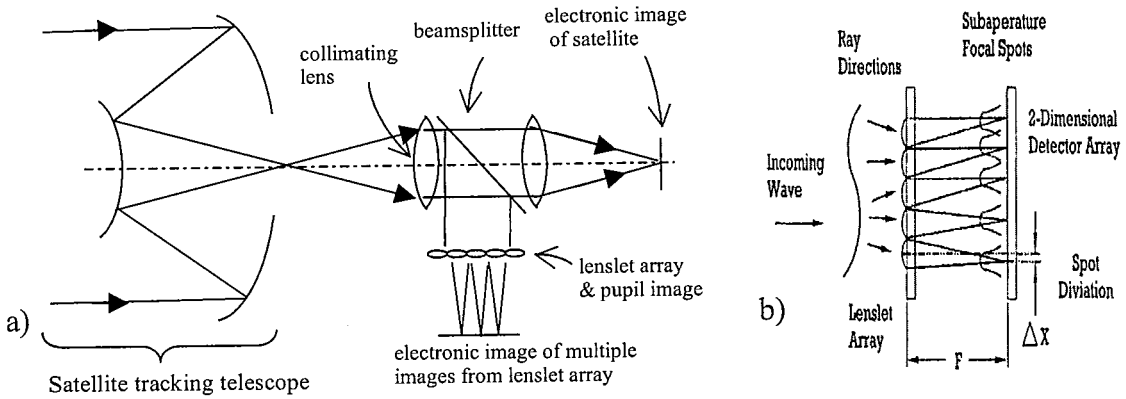


**Figure 1.34 Schematic diagram of a) the Hartman Shack sensor, and b) the displacement of spots within the array representing local wavefront tilt (adapted from Platt and Shack 2001).**

If the wavefront aberrations are relatively small and vary smoothly across the pupil, and the sampling rate is high enough, then the wavefront can be conceptually decomposed into local regions of pure tilt across each subaperture. The local wavefront tilt over each subaperture is proportional to the transverse displacement of each spot within its subfield and the focal length of the lenslet. By measuring these two parameters, the local tilt (in both $x$ and $y$ directions) across each subaperture can be determined and the incident wavefront may then be reconstructed into a 3D phase surface by integrating the values of local tilt across the pupil. This is a zonal reconstruction technique as opposed to the modal reconstruction technique we use in this work.

The modified arrangement of the Hartmann test is usually referred to as Hartmann-Shack in recognition of work in the field by Dr Roland Shack in the 1970s (Platt and Shack 2001). The high quality of modern instrument manufacturing combined with large telescope diameters, means that Hartmann-Shack (HS) wavefront sensing for astronomy applications is typically directed at measuring both defects within the telescope itself (e.g. mechanical sagging or thermal expansion of the primary mirror which vary on a slow time scale), and aberrations due to turbulence of the earth's atmosphere which vary on a much faster time scale.

# CHAPTER TWO

## Introduction to the eye, refraction and ocular aberrometry

This chapter gives an introduction to the anatomy (biological structure) and physiology (biological function) of the visual system. The visual system is such a vast topic that priority of detail is given to the eye (fig. 2.1) for the sake of being succinct. Traditional refraction techniques are outlined and a historical review of ocular aberrometry is given.

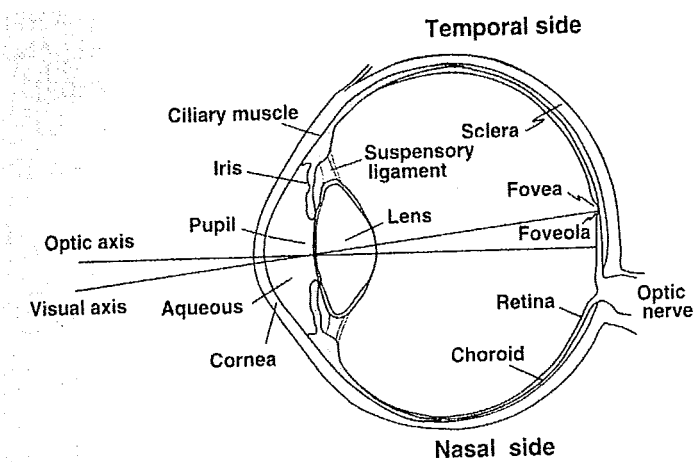


**Figure 2.1 Schematic drawing of the human eye (Tunnacliffe 1993).**

### 2.1 The eyelid

The eyelid functions in the defence of the eye via its opening and closing action which can be either voluntary or involuntary. It maintains the integrity of the optics of the eye through the distribution of tears and by controlling the amount of light incident upon the eye. The resting position of the superior lid may partially obscure a pharmacologically dilated pupil (occasionally this occurred during ocular aberration measurements performed throughout this work, see chapters 6-8). It consists structurally of skin, fatty subcutaneous tissue, muscles, nerves, conjunctiva and a fibrous plate. Some glands associated with the eyelid produce components of the tear secretion and are positioned at the base of the eyelash follicles. The eyelashes function in a defence capacity in conjunction with the eyelids.

## 2.2 The tear film and lacrimal system

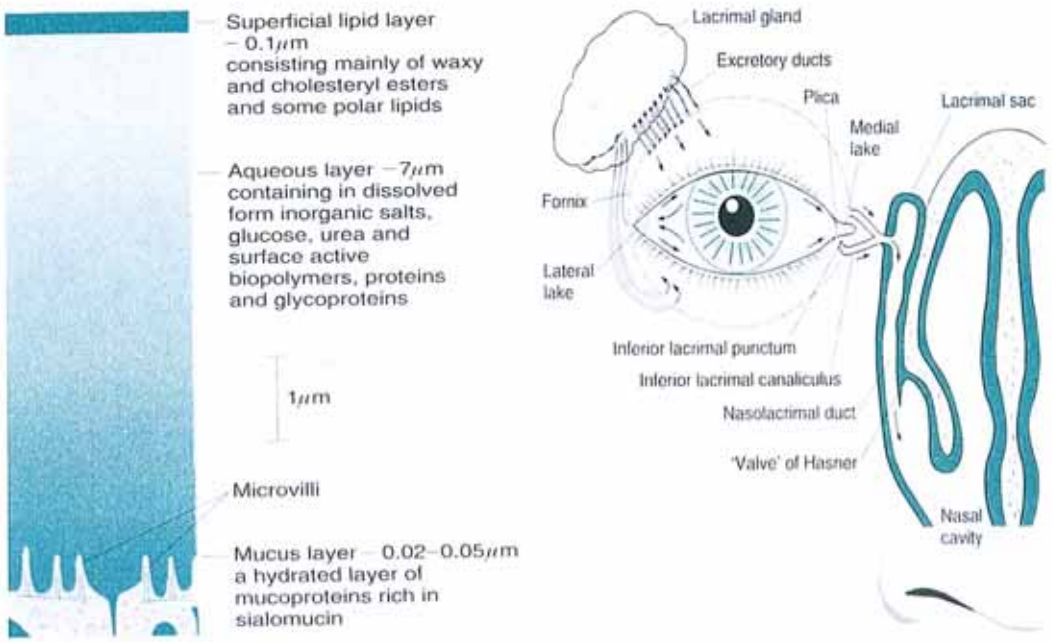


**Figure 2.2 a) Scale drawing of the tear film and b) the lacrimal system and drainage apparatus (Korb *et al.* 2002).**

Tear film stability and integrity is crucial to imaging in the eye because it forms the principal refracting surface. The tear film has a typical refractive index of 1.336 (Tunnacliffe 1993). Other important functions of the tear film include lubrication, nutrient exchange, and immunological defence. The tear film contains a lipid layer, an aqueous layer, and a mucous layer (fig. 2.2a). Many different glands are responsible for producing tears - the largest is the lacrimal gland (fig 2.2b). Ducts are responsible for transporting tears from glands to the ocular surface. For the most part, tears are drained via a system of canaliculi, a sac, and then via a duct into the nasal cavity. The lacrimal system is under nervous supply from the fifth cranial nerve. Tear film quality and time elapsed since last blink are important factors that dramatically affect the reliability of aberration measurements performed with a HS WFS. Poor tear quality can substantially increase aberrations experienced by a subject and this is particularly troublesome during HS wavefront sensing because the tear break-up area is typically less than the lenslet sample area (Roorda 2005).

## 2.3 The conjunctiva

The conjunctiva is a mucous membrane that originates at the lid margin and covers the inner surface of the lid and the outer surface of the globe (but not the cornea). It provides a lubricating action that aids in the smooth movement of the lids over the globe. It consists of epithelium, secretory cells, blood vessels and nerves. The conjunctiva is highly vascular and receives sensory innervation from the fifth cranial nerve.

## 2.4 The cornea

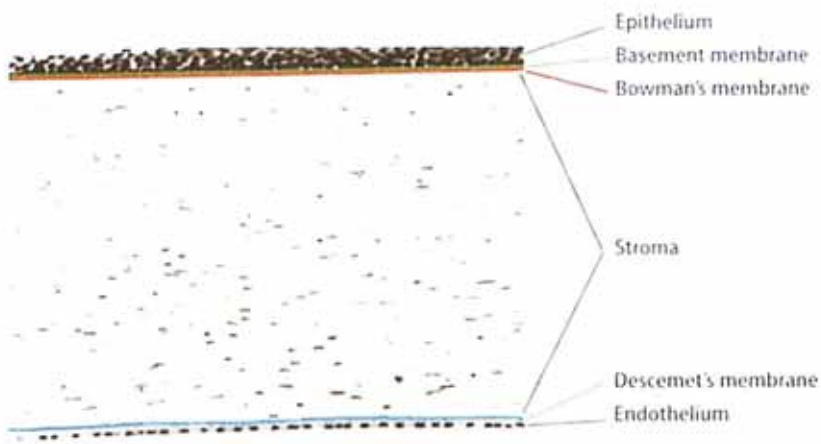


**Figure 2.3 Histological section of human cornea with modified colour representation (Krieglstein *et al.* 2000).**

The cornea is the transparent, avascular surface at the front of the eye (fig. 2.3). Together with the tear film it forms the principal refracting surface of the eye and has a typical refractive index of 1.376 (Tunnacliffe 1993). Contributing approximately 3/4 of the total refractive power of the eye, the corneal shape is important in limiting ocular aberrations. Typically it has a central anterior radius of curvature of 7.50mm to 8.00mm (Coster 2002) and a posterior radius of the curvature of 6.20mm to 7.40mm (Tunnacliffe 1993). It is an aspheric surface with flattening curvature towards the periphery – this helps to reduce spherical aberration in the eye (Tunnacliffe 1993). The

cornea has a diameter of 11mm to 12mm horizontally and 9mm to 11mm vertically (Coster 2002). The circumferential edge of the cornea is called the limbus. Corneal thickness varies from 0.52mm at the centre to 0.70mm at the periphery (Coster 2002). It consists of 5 layers; the epithelium, Bowman's layer, the stroma, Descemet's membrane, and the endothelium (Heath and Young 2000).

The corneal epithelium has important functions including anchoring the tear film and providing a defensive barrier to chemical and biological insults. The epithelial layer is approximately five cell layers deep and rests on a basement membrane called Bowman's layer. The stroma constitutes about 90% of the thickness of the normal human cornea and is typically 78% water by mass (Coster 2002). It consists of keratocytes, collagen fibrils, proteoglycans and water. The collagen fibrils are uniform in diameter and arranged in regular parallel groups of differing orientations called lamellae. It is this strict arrangement of fibril size and spacing (primarily determined by the hydration level), which maintains corneal transparency and allows the eye to image effectively. Descemet's membrane acts as the basal lamina of the corneal endothelium. The corneal endothelium is a posterior single layer of hexagonal cells principally responsible for maintaining the hydration level of the stroma. If corneal hydration is impaired, the resulting corneal cloudiness will increase scatter of light entering the eye.

The limbus is the transition zone between the cornea and the sclera and conjunctiva. The cornea receives sensory innervation from the fifth cranial nerve. As the nerve trunks enter the limbus they lose their myelin sheaths and become transparent. At the limbus the cornea losses it's transparency as the collagen fibrils lose their orderly size and arrangement. The epithelial layer also loses its highly regular arrangement.

## 2.5 The sclera and Tenon's capsule

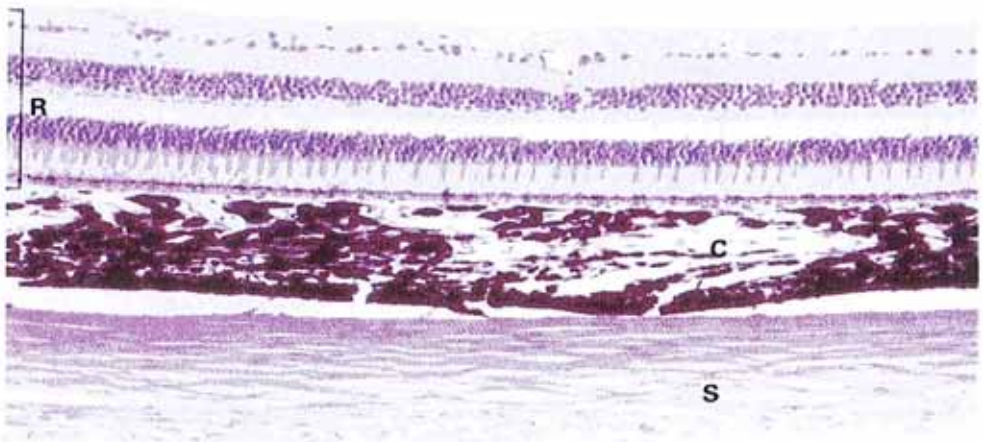


**Figure 2.4 Histological section of the wall of the eye. R (retina), C (choroid), and S (sclera) (Heath and Young 2000).**

Together with the cornea, the sclera forms the outer fibrous layer of the eye. The sclera is significantly larger than the cornea. It is an opaque, white coloured tissue with variable thickness, being thinnest (approximately 0.3mm) anteriorly where the extraocular muscles attach to the globe. At the equator the sclera is approximately 0.6mm thick and at the posterior of the globe it is approximately 1mm thick near the optic nerve. It consists of three layers; the episclera, scleral stroma, and basal layer. The episclera is a loose outer layer that attaches to Tenon's capsule and merges with the underlying stroma. The scleral stroma is a dense and bulky fibrous tissue of collagen fibres with variable diameter and arrangement. The basal layer of the sclera attaches to the underlying choroid. Tenon's capsule is a sheath that gives an outer covering to the globe. It separates the globe from the other structures in the orbit (eye socket) such as fat and muscle. In the anterior direction it attaches to the sclera about 1.5mm behind the limbus and in the posterior aspect it attaches to the optic nerve. The capsule supports the globe and allows it to move readily. Fig. 2.4 shows a histological section of the wall of the eye and the arrangement of the sclera, choroid and retina (outer to inner).

## 2.6 The anterior chamber, posterior chamber, and aqueous outflow apparatus

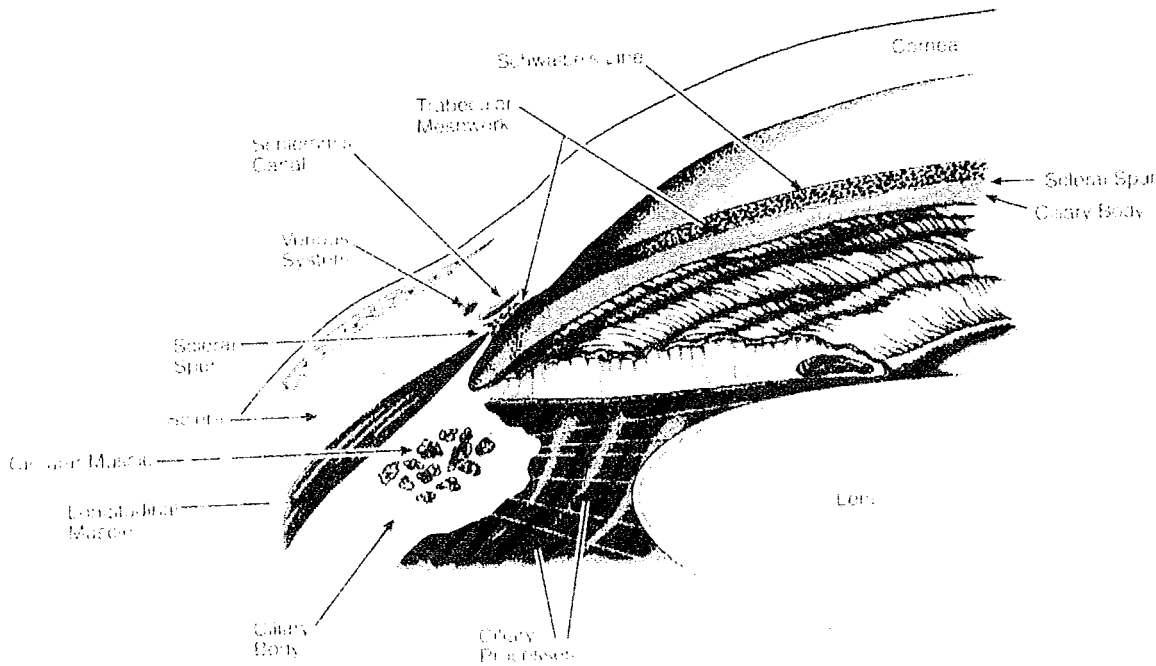


**Figure 2.5 Schematic drawing of the anterior segment of the human eye (Tasman and Jaeger 2001).**

The anterior chamber is the space occupied between the cornea and the iris and crystalline lens. The typical anterior chamber depth is 2.7mm to 4.5mm (Tunnacliffe 1993). The posterior chamber is the space occupied between the iris, crystalline lens, and ciliary body. Both chambers are filled with a clear secretion called aqueous humour. Aqueous humour is produced (see section 2.10) and circulates from the posterior chamber through the pupil to the anterior chamber where it provides nutrient and waste exchange with the corneal endothelium. The outflow apparatus (fig. 2.5) drains aqueous humour from the anterior chamber to eventually unite with the vascular system. The primary components of the outflow apparatus are; the trabecular meshwork, the canal of Schlemm, collector channels and associated blood vessels. Due to its intimate relationship with glaucoma (an important eye disease), AO imaging systems may soon be designed specifically for high resolution imaging of the anterior segment angle.

## 2.7 The uveal tract

The uveal tract is a pigmented and highly vascular tissue consisting of the iris, ciliary body, and choroid. Its has many functions including nutrient exchange, production of aqueous humour, accommodation (a change in tone of the ciliary muscle in the ciliary body changes the shape of the lens and thus the focussing state of the eye), absorption of scattered light inside the eye, and control of pupil size. As previously mentioned, pupil size directly influences the irradiance of the retinal image, diffraction effects and aberration levels (Tunnacliffe 1993).

## 2.8 The iris

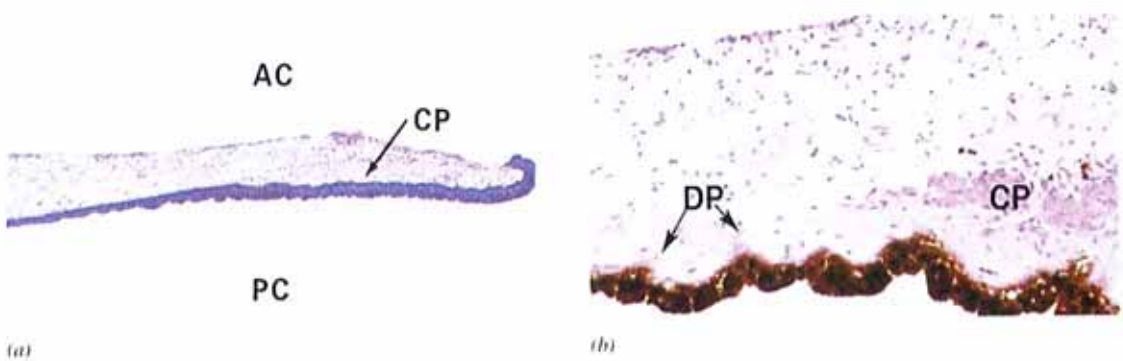


**Figure 2.6 a) Histological section of human iris, b) same at greater magnification. AC (anterior chamber), PC (posterior chamber), DP (dilator papillae) CP (constrictor papillae) (Heath and Young 2000).**

The iris is the most anterior portion of the uveal tract, and arises from the ciliary body. The stromal pigment of the iris endows the 'eye colour' observed by casual inspection. The iris is a mobile diaphragm that bulges anteriorly because it rests on the crystalline lens. It is a roughly circular annulus with a 12mm diameter and it is pierced near the centre by a variable sized aperture (the pupil). The pupillae sphincter and pupillae dilator muscles of the iris (fig. 2.6b) control pupil size. The blood vessels of the iris are coiled tubes, enabling them to move and stretch as the iris dilates and contracts. When performing aberration measurements, researchers often pharmacologically dilate the

pupil (mydriasis) to allow standardised comparison between subjects and investigation of aberrations at their most deleterious. The posterior epithelium of the iris is very heavily pigmented (fig. 2.6a) to absorb scattered light inside the eye. Sensory and autonomic nerve supply to the iris is from the fifth cranial nerve and the third cranial nerve. The ultra-structure of the iris is divided into the anterior boarder layer, the stroma, and the posterior pigmented epithelium (continuous with the non-pigmented epithelium of ciliary body).

## 2.9 The crystalline lens

The primary function of the crystalline lens is to act as a dynamic focussing mechanism. It is biconvex, with the anterior surface being flatter in the unaccommodated eye. The average adult lens has an equatorial diameter of 10mm and an axial thickness 3.6mm (Tunnacliffe 1993). The crystalline lens has a gradient refractive index (in both the axial and radial directions) with an optical power *in situ* of approximately fifteen dioptres. Landmarks of the lens include the anterior pole, posterior pole, lens axis, and the equator. From outermost to innermost the major components of the lens are; the lens capsule, the anterior epithelial layer, and the lens proper. The zonules are a fibrous system that supports the lens and keeps it positioned behind the pupil (see section 2.12). The capsule is essentially a transparent elastic bag and shape determinant. It is thinnest at the posterior pole and thickest at the equator. Lens fibres are continuously added throughout life and they must maintain a highly ordered arrangement to maintain transparency. It is thought that higher-order aberrations inherent to the crystalline lens may play an important role in compensation for corneal aberrations in some individuals and vice-versa (Artal *et al.* 2001, Artal and Guirao 1998).

Although opacities in the crystalline lens (a common ocular condition) are theoretically detectable by a HS WFS, due to the simplicity and effectiveness of traditional techniques to detect and classify such opacities, it is unlikely that WFSs will find clinical use for this purpose.

## 2.10 The ciliary body

The ciliary body produces aqueous humour, zonular fibres (see section 2.12) and vitreous hyaluronic acid (see section 2.14). It also has a crucial function in accommodation via the action of the ciliary muscle. The ciliary body butts onto the iris and proceeds back to the retina (demarked by the ora serrata). It is a ring of tissue, roughly triangular shape in the long cross section with its base directed anteriorly. Attachments to the ciliary body include the scleral spur, the trabeculum, and the vitreous base. The ciliary body consists of two major zones: the pars plicata (the site of aqueous production) and the pars plana (a relatively avascular structure and the origin of the zonules).

The ciliary body is composed of epithelium, stroma and the ciliary muscle. The elasticity of the ciliary body provides a synchronised movement in an anterior and internal direction with contraction. Parasympathetic innervation is responsible for the majority of ciliary muscle innervation, while sympathetic innervation is thought to have minor physiological significance (Bron *et al.* 1997). When performing aberration measurements, researchers often paralyse the ciliary muscle (cycloplegia) to stabilise the accommodation of the eye. It is typical to use a drug that has both mydriatic and cycloplegic effects. The venous drainage of the ciliary body is directed to the choroid via the vortex veins.

### 2.11 The zonules

Zonules are suspensory fibres that hold the crystalline lens in place. They originate at the pars plana (approximately 1.5 mm anterior to the ora serrata) and insert into the crystalline lens at the anterior and posterior marginal zones. In an eye there are approximately 140 bundles of zonular fibres, which are composed of microfibrils having similar properties to elastin.

### 2.12 The choroid

The choroid is the most posterior part of the uveal tract. It extends from the optic nerve to the ora serrata. It is heavily pigmented and highly vascular, consisting of a network of blood vessels embedded in a ground substance of loose connective tissue, collagen, elastic fibres, reticular fibres, melanocytes and immunological cells. It is approximately 0.22 mm thick posteriorly, thinning to approximately 0.1 mm anteriorly. The choroid provides nutrition and waste exchange for the outer retina (and the full thickness of the macula), regulates ocular temperature, controls intraocular pressure, supports the retina in general, and limits scatter by absorbing light. It is bounded by the sclera externally and the retina internally (fig 2.4), and consists of four layers: the suprachoroid, stroma, the choriocapillaris and Bruch's membrane. The choroid is extensively innervated via the short posterior ciliary nerves (sympathetic, parasympathetic and sensory fifth cranial nerve fibres). The systolic pulse of blood flow through the choroid is thought to cause a predictable cyclic fluctuation of ocular aberrations (Collins *et al.* 1995, Hampson *et al.* 2005). WFSs using red or infrared sources actually penetrate through the retina and reflect the retinal beacon from the deeper choroidal tissue (Delori and Pfilbsen 1989). When interpreting WFS measurements this effect must be considered in addition to the chromatic aberration of the eye.

## 2.13 The vitreous body

The vitreous body provides support to the lens and retina. Its viscosity acts to dampen the effects of inertia on the retina and lens following eye movements. The vitreous humour volume is approximately 4 ml and is composed of 80% gel and 20% liquid, both of which are transparent. The vitreous gel is 99% water but it also contains collagen and hyaluronic acid. The vitreous gel attaches via the basal lamina to the retina, ciliary body and crystalline lens. The collagen in the vitreous gel is organised into a random meshwork and provides the elasticity and plasticity of the eye. Vitreous cells are mainly immunological and involved in the secretion of collagen.

## 2.14 The retina

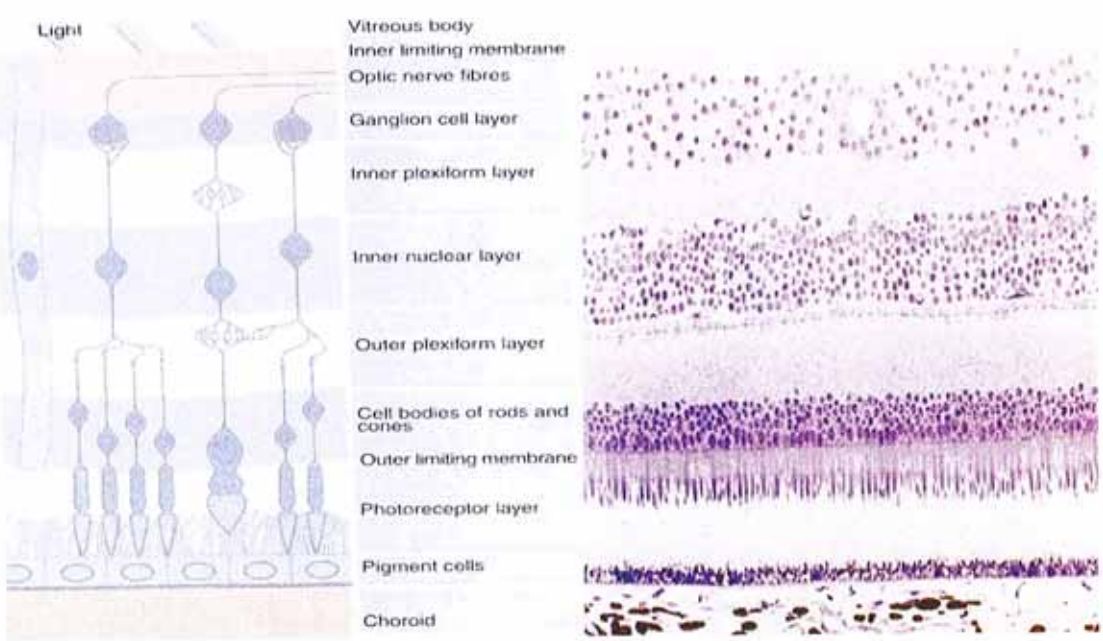


**Figure 2.7 a) Schematic drawing of human retina (Heath and Young 2000) and b) histological section of human retina (Freeman and Hull 2003).**

The retina is approximately 310 microns thick with significant geographical and inter-subject variation (Yang and Du 1999). The gross anatomy of the retina is divided into the outer pigmented epithelium layer and the inner neural sensory layers. The ultrastructure consists of ten layers, from outermost to innermost these are; retinal

pigment epithelium (RPE), photoreceptor layer, outer limiting membrane, outer nuclear layer, outer plexiform layer, inner nuclear layer, inner plexiform layer, ganglion cell layer, nerve fibre layer, and inner limiting membrane (fig. 2.7a, fig. 2.7b). The plexiform layers are communicating layers, while the nuclear layers contain cell nuclei. The anterior boundary of the retina is the ora serrata, which marks the merging of the neural retina with the inner nonpigmented epithelium of ciliary body. Posteriorly there are areas of special distinction as illustrated in fig. 2.8; the macula lutea (~ 5.85 mm diameter), fovea centralis (~1.85 mm diameter), and the foveola (~0.35 mm diameter) (Kanski 2003).

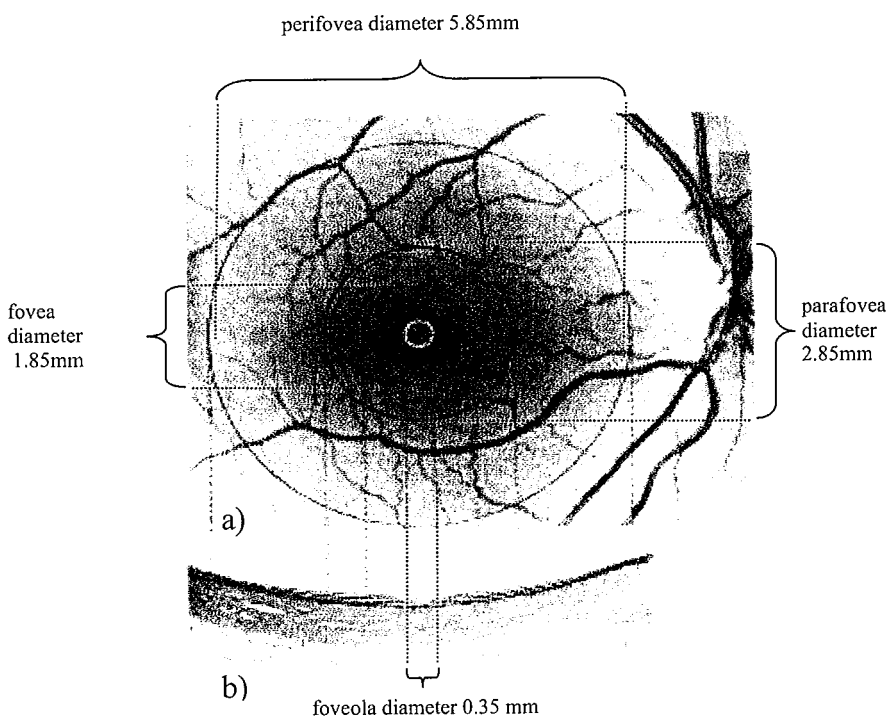


**Figure 2.8 An anatomical view of the macula region as viewed in a) coronal section and b) cross section (adapted from Thibos *et al.* 2000).**

The RPE is a single layer of cells that act as the major barrier between the neural retina and the leaky blood vessels of the underlying choroid. It generally supports the photoreceptors and phagosomes within the RPE have an important role in debris breakdown and removal of waste from the photoreceptor layer. Photoreceptors are

highly specialised cells that are sensitive to light and responsible for converting light into a neural impulse. There are two main types of photoreceptors: rods and cones. Rods are very sensitive to light and are mainly responsible for peripheral vision and scotopic vision. They have high spatial and temporal summation abilities. Cones are responsible for central vision and colour perception. They operate best in photopic conditions and are capable of high spatial and temporal resolution. Typically there are approximately 110 to 125 million rods and 6.5 million cones in an eye (Heath and Young 2000). There are three subtypes of cones – the differing absorption spectra between their pigments give rise to colour perception. The short wavelength cone (SWC) class is the least populated cone type and is absent at the very centre of the foveola but has a peak density at approximately one degree. This may have implications for reducing sensitivity to chromatic aberration in the eye. The two remaining cone classes (medium and long wavelength cones) combine with the SWC class to provide a typical range of sensitivity to wavelengths between 390nm and 760nm (Tunacliffe 1993).

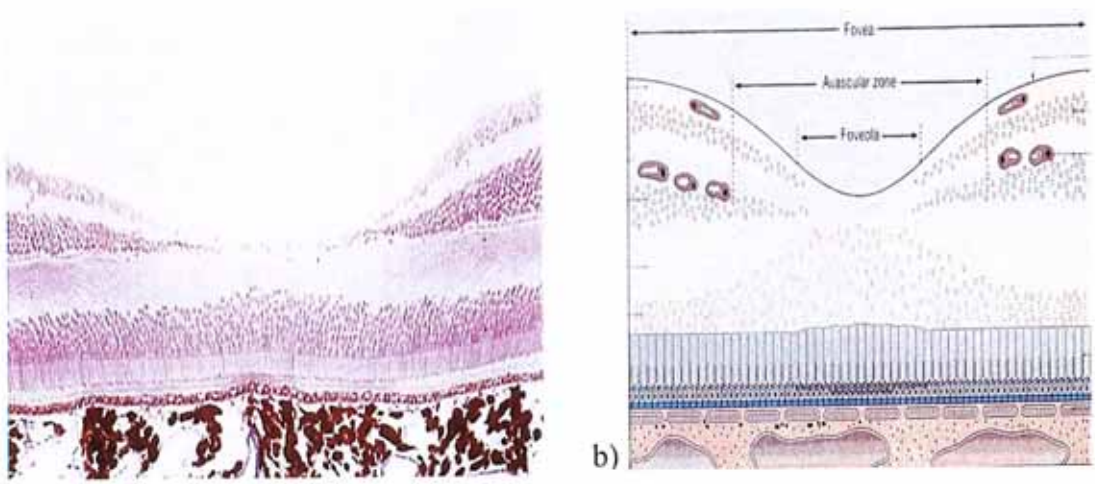


**Figure 2.9 a) Histological section of human foveola (Heath and Young 2000), and b) schematic drawing of human foveola (Kanski and Milewski 2002).**

Most layers of the sensory retina are displaced sideways at the foveola to create the foveal pit (fig. 2.9). Thus central photoreceptors have unimpeded stimulation from light

forming the retinal image. The small cone size and tight cell packing at the fovea increases the spatial resolution of the visual system for on-axis imaging (Heath and Young 2000). At the foveola the cones are packed in a directionally sensitive manner which allows them to act as waveguides. This produces the Stiles-Crawford effect (first described in 1933) and reduces the impact of aberrations at the pupil edge. The Stiles-Crawford effect is often described as an apodised pupil function, illustrated by fig. 2.10 which plots the relative luminosity for a pencil of rays as a function of location in the entrance pupil.

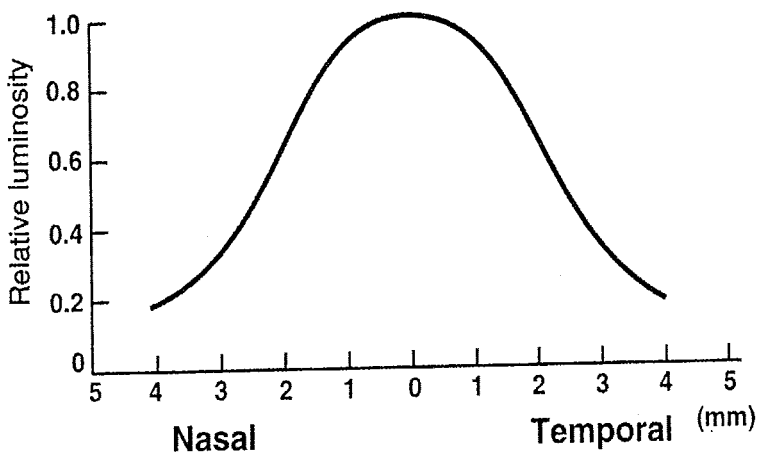


**Figure 2.10 Stiles-Crawford effect showing relative luminosity of rays as a function of pupil entry position (Tunnacliffe 1993).**

The outer limiting membrane is not a true membrane structure but rather an artefact created by extensive interconnections between Müller cells and adjacent photoreceptors (Bron *et al.* 1997). The outer nuclear layer contains the nuclei of the photoreceptors and their surrounding cytoplasm. Photoreceptor axons and synaptic processes extend up to the outer plexiform layer (a communication layer) where they synapse with the neural layers. The inner nuclear layer contains the nuclei of

- Bipolar cells which communicate between one or more ganglion cells and one or more photoreceptors. They also may synapse with horizontal or amacrine cells.

- Horizontal cells which have many short processes and one long process. They form lateral connections between photoreceptors and between photoreceptors and bipolar cells.
- Amacrine cells which communicate with bipolar cells, fellow amacrine cells, ganglion cells, and occasionally provide a feedback loop to photoreceptors.
- Interplexiform cells which communicate from ganglion cells to photoreceptors.
- Müller cells which are non-neural support cells (Heath and Young 2000).

There are many sub-types of bipolar cells, which are important for summation and retinal processing. Horizontal cells are used in coding colour vision and they can act to dampen rod signal if the cone signal is strong or vice-versa. Amacrine cells are large cells predominant located in the retina periphery. Müller cells are the largest cells in the retina. They are a type of glial cell (a supporting non-neural cell) and responsible for providing insulation around individual cells, comparatively similar to the function of myelin sheaths that surround other neural cells. The inner plexiform layer is thicker than the outer plexiform layer, except at the fovea where it is absent. It is a communication layer where impulses are relayed between bipolar, amacrine and ganglion cells.

There are 1.2 million ganglion cells in the retina. Ganglion cells are the only cell type in the ganglion cell layer. Their cell size increases and the layer thickness decreases with retinal eccentricity (increased spatial summation). A 1:1 relationship between cones and ganglion cells exists at the fovea, compared to a 100:1 rod to ganglion cell relationship at the periphery. This difference in coupling ratios exemplifies the low spatial summation at the fovea, which is important for the eye to extract the maximum resolution it can from the retinal image provided by the optics of the eye. The reduced

resolution capability of the peripheral retina is economically matched in terms of biological demands to the reduced image quality provided by the eye's optics in the peripheral visual field.

The nerve fibre layer contains the axons from ganglion cells. It takes a radial pathway across the nasal retina and an arcuate pathway across the temporal retina to the optic nerve head. The only exception is the papillomacular bundle where some axons in the central macula region take a radial path to the optic nerve head. The nerve fibre paths are strictly demarked between the superior and inferior retina by the horizontal raphe. Although the nerve fibres are unmyelinated, they are insulated by glial cells. Due to the importance of ganglion cells in eye disease (particularly glaucoma), AO imaging systems are currently striving to develop technology capable of imaging the ganglion cells *in vivo* and preferably without the need for invasive retrograde labelling (Gray *et al.* 2006).

The inner limiting membrane marks the boundary between the vitreous and the retina. A true basement membrane is present and it is associated with condensing Müller cell membranes and a thickening of the vitreous basal laminar. The inner limiting membrane has variable adherence to both the sensory retina and the vitreous.

The retina receives vascular supply from both the choriocapillaris and the retinal vasculature system. The retinal vessels are absent centrally at the fovea. The retinal venous system exits the eye via the central retinal vein.

## 2.15 Extraocular muscles

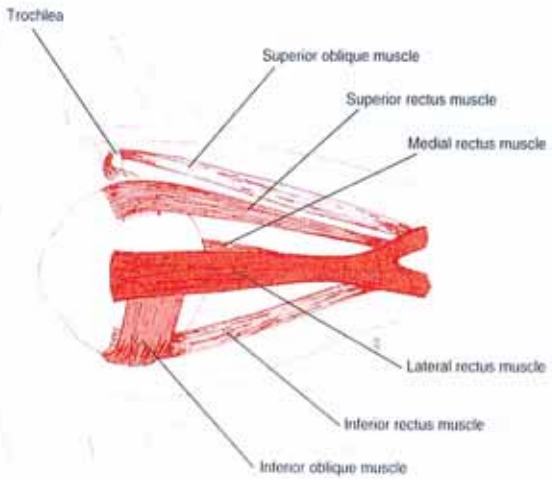


**Figure 2.11 The extraocular muscles of the human eye as viewed from a lateral position (Remington 2005).**

Eye movement is possible because extraocular muscles attach the outside of the globe (eyeball) to the orbit (bony eye socket) and to the annulus of Zinn (a special ring-shaped tendon) (fig. 2.11). There are six extraocular muscles; the lateral rectus, medial rectus, superior rectus, inferior rectus, inferior oblique, and superior oblique. Innervation of the extraocular muscles is via the third, fourth, sixth cranial nerves. There are five basic categories of monocular eye movement; saccades, tracking/smooth pursuit, microsaccades, drift, and microtremor. The former two movement categories are important when fixating a moving target, while the latter three movement categories are important when fixating a stationary target. Eye movements allow foveal-fixation, taking advantage of the superior optics on-axis and the high photoreceptor density at the fovea. This ability vastly reduces the demand for biological resources that would otherwise be required for good vision. The visual system performance degrades if eye movements are totally neutralised (Troxler's effect) because, like the other senses, vision is more sensitive to a change in stimulus than a constant stimulus. It is known that steady-state accommodation fluctuations provide a feedback mechanism to

maintain a high level of focus response (Plainis *et al.* 2005). A similar feedback mechanism occurs in gaze feedback where retinal image motion drives the optokinetic fixational response (Carpenter 2000). Researchers speculate it is likely that some amount of temporal fluctuation of higher-order aberrations is beneficial to visual performance for this purpose (Plainis *et al.* 2005).

## 2.16 Post-ocular visual system

The visual system begins organising and processing retinal images immediately following stimulation of the photoreceptors. This neural processing continues while the signal (called an impulse) is conducted via the optic nerve through the remainder of the visual system. Some landmark components of the visual pathway include; the optic nerve, optic chiasm, optic tract, lateral geniculate nucleus, optic radiations and visual cortex (fig. 2.12a and 2.12b). When impulses reach the visual cortex of the brain, vision is consciously perceived by the subject. The adaptive nature of visual development means that some ocular aberrations an individual has adapted to throughout life may actually result in reduced visual performance if neutralised by a corrective device (Artal *et al.* 2001, McLellan *et al.* 2006).

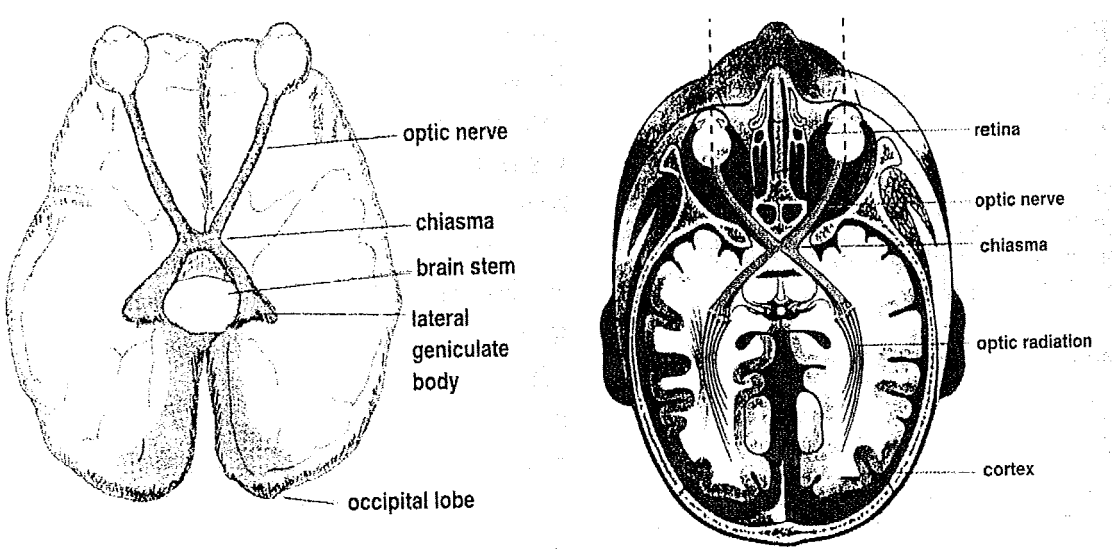


**Figure 2.12 a) and b) Schematic drawings of a transverse section of the visual pathway (Tunnacliffe 2003).**

## 2.17 Refractive error

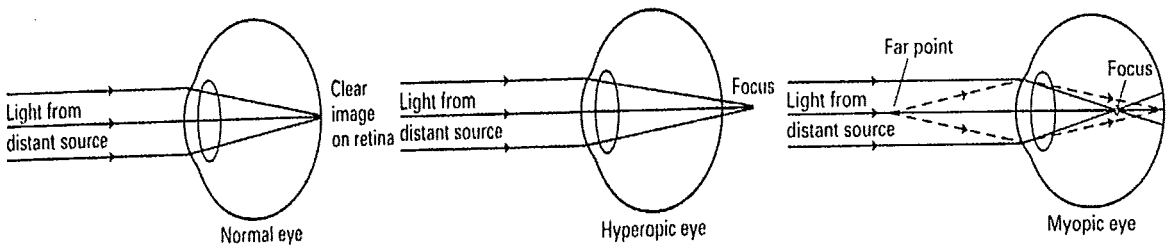


**Figure 2.13 Schematic drawing of emmetropia, hyperopia and myopia in an unaccommodated eye (Wakefield 1994).**

The lower-order aberrations are typically the overwhelmingly dominant aberrations of the eye and traditionally they are corrected with spectacles, contact lenses or refractive surgery. For the visual system to function well, light from an object of interest must be focussed onto the retina. When this occurs to within clinically measurable limits the subject is 'emmetropic' (fig. 2.13a). When some measurable level of blur exists in the retinal image the subject is 'ametropic'. Ametropia is not the sole requirement for good vision (as the remaining components of the visual system must also function properly), but it is the most common and the most amendable malfunction of the visual system. Practitioners traditionally quantify ametropia by specifying the *refractive error*. The refractive error is the dioptric strength of a spectacle lens at the spectacle plane (typically 13mm in front of the cornea) that is required to remove blur from the retinal image and focus light from an infinite source on the retina. Many physiological processes can influence refractive error and complicate this definition (e.g. the dynamic focussing ability of the crystalline lens). In very simplified terms, refractive error can be categorised as myopia (refractive power of the eye too great for the axial length – see fig. 2.13c), hyperopia (refractive power of the eye too weak for the axial length – see fig. 2.13b) and astigmatism (varying refractive power at different meridians giving rise to two line foci when viewing an infinite source). In the vast majority of eyes if

refractive error is corrected for defocus and astigmatism, functional and satisfactory vision is achieved (assuming a normal healthy visual pathway).

Because the visual system is binocular and sensitive to monocular spatial direction, it is sometimes necessary to correct the first order aberrations of tip and tilt by use of prisms or surgery on the extraocular muscles. Practitioners quantify such a defect in units of prism dioptres required to provide comfortable binocular vision to the patient. Misalignments in the binocular system requiring first order corrections are generally due to a fault in the alignment of the globe itself (and not a misalignment of the optical elements of the eye), and therefore primarily a fault of the extra ocular muscles or their innervation. Again this is a greatly simplified explanation with many exceptions.

The aetiology of ametropia and the distribution of refractive error is a detailed topic beyond the scope of this thesis. It suffices to explain that a subject's refractive error will change throughout life for various reasons, some of which are known and others unknown. Typically an individual's refractive error will fluctuate across a range of time scales. Higher-order aberrations are likely to fluctuate on various time scales as well (Hofer *et al.* 2001). Traditionally, practitioners have only corrected lower-order aberrations. If higher-order aberrations of the eye are also corrected, there is potential to improve the visual resolution of the subject and the resolution of ocular images (typically, but not limited to, retinal fundus images) (Liang *et al.* 1997).

## 2.18 Traditional refraction techniques

Practitioners determine refractive error using a variety of tests, which may be either objective or subjective. It should be noted that when specifying refractive error practitioners colloquially refer to tip/tilt as 'prism', defocus as 'sphere', and astigmatism as 'cylinder'. Vision scientists typically refer to astigmatism as an even, symmetric function with zero power, whereas clinical practitioners typically refer to astigmatism as the dioptric power difference between the two principal meridians of the eye. For studies involving comparisons and statistical distribution of refractive errors, power vectors have been promoted as more appropriate descriptors than traditional formats (Thibos *et al.* 1997).

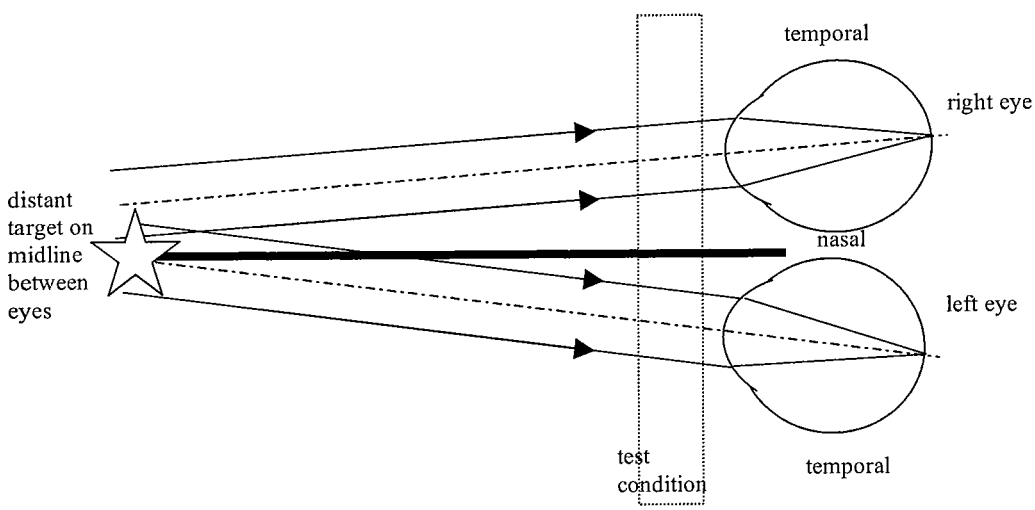


**Figure 2.14 An example of deviation between the visual axes of the eyes: right exotropia.**

A binocular misalignment of the visual system is measured as a relative difference in the direction of the visual axes of the eyes. Such misalignment can be likened to a tip/tilt (1$^{st}$ order aberration) difference between the eyes (fig. 2.14). Misalignments are referred to as fixational disparities and phorias, (types of latent deviation) or strabismus' (a manifest deviation), depending on the testing circumstances required to illicit the misalignment. There are many tests used to investigate these misalignments including;

the cover test, motility exam, Hirschberg test, septum test for phorias, Howell-Prentice test, and the fixational disparity test.

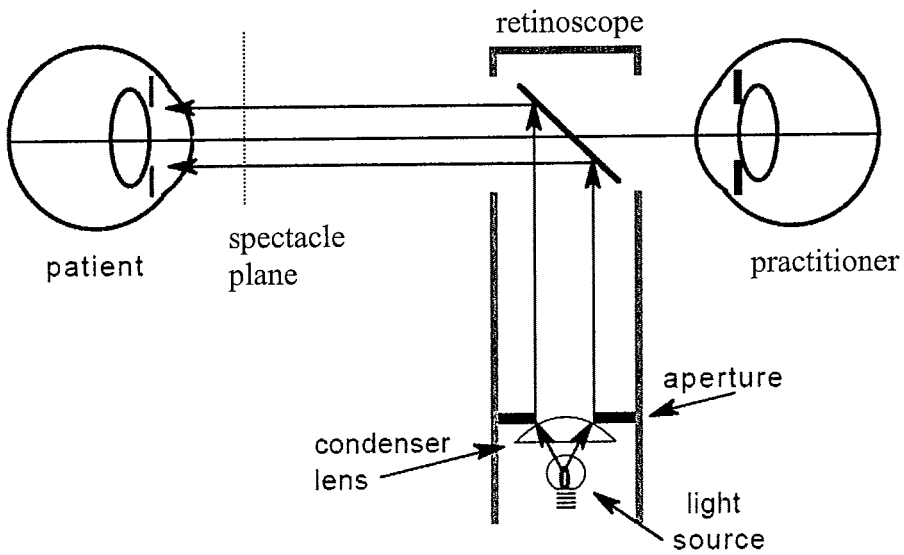


**Figure 2.15 Schematic diagram of a retinoscopy examination. Note that trial lenses are placed in the spectacle plane (including a working distance lens) to neutralise the reflex.**

Defocus and astigmatism ($2^{nd}$ order aberrations) may be measured using a variety of tests, which may be objective or subjective. Retinoscopy is a partially objective test where the practitioner shines light into the subject's eye and then moves the beam while observing the direction and speed of the reflection ('reflex') from the subject's retina. Fig. 2.15 shows a schematic diagram of the retinoscopy examination. The apparent motion of the reflex occurs due to vignetting created by the practitioner's pupil and the subject's pupil when the retinoscope is moved. It is essentially a Foucault knife edge test. The practitioner rotates the retinoscope beam ('streak') to eliminate oblique motion in the reflex and then neutralises each principal meridian in turn, resulting in a sphero-cylindrical refraction. The nearer the subject's retina is conjugated to the practitioner's pupil by the trial lens, the faster and brighter the reflex appears. When the subject's refractive error is completely neutralised the reflex's angular motion is infinitely fast and maximally bright. Retinoscopy does not rely on responses from the subject, but it

does rely on the skill and interpretation of the practitioner. In addition to refractive error measurement, retinoscopy provides the practitioner with information regarding the internal structures of the eye and media quality.

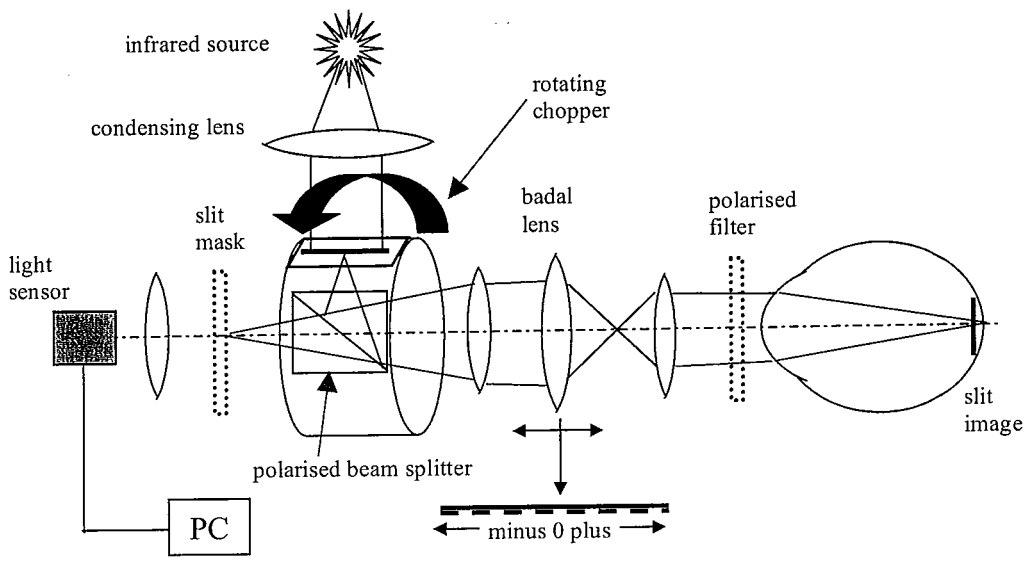


**Figure 2.16 Generic design of autorefractor (from Dave 2004).**

Autorefractors are instruments used to provide an automated and objective estimate of refractive error. This refraction technique uses a fixed pupil diameter and typically samples the eye in three meridians before fitting the data to a sine-squared function. The main components of an autorefractor are the light source (typically infrared), a fixation target, a Badal optometer, and a CCD detector. Fig. 2.16 shows a schematic design of a generic autorefractor. Early designs of autorefractors were based on an optimal focus principle where the vergence of the ingoing beam is adjusted until the signal through an aperture conjugate to the emmetropic retinal plane is maximised. Modern designs are more commonly based on the Scheiner principle or the Foucault knife edge test (Dave 2004).

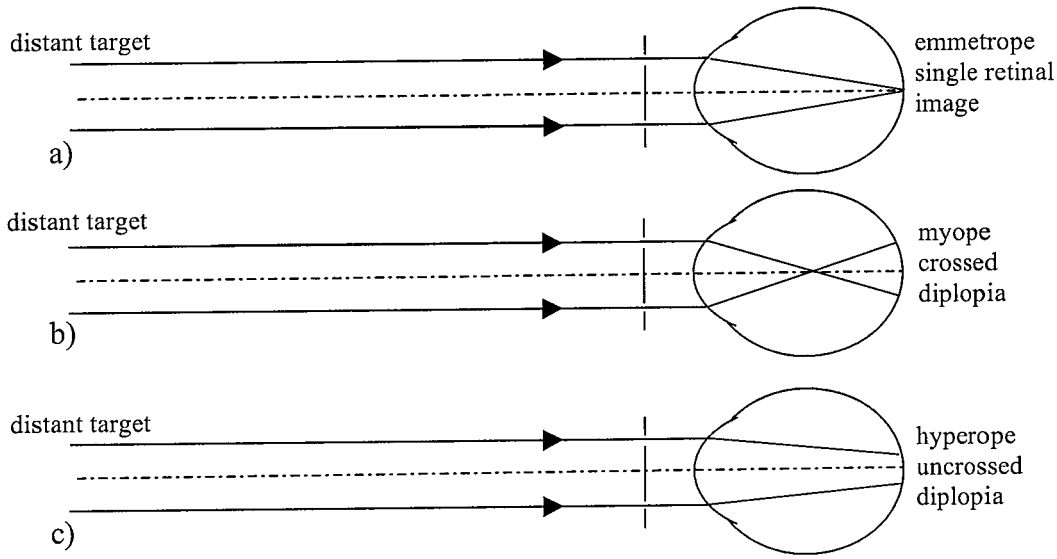


**Figure 2.17 Scheiner double pinhole principle creates a) a single retinal image in the emmetropic eye, b) two crossed retinal images (diplopia) in the myopic eye and c) two uncrossed retinal images (diplopia) in the hyperopic eye (adapted from Atchison and Smith 2000).**

Scheiner's principle (fig. 2.17) describes the doubling of an image for an object at infinity, when the pupil is masked by a double pinhole. The double pinhole creates two narrow pencils of light which are observed either; in front of the focus in the uncrossed form (analogous to hyperopia), in focus with only a single image is observed (analogous to emmetropia), or behind the focus in the crossed form (analogous to myopia).

In the Foucault knife edge test, a knife edge is introduced into a plane were the beam focus is expected (fig. 2.18). If the beam is well focused in this plane, the image is quickly extinguished in the image plane. If the beam is defocused in front of the plane, the image plane reveals a slow extinction in the mutual direction and orientation. If the beam is defocused behind the plane, the image plane reveals a slow extinction in the opposite direction. Autorefractors using either the Scheiner principle or the Foucault knife edge test require a synchronisation mechanism between the ingoing beam orientation and the detector. Typically a practitioner would not dispense spectacles directly from the results of an automated refraction exam.

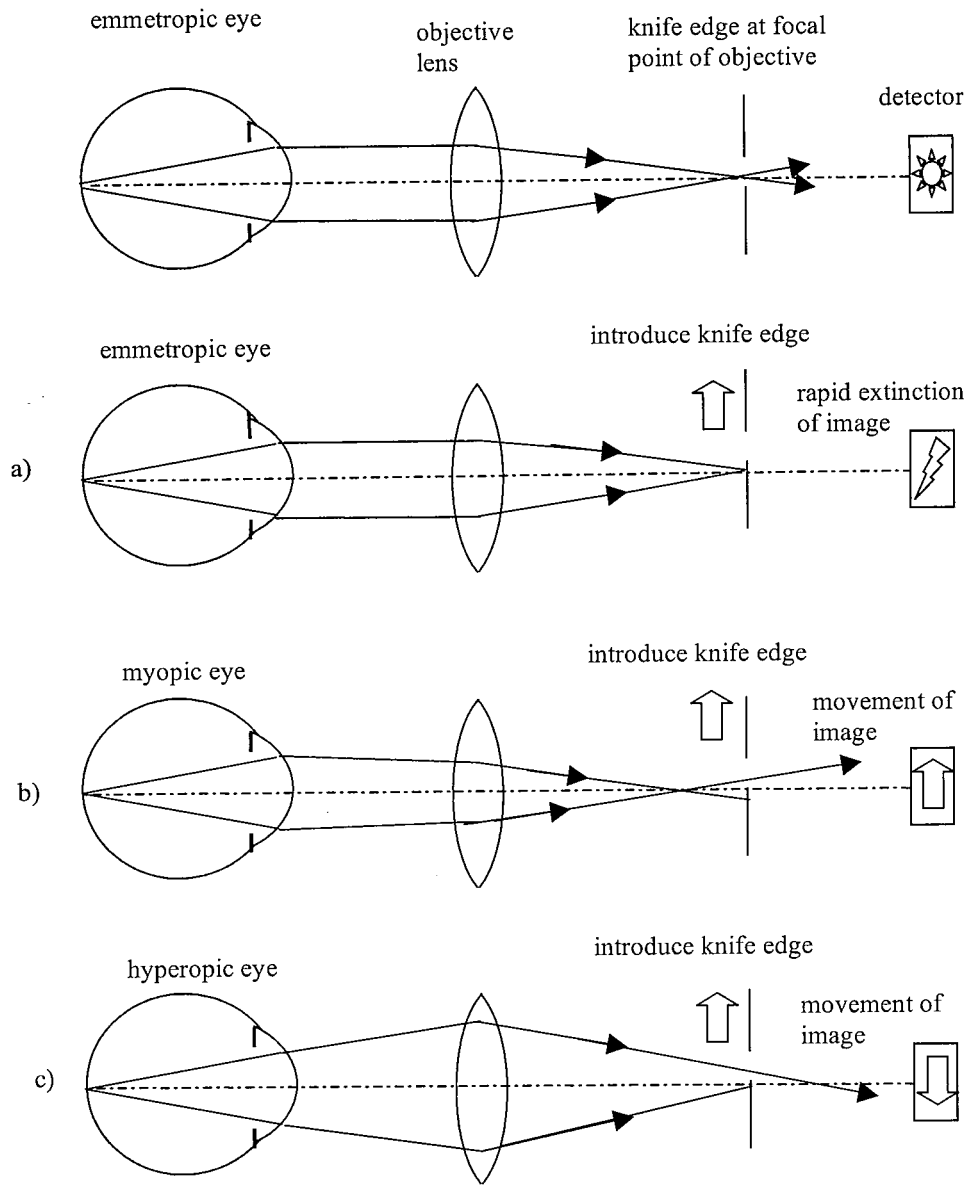


**Figure 2.18 Foucault knife edge test for a) emmetropic eye b) myopic eye and c) hyperopic eye. The direction and speed of the reflex across the detector provides information on the type and magnitude (respectively) of refractive error.**

Subjective refraction relies on responses from the subject and their interpretation by the practitioner. It measures refractive error iteratively and is sometimes ambiguous, relying on the art of the practitioner. Cycloplegic subjective refraction (where the accommodation ability of the eye is paralysed) is usually considered the most accurate

refraction technique. Typically a practitioner prescribes to a precision of +/- 0.125 dioptres.

Wavefront sensing provides the practitioner with greater detailed information compared to traditional refraction techniques such as retinoscopy, automated refraction, and subjective refraction. It provides objective information about the optical quality of the eye at high temporal and spatial sampling rates. Even lower-order aberrations measured by WFSs are potentially more accurate than those measured by autorefractors because they typically possess higher spatial and temporal sensitivity, and they do not use a fixed pupil diameter. However, the most appropriate refraction technique (or combination of techniques) is dependent on each individual's circumstances and prioritising the importance and relevance of the available techniques requires the technical knowledge of the practitioner.

## 2.19 Historical review of ocular aberrometers

The aberrations of a wavefront can be measured using interferometry or ray-tracing techniques. Most technologies discussed in this thesis are based on ray-tracing techniques and the assumption that a wavefront can be sampled and approximated to a local tilt in the pupil plane (or equivalently a transverse aberration in the image plane). Aberrometers are typically categorised as either subjective or objective and may also be categorised depending on whether the wavefront is subdivided into samples before the first pass into the eye (ingoing) or after the second pass out of the eye (outgoing) (Atchison 2005).

In 1894 Tscherning described a subjective ingoing technique where a mask was used to create a grid of narrow pencils that were imaged onto the retina using a five diopter spherical lens. The subject viewed a distant point source and observed the pattern cast by the grid. The subject was then asked to relate their observations and the displacement of each spot from the regular spacing of the mask was used to describe the aberrations of the eye. Modern adaptations to this technique include the use of a cross-cylinder lens instead of a spherical lens (Howland 1960) which provides advantages such as clearer retinal grid lines (achievable with specific orientation of the cross-cylinder) and a more clearly indicated the zero defocus position. Howland and Howland (1977) used the technique to provide the first measurements of coma in the human eye and introduced Zernike polynomials to describe ocular aberrations. Later, Walsh and colleagues (1984) modified the technique to re-image the retinal image onto a CCD after the second pass, thus making the measurement objective.

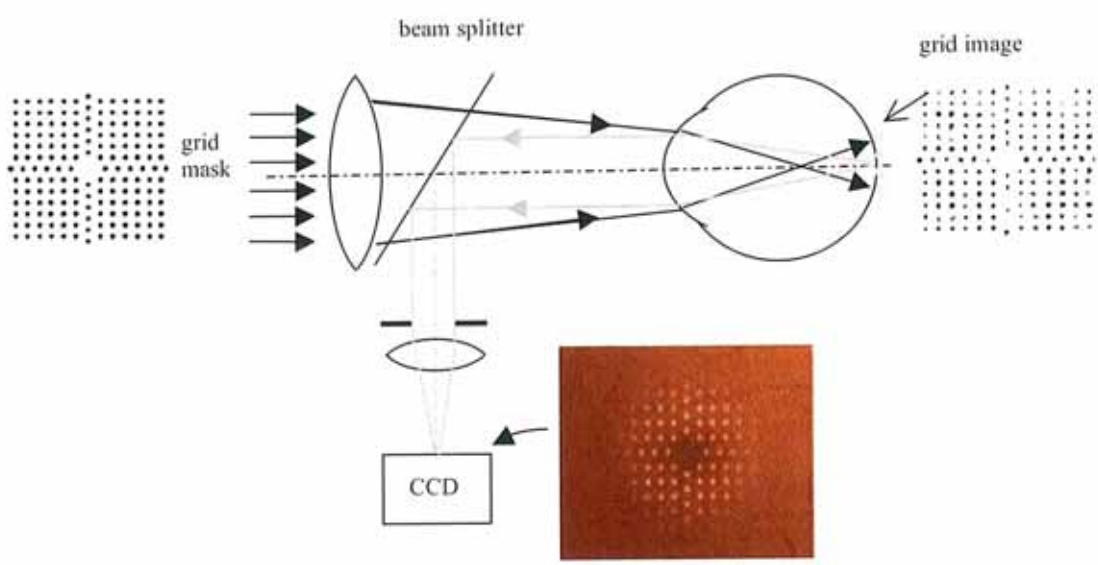


**Figure 2.19 Schematic diagram of the Tscherning aberroscope with modern adaptations (adapted from Yoon 2006).**

In 1992, Webb Penny and Thompson described an aberrometer called the Spatially Resolved Refractometer (Webb *et al.* 1992) which was a further development of the works of Ivanoff (1953) and Smirnov (1962). It used a subjective, ingoing technique that presents a reference target to the subject and a narrow pencil of light that samples a particular point in the pupil. The subject adjusts the angle of incidence of this pencil until the retinal image coincides with the reference target. The process is repeated at many pupil locations to collect multiple local slope values and reconstruct the wavefront.

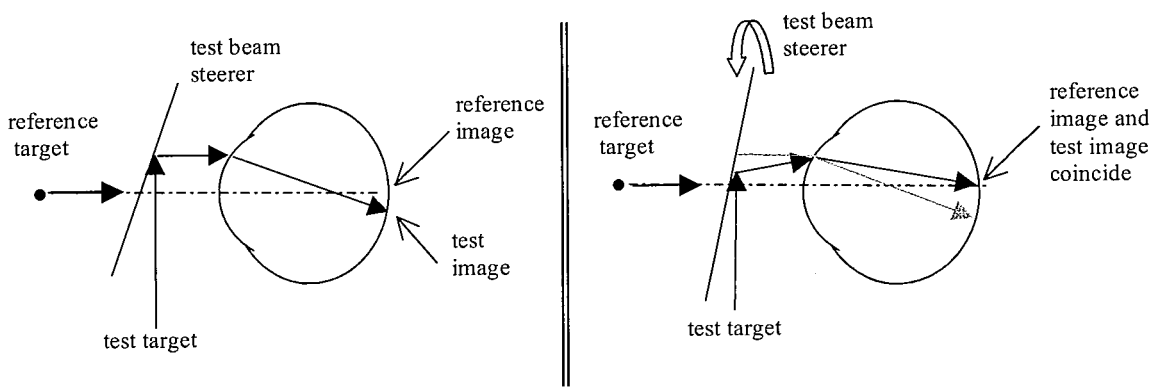


**Figure 2.20 Schematic diagram illustrating the principles of the spatial resolved refractometer (adapted from Webb *et al.* 1992).**

Laser ray tracing (Navarro and Losada 1997, Molebny *et al.* 1997) is an objective, ingoing technique. A reference target is presented to the subject and a narrow collimated pencil from a laser is introduced to sample a particular point in the pupil. The retinal spot reflects light back out of the eye where it is imaged onto a CCD. The laser is scanned over the pupil to collect multiple samples. The first pass is the measurement pass and in the second pass all pencils are assumed to be equally affected by the overall aberrations of the full pupil (i.e. spatial invariance). Note the differing conceptual approach compared to the HS WFS. The assumption of spatial invariance (isoplanatism) is somewhat contradictory because the test itself exists because the eye is known not to be spatially invariant. The displacement of the spot image on the CCD relative to the

reference position is used to calculate the local tilt of the wavefront at that particular pupil position and reconstruct the wavefront.

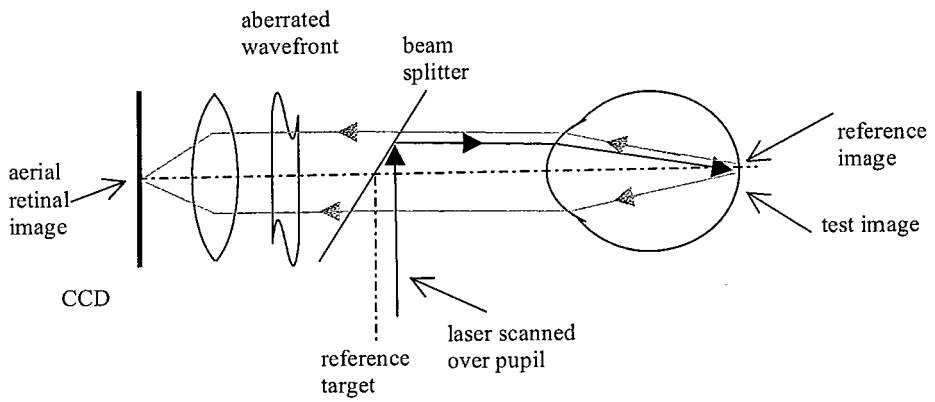


**Figure 2.21 Schematic diagram illustrating the principles of laser ray tracing (adapted from Navarro and Losada 1997).**

The HS WFS was first used in ocular applications by Liang, Grimm, Goelz, and Billie (1994). It is an objective, outgoing technique which has become a popular choice for modern commercial WFSs designed for the eye. Comparison studies between HS wavefront sensing and other aberrometry techniques have been made by many researchers including Salmon *et al.* (1998) and Liang and Williams (1997). HS WFSs for the eye are comprehensively discussed in chapter 3.

## 2.20 Types of wavefront sensors

There are many technologies available to perform optical wavefront sensing and each type often has various possible configurations (Tyson 1998 p142). The HS type is by far the most common and well understood in the vision science community. Essentially the HS is a local tilt detector and thus senses the first derivative of the wavefront. If this concept is extended to the second derivative (the Laplacian of the wavefront), the operational principles of the curvature WFS can be understood. The curvature WFS examines intensity profiles an exact distance before and after the focus of a beam.

Curvature in the wavefront produces radial displacements in the edge of the beam and changes in the average intensity of the beam. Local changes in wavefront curvature produce intensity changes of opposite polarity at the two planes and the normalised ratio of intensities for corresponding CCD pixels is a measure of wavefront curvature.

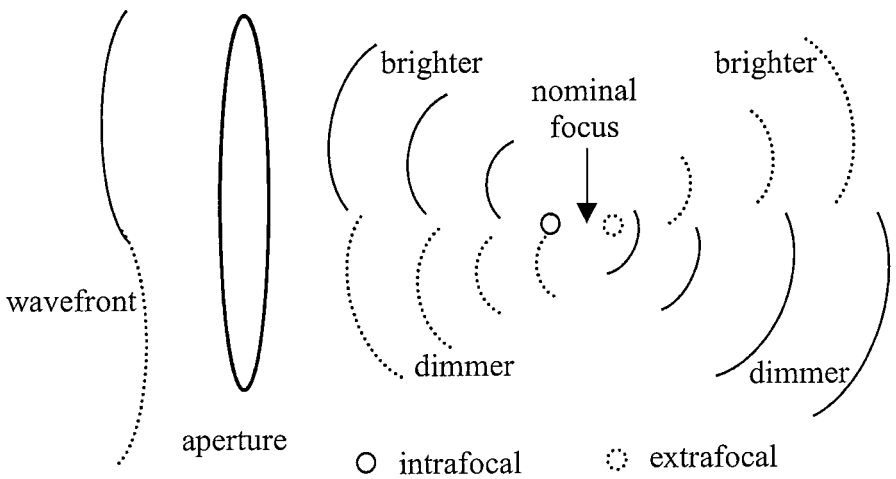


**Figure 2.22 Schematic diagram illustrating the principles of curvature wavefront sensing (adapted from European Southern Observatory 2003).**

An important issue to consider in curvature wavefront sensing is the focus-switching device. Mechanical switches can give noisy results and it may be preferable to use a variable focusing device (e.g. a spatial light modulator or a deformable mirror). Such a switching device producing AC modulation of the pupil conjugate simplifies subaperture positioning because the measurements are relative (Tyson 1998 p143). Another advantage of this arrangement is the ability to alter the spatial and temporal sensitivity of the sensor by varying the amplitude and speed of the switch modulation (Tyson 1998). This capability would be useful when trying to cope with the large inter-subject variation of ocular aberrations encountered in a clinical setting.

The pyramid WFS is another type of sensor capable of altering its spatial and temporal sensitivity via a modulation process. This sensor is based on the principle of the Foucault knife edge test. The wavefront is typically replicated into four pupils by rapidly steering the beam over the apex of a pyramid. The intensity at each corresponding pixel in each replicated pupil is then analysed to determine the wavefront aberrations.

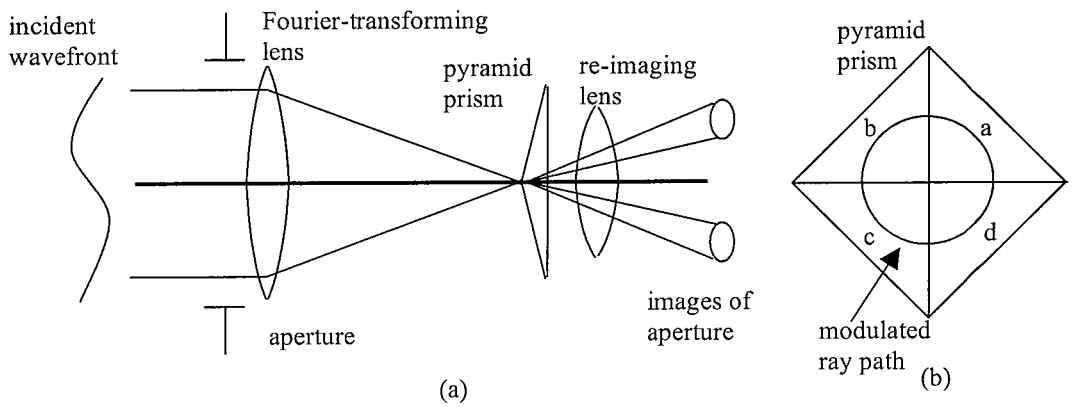


**Figure 2.23 a) Principle of the pyramid wavefront sensor. Light from the pupil is split at the Fourier plane and re-imaged as four separate pupils (only two are shown in the image). b) The beam is modulated, i.e. rotated around the pyramid centre (from Burvall *et al.* 2006).**

Interferometry is another technology that can be used to measure the profile of a wavefront. This technique is used in optical metrology and is especially suited to measuring high spatial frequencies and low amplitude aberrations. It is prone to vibrational noise and is especially difficult when testing large beam diameters (Spiricon 2004). Additionally, the interpretation of interferograms requires sophisticated software. WFSs using shearing interferometry technology have successfully measured aberrations of the tear film (Dubra *et al.* 2004). There are other novel WFSs, for example that described by Neil *et al.* (2000), the discussion of which is beyond the scope of this thesis.

## 2.21 Modern commercial ocular wavefront sensors

The commercial market is predominantly shared amongst 5 main ocular WFSs; COAS by Wavefront Sciences, ZyWave by Bausch and Lomb (fig. 2.24a), WASCA aberrometer by Zeiss, OPD Scan by Nidek, and LADAR Wave by Alcon (fig 2.24b). Most are based on HS technology. These WFSs are predominantly used by refractive surgeons and are incorporated into excimer laser instruments. Because their source code is protected and their optics have restricted physical manipulation, they are not always well-suited to research.

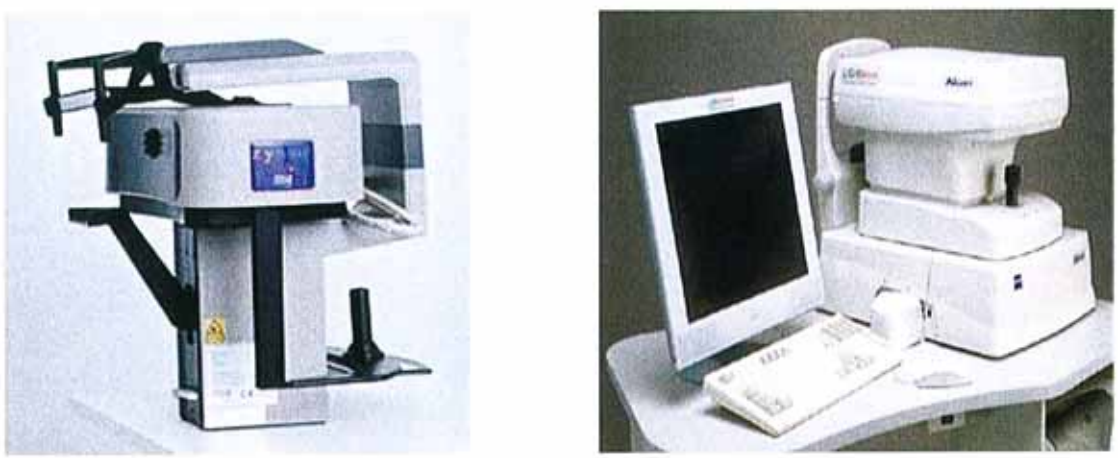

**Figure 2.24 Photograph of a) ZyWave and b) LADAR Wave commercial ocular wavefront sensors.**

One general criticism of commercial instruments is their insufficient treatment of error analysis and significant figure analysis. Some instruments give data in conflicting formats and do not allow some results to be manipulated or even accessed. Some commercial instruments do not conform to the OSA standards (Thibos *et al.* 2000) although this is to be expected as most instruments were developed before the standards were published. The most dramatic departure from the OSA standards occurs in instruments that define wavefront aberrations relative to the video-keratoscope axis instead of the line of sight (Salmon and Thibos 2002). Commercial WFSs do not require

a skilled operator, although interpreting their results does require a skilled practitioner. Our experimental WFS (see chapters 4 and 5) requires an operator with a moderate skill level, as some mechanical and software parameters are operator-defined (eg. the Badal optometer requires a manual setting).

Various limitations remain in the current designs of commercial WFSs. Their aberration measurements are only concerned with monochromatic light and they involve an unnatural viewing field for the subject. They do not provide information regarding chromatic aberration in the eye, scatter in the eye, subjective preference and acceptance, or the binocular vision status of the subject. They are sensitive to accommodation-induced fluctuations of aberrations. Many of these limitations also affect autorefraction technology and may be addressed in a similar way that autorefractors have attempted to address them (e.g. by using a fogging technique) (Dave 2004). Just as autorefractors can give inaccurate results in the presence of media opacities, corneal irregularities, or poor tear film quality, so too can WFSs. Ginis and colleagues (2004) outline areas where practitioners should be careful in interpreting results from WFSs such as re-scaling procedures, pupil edge determination, pupil centre determination, and noise levels.

### 2.22 Standards for reporting ocular aberrations and nomenclature

The OSA standards recommend that ocular aberrations be described by Zernike polynomial coefficients for the wavefront conjugate to the pupil plane and with the origin and axis defined along the line of sight (Thibos *et al.* 2000). The standards do not define a specific pupil diameter over which aberrations should be reported, nor is there a specific wavelength recommended for reporting aberrations. Although higher-order aberrations may not differ significantly across the visible spectrum (Fernández *et al.*

2005, Llorente, *et al.* 2003), defocus is certainly dependent on wavelength. Given the typical peak of the relative luminous efficiency curves for the standard photopic observer, 555nm would seem a reasonable selection for a standard wavelength and this would require a conversion from the red and infrared wavelengths that most WFSs use.

Visual scientists use various axes for describing ocular alignment and a brief definition of these axes is worthwhile mentioning here[6]. Because the eye is not rotationally symmetric it does not have a true optical axis. Instead, the optical axis is approximated by the line passing through or near to the centres of rotation of the four optical surfaces of the eye. The visual axis is defined by the line connecting the fovea to the fixation target via the eye's nodal points. The line of sight is defined by the line connecting the fovea to the fixation target via the centre of the entrance pupil. The horizontal angular separation between the visual axis and the optical axis, commonly referred to as angle $\alpha$, varies from +17 degrees temporal to -2 degrees nasal (fig 2.1). Typically an average value of 5 degrees temporal displacement is quoted (Bradley and Thibos 1995).

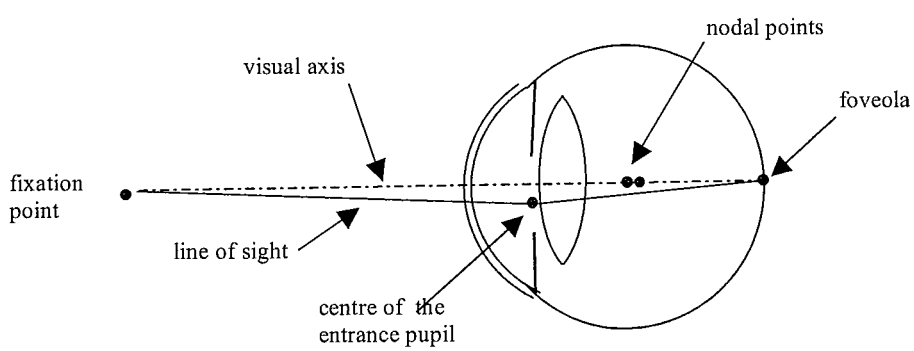


**Figure 2.25 The line of sight and the visual axis (adapted from Bradley and Thibos 1995).**

[6] Ambiguity exists regarding the definition of some axes of the eye. For further reading see Atchison and Smith (2000) chapter 4.

The OSA standards recommend that wavefront aberrations be reported from the clinician's point of view while observing the wavefront in the exit pupil of the subject. Positive phase values represent a phase-advanced wavefront and negative values represent a phase-retarded wavefront. The coordinate system is illustrated in fig 2.26 and full details of the standards are given by Thibos *et al.* (2000).

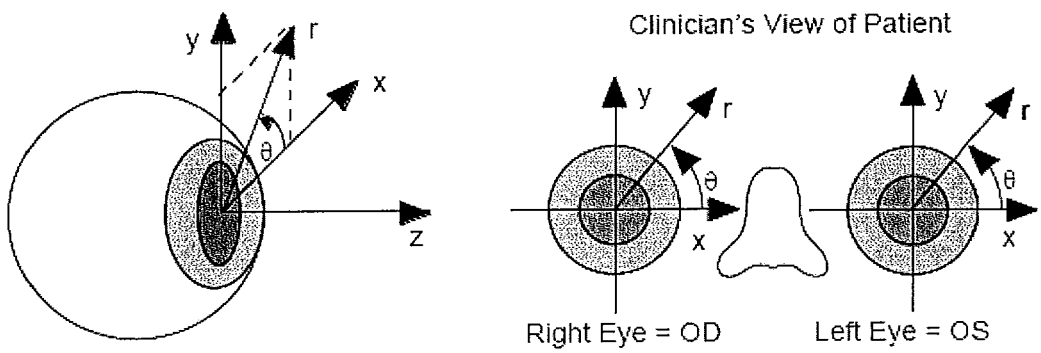


**Figure 2.26 OSA standard coordinate system for reporting ocular aberrations (Thibos *et al.* 2000).**

Apart from not being rotationally symmetric, the eye has other features that make the standardisation of aberration reporting difficult. The pupil of an individual's eye may not necessarily be circular, the foveola is displaced temporally, and it is not uncommon for optical elements such as the crystalline lens to be tilted or decentred. It should be noted that Zernike polynomials lack any biological or anatomical basis to be applied to the eye – it is simply mathematically convenient to use them (Smolek and Klyce 2003). Interpretation of Zernike coefficients requires particular care, for example, orthogonality of Zernike modes in the pupil plane should not be misinterpreted as independence of optical consequences at the image plane (typically the retina).

## 2.23 Current and future applications of wavefront sensing in vision science

HS technology has its foundations in astronomy and is a fundamental component of many active optics and adaptive optics (AO) systems used on large telescopes. Outside of astronomy, HS WFSs have been adapted to a wide variety of applications including meterology and vision science (Liang *et al.* 1997, Spircon 2004, Schäfer and Mann 2002, Booth *et al.* 2002).

The term 'super vision' originated after applying the Nyquist sampling theorem to the anatomical limit of spatial resolution created by the typical foveal cone spacing of 120 cones/degree (Liang *et al.* 1997). The Nyquist frequency limit of 60 cycles/degree is equivalent to a visual acuity Snellen fraction of 6/3 (cortical hyperacuity notwithstanding). Measuring the wavefront aberrations of the eye is the first step in providing an aberration correction treatment aimed at potentially reaching this 'super vision' limit. Various modalities for higher-order aberration correction in the eye are being investigated, such as spectacles (Steinhübel 2007), intraocular lenses (Piers *et al.* 2004), contact lenses (Thibos *et al.* 2002b) and refractive surgery (Marcos *et al.* 2001). If we attempt to improve visual performance by correcting higher-order aberrations, consideration must be given to the choice of which aberrations to prioritise. It is unknown how visual performance is affected by different aberration modes of equal wavefront variance (Thibos *et al.* 2002a), although in general, modes with lower angular frequency terms seem to be more deleterious on visual performance than higher angular frequency terms (Schwiegerling 2004).

Customised refractive surgery attempts to compensate for both the lower-order and the higher-order static aberrations of the eye. Dynamic aberration correction might also be

possible in the future with adaptive devices (Vdovin *et al.* 2003). Currently customised refractive surgery does not reduce pre-operative higher-order aberrations. Instead, it is aimed at not exacerbating the higher-order aberrations as much as conventional refractive surgery does (LASIK leader 2002, Marcos *et al.* 2001). The variation of higher-order aberrations over different time scales complicates the potential for higher-order aberration correction modalities such as laser in situ keratomileusis (LASIK) refractive surgery where multiple surgeries are not desirable. Research into a more precise treatment delivery is continuing with femtosecond lasers capable of faster pulses and a smaller focal spot size (Heisterkamp *et al.* 2004).

Because spherical aberration is rotationally symmetric and often a greater magnitude than fellow higher-order aberrations, some advances are being claimed in a contact lens correction modality. Contact lenses might become a successful modality for correcting higher-order aberrations if rotation and centration on the eye can be controlled without a detrimental effect on eye health (Cox and Lagana 2004). Perhaps the development of higher-order aberration correction for improved visual performance will require the creation of a totally novel correction modality.

The counter argument is that correcting higher-order aberrations may not offer a significant improvement in real-world visual performance for the majority of normal eyes. For example, practitioners often find that subjects can be tolerant to more than 0.25 dioptres defocus during subjective refraction (equivalent to 0.33 microns RMS for a typical pupil diameter). For these subjects, the correction of higher-order aberrations (typically a lower magnitude than 0.33 microns RMS) may have no real world benefit, assuming the MTF analysis of Guiro *et al.* (2002) can be extrapolated to infer a similar

equivalency of retinal image blur would occur for a mean higher-order RMS of 0.33 microns. Any number of physiological processes could potentially negate any higher-order aberration correction treatment. For example, the steady-state accommodation microfluctuations are typically of greater magnitude (Charman and Heron 1988) than the higher-order aberrations in normal eyes (Thibos *et al.* 2002a). Additionally, consideration must be given to neural processing which is unique for each individual. Research suggests that the visual system may actually benefit from a small, specific, aberration level (Artal *et al.* 2003). As such, optimal visual performance may require some unique residual non-zero aberration level of some modes.

Most researchers now accept that 'super vision' is not immediately achievable due to temporal fluctuations, neural processing issues, scatter (Cox *et al.* 2003), diffraction, chromatic aberration, and the technical challenges of creating a delivery modality for the correction of higher-order aberrations. The likely near-future success of applications aimed at improving vision via a dispensed device or treatment is arguable. Even if the technology existed today in a practical form, its level of uptake in a population with normal eyes, likely to find the visual improvement in the real world insignificant, is arguable. Currently the most promising, realistic and successful vision science applications of HS/AO technology are the improvement (not perfection) of refractive surgery (LASIK leader 2002) and high resolution ocular imaging (fig. 2.27).

Measuring wavefront aberrations is the first step in AO imaging – a process that compensates for dynamic aberrations (and typically higher-order aberrations) to create a high resolution image. AO imaging systems are capable of photoreceptor imaging, high-resolution blood flow imaging, microperimetry, and high-resolution pathology detection

(e.g. microaneurysm and exudate detection) (Roorda 2005). Photoreceptor imaging can be combined with retinal densitometry to allow non-invasive *in situ* photoreceptor cone classing (fig. 2.27) (Roorda and Williams 1999). This technology could possibly be extended to include other retinal cell types if the contrast problem can be addressed. Successful imaging requires good resolution (typically provided by AO modalities) but it also requires contrast in the object, which is typically provided by invasive dye agents if no natural contrast exists (Gray *et al.* 2006).

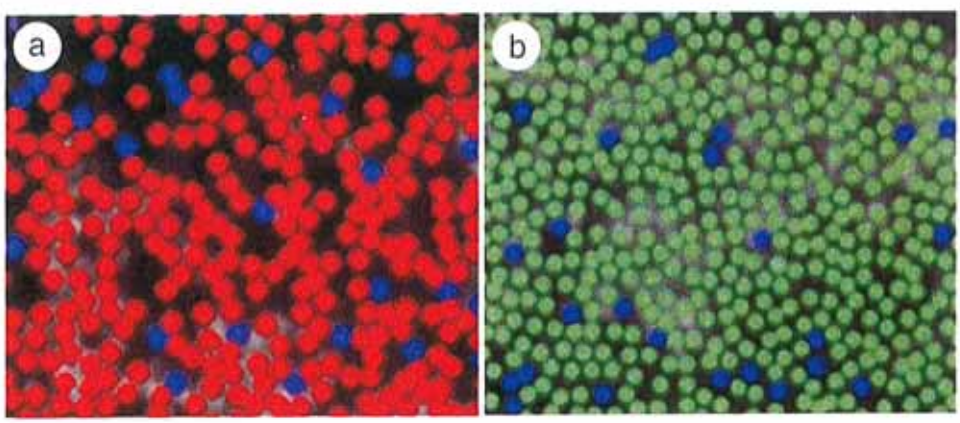


**Figure 2.27 Pseudocolour images of the dichromatic cone mosaic (Carroll *et al.* 2004). Blue, green and red are used to represent the short, medium and long wavelength cone subclasses respectively.**

*"For visual disorders involving cone loss, AO imaging will enable much earlier detection and diagnosis and prove to be a very valuable tool to detect retinal pathology that is otherwise invisible to current clinical methods."* (Carroll *et al.* May 17 Proceedings of National Academy of Sciences 2004).

Single photography is convenient for retinal imaging if the aim of the research is cone classification, however, video imaging is useful for dynamic studies that may wish to investigate blood flow, the dynamic reflectance of cones, and to allow the examiner to establish orientation bearings for a specific fundus location (Roorda 2005). Ocular imaging modalities have shown excellent potential to be enhanced with AO technology.

Optical Coherence Tomography and the Scanning Laser Ophthalmoscope offer non-contact, non-invasive, *in-vivo*, imaging (Fercher *et al.* 2003, Roorda 2005). With the incorporation of AO technology they produce extremely high resolution retinal images (Carroll *et al.* 2005). AO is not the only technique available to improve image quality in these applications. There are numerous post-processing techniques used to enhance images, including deconvolution and stacking multiple images to improve signal to noise ratio (SNR) (Christou *et al.* 2004).

The technological advances in WFS/AO hardware components are as equally impressive as the vast development of WFS/AO applications. Hardware advances include front end on-chip CMOS fabrication which dramatically increases WFS processing speed and has the potential for significant cost reduction per unit device if mass produced (Hean Pui *et al.* 2002). Similarly, CCD camera developers are investigating the integration of microlenslet arrays with CCD detector fabrication. This will improve the CCD chip fill factor and responsivity (Ke *et al.* 2005). Another key element in an AO system is the correcting device and the development of MEMS technology holds promise to make this component inexpensive and small (Doble and Williams 2004).

# CHAPTER THREE

# The Hartmann Shack wavefront sensor for the eye – overview, optical design aims, and optical design compromises

This chapter begins with a description of the basic elements required in a HS WFS for the eye. The design aims of our experimental HS WFS (e.g. off-axis capability, compactness, and simultaneous pupil centre monitoring) are discussed along with less project-specific optical design issues (e.g. the double pass approximation, dynamic range and sensitivity). Because our WFS contained only a few moving parts and simple electronics we have chosen not to discuss mechanical and electrical design issues.

## 3.1 Hartmann-Shack wavefront sensor principles

Most HS WFSs for the eye are arranged similarly. A description of a typical generic configuration and the associated operational principles follows. A fixation target is presented to the subject to aid alignment, control eye movement, and to control accommodation. A monitoring system is required for the operator to judge subject alignment and focus (working distance between the instrument and the subject). A narrow beam of light is focused onto the retina in the first pass. The small entrance pupil size, the central location at the cornea, and scatter off the retina act to negate any phase information obtained during the first pass. The spot of light focussed on the retina now acts as a secondary source called the 'retinal beacon'. Scattered light passes back through the eye and develops aberrations due to imperfections in the elements of the eye before exiting through the whole pupil. The pupil conjugate is focussed onto a lenslet array which samples the wavefront into subapertures. Each lenslet creates an image of the retinal beacon which is focussed onto a CCD. A computer program analyses the image from the CCD (an array of spots) and compares it to a reference image created

prior by a plane wavefront incident on the lenslet array. In this way, aberrations within the instrument itself are accounted for by the reference image. The spot displacement of each subaperture with respect to its reference position allows the local slope of the wavefront over the subaperture sample to be determined in two dimensions. The local slopes (transverse aberrations) can be integrated over the pupil to reconstruct the wavefront topography (zonal reconstruction). Alternatively, a least-squares technique can be used to fit the data to a set of Zernike polynomials (modal reconstruction). The coefficients of the Zernike polynomials are then used to describe each individual aberration mode's contribution to the entire wavefront RMS error.

### 3.2 Novel optical design aims

The novel features of the optical design are briefly mentioned here and then discussed in greater detail throughout this chapter and chapter 4. Our experimental WFS was designed to combine desirable research features (e.g. adaptability for future modifications) with advantages commonly found in commercial instruments (e.g. compactness and transportability). Unique features of the optical design include; simultaneous pupil centre determination, a superimposed two-channel system, off-axis capability, optimised lenslet sampling orientation, and telecentric imaging. Subject alignment is achieved by the use of a parallel channel that is recombined with the sensing channel to simultaneously image the external eye and the HS spots onto a single CCD. The pupil centre is determined using this image of the eye rather than from the HS spots. Off-axis measurements are possible with our experimental WFS which has an unobstructed 10 degree field of view. The rotated lenslet array increases dynamic range in those meridians where astigmatism is most typically expected in the eye. Telecentric re-imaging of the HS spots increases the system's robustness to CCD misalignment.

The optical design process was iterative, with many practical difficulties requiring design alterations. In consideration of our stated preferences for features, the design parameters had to be balanced to provide the best compromise possible. The constructed wavefront sensor proved to be successful in a clinical research setting as evidenced by the experiments presented in chapters 7 and 8.

### 3.3 The double pass approximation

To objectively measure the aberrations of the eye *in situ*, we are confronted with the problem of only being able to readily access object space. Most subjects would complain if we tried to access the image space! Light used to measure aberrations must therefore pass through the optics of the eye twice. If the entrance and exit pupils are equal sizes, then this double-pass imaging process is described by the autocorrelation of the single-pass PSF (Artal *et al.* 1995). The autocorrelation results in a doubling of even functions (even aberrations appear to have double the magnitude of a single pass measurement) and negates odd functions (odd aberrations appear to have zero magnitude, regardless of the single pass measurement). Even aberrations have symmetric functions described by

$$W(\rho,\theta) = W(\rho,-\theta)\ . \tag{3.1}$$

Whereas odd aberrations have symmetric functions described by

$$W(\rho,\theta) = -W(\rho,-\theta). \tag{3.2}$$

*In situ*, single pass measurements are possible with configurations that excite naturally occurring pigments in the retina such as Lipofuscin (Diaz-Santana and Dainty 1999). However, typical HS WFS configurations are dependent on the double pass process. The solution that vision scientists use is to create a small entrance pupil and a large exit

pupil (Artal *et al.* 1995). Aberrations over the small pupil of the first pass are quite low (assuming a normal eye) and this argument is convincing if the probing beam is positioned close to the line of sight. Effectively, this means that only paraxial rays are being used to create the retinal beacon and any phase change experienced by the principal ray is experienced by all rays. Additionally, during a typical measurement period (~50 msec), small movements of the retina act to destroy any phase structure the probing beam may have developed during the first pass (Diaz-Santana and Dainty 2001). This also helps to reduce coherence from the beam and speckle in the HS spot images.

### 3.4 Shannon sampling theorem, Nyquist frequency and aliasing

The HS WFS relies on a sampling procedure to reconstruct an original signal (the wavefront). We are therefore bound by the Shannon sampling theorem which describes the limit of information obtainable. A sampling technique is only sensitive to frequencies at values less than half of the chosen sampling frequency. The Shannon sampling theorem applies to time (which limits our knowledge of temporal fluctuations in aberrations) and space (which limits our knowledge of higher aberration modes). With regard to ocular aberrations, it is unknown what the Nyquist frequency might be – assuming that the signal is band limited. Although, it is probably not of practical importance in many vision science experiments because at high spatial and temporal frequencies, noise is likely to swamp any signal present and no additional useful information would be gained by sampling above this rate. During the optical design process it was important to predict as much as possible about the type of wavefronts we expected to encounter. These predictions made it easier to find the best compromise

between sampling resolution and dynamic range - which subsequently balances the problems of aliasing and saturation.

### 3.5 Temporal resolution and dynamic range

The temporal sampling requirements in the eye are not as demanding a constraint as they are for astronomy. This is partially due to the higher temporal fluctuations in atmospheric aberrations compared to ocular aberrations, but also due to the lower optical flux available for sensing in astronomy. In general, the faster you can sample the signal the better, and even a modest CCD working at its maximum read-out rate won't generally encounter SNR problems when used for wavefront sensing in the eye. One of our design aims was to sense and display wavefront data in real time and this partially influenced our choice of temporal resolution, although software processing speed proved to be a tighter bottleneck that limited our ability to present data in real time (see chapter 5). For wavefront sensing in the eye, it is important to consider the time scales of various mechanisms such as blinking, tear film degradation, accommodation, fixational eye movements, and contact lens movement.

The average blink rate is approximately 12 blinks per minute, although there are many stimuli that can alter this rate. A spontaneous blink occurs in about 260 milliseconds. Approximately 1/3 of this time is spent closing and 2/3 is spent opening. The tear film flow rate is not a significant consideration for wavefront sensing, tear film stability is the more important issue. It's most common metric (tear break up time), can be less than 10 seconds for a patient with dry eye. Aberration evolution associated with tear film dynamics can be measured with interferometric techniques and are not negligible for diffraction-limited imaging applications (Dubra *et al.* 2004).

The accommodation system's positive response to stimulus is faster than the negative response. It occurs with approximately 370 millisecond latency and reaches a maximum amplitude in 1 to 2 seconds. Steady state microfluctuations in the accommodation system are controlled through a negative feedback loop using retinal blur. These variations have an envelope of 0.5 dioptres and occur with frequencies up to 3 Hz (Simmers *et al.* 2001). High frequency components of microfluctuations in accommodation show correlation with arterial pulse (Collins *et al.* 1995, Hampson *et al.* 2005).

Even with well-trained observers, eye movements will occur during any ocular measurement. Fixational eye movements are typically categorised as;

- drift - a slow variation in gaze direction occurring at about 5 Hz and ranging over 3-12 minutes of arc.
- microsaccades - rapid changes in fixation of up to 100 degrees/second speed, occurring at 0.5Hz to 3Hz, and ranging over 6-120 minutes of arc.
- microtremor - high frequency oscillation occurring between 40 Hz and 100 Hz and range over less than 1 arc minute.

Researchers using AO imaging systems typically correct eye movements if using video or multiple frame modalities. This is commonly achieved either with gimbal mirrors or post-processing techniques (Roorda 2005). Drift and microsaccades should not pose a significant problem for our WFS because it operates at approximately 10Hz and defines the pupil centre uniquely for each HS spot image. The small magnitude of fixational eye movements means that they will still be within the measurement field of our WFS which can tolerate lateral movements of up to 1 mm (assuming a 6 mm pupil diameter).

Although our WFS is susceptible to the effects of microtremor, the small movements involved would only become significant if our WFS was incorporated into an AO system attempting diffraction-limited imaging of structures subtending approximately one minute of arc (e.g. parafoveal photoreceptors). Our experimental WFS operates at approximately 10 Hz and useful aberration measurements should even be obtainable for subjects with fixation problems such as nystagmus.

It is important to understand how contact lenses affect higher-order aberrations, especially as they are being considered as a possible modality for higher-order aberration correction (Thibos *et al.* 2002b). Contact lens movement relates to fitting characteristics, tear composition, and blink characteristics, all of which are unique for each patient. A high temporal sampling rate is necessary for studies investigating aberrations and contact lens movements. We found a 10 Hz data display rate was sufficient at capturing contact lens dynamics when wavefront aberrations of subjects wearing contact lenses were measured on our WFS (see chapter 6).

Temporal sensitivity is also dependent upon the CCD exposure time and the CCD read-time, which in turn is dependent upon factors such as quantum efficiency of the CCD, intensity of the source, and system efficiency to ensure an adequate SNR in the HS spot image. Commercial HS WFSs can capture frames at rates as fast as 10 Hz (COAS) but most operate at much lower speeds. Non-commercial ocular HS WFSs can operate at up to 300 Hz (Nirmaier *et al.* 2003) and have the potential to operate in the MHz range (Hean Pui *et al.* 2002). Our experimental WFS can capture data at 10 Hz.

### 3.6 Spatial resolution and dynamic range

Wavefront sensing in the eye requires a difficult balance between dynamic range and spatial sensitivity. Our experimental WFS was designed with sufficient dynamic range to allow aberration measurements on a large proportion of the normal population. We expect the dynamic range will be sufficient to allow measurements on more challenging populations such as eyes that have undergone surgery or those that have irregular aberrations. Our WFS was designed to measure off-axis aberrations – which also requires a large dynamic range to manage the expected increase in off-axis astigmatism. Prior knowledge tells us that $2^{nd}$ order aberrations greatly exceed higher-order aberrations in most eyes. Therefore, it is logical to remove as much of the $2^{nd}$ order aberrations as possible before sensing the wavefront. Indeed HS principles rely upon the assumption that the wavefront sensed at the lenslet array is almost plane and contains only small residual aberrations. Removing $2^{nd}$ order aberrations can be approached in many ways, each with its own merits and limitations. Ametropia correction typically requires the use of one or more of the following elements; daisy wheel, trial lens, spectacles, contact lens, rotating cross cylinders, and/or a Badal optometer.

The ametropia correction device determines the gross dynamic range. Some wavefront sensor configurations also incorporate a rotating cross-cylinder element to correct astigmatism prior to sampling the wavefront at the lenslet array. Our design avoided rotating cross cylinders because of the added complexity and difficulties in maintaining consistent instrumental aberration (and consequently, difficulties in maintaining accurate reference positions for the HS spots). The use of trial lens was avoided due to the potential problems of scratches, dirty surfaces, uncontrolled reflections, and unknown aberrations within the trial lenses themselves. Some commercial instruments

translate the CCD along the optical axis of the WFS to correct for ametropia. This has the disadvantage of introducing blur, variation in spot magnification, variation in spatial sampling, and the process is prone to misalignment. A daisy wheel element (commonly used in the direct ophthalmoscope) offers benefits of compact size and speed of manipulation but disadvantages of variable instrumental aberration. For our optical design it was decided that a Badal optometer[7] was the most suitable device. The Badal optometer provides a constant magnification at all settings, and its components are consistent for each setting (and therefore instrumental aberration is almost consistent for each setting). Depending on the optical configuration, it also provides flexibility in controlling the accommodation stimulus and fogging levels. The choice of focal length for the Badal lenses is critical to beam magnification, overall instrument size, and spatial sampling. Setting the Badal optometer position requires either prior knowledge (e.g. a recent spectacle prescription) or a 'preliminary' subjective-focus procedure (see section 6.3). Because the Badal optometer corrects defocus, we expect for most eyes that astigmatism will be the predominant aberration that is detected by the sensor (tip and tilt are ignored because they are not relevant to our application).

Apart from the Badal optometer, the dynamic range is also determined by the range of the sampling element (the lenslet array). The principal limitation of the sampling element's dynamic range relates to the necessary restriction of HS spot movement to avoid cross-talk. Each HS spot is only allowed to fall inside the designated subfield of its parent lenslet and confusion between neighbouring spots is avoided. Powerful unwrapping algorithms (Lundström and Unsbo 2004) and shift-masking technologies (Yoon 2006) are available to overcome this restriction. However, both techniques result

[7] For a description of various Badal optometer configurations and their associated features see Atchison and Smith (2000) chapter 8.

in a compromise of reduced resolution, either temporally or spatially. The dynamic range of the lenslet array can be increased by increasing the lenslet pitch (equivalent to decreasing the sensing beam diameter) or by decreasing the focal length of the lenslets. These actions consequentially reduce sensitivity to higher-order aberrations and to the wavefront aberration magnitude in general. A designer may elect to manipulate the beam magnification to achieve the desired lenslet sampling rate for a given lenslet pitch, however the CCD chip size (and the CCD pixel size) are often not free design parameters. Binning and region of interest capabilities allow the designer some limited freedoms. CCD chips are necessarily small so that they can be read quickly, and therefore the HS spot image must also be small to fit onto the CCD chip. The ratio between the HS spot size and CCD pixel size (and subsequently the CCD fill factor) is an important issue for centroiding, sensitivity, range of linearity, and pixelisation (Neal *et al.* 2002).

We use prior knowledge to increase the dynamic range of our experimental WFS. Because the Badal removes defocus, typically the largest aberration to be sensed at the lenslet array will be astigmatism. It is known that astigmatism in human eyes has a tendency for alignment close to either the vertical or horizontal meridian rather than an oblique meridian (McKendrick and Brennan 1996). Therefore, the typical HS spot movement in each subaperture will be close to the vertical or horizontal directions rather than along diagonal directions. By rotating the lenslet array at 45 degrees to the horizontal meridian of the eye, the instrument will sample less densely in the horizontal and vertical meridians by factor of $\sqrt{2}$ and the dynamic range is increased accordingly (see fig. 3.1). Future modifications can be envisaged where the lenslet array has a two (or multiple) rotation-position arrangement and the astigmatic dynamic range can be

even further enhanced. To the best of the author's knowledge this feature is unique to our experimental WFS. Our design uses a square geometry lenslet array with a 10 mm focal length and 190 micron pitch. Due to magnification the spatial sampling density at the eye is 380 microns and reduces by a factor of 1.41 in the horizontal and vertical meridians.

Our experimental WFS has a dynamic range of –8.00 DS to +15.00 DS within the Badal optometer, and +/- 2.23 DC within the lenslet array assuming a 6 mm pupil. In traditional optometric terms this transposes to a dynamic range of –9.50 DS to +13.00 DS / -4.75 DC at the spectacle plane for a 6 mm pupil. This dynamic range is comparable to that available in commercial HS WFSs.

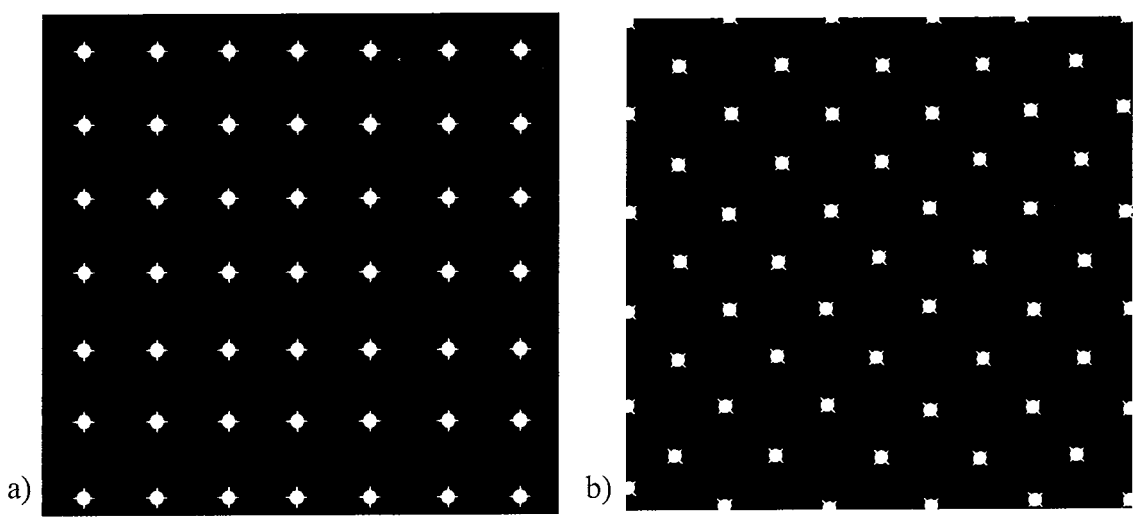


**Figure 3.1 Schematic drawing of HS spots a) traditional HS spot pattern b) our experimental HS spot pattern created by mounting the lenslet array and CCD at 45 degrees to the eye. A more efficient balance between sampling resolution and dynamic range is achieved by using prior knowledge of the eye.**

There are two principal restrictions that apply to the spatial sampling rate at the lenslet array. Firstly, the sample size must be small enough to satisfy the assumption that the wavefront can be accurately represented by a pure tilt over the sample. Secondly, sampling must be at a sufficient rate to satisfy the Shannon sampling theorem in respect

to the desired order of Zernike polynomial fitting or wavefront reconstruction. Our experimental WFS fits aberration data up to $5^{th}$ order Zernike polynomials. We considered this would be sufficient for our application because the magnitude of ocular aberrations above the $5^{th}$ order are likely to be drowned within instrumental noise. Commercial instruments fit aberration data up to similar orders, for example the ZyWave fits aberration data to the $5^{th}$ order. The highest spatial sampling in a commercial HS WFS is every 120 microns by the COAS. Lower temporal sampling rates have advantages of decreased demand on computational resources and increased photon integration (and therefore brighter HS spots with a possibly higher SNR). The spatial sampling rate of our WFS is 21 x 21 samples across an 8 mm pupil (sampling every 380 microns). This sampling rate satisfies the Shannon sampling theorem to fit aberrations up to the fifth order even for pupils as small as 3.76 mm diameter.

Ocular WFSs must be capable of detecting aberrations of relatively low magnitude. As such, the lenslet focal length must be of sufficient length to allow detection of aberrations that are likely to be in the order of magnitude of hundredths of microns RMS. The sensitivity of a WFS is dependent upon numerous factors including centroid determination accuracy, pupil centre determination accuracy, operator judgement of focus and alignment, and other sources of noise (see chapter 6). Traditional subjective refraction techniques are sensitive to within +/- 0.12 dioptres. HS WFS technology offers a dramatic increase in sensitivity to a typical level of +/- 0.01 microns RMS for a generic set of WFS parameters (of course this is dependant on pupil size).

### 3.7 Compact size

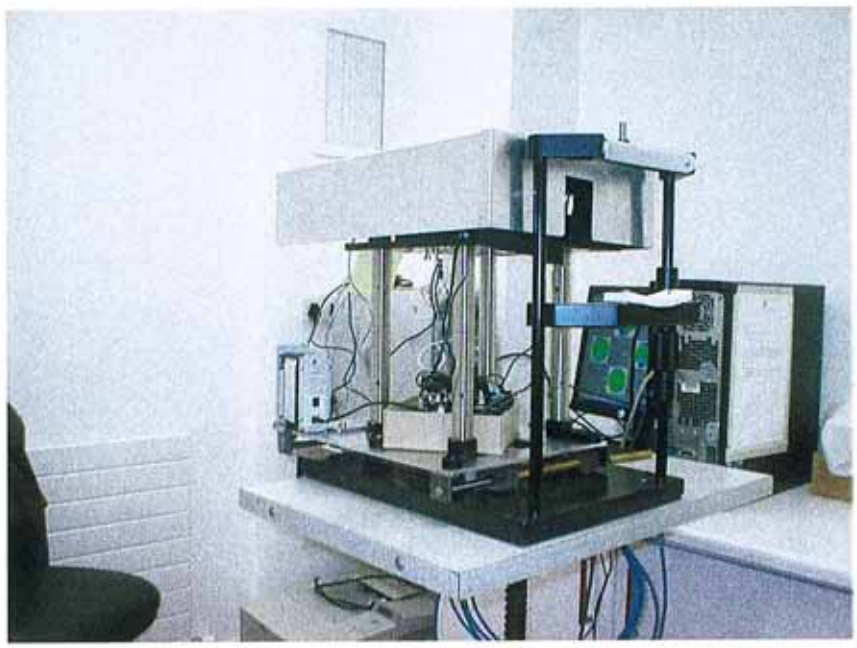

**Figure 3.2 Photograph of the experimental wavefront sensor.**

To use our WFS in a clinical setting its mechanical design had to produce a compact instrument that was transportable. The Linos Microbench ® system was used because it provided a compact and robust mounting. Numerous assembly arrangements were considered in an effort to minimise the overall size and our relatively small CCD helped to achieve this aim. The optical design minimised the optical paths and the overall footprint was compressed with the use of mirrors and the shared use of a single CCD for both the sensing and alignment channels. The WFS itself is bracketed to a stage and headrest base that is familiar to many optometric instruments. It has a locking mechanism and 3 degrees of freedom to achieve subject alignment. It does not use a bite bar. Our WFS is transportable and it has successfully been transported between Galway and Dublin. Relocation of the WFS requires an optical realignment to ensure accurate measurements. The size of our WFS is 20cm x 36cm x 7cm, which is comparable to commercial WFSs.

### 3.8 Off-axis capability

Off axis aberration measurements are not possible on commercial HS WFSs without modification or an external fixation target. The measurement field of our WFS is approximately 10 degrees (5 degree half angle). Measuring over this relatively small field avoids evoking many of the difficulties associated with measuring aberrations at greater field angles. When operating at larger field angles, WFS must be capable of dealing with high amounts of astigmatism and very aberrated wavefronts. As a rough estimate, an extra 2 dioptres of astigmatism can be expected for a 10 degree field angle compared to the on-axis value (estimated from Atchison and Scott 2002), although significant individual variation exists. Some optical elements require larger diameters and closer proximity to the eye to allow an eccentric internal fixation target to be presented to the subject.

When measuring off-axis aberrations, circular pupils appear as ellipses and this causes difficulties because Zernike polynomials are defined over a circle (Atchison and Scott 2002). Another consequence of off-axis measurements is the reduction of spatial sampling in the meridian perpendicular to the axis of rotation. Additionally, subject alignment is prone to greater error because the pupil is tilted and oblique to the instrument axis. Subject alignment requires the operator to focus on the mid-focus position of the tilted pupil. Finally, the double pass problem becomes exacerbated because the first pass develops greater aberration passing obliquely through the cornea and lens at an eccentric location. Anecdotal evidence suggests that nearly all of these potential difficulties are insignificant for measurements on our experimental WFS performed at the maximum field angle of 5 degrees (see chapter 8).

The off-axis capability of our WFS affords unique research opportunities. Information on aberrations and how they vary with field angle is essential for designing future wide field AO systems for the human eye. High resolution AO images of the parafoveal photoreceptors (Carroll *et al.* 2004) are currently possible at a handful of research facilities around the world. It is predicted that multi-conjugate adaptive optics (MCAO) technology will increase the field of view (equivalently the isoplanatic patch), and that other clinically relevant anatomical features which may be located eccentrically in the eye will be imaged with high resolution AO systems. Additionally, off-axis wavefront sensing can provide refraction data for patients with central vision loss who fixate with an eccentric area of their retina. This capability is another example of a clinically practical feature of our WFS.

### 3.9 Unwanted reflections and pollution

Unwanted reflections originate both from elements within the optical system and the subject's eye. Particularly the 1$^{st}$ and 3$^{rd}$ Purkinje reflections are bothersome due to their brightness and proximity to the pupil conjugate. Reflections generated in the first pass through the WFS and the eye are a more important consideration for unwanted reflections because the intensity of the first pass is approximately five orders of magnitude greater than the second pass (Delori and Pflibsen 1989). In our optical design, reflections are minimised by collimating the probing beam along the optical axis but then laterally displacing the beam off-axis by approximately 1 mm at the cornea. Other potential solutions such as using polarisation to minimise corneal reflections were considered but they were not included in the final optical design. Instead, our optical design principally relies on a diaphragm conjugate to the retina to act as a spatial filter and minimise unwanted reflections. Initially the diaphragm was incorporated into the

Badal optometer, this made the system very compact but compromised the dynamic range of the Badal, and so the diaphragm was positioned outside of the Badal optometer in the final design. In designing the Badal optometer we considered using mirrors instead of lenses which would have avoided creating any unwanted back reflections. However they were not included in the final design due to anticipated difficulties in mirror alignment. In the final optical design the first pass probing beam does not pass through the Badal optometer and such considerations became academic. This design compromise of positioning the first pass outside the Badal is unfortunate because pilot studies (see chapter 6) suggest that alternative arrangements to correct refractive error in the probing beam are clinically inconvenient and time consuming. If we choose not to correct refractive error a significant deterioration in HS spot quality is observed (see chapter 6). All optical elements were coated with appropriate anti-reflection coatings.

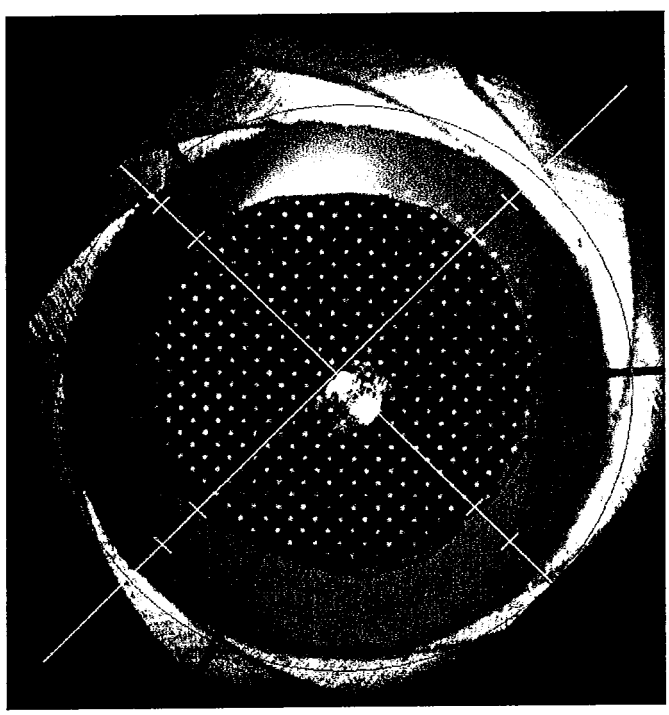

**Figure 3.3 An example of unwanted central reflections created in the sensing channel when the spatial filter diaphragm is not sufficiently closed. An artificial eye was used to generate this image and so the mislocation of the red pupil overlay is expected and does not indicate a software error.**

### 3.10 Reference wavefront

It is preferable that the wavefront used to create the reference HS spot positions originate from the same source as the probing beam. It should share a common optical path through all elements of the sensor if possible. This is something that WFSs incorporating daisy wheels or trial lenses for ametropia correction can't do. They compulsorily have a non-common optical path. The Badal optometer has the advantage that the elements themselves are constant no matter what ametropia setting is required, although the beam width at each Badal element does vary with the ametropia setting and so the reference wavefront isn't perfectly consistent in this configuration either. The Badal is positioned at the null setting during the reference wavefront generation, thus the reference HS spot positions are exact for emmetropic subjects and become less accurate for high ametropia settings.

It is also important to generate the reference wavefront without altering too many elements in the WFS due to the risk of accidentally causing a misalignment. Flip-down elements are very convenient and practical for this purpose although we have not incorporated them into our optical design. Instead we generate a reference wavefront via a simple latchable plane mirror that is also used during instrument alignment. A high quality mirror (surface figure $\lambda/10$) is used to minimise aberration in the reference wavefront. During reference wavefront generation the laser intensity must be reduced to avoid saturating the CCD. The magnification settings of the sensing channel are such that the reference beam diameter does not require any additional expansion beyond the 5 mm diameter produced by the laser collimator. A new reference wavefront is recorded whenever the experimental WFS is realigned.

### 3.11 Optics

Achromatic doublets with f-numbers greater than 10 and high quality mirrors with surface figures less than $\lambda/10$ were used in the construction of our WFS to help achieve high quality images. Computerised ray tracing was used to optimise the optical design and minimise vignetting. Transmission rather than reflection was used wherever possible in the sensing channel to reduced internal instrumental aberration. As one would expect, photon conservation was a general consideration that influenced most optical design decisions, especially those regarding wavelength selection (for the probing beam source, alignment channel illumination, and fixation target illumination) and beam splitter ratios.

### 3.12 Probing source

A band-limited probing source (typically a laser) is used by HS WFSs to avoid chromatic aberrations that would otherwise enlarge the retinal beacon and flood the lenslet sensor with chromatic difference in focus. Studies suggest that higher-order monochromatic aberrations measured in the eye are independent of wavelength at current instrument sensitivity levels (Marcos *et al.* 1999). Considerable design and testing effort was dedicated to exploring the possibility of using a LED as the probing source. LEDs have advantages over the use of lasers because they are less expensive, require simpler drivers, they are highly efficient, and they have a long life span. Another advantage LED light has compared to laser light is its lack of coherence, which consequently would remove speckle from the HS spot image. The coherence of the laser and the diffuse reflection off the retina produces speckle that can cause some HS spots to be dull and difficult to detect (Bará 2003). Speckle can also result in confusion between multiple maxima for a single spot. A SLD would also offer similar advantages

compared to lasers but they are considerably more expensive than LEDs and only commercially available at a few selected wavelength parameters. A 735 nm LED was selected to experiment with. To the author's best knowledge it produced the highest flux commercially available in the red or infrared spectrum. Unfortunately we were unable to generate sufficient optical flux from the LED to successfully incorporate it as a probing source. The LED was simply not powerful enough to satisfy the superseding constraints of a small entrance pupil (1.2mm diameter), a small retinal beacon size (< 75 microns FWHM), limited CCD exposure time (preferably < 200 milliseconds), constrained CCD quantum efficiency, and limited photon efficiency in the overall optical design.

In the final optical design, a 677 nm laser diode was used as the probing source. Most commercial and research WFSs use a source in the red or infrared bandwidth because it is less powerful than shorter wavelengths and provides a safety advantage. It is also more comfortable for the eye and therefore subjects are more likely to maintain accurate fixation. The reduced relative luminous efficiency of red wavelengths (see fig. 1.6) helps to minimise disturbances to accommodation and fixation. The 677 nm wavelength is visible and therefore instrument alignment of the sensing and probing channels is not complicated by invisibility. Longer wavelengths penetrate deeper into the retina before reflection and this effect also occurs in eyes with reduced ocular pigment. This overestimation of myopia must be taken into account when transposing wavefront data into refractive data such as an equivalent sphero-cylindrical refraction or a LASIK ablation pattern. However, this effect is outweighed by the conversion required due to the effects of longitudinal chromatic aberration in the eye. An additional benefit of using a longer wavelength to create the retinal beacon and a shorter wavelength to

illuminate the fixation target is the mild fogging effect that occurs as a natural consequence. The retinal beacon can retain a good focus on the retina even while the fogged fixation target is focus in front of the retina.

# CHAPTER FOUR

## Optical system components

The optical design process is an exercise in finding an acceptable balance of compromise between competing considerations. In this chapter considerations specific to each of the four system channels; fixation, probing, sensing and alignment, are discussed.

### 4.1 Optical system diagram and list of elements with technical specifications

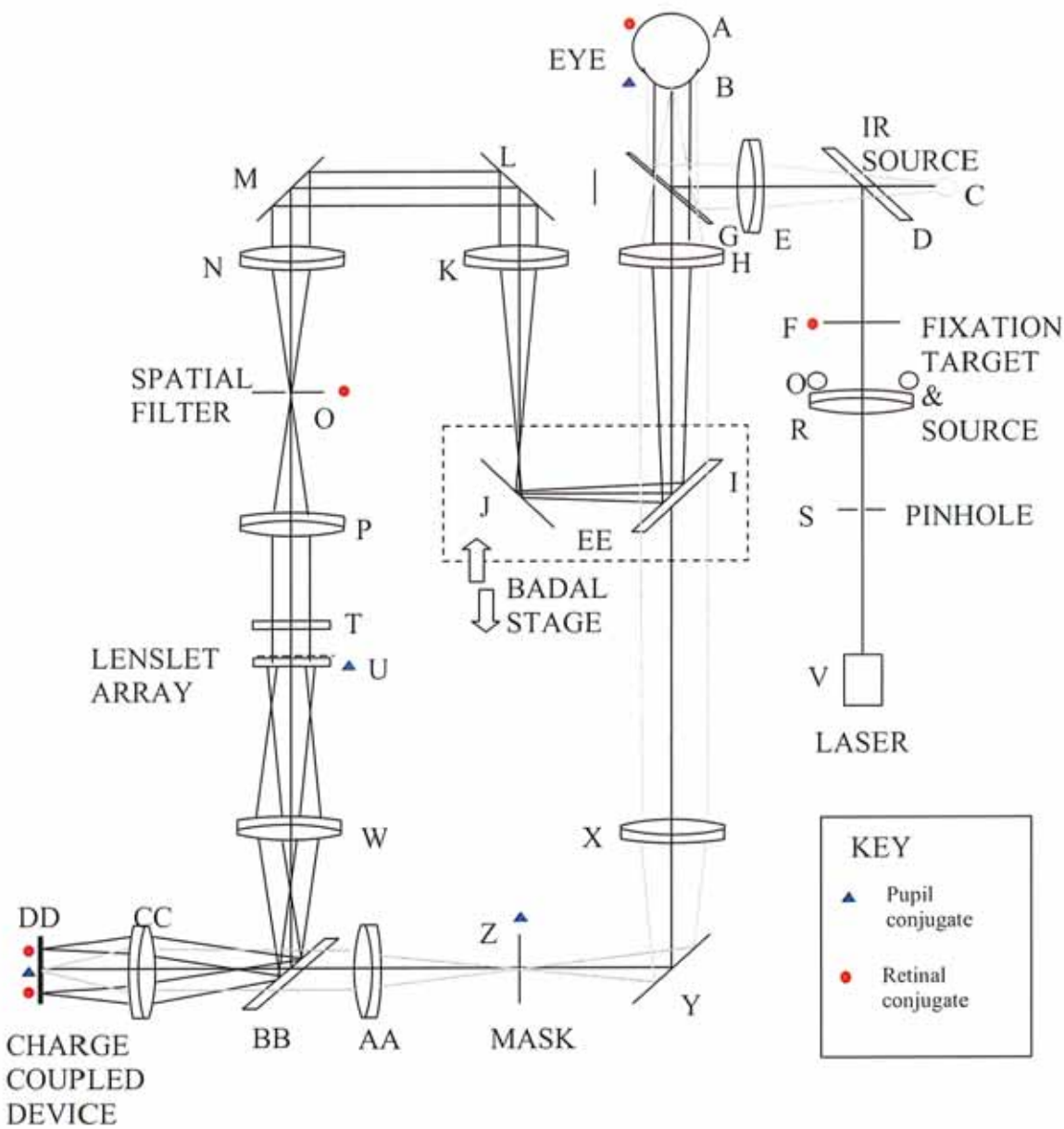


**Figure 4.1 Schematic diagram of the optical layout of our experimental wavefront sensor.**

**A**: Retinal spot

**B**: Pupil plane of the eye

**C:** Alignment channel illumination source. 880 nm wide angle IR LED (from Optoelectronics 327-384)

**D**: Long wavelength pass dichroic beamsplitter plate (from CVI)

**E**: Lens #1. Near infrared anti-reflection coated doublet with focal length f 60 mm, diameter 23 mm

**F:** Fixation target

**G:** Pellicle beamsplitter, 92% transmittance, 8% reflectance

**H:** Lens #2. Near infrared anti-reflection coated doublet with focal length f 120 mm, diameter 30 mm

**I:** Long wavelength pass dichroic beamsplitter plate (from CVI)

**J:** Mirror #1. Plane mirror (Near infrared laser quality)

**K:** Lens #3. Near infrared anti-reflection coated doublet with focal length f 60 mm, diameter 23 mm

**L:** Mirror #2. Plane mirror (Near infrared laser quality)

**M:** Mirror #3. Plane mirror (Near infrared laser quality)

**N:** Lens #4. Near infrared anti-reflection coated doublet with focal length f 40 mm, diameter 17 mm

**O:** Diaphragm to block unwanted reflections, aperture range 1 to 5 mm diameter

**P:** Lens #5. Near infrared anti-reflection coated doublet with focal length f 40 mm, diameter 17 mm

**Q:** Fixation target illumination sources. Two 526 nm LEDs (from Aligent Technologies 301-5312)

**R:** Lens #6. Visible anti-reflection coated singlet with focal length f 30 mm, diameter 13 mm

**S:** Pinhole 0.6mm diameter

**T:** Filter #1. Red filter (absorbs wavelengths below 630 nm)

**U:** Square geometry lenslet array with focal length 10 mm and pitch 190 microns (from AOA Inc.)

**V:** Probing source. 677 nm laser diode (from Hitachi) and collimating lens

**W:** Lens #7. Near infrared anti-reflection coated doublet with focal length f 40 mm, diameter 17 mm

**X:** Lens #8. Near infrared anti-reflection coated doublet with focal length f 80 mm, diameter 30 mm

**Y:** Mirror #4. Plane mirror (Near infrared laser quality)

**Z:** Alignment channel pollution-blocking mask

**AA:** Lens #9. Near infrared anti-reflection coated doublet with focal length f 40mm, diameter 17mm

**BB:** Long wavelength pass dichroic beamsplitter plate (from CVI)

**CC**: Lens #10. Near infrared anti-reflection coated doublet with focal length f 40mm, diameter 17mm

**DD**: Pixelfly QE charge coupled device (by Photonlines)

**EE**: Badal sliding linear translation stage with 105 mm of travel

**Mounting System**: LINOS Microbench®

**Power Source**: AC/DC adapter powers laser diode and LEDs. CCD powered through ethernet cable from a personal computer.

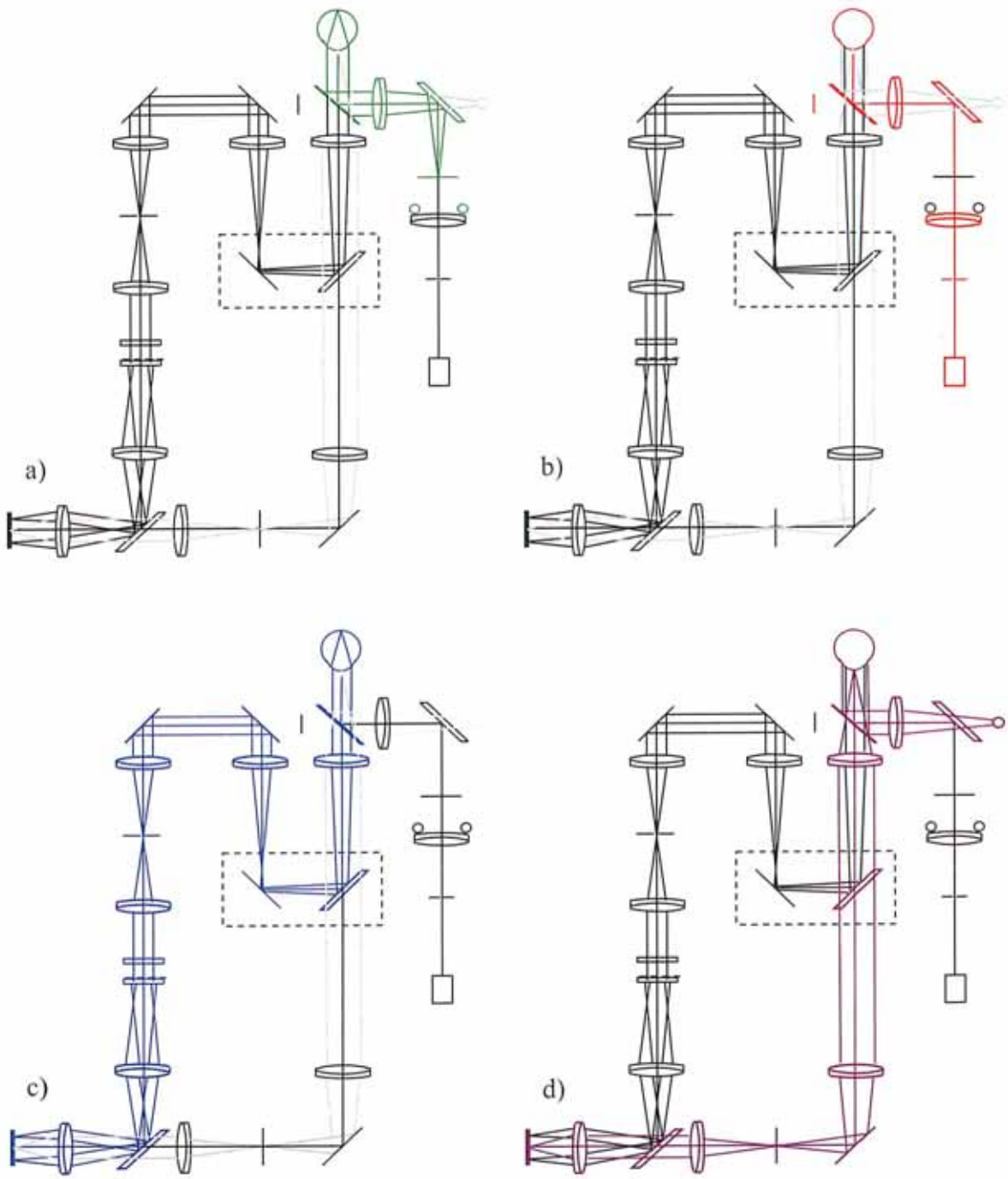


**Figure 4.2 Schematic diagram emphasising the optical elements that forming each specific channel of the experimental wavefront sensor a) fixation channel b) probing channel c) sensing channel d) alignment channel.**

## 4.2 Fixation channel

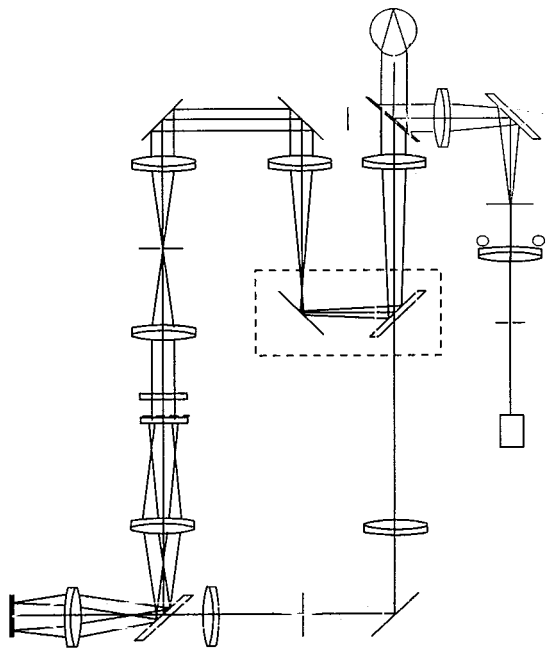

**Figure 4.3 Schematic diagram of fixation channel.**

Providing a suitable fixation target (element F in fig. 4.1) is a fundamental requirement for controlling eye movement and accommodation. Initial optical designs attempted to position the fixation target via the Badal optometer, for example, in the same plane as the spatial filter (element O in fig. 4.1). Such an arrangement would allow the fixation target to be corrected for ametropia simultaneously by adjusting the Badal optometer to remove refractive error from the sensing channel. This configuration would have conveniently allowed studies of aberrations and accommodation by manipulating the Badal optometer setting to control accommodation stimulus demand. However, to increase the field of view provided by the fixation target it was incorporated into the probing channel instead - closer to the eye and independent of Badal focussing (fig. 4.3). The shorter working distance provides a greater field angle in the fixation target but the comfort of the subject's nose requires that a minimum working distance of approximately 80 mm be maintained. The fixation target can be translated along the optical axis to correct for ametropia, however this technique proved to be somewhat

cumbersome and has a limited dynamic range (see chapter 6). The independent focussing of the fixation target allows it to be 'fogged' (intentional myopic-blur which encourages relaxation of accommodation) regardless of the Badal setting. The wavelength selection of 677 nm for the probing source and 526 nm for the fixation source also creates a small inherent fogging effect when both channels are set to their null positions due to longitudinal chromatic aberration.

During off-axis measurements the subject was asked to fixate a peripheral mark within the fixation target reticule. The probing beam then passes obliquely through the eye to an eccentric retinal focus and predominantly suffers from off-axis astigmatism. Comparatively the imagery of the fixation target (whose principal ray is aligned with the optics of the eye) requires a slightly different focus correction. Therefore there is another minor advantage in separating the fixation channel and the sensing channel (Badal optometer) so that each has independent focussing.

Our fixation target is a reticule image consisting of high contrast and predominantly high spatial frequency content (concentric black circles on white background). It is illuminated by wide angle LEDs with a principal wavelength of 526 nm and a typical bandwidth of Δ47 nm. It can be translated along the optical axis and therefore has focusing capability independent of the Badal. The fixation target provides a field of view up to 5 degrees half angle. A slightly concave surface was introduced into the fixation target to help compensate the intrinsic curvature of field problem.

a)  b) 

**Figure 4.4 Fixation targets of a) the experimental WFS, b) ZyWave.**

In hindsight a design flaw is evident in the use of a parallel plate as the substrate for the long-wavelength-pass beamsplitter (element D in fig. 4.1). Future modifications to the optical configuration may address this flaw. The parallel plate creates a ghost image of the fixation target and if it was replaced with an optical wedge this flaw could be eliminated. The fixation target can easily and quickly be changed according to the requirements of the experiment. For example, the examiner may prefer to use a reticule pattern or an illusion-based image to help control accommodation. During the design process we considered using a dust guard at the measurement aperture directly adjacent to the subject's eye, however this element was not included in the final optical design.

### 4.3 Probing channel

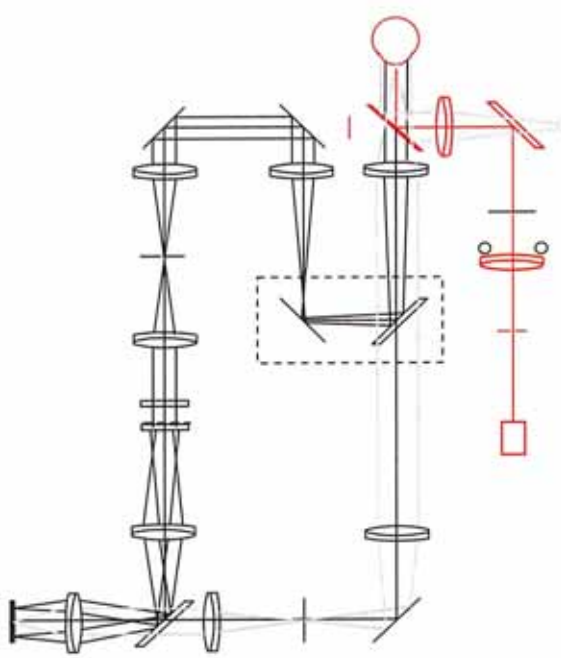

**Figure 4.5 Schematic diagram of probing channel.**

The probing channel creates the retinal beacon (fig. 4.5). It is typically preferred to position the probing channel such that it passes via the Badal optometer before incidence on the eye. This arrangement has the advantage of producing a constant beam diameter at the pupil regardless of the ametropia correction and minimises the size of

the retinal beacon. The greatest variation in retinal beacon size would then be due to inter-subject variation in the circle of least confusion. Applying an accurate ametropia correction to the probing beam is important to restrict the retinal beacon size below the diffraction limit of the lenslets. This ensures isoplanatism (spatial invariance of the wavefront's source) and prevents the lenslets from resolving the internal architecture of the laser diode, thus simplifying centroid determination. Restricting the retinal beacon below the diffraction limit of the lenslets also minimises the HS spot : subfield ratio which increases dynamic range. Unfortunately, due to competing considerations (principally the requirement to minimise unwanted reflections), the probing channel was not incorporated with the Badal optometer and alternative forms of ametropia correction were necessary. Ametropia correction of the ingoing probing beam could be achieved by shifting lens #6 (element R in fig. 4.1), along the optical axis however, this is cumbersome, has a limited dynamic range, and produces a variable beam diameter at the pupil. Another possible solution is to use trial lenses positioned in the spectacle plane but this approach would cause eye-aberration and lens-aberration mixing problems. Although satisfactory, neither of these alternative solutions are ideal in the long term and future WFS measurements would benefit from modifications to the probing channel to improve the ametropia correction technique.

All elements in the probing channel are aligned with the optical axis ($z$) except for the pinhole. The pinhole is translated in the $xy$ plane to create a collimated probing beam parallel to the optical axis but displaced by approximately 1 mm at the pupil. This helps prevent unwanted reflections from passing back through the WFS because the corneal reflection occurs at such an extreme angle. Throughout the entire optical design, plate beamsplitters were used because of their increased robustness and compact mounting. The one exception is the use of a pellicle beamsplitter adjacent to the eye (element G in

fig. 4.1), which was selected for its high transmittance and low reflectance values. Such a ratio is a purposely selected for the sake of minimising exposure of the eye to laser radiation. This safety compromise sacrifices general efficiency in the probing channel while conserving the more valuable photons of the sensing channel. The magnification in the probing channel is approximately x2 and at null settings the probing beam intercepts the eye 1 mm from the pupil centre with a diameter of 1.2 mm. The diameter of the probing beam at the eye defines the entrance pupil of the first pass and must be small compared to the exit pupil diameter of the second pass (Artal *et al.* 1995).

The laser diode source used in the probing channel produces a predominantly linearly polarised beam which is later incident on the long wavelength pass dichroic beamsplitter (element D in fig. 4.1) at 45 degrees. As such the alignment of the polarisation axis is an important efficiency consideration. Fig. 4.6 shows that a simple rotation of the polarisation axis of the laser diode to ensure that it coincides with the *TE* polarisation plane will maximise the reflection coefficient and overall photon efficiency of the probing channel. The differences in the reflection amplitudes of *TE* and *TM* polarisation is used by some ocular instruments (e.g. the direct ophthalmoscope) to limit unwanted corneal reflections.

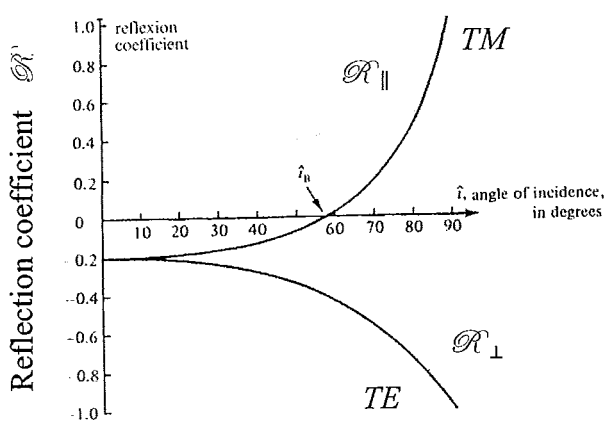


**Figure 4.6 Reflection coefficients at the surface of a medium with refractive index n = 1.5 plotted against angle of incidence in degrees (Lipson *et al.* 1995).**

### 4.4 Sensing channel

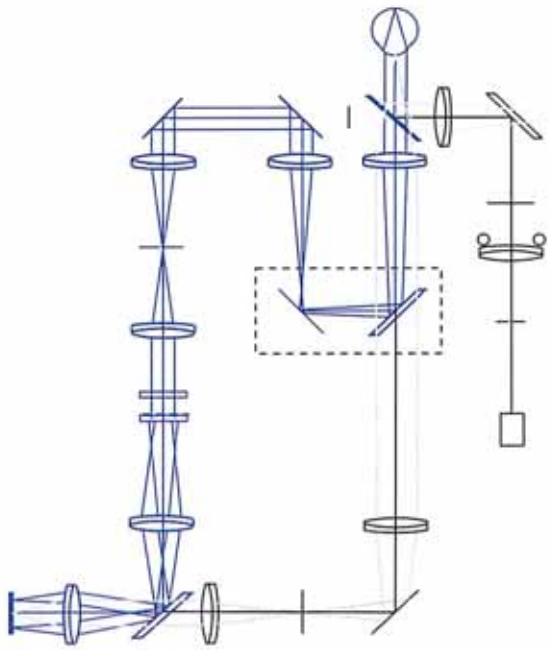

**Figure 4.7 Schematic diagram of the sensing channel.**

The sensing channel (fig. 4.7) is used to capture the image of the HS spots. In our design it is the only channel to make full use of the Badal optometer. Various design options were considered for the Badal optometer with each variation offering different advantages. For example, the inclusion a polarisation filter or concave Badal mirrors could be used to reduce unwanted reflections. Another consideration was to include a fixed spatial filter diaphragm or a fixation target into the Badal optometer which would have reduced the overall instrument size. In its final configuration the Badal optometer is composed of two lenses, and a flat mirror, and plate beamsplitter mounted on a stage (elements H, K, J, I, and EE respectively in fig. 4.1).

The focal length selection for the lenses used in the Badal optometer was influenced by magnification and working distance requirements. To achieve the desired lenslet sampling rate a magnification of approximately x0.5 is required in the sensing channel. A working distance of at least 80 mm between the instrument and the subject's pupil is

required to cope with inter-subject variation in nasal size and facial depth of the eye socket. The Badal stage allows 105 mm translation and future motorisation of the stage is possible. A large maximum value for the Badal optical path length is important for providing good dynamic range to correct hyperopia. However, a compact mounting arrangement that allows a small minimum value for the Badal optical path length (which determines the range of myopia correction possible) is considered the more restrictive and important consideration.

The total magnification of the sensing channel was designed to be x0.5 (i.e. the re-imaging lenses elements W and CC in fig. 4.1 provide unity magnification). This makes efficient use of the CCD chip and allows measurements on a maximum pupil diameter of 9 mm. If necessary pupil diameters up to 9.5 mm can be measured, provided the subject alignment is very accurate. The maximum pupil diameter restriction seemed too limiting when performing measurements on a large group of pharmacologically dilated pupils because occasionally subject's pupil diameters exceeded 9.5 mm (see chapter 6).

A balance of magnification is required between competing considerations. The arrangement of the sensing channel and the alignment channel are coupled such that a decrease in magnification for one channel requires a mutual decrease in magnification for the fellow channel. The size of the pupil mask sets a boundary between the minimum pupil size measurable (alignment channel) and the maximum pupil size measurable (sensing channel). The size of the CCD chip sets a limit on the maximum pupil size measurable (for a given alignment channel magnification). And overriding all of these magnification considerations is the fact that the optical path length of both the

alignment channel and sensing channel is strictly restricted by the requirement to separate and then reunite the two channels within a compressed space.

For each subject the Badal optometer is uniquely set to the 'best sphere' value of the refractive error. This removes defocus, creates a circle of least confusion at the spatial filter (conjugate with the retina), and produces a *relatively* flat wavefront incident on the lenslet array. The sensed wavefront is typically dominated by global tip and tilt, which are generally not of interest unless attempting to correct the aberrations of the wavefront with an AO system. Global tip and tilt represent a simple transverse shift in the retinal image rather than a degradation in image quality. Typically the next most prominent aberration in the sensed wavefront is astigmatism.

The arrangement of the dichroic beamsplitters throughout the WFS was determined by the higher efficiency achievable in reflection. In creating the parallel channel design the photon budget therefore dictated that the sensing beam be reflected by the dichroics, rather than be transmitted. This arrangement is a compromise because any surface aberrations on the dichroic plates themselves are amplified in reflection compared to transmission. Accordingly it is important that the dichroic beamsplitters have high quality surfaces, and consequentially the manufacturing process required extra thickness (5 mm) in the glass substrate.

The diaphragm (element O in fig. 4.1) is a spatial filter that blocks unwanted reflections. The red filter (element T in fig. 4.1) removes the polluting 526 nm wavelength light before the wavefront is sensed by the lenslet array at the pupil conjugate. The focal length of the lenslets is 10 mm, which is too short a distance to provide sufficient space

for recombining the parallel alignment channel. Re-imaging lenses (elements W and CC in fig. 4.1) are necessary to generate the required space to recombine the parallel alignment channel. Additionally, the CCD chip sits 17 mm inside its housing and this consequentially also requires re-imaging lenses to generate sufficient mounting space. Optimal re-imaging required the use of two doublets and our arrangement creates a telecentric pass despite the absence of a field lens. Thus, for a plane wavefront, the principal ray of each subaperture is parallel to the optical axis and the instrument is tolerant to small misalignments of the CCD along the optical axis, with the additional benefit of reduced curvature of field aberration in the HS spot image. If the re-imaging was not telecentric, the principal ray from each cone of light would be angled relative to the optical axis and this would cause transverse HS spot movement if there was any misalignment of the CCD along the optical axis. Our telecentric re-imaging focuses the retinal conjugate onto the CCD while placing the pupil conjugate at infinity. It is worth noting this distinction compared to the alignment channel which focuses the pupil conjugate onto the CCD. The depth of focus for positioning the CCD is 0.33 mm. Combining the sensing channel and the alignment channel into a parallel path allows the use of a single CCD making the instrument more compact, less expensive, and easier to synchronise alignment between the two channels for pupil centre determination. This also simplifies database management as only one image file is recorded per wavefront measurement, not two.

## 4.5 Alignment channel

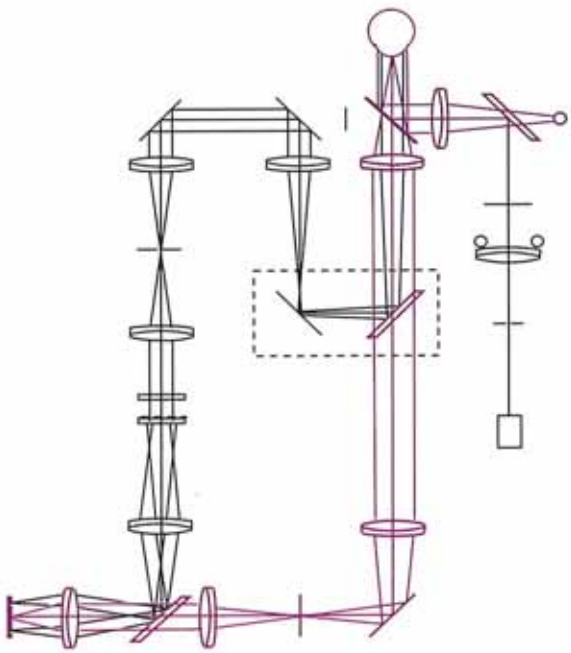

**Figure 4.8 Schematic diagram of the alignment channel.**

The alignment channel (fig. 4.8) creates an image of the external eye which is used by the operator to correctly align and focus the WFS on the subject. The image also provides valuable ancillary information to the operator such as the location of a contact lens being worn during measurement or the eyelid position of a subject. Simultaneous imaging of the eye via the alignment channel allows the pupil centre to be determined independently of the HS spots. The pupil centre is found by analysing the image of the iris with an edge-detection algorithm. Data points for the iris edge are fitted to a circle by a least squares technique and the centre of this circle is defined as the pupil center. The same fitted circle is used to estimate the pupil diameter. Small errors are associated with this approximation because not all pupils are perfectly circular and this is especially true upon pharmacological dilation.

Determining the pupil centre is a critical function because it defines the origin of the polar coordinate system to which the Zernike polynomials are fitted. This photon-abundant (high SNR) technique is potentially superior to the traditional technique of using the HS spots themselves to determine the pupil centre. The traditional technique can only determine the pupil edge to a maximum resolution of one lenslet subaperture and it is dependent on peripheral HS spots that may be ambiguously dim. The resolution and stability of our alignment channel pupil centre determination anecdotally appears satisfactory (see chapter 6), but future studies should quantitatively characterise and compare the two techniques. Certainly our novel approach is dependent on the edge-detection algorithm used and the related smoothing function.

High quality optical elements were used in the alignment channel to help ensure high resolution images and accurate pupil centre determination. To reduce surface figure the beamsplitter plates are necessarily thick (5 mm), consequentially this thickness horizontally translates the infrared alignment beam at three separate locations (elements D, I and BB in fig. 4.1). At each location the beam is displaced by 1.87 mm from the optical axis however this translation is compensated for because the LINOS Microbench® cage mounting system allows variation in the piston ($z$ axis) value of mirror #4 (element Y in fig. 4.1).

The alignment channel uses an 880 nm infrared LED (element C in fig. 4.1) to illuminate the eye. This avoids unnecessarily distracting the subject from the fixation target and altering the accommodative state of the eye. Infrared wavelengths are strongly reflected from the eye (particularly the chorioretinal reflection is strong) and

the high quantum efficiency of the CCD to the infrared bandwidth leads to an abundance of photons in this channel.

Early in the construction process the infrared illumination was assembled as a ring of wide angle LEDs surrounding the front aperture of the WFS and approximately 80 mm from the subject. This arrangement was problematic and required alteration. Each LED created its own unwanted reflection, typically positioned in the mid-periphery of the cornea at a potentially disruptive position for the pupil edge detection algorithm. The ring of LEDs was replaced with a simpler on-axis infrared source creating a single, central, unwanted reflection that is subsequently blocked with a mask (element Z in fig. 4.1). The annulus mask is conjugated to the pupil and blocks out a central zone. This design, combined with the magnification settings of the alignment and the sensing channels, constrains the measurable the pupil size to diameters between 6 mm and 9 mm.

The operator requires a reasonably large field of view in the alignment channel. Our design allows a 12 mm field of view and provides the examiner with distinguishing landmarks for orientation and the potential to monitor contact lens and/or eyelid properties during aberration measurements. The magnification of the alignment channel is 0.66 and this magnification value was selected to balance the concerns of creating a maximal field of view, maximising image resolution, the need to allow measurements on a range of pupil diameters, and the need to superimpose the sensing channel within a limited optical path length (see section 4.4). The alignment channel is arranged parallel to the sensing channel and it shares a mutual CCD, thus making efficient use of the time and memory resources required to read the CCD chip. The chip is a rectangular shape

and in early designs we envisaged that each channel would be imaged side-by-side adjacently on the chip. However, our final design superimposes the two channels with the optical axes coincident and this proved to be both simpler and optically superior.

The potential of replacing the scientific CCD with a webcam was investigated during the optical and software design process. Webcams offer specific advantages – they are extremely compact, light-weight, inexpensive, and USB powered. Most webcams are insensitive to infrared wavelengths although this difficulty can readily be addressed by removing the infrared filter incorporated into the optics. The preliminary concerns in assessing the suitability of various webcams to our application were; What software is available to control and operate the webcam? Is the frame rate acceptable? Is the read noise acceptable? Is the spatial resolution acceptable? Is the dynamic range acceptable? In many circumstances the limiting condition for our application was the lack of suitable software. Some manufacturers have software development kits that are typically available at a significant expense. Recently, National Instruments released a version of LabView (our chosen software platform) that contained drivers compatible with some common webcams. This is a significant advance that facilitates inexpensive and speedy investigations into the possibility of replacing scientific CCDs required by WFSs with simple webcams. Unfortunately this LabView software version only became available after our WFS had already been assembled. Future instrument modifications may revisit this unattained design aim.

Researchers are working towards replacing expensive components in WFS/AO systems with more economical substitutes and if our design attempts to utilise a webcam and a LED source (see section 3.12 p.111) had of been successful they would have

significantly contributed to the development of low-cost WFS/AO systems. Apart from the CCD and the probing source, the other key elements in a WFS/AO system are the lenslet array and the correction device. Lenslet arrays of reasonable optical quality have already become relatively inexpensive with mass production scales, while low-cost micro-electro-mechanical mirrors hold excellent potential to replace traditional deformable mirrors in AO systems (Doble *et al.* 2002).

### 4.6 Design summary

The optical design of our experimental WFS was successful in achieving our stated preferences for off-axis capability, adaptability to new projects, compactness, and transportability. Unfortunately some of our design attempts were unsuccessful such as; using a LED source to create the probing beam and using a webcam to replace the scientific CCD. It is hoped that future technology advances may allow these design aims to be revisited in future instrument modifications. In hindsight, some optical design decisions should be modified – especially refractive error correction for the ingoing probing channel (see section 4.3 p.120) and the use of a wedge plate at element D in fig. 4.1 (see section 4.2 p119). The design process was painstakingly iterative and the inter-relatedness of seemingly unconnected parameters was a true test in managing competing considerations. Assembly and construction encompassed many issues not discussed in this thesis such as fiscal budgeting, optical mounting, and optical alignment. Only after the optical assembly was finalised could the software development (discussed in the following chapter) really progress to complement the optical design because much of the software development required a live feed from the CCD, that mimicked (at least somewhat) the HS spot and the external eye images expected during wavefront measurements.

# CHAPTER FIVE

## Software development and functions

This chapter explains the operational principles of the original software developed to control the experimental WFS. Although mainly non-novel, the software development consumed a large proportion of time resources and it is discussed here to provide a comprehensive outline of the work done. The software design aims included real time data displays, user-friendly operation, adaptability to future research modifications, and an aesthetic user interface. A basic description of user functions and operational guidelines are provided throughout the chapter where they complement an understanding of the work done in software development. Some detail is given to key functions such as determining the pupil parameters, centroid determination, wavefront reconstruction and Zernike fitting.

### 5.1 General structure of the software program

All operations necessary for the experimental WFS are executed from a single platform on a personal computer. We developed this program using a graphical computer language (LabView by National Instruments) to control the CCD, capture and handle images, perform the required data analysis, display results, and manage the associated database. The structure of the program can be conceptually divided into 5 separate actions to simplify understanding the program. Many operations of the sub programs are compartmentalised and it is beyond the scope of this thesis to describe their operations in detail.

Each time the program is run it executes one of five possible actions. These actions are exclusively independent (ie. it can only execute one action at a time) and each action can be executed by a single mouse click on the ⇨ button on the LabView toolbar. The five possible actions to choose from are;

1 Enter examination details

2 Generate a reference wavefront / perform alignment

3 Capture a series of measurements (process images off-line)

4 Capture individual measurements (process images in real-time)

5 Generate a darkfield frame

The operator selects which action to execute by using the tab control on the graphical user interface (GUI). The tab control then displays the relevant controls and indicators for the action requested. A conceptual layout of the program's structure is illustrated in fig. 5.1.

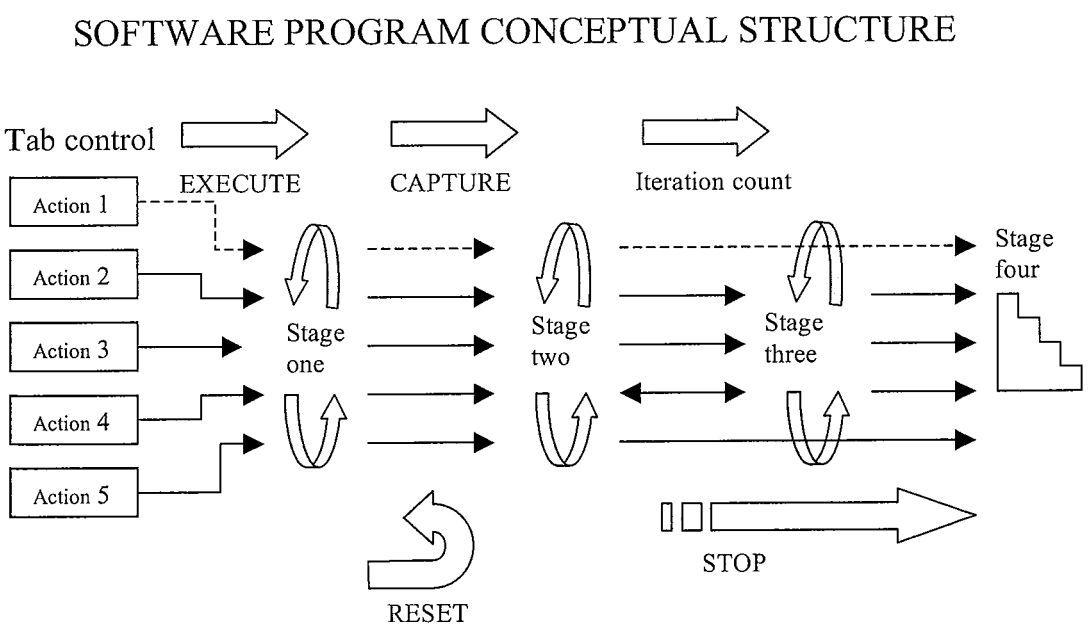


**Figure 5.1 Conceptual structure of the software program.**

Action 1. This action (which is the default setting of the tab control) displays a screen that requests the operator to input subject details and some other identifying comments about the measurements to be performed. The operator should enter the examination details into the appropriate fields before measurements are taken and update them when swapping between the right eye and left eye. The most recent refraction available should be entered and the Badal setting should be at the 'best sphere' value (sphere power + half the cylinder power in traditional sphero-cylindrical terms) for optimal operation. Executing action 1 will display the CCD image to the operator in a floating window. This allows the operator to confirm that the subject is aligned and the Badal is appropriately positioned. The CCD will expose as many frames as requested by the iteration control and then all images will be trashed and the CCD will be closed down. No data is recorded or analysed by executing action 1. However, executing action 1 is a useful tool for software development and de-bugging because it provides a live feed of CCD pixel grey level values to the software program. Fig. 5.2 shows the GUI for action 1.

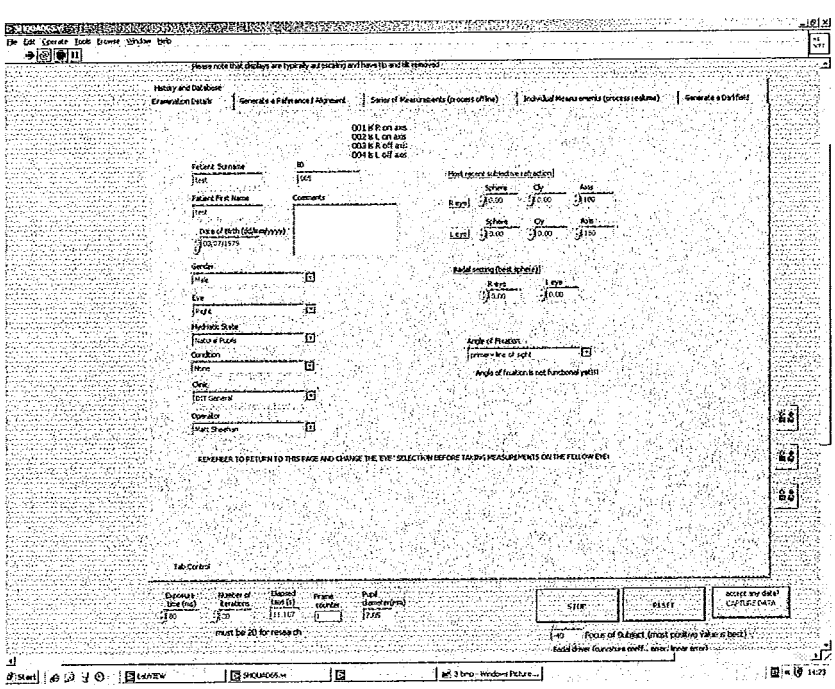

**Figure 5.2 The GUI of the software program when action 1 (enter examination details) is selected in the tab control.**

Action 2. This action is executed as the final step in performing an optical alignment of the WFS. It is used to generate the reference HS spot positions on the CCD and record this data for future wavefront measurements. It also performs related operations such as determining the exact subfield size of the lenslet array (equivalent to determining the exact re-imaging magnification of elements W and CC in fig. 4.1) and determining the exact null position of the Badal optometer. Action 2 should be executed on a regular basis to help compensate for vibrational and thermal misalignments that accrue with use. Each time the WFS is moved it must be optically realigned. As part of the alignment process, the operator attaches a latchable plane mirror mount to the front of the WFS, producing an optical layout as per fig. 5.3.

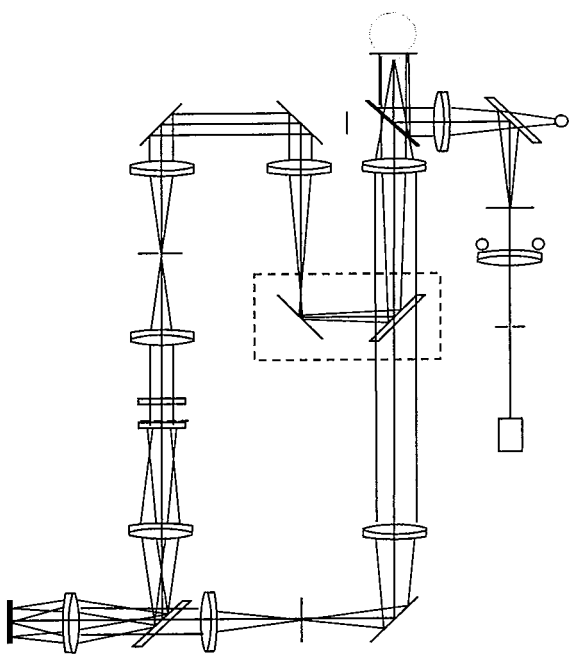

**Figure 5.3 Optical layout of the experimental wavefront sensor during realignment.**

During alignment the pinhole (element S in fig. 4.1) is temporarily replaced with a variable diaphragm which is opened fully when executing action 2. Once all channels are aligned the laser power is reduced to avoid saturating the CCD and action 2 is

executed. The 5 mm diameter laser beam in the probing channel is magnified by x2, generating a 10 mm beam diameter at the pupil plane of the eye. This beam is reflected from the plane mirror and travels through the sensing channel.

The HS spot pattern is analysed and through an iterative process the exact null position of the Badal optometer and the exact subfield size are determined. The software program analyses the HS spot locations and the spacing between spots. The Badal optometer is adjusted iteratively to minimise the variance of the distance separating the spots and resets the estimate of the subfield size with each iteration. This process makes the WFS tolerant to small errors in the estimates of various optical parameters including the lenslet pitch, the magnification of the sensing channel, the Badal positioning, and the subfield size. When generating reference HS spot positions, this process is crucial in distinguishing between true defocus (Badal not positioned at its exact null point) and a simple departure from the expected subfield size (e.g. re-imaging magnification of the sensing channel not exactly unity). The operator executes action 2 repeatedly with iterative Badal adjustments until a satisfactory endpoint is achieved. With each execution the determined subfield grid is realigned with the four most central HS spots. The subfield grid is then mapped relative to the CCD chip and recorded. The centroids of the corresponding HS spots are recorded as the reference spot positions produced by a plane wavefront incident on the lenslet array. We generate the reference spot positions in this way, using the centroid positions rather than simply using the geometric centre of each subfield, to account for internal aberrations within the WFS itself. Additionally, this approach dampens any systematic bias that could potentially occur if there is an undetected bug in the software code of the centroiding subprogram. Fig. 5.4 shows the GUI for action 2.

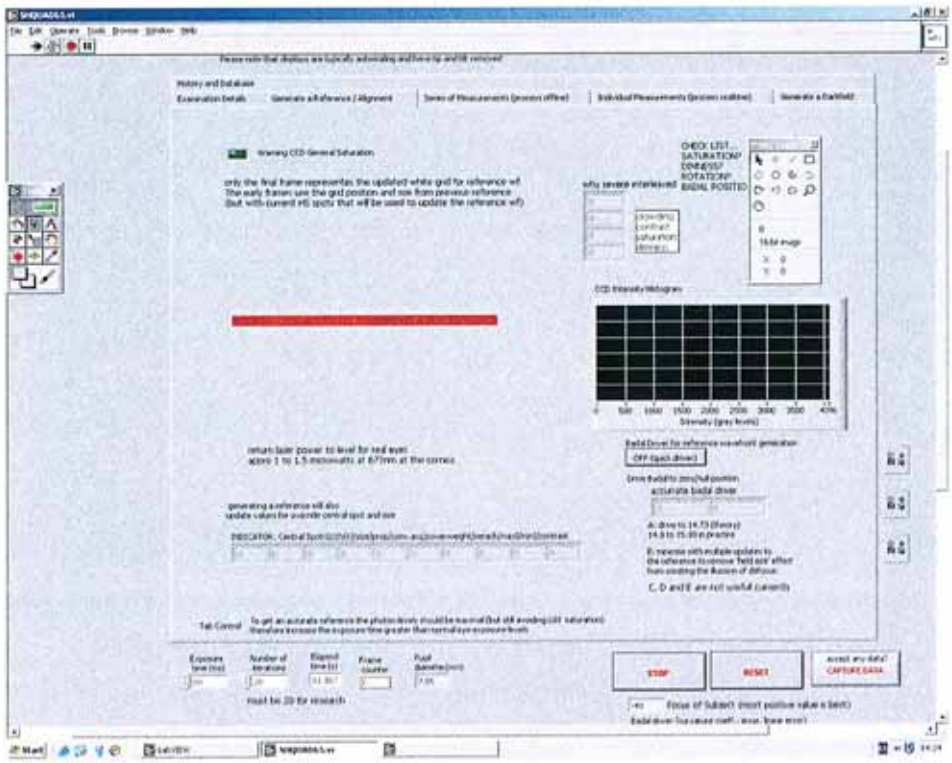

**Figure 5.4 The GUI of the software program when action 2 (generate reference wavefront) is selected in the tab control.**

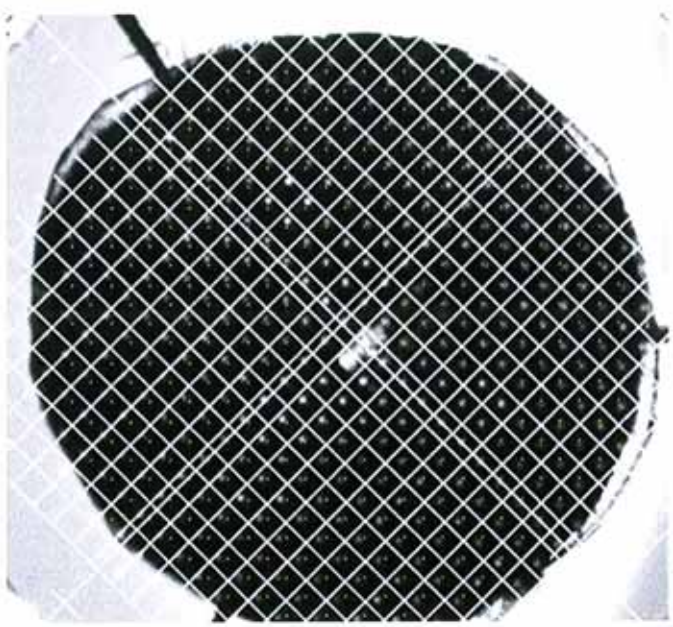

**Figure 5.5 An example of the manual inspection image displayed after executing action 2. The subfield grid and reference HS spots are visibly misaligned indicating that the alignment process is not at an endpoint. This particular example also reveals a number of issues that the operator needs to address including infrared saturation of the alignment channel and a large unwanted central reflection in the sensing channel.**

The subfield grid and various associated overlays are displayed so that the operator can make a manual inspection of the outcomes of action 2 (fig. 5.5). The grid is purposely oversized (25 x 25 subfields) to make the program flexible for future design modifications. Subfields that fall outside or overlap the central pupil mask are polluted by infrared light and their HS spot centroid can't be accurately analysed. In our current configuration these subfields are rejected and analysis is limited to subapertures that are fully contained within the central pupil mask. Correspondingly, analysis of ocular aberrations is limited to a maximum pupil diameter of 8.36 mm. Note that subjects with pupil diameters up to 9.5 mm can be measured on the WFS, it is only the aberration analysis that is limited to a maximum diameter of 8.36 mm. This limit is predominantly determined by the difference in magnification between the alignment and sensing channels and the size of the pupil mask. These parameters can be altered to increase this limit of aberration analysis, however, assuming the CCD chip size and CCD pixel size is set, such alterations in the re-imaging magnification act to decrease the HS spot size : CCD pixel size ratio, which compromises centroiding accuracy and increases pixelization error. Alternatively, if alterations are made to the magnification of the sensing channel proper, it will result in decreased spatial resolution. If the alignment channel magnification is increased the most immediate compromise is the decrease in maximum pupil size measurable. If the pupil mask is increased the most immediate compromise is the increase in the minimum measureable pupil diameter from its current value of 6.27 mm.

Each subfield signal must satisfy the minimum contrast criteria, the minimum brightest pixel intensity criteria, and the saturation criteria, or it is excluded from analysis by the software program. All of these criteria values can be operator-defined although typically

the default values are easily satisfied while generating a reference wavefront by adjusting the laser power setings.

Various overlays are used when the reference image generated by action 2 is displayed to the operator (fig. 5.5). A blue overlay spot is used to designate subfields contained within the central pupil mask, a red overlay spot is used to designate subfields with an unacceptable signal, and a green overlay spot is used to designate subfields with an acceptable signal. These overlay spots do not represent the HS spot centroids, they are purposely displaced from the centre of the subaperture to allow the HS spot itself to be inspected simultaneously. Both the reticule cross and the subaperture grid are marked by a white overlay. Two red arc overlays are used to indicate the edge of the pupil and a white box overlay is used to mark the pupil centre as determined by the alignment channel. The last two overlays described are irrelevant to action 2, but they are used by other actions and mentioned here for completeness. Note that the differing magnification and inversion between the alignment and sensing channels means that the white box overlay may not coincide with the centre of the HS spots.

Action 3. This action is selected when the operator wishes to capture a series of images and then process the data off-line. It provides the highest temporal resolution and can capture data at speeds above 10 Hz. This speed compares favourably to other commercial WFSs but it is slower than a WFS component of an AO system which might typically operate at approximately 30 Hz (Roorda 2005). Using action 3 to perform a wavefront measurement may be preferable compared to action 4 because it minimises the length of time the subject is exposed to the laser. When action 3 is executed the CCD is exposed and pixel values are read out in a repeating command loop

that stores the CCD intensity values into the computer memory. No data processing is performed until the CCD has captured (and displayed) the requested number of frames. The program then analyses the raw data held in memory. Once the series of fitted Zernike coefficients have been determined, they are statistically evaluated for median, mean, and standard deviation values. The statistical values of the comprising individual Zernike coefficients for modes 1 to 20 are displayed. This helps the operator judge the reliability/repeatability of each measurement and it offers an advantage over commercial WFSs that typically only provide the operator with 'averaged' coefficient values. Phase maps are generated from the mean coefficients and displayed. In recognition that mean Zernike coefficients may not be suitable for all experiments or subjects (e.g. because of the reduced temporal sensitivity) - the series of original Zernike coefficient values are saved to file and can be retrieved as required. Fig. 5.6 shows the GUI for action 3. Fig. 5.7 shows an example of the final manual inspection image displayed after executing action 3.

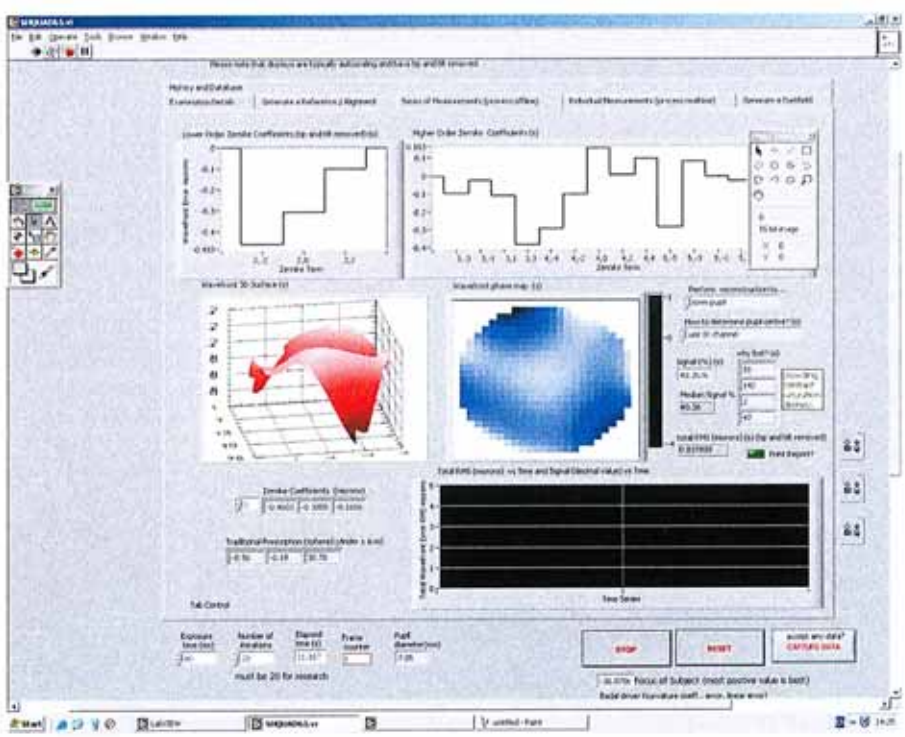

**Figure 5.6 The GUI of the software program when action 3 (capture a series of measurements – process off-line) is selected in the tab control.**

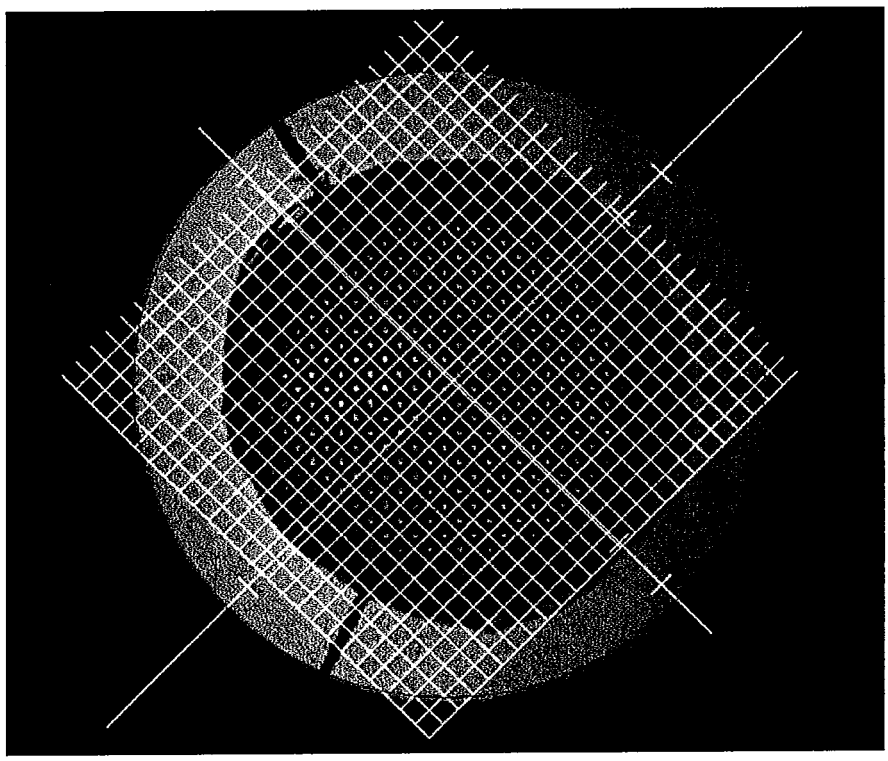

**Figure 5.7 An example of the final manual inspection image displayed after executing action 3. The reticule and the subfield grid are designated in white, the pupil edge designated in red, and each accepted HS spot is designated by one green spot overlay per measurement frame.**

Action 4. Action 4 initialises a loop command that captures an individual frame, analyses it, and displays the results immediately. The CCD will only expose the next frame once the current frame has been analysed and trashed. The program remains in this loop command until it has captured the requested number of measurements. The software development for action 4 was aimed at producing real time functionality in our WFS. In its current stage of development, action 4 can operate at speeds just over 2 Hz. Although action 4 has reduced temporal sensitivity, we envisage numerous future experiments that may benefit from real time data displays. Experiments that require high temporal sensitivity should use action 3 (e.g. studies of aberrations and accommodation, the tear film, the blink mechanism, or contact lenses), whereas studies requiring immediate feedback to the practitioner should use action 4 (e.g. studies of

aberrations that may require continuous operator adjustments or subject instruction). Fig. 5.8 shows the GUI for action 4.

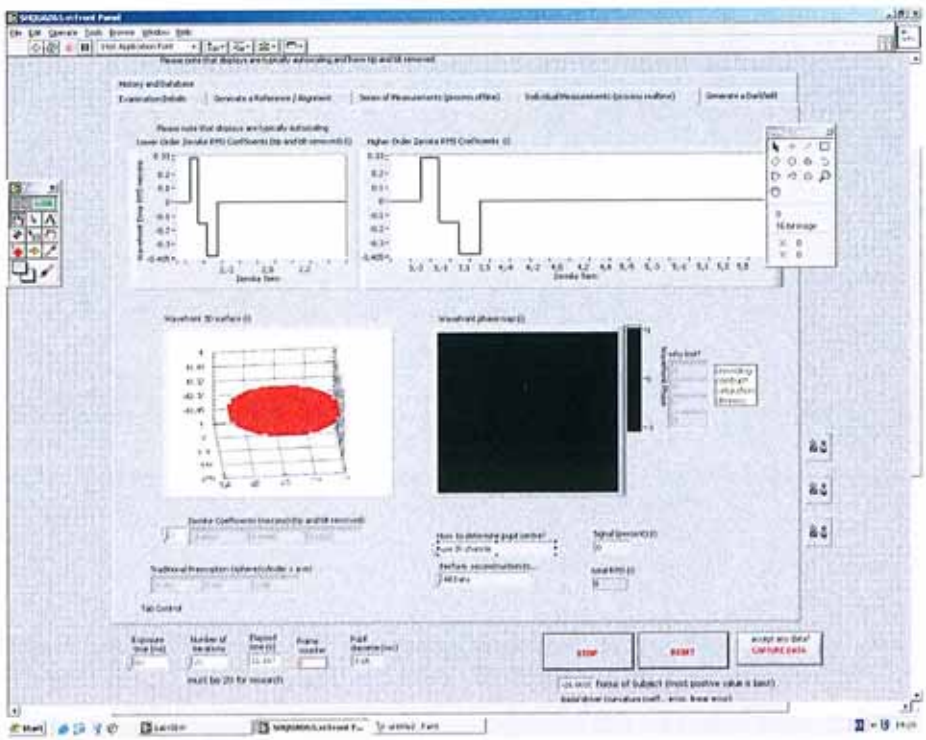

**Figure 5.8 The GUI of the software program when action 4 (capture individual measurements – process real-time) is selected in the tab control.**

Action 5. This action is used to generate a new dark frame. The dark frame is recorded over a minimal exposure time and with all instrument and room lights turned off. The operator must ensure that the WFS housing is closed. The pixel values of the dark frame are recorded for later use when they will be subtracted from measurement frames. This process minimises pollution from hot pixels and non-uniformity in sensitivity of the CCD chip. Action 5 should be executed on a regular basis to update the dark frame values. Executing action 5 also updates operator-specified control values including the minimum acceptable contrast level for HS spots, the minimum acceptable brightest pixel for HS spots, the initial centroid search area, the centroid algorithm power weighting, and the centroid convergence accuracy. The default values for all of these controls have been determined through pilot studies on real eyes (see chapter 6) and can

be assumed suitable for measurements on normal healthy caucasian eyes. Fig. 5.9 shows the GUI for action 5.

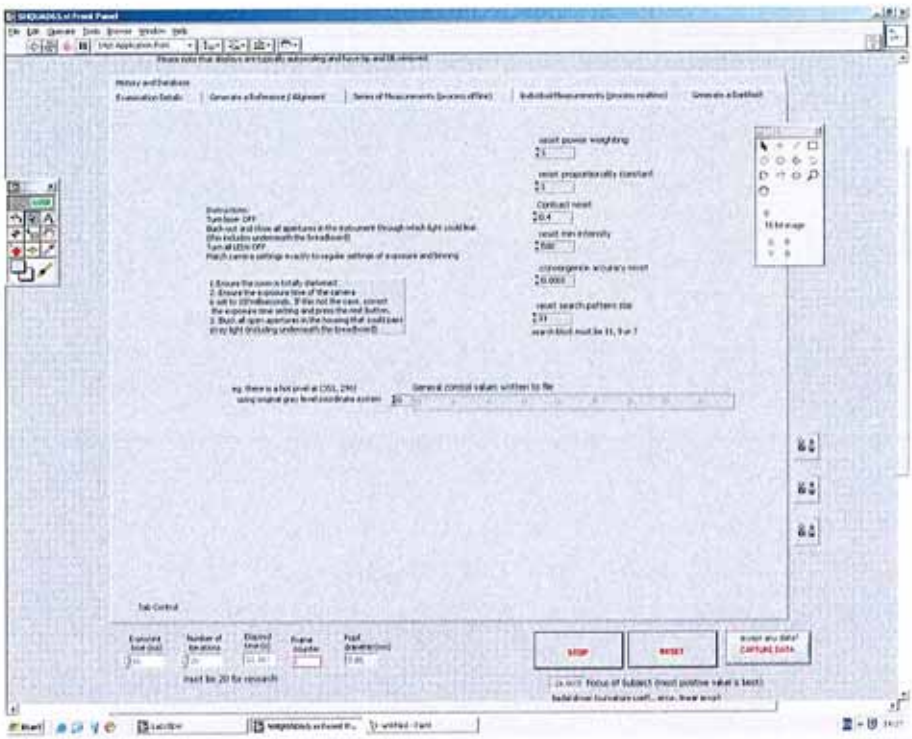

**Figure 5.9 The GUI of the software program when action 5 (capture a dark frame) is selected in the tab control.**

## 5.2 General data flow and execution sequence

Fig. 5.1 illustrates the conceptual design of the software program which can be separated into 4 stages. Stages 1-3 of the program are loops that repeat a set of commands until the operator sends a new command, the iteration count for the number of frames is reached, or a time-out value is reached. Stage 4 is a close-down stage. All actions of the software program described in section 5.1 execute in a similar order that relies on data flow to control the execution sequence. Note that it is unnecessary to execute action 1 for the purpose of updating the examination details entered into the tab control - they are automatically updated when measurements are taken (i.e. during the execution of action 3 or action 4).

Once executed, all actions loop inside stage 1 which displays a live preview of the CCD image to the operator. At this time the operator can alter the pupil fitting parameters to obtain a stable and accurate fit of the pupil overlay. However, such adjustments are typically unnecessary and the operator is primarily required to adjust the Badal setting, the subject alignment, subject focus, and probing beam location in the corneal plane. When the operator is satisfied with the parameters listed above, he/she presses the capture button and all actions enter stage 2.

Stage 2 captures and displays the CCD image with the intent of analysing the HS spots. The images are saved for later analysis (in stage 3), unless action 4 is executed - in which case the program steps between stage 2 and stage 3 for each individual image. Stage 2 loops until the reset button is pressed (which returns the program to stage 1), the iteration count is reached (and the program proceeds to stage 3), or the stop button is pressed (which sends the program directly to stage 4).

During stage 3 the captured image/images are analysed to determine the pupil centre, the centroids of the HS spots, and the least squares solution of fitting Zernike coefficients to the local tilts. If poor images are detected they are discarded and the program immediately steps back to stage 2 to replace the discarded images. Once stage 3 receives a full complement of acceptable images it finalises the analysis of the wavefront data and displays and records the results.

The program then proceeds to stage 4. The CCD is closed down, all images are discarded, all windows are closed, any errors are reported, and all memory and buffer

allocations are released. Pressing the stop button while executing any action will send the program directly to stage 4 to close down the program.

Over-riding the transfer between each stage is a time-out feature that closes the program if it does not finish executing after an extended period of time. This time-out feature is important tool for de-bugging and also represents some computer memory constraints.

During a measurement if the operator feels the image quality or image analysis is poor, he/she should attempt to remedy the cause of the problem and then press the reset button. The reset button will trash all images, clear all data from memory, and return the program back to stage 1. For example, during a measurement the HS spots might appear dull and the operator may decide to increase the exposure time of the CCD. The operator should simply re-enter the required exposure time and then press the reset button. The reset feature trashes all measurements held in memory and then reinitialises the program back to stage 1, ready to capture new data with minimal disruption to the subject.

The main software program relies on numerous smaller subprograms, some of which are generic LabView subprograms, third party developments, or our own original developments. Often a particular subprogram may be called at many different times during the execution of the main program. Three of the originally developed subprograms critical to a HS WFS will be described in the following sections 5.3 to 5.5.

### 5.3 Determining the parameters of the pupil

Traditionally, the HS spots are used to determine the pupil centre as discussed by Atchison and Scott (2002). The spatial resolution of this technique is equal to the size of the subfield. This process has potential for error because it assumes the reference spots are unaberrated (i.e. the internal instrumental aberration is negligible). It also assumes that speckle is negligible and that the critical subapertures at the pupil edge do not suffer from irregular irradiance. However, it is possible that speckle and/or high aberrations could cause HS spots at the pupil edge to have a reduced SNR and reduced certainty of detection. Circumstances in which a few HS spots at the edge of the pupil are erroneous detected or rejected can easily occur. For a WFS with the same parameters as ours, this could produce an error in pupil centre determination with a magnitude of nearly 0.5 mm. Some researchers recognize the uncertainty in detecting peripheral HS spots and suggest the pupil centre be determined by averaging the position of the central HS spots as these spots are expected to have the lowest tilts (Cox personal communication 2006). However, the assumption that the location of the central HS spots are 'well known' can be often be disrupted by unwanted corneal reflections which tend to pollute the central HS spots.

To explore alternative techniques for determining the pupil centre, our WFS images the subject's eye using infrared light onto the same CCD that is used for imaging the HS spots. We use this image of the external eye to determine the pupil centre. The technique relies on an accurate calibration between the alignment channel (image of the eye) and the sensing channel (image of HS spots). We estimate that our dual channel alignment process, combined with our pupil edge detection algorithm, has a resolution better than 0.5 mm at the subject plane. The performance of our alternative technique

for determining the pupil centre has not yet been compared to the traditional HS spot technique in a robust quantitative experiment. We hope to investigate this aspect of our WFS design in the future (see chapter 9).

It was not appropriate to use the generic LabView edge detection algorithm because it was slow and analysed the image data after it had been displayed (and hence converted from a 12 bit scale to a 8 bit scale). It was preferable to develop an original subprogram with improved speed, the ability to use the original 12 bit data, and increased operator-control over the degree of smoothing.

Our subprogram uses an edge-detection algorithm on the image of the eye. Initially a binarised intensity threshold approach was used to determine the iris-edge. Pilot studies concluded this approach was too simplistic and unable to cope with the variability of reflectance and pigmentation within a clinical population. In its final form the subprogram takes radial line samples of intensity data outwards from the approximate pupil centre (an annulus is actually used to account for the central pupil mask). The line profiles are passed through a Gaussian filter to smooth the profile, before the second derivative is used to estimate the iris-edge position. The detected edge points are then fitted to a circle by a least-squares method and the circle is used to define specific parameters of the pupil (e.g. pupil radius, pupil centre coordinates, roundness).

### 5.4 Centroid determination

The centroid of each HS spot of light is used to describe its location. The centroid of an object can be defined by its centre of mass or its 'balance point'. Because we are

describing a spot of light on a CCD, determining the centroid is a two-dimensional problem of finding the first moment of the intensity pattern. In the discrete case,

$$X_c = \Sigma_i x_i I_i / \Sigma_i I_i \qquad \text{and} \qquad Y_c = \Sigma_i y_i I_i / \Sigma_i I_i , \tag{5.1}$$

where $X_c$ and $Y_c$ are the centroid location in the x and y directions respectively, and $I$ represents irradiance (Jiang *et al.* 2004). Equation 5.1 shows that the greater a pixel's intensity, and the further its distance from the origin, the greater effect it has in "pulling" the centroid position. Finding the centroid of a spot of light is an iterative process with various techniques available to increase signal and dampen the effects of noisy or outlying pixels (hopefully without making any unreasonable assumptions) (Jiang *et al.* 2004). However, before outlining our implementation of these centroiding techniques the nature of the HS spot image, pre-processing techniques, and post-processing techniques will be mentioned.

The coherence of the laser diode can produce an irregular irradiance profile in the pupil and speckle in the HS spot image. This phenomenon may cause some HS spots to be dull and difficult to detect and locate (Bará 2003). It can also result in confusion between multiple maxima within an individual HS spot. Scanning the probing beam on the retina would help reduce coherence, as would incorporating a rotating diffuser into the probing beam. Simply increasing the CCD exposure time achieves a similar result by relying on small retinal dynamics to decrease the coherence of the retinal spot. Substituting the laser diode source with a superluminescent diode (SLD) could also reduce the coherence problem but this is an expensive solution. Initially our WFS was designed to use a very bright red LED. This would almost completely avoid the coherence problem and provide a very inexpensive, efficient and easily driven source.

Unfortunately, testing indicated the maximum optical flux produced from the most powerful LED commercially available (in our required bandwidth) was insufficient. Hopefully future advances in super-bright LED technologies will facilitate this solution to the coherence problem. In regard to speckle, post-processing techniques are also available to reduce its effects. Such a process may filter the whole HS image (rather than filtering locally) with a low-pass filter. The size limit of the filter would be set lower than the speckle detail but greater than the HS spots (Cox, private communication 2006).

Our subprogram subtracts a dark frame from each HS spot image and applies numerous rules and conditions designed to deal with potential problems within the HS spots such as saturation, speckle, crowding, dull intensity, and low contrast. During a measurement the operator inspects the iris-edge determination process, spot brightness, spot quality, subject focus, subject eye movements, subject blinking, tear film quality, and subject alignment. The manual inspection process has a problem-prevention aspect while the software program is in stage 1. Once the program enters stage 2 the frame rate (~ 11 fps) can hinder the manual inspection because each measurement series occurs over such a short duration (approximately 2 seconds). For each measurement series of 20 frames the operator views frames 1 to 19 in real-time and then reviews the final frame (which is assumed to be representative of the other images captured in the series) without any time constraints. If any bias is present the final image is more likely to produce a conservative assessment of image quality for the entire series. The final review image is not discarded until the operator has inspected the HS spot accept/reject process, iris-edge detection and the centroiding process. Currently the manual inspection controls don't allow individual data points to be added/deleted/moved. If the

operator feels that the image or the image-analysis is poor, the entire measurement series should be discarded and a replacement measurement taken. If the operator recognizes a problem during measurement they should attempt to remedy the problem and then use the reset feature. Pilot studies (see chapter 6) were used to refine the iris-edge detection algorithm, the HS spot acceptance/rejection criteria and the centroiding process. For our WFS to be fast and user-friendly it was important that these processes be largely automated and reliable.

It has been recognized that the central pupil area in a HS spot image may have greater intensity than other areas of the pupil (Bará 2003). This effect thought to be due to the light-guide properties of the photoreceptors and the resultant directional characteristic of the retinal scatter (van Blockland and van Norren 1986). This phenomenon can be addressed with a whole-image band-passing filter as opposed to filtering each local subfield (Cox, private communication 2006). A very low pass filter is applied to the whole image and this is then subtracted from the original image. The bright pedestals that affect the central HS spots are thereby reduced and the peripheral HS spots are unchanged as they do not develop such pedestals. The image is then ready to undergo centroid analysis for each subaperture (Cox, private communication 2006).

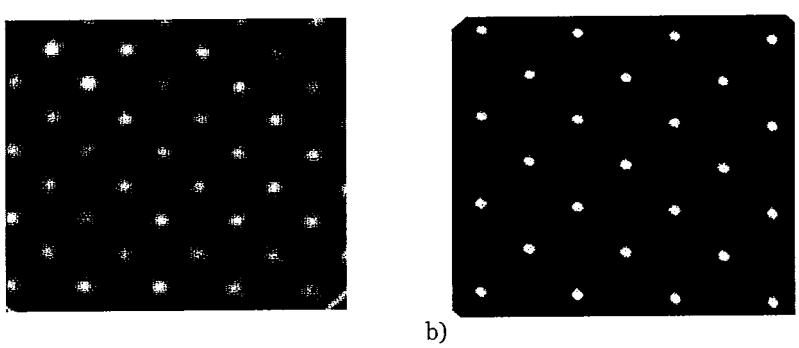


**Figure 5.10 An example HS spot images a) with, and b) without pedestal formation**

It was not appropriate to use the generic LabView centroiding subprogram because it is relatively slow and analysed the image data only after it had been displayed (and hence converted from a 12 bit scale to a 8 bit scale). We prefered to develop an original subprogram because of the improved speed, the ability to use the original 12 bit data, and the greater control it provided over centroid parameters such as the region of interest (ROI) window and convergence accuracy.

Our subprogram uses the brightest pixel within the CCD subfield to make an initial estimate of the centroid. It then applies a square ROI window of a suitable initial size (typically 11 x 11 binned pixels) centered over this location. The initial ROI window size is conservative so as to enclose the entire HS spot, in recognition that the brightest pixel is a very crude initial estimate of the centroid. The centroid is calculated with a linear weighting and repositioned with each iteration. Gradually the ROI window size is decreased to a minimum value (typically 5 x 5 binned pixels), which is still greater than the estimated size (full-width-half-maximum, FWHM) of the HS spot sinc function. A square aperture diffraction pattern is a suitable model for our HS spots because our lenslet array has a square geometry and the retinal beacon is smaller than the diffraction limit of the lenslet subaperture. Smaller ROI windows reduce the potential for neighbourhood bias but if allowed to shrink too small the window may not enclose all of the relevant pixels - giving inaccurate results. The subprogram repeats its calculations, shifting the origin to the centroid estimate of each previous iteration until the shift between iterations falls below the convergence accuracy level. Simulations of the centroiding process were used to determine the underlying noise level in our algorithm (see chapter 6). The default convergence accuracy level is set to this noise level of 0.5 microns. The ROI window uses a square geometry for the sake of simplicity

to match the CCD geometry. Additionally, the CCD is mounted at 45 degrees to the optical board to match the orientation of the lenslet array (and therefore the HS subfields) – this simplifies centroiding and coordinate calculations.

If a HS spot falls near the boundary of its subfield a neighborhood bias could be introduced. Specific rules are defined to limit this error and the potential confusion between neighbouring spots. It is arguable whether a ROI window should be allowed to overlap into a neighbouring subfield because there isn't a rigorous way to avoid confusing which spot belongs to which subaperture. Generally the dominance of lower-order aberrations means that it is more likely that neighbouring spots will move in similar directions rather than diametrically opposite directions. This prior knowledge can be used to adjust the initial position the ROI window depending upon the position and spacing of neighbouring spots that have already been located (Cox 2006). This is a hierarchal approach were the location of central HS spots is assumed to be more accurately known and so these spots are analysed first (Atchison and Scott 2002). Extending this argument to assume that the local spacing of HS spots will not change rapidly, the size of the initial ROI window might be allowed to expand or shrink based on neighbouring spots. For example, the size of peripheral ROI windows will shrink in the presence of positive spherical aberration. The idea of using known neighbouring data points to make predictions about fellow data points yet to be measured is already used in other visual science instruments such as computerized perimeters (e.g. the Swedish Interactive Thresholding Algorithm used by the Zeiss/Humphrey™ visual field analyzer uses neighborhood prediction to increase the speed and accuracy of computerized perimetry). Similar technology may increase centroiding speed in HS WFSs for the eye with only modest assumptions about the aberration profile. The

potential improvements in processing speed are marginal because the 'brightest pixel' starting point for the initial centroid estimate is computationally both simple and fast. However there are greater potential benefits for increased dynamic range if prior knowledge allows HS spots to encroach on their neighbour's subfield.

Various alternatives to traditional centroiding may be found in other HS WFS applications. For example, although quadcell centroiding is not appropriate for our WFS, it is often used by WFS components of AO systems operating in closed-loop. Quadcell centroiding is advantageous because the read time of such a small number of pixels per HS spot is low and the computational demands are likewise reduced. This centroiding technique relies on the corrective device (typically a deformable mirror) driving the residual wavefront aberrations towards zero (and hence the HS spot position towards the origin). The closed-loop environment is crucial to maintain at least some signal in all quadrants, to maintain linearity, and to protect the system from collapse.

Another alternative approach to the task of locating the HS spots is a maximum-likelihood technique. This approach avoids centroiding calculations and uses the pixel intensities to determine the most likely HS spot location. The application of this technique has been modelled by Barrett *et al.* (2007). The pixel intensities of a subfield are compared to a previously constructed lookup table. The 'best match' in the lookup table then determines the estimates of the local tilts. Such an approach may be faster that traditional centroiding. The construction of a lookup table would be time demanding but it would only have to be produced once. A spatial light modulator could be used to generate the incremental increases in the global tip and tilt of a plane wavefront, which when incident on the WFS, is used to construct the lookup table.

## 5.5 Zernike polynomial fitting and wavefront reconstruction

Local tilt data produced by a HS WFS is typically used to reconstruct the wavefront phase using either zonal or modal reconstructors. Zonal reconstructors develop a model of the wavefront by using local increments or decrements in phase for each sample in the pupil. Modal reconstructors fit the entire data set all at once by fitting to a pre-defined basis set of polynomials. Li *et al.* (2002) compared both types of algorithms in models of AO systems operating to correct atmospheric turbulence. Zonal reconstruction algorithms were found to be generally suitable, although modal reconstruction was superior in lower SNR conditions. Southwell (1980) notes that modal estimation may be superior to zonal estimations of wavefront phase with regard to noise propagation and computational demands. OSA standards for describing ocular aberrations specify the use of Zernike polynomials – a modal estimation of wavefront phase. Our WFS fits Zernike polynomials to the local tilt data by an ordinary least-squares method. Once the Zernike coefficients (estimates of the true values) are known, reconstruction of the wavefront phase is trivial.

Fig. 5.11 illustrates the wavefront approximation as pure tilt over a subaperture in the horizontal ($xz$) plane. The local tilt of the wavefront ($\alpha$) is found experimentally by dividing the shift in the HS spot location ($\Delta x$) by the focal length of the lenslet ($f$). A local tilt value is determined for both the vertical ($\Delta y / f$) and horizontal ($\Delta x / f$) directions and these partial derivatives of the phase are equivalent to those expressed later in equation 5.2.

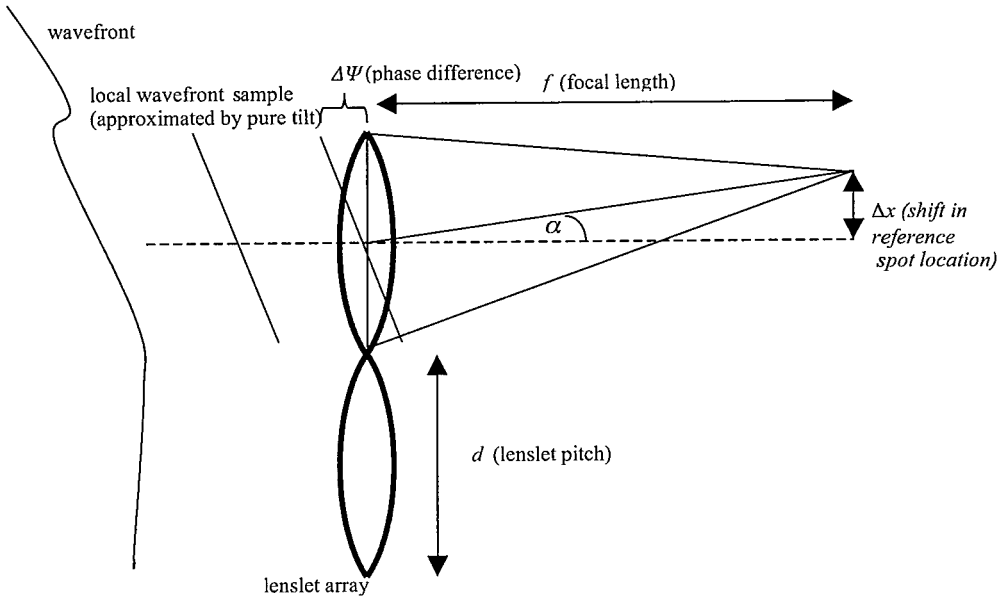


**Figure 5.11 A diagram of local wavefront sampling by the lenslet array.**

It is assumed that the wavefront, $\Psi_{(x,\,y)}$, can be expressed as a weighted sum of Zernike polynomials,

$$\Psi_{(x,\,y)} = \Sigma_{n=1}\ C_n\, Z_{n\,(x,\,y)}\,, \tag{5.1}$$

where $Z_{n\,(x,\,y)}$ are Zernike polynomials and $C_n$ are coefficients of the Zernike modes. In practice we do not use an infinite sum of polynomials to represent the wavefront, instead we use $n$ Zernike modes. The value for $n$ is arbitrary but it must be sufficiently high to satisfy the approximation and avoid aliasing. In our WFS we fit the wavefront up to $5^{th}$ order Zernike polynomials which is equivalent to $n = 20$ modes.

From equation 5.1 we can define the partial derivates of $\Psi_{(x,\,y)}$ as,

$$\frac{\partial \Psi_{\,(x,y)}}{\partial x} = \Sigma_{n=1}\, C_i\, \frac{\partial Z_{n\,(x,y)}}{\partial x} \qquad \text{and} \qquad \frac{\partial \Psi_{\,(x,y)}}{\partial y} = \Sigma_{n=1}\, C_i\, \frac{\partial Z_{n\,(x,y)}}{\partial y} \tag{5.2}$$

Typically a HS WFS has a large number of subapertures that sample the wavefront. As a result the task of fitting Zernike coefficients to the data is over-determined and a unique solution is not possible. The ordinary least-squares solution to this problem has minimal fitting error. The partial derivatives in equation 5.2 can be replaced with the local tilt data ($\Delta x_i / f$ and $\Delta y_i / f$) with the understanding that these values are estimates and include noise. Using a least squares fit both parts of equation 5.2 can be represented in matrix form by

$$\mathbf{ZC} = \mathbf{\Psi}, \tag{5.3}$$

where $\mathbf{\Psi}$ is a column vector ($2i$ x 1) whose elements are the local slopes of the wavefront, **C** is a column vector (n x 1) whose elements are the coefficients of Zernike polynomials, and **Z** is a rectangular matrix ($2i$ x n) whose elements are the partial derivatives of the Zernike polynomials. Fig. 5.12 is a diagrammatic representation of the matrices described in equation 5.3. The parameter $i$ denotes the number of data points sampled in the wavefront. The values of Px and Py designate the position of the data sample within the pupil in the horizontal and vertical directions respectively. Note that these are fractional values of a unit circle, where;

$$-1 \le Px \le +1 \ , \qquad -1 \le Py \le +1 \qquad \text{and} \qquad Px^2 + Py^2 \le 1 \ . \tag{5.4}$$

Solving equation 5.3 for the vector **C** gives;

$$\mathbf{C} = \mathbf{Z}^{-1}\mathbf{\Psi}, \tag{5.5}$$

But $\mathbf{Z}^{-1}$ does not exist because **Z** is not a square matrix and it can't be inverted.

Instead, if we multiply equation 5.3 by the transpose of **Z**,

$$\mathbf{Z}^T\mathbf{Z}\mathbf{C} = \mathbf{Z}^T\mathbf{\Psi}. \tag{5.6}$$

And then solving for **C** we get;

$$\mathbf{C} = (\mathbf{Z}^T\mathbf{Z})^{-1}\mathbf{Z}^T\mathbf{\Psi}. \tag{5.7}$$

where $(\mathbf{Z}^T\mathbf{Z})^{-1}\mathbf{Z}^T$ is the pseudoinverse of **Z** and can be found using a singular value decomposition technique. The condition number of **Z** can be calculated to examine the stability of the solution.

Our software program solves equation 5.7 after measuring the local tilts of each subaperture (see fig. 5.11). The details of solving equation 5.7 involve some coordinate system transposing from the CCD to the lenslet array, as well as some scaling procedures. The shift in the HS spot location (meters) is divided by the focal length of the lenslet array (meters) to give the values of the local slopes (radians). The elements in **Z** are unitless, and so to solve the elements of **C** with units of microns, the slope values **Ψ** (radians) are multiplied by the pupil radius at the lenslet array (microns). As the magnification in the optical system only affects transverse dimensions ($x$ and $y$) of the wavefront but not the longitudinal dimension ($z$) (i.e. phase), the Zernike coefficient values determined at the plane of the lenslet array require no further magnification conversion. Once the rotation of the coordinate system is accounted for the Zernike coefficient values determined at the plane of the lenslet array are equivalent to those at the pupil plane of the eye. The estimates of the Zernike coefficients are then known and

the wavefront phase can be reconstructed with a modal technique and displayed to the operator as a phase or contour map.

$$\Psi = \begin{bmatrix} \Delta x_1/f \\ \Delta x_2/f \\ \Delta x_3/f \\ \vdots \\ \Delta x_{i-1}/f \\ \Delta x_i/f \\ \Delta y_1/f \\ \Delta y_2/f \\ \Delta y_3/f \\ \vdots \\ \Delta y_{i-1}/f \\ \Delta y_i/f \end{bmatrix} \quad \mathbf{Z} = \begin{bmatrix} \partial Z_1(Px_1Py_1)/\partial x & \partial Z_2(Px_1Py_1)/\partial x & \cdots\cdots & \partial Z_n(Px_1Py_1)/\partial x \\ \partial Z_1(Px_2Py_2)/\partial x & \partial Z_2(Px_2Py_2)/\partial x & \cdots\cdots & \partial Z_n(Px_2Py_2)/\partial x \\ \partial Z_1(Px_3Py_3)/\partial x & \partial Z_2(Px_3Py_3)/\partial x & \cdots\cdots & \partial Z_n(Px_3Py_3)/\partial x \\ \vdots & \vdots & & \vdots \\ \partial Z_1(Px_{i-1}Py_{i-1})/\partial x & \partial Z_2(Px_{i-1}Py_{i-1})/\partial x & \cdots & \partial Z_n(Px_{i-1}Py_{i-1})/\partial x \\ \partial Z_1(Px_iPy_i)/\partial x & \partial Z_2(Px_iPy_i)/\partial x & \cdots\cdots & \partial Z_n(Px_iPy_i)/\partial x \\ \partial Z_1(Px_1Py_1)/\partial y & \partial Z_2(Px_1Py_1)/\partial y & \cdots\cdots & \partial Z_n(Px_1Py_1)/\partial y \\ \partial Z_1(Px_2Py_2)/\partial y & \partial Z_2(Px_2Py_2)/\partial x & \cdots\cdots & \partial Z_n(Px_2Py_2)/\partial y \\ \partial Z_1(Px_3Py_3)/\partial y & \partial Z_2(Px_3Py_3)/\partial x & \cdots\cdots & \partial Z_n(Px_3Py_3)/\partial y \\ \vdots & \vdots & & \vdots \\ \partial Z_1(Px_{i-1}Py_{i-1})/\partial y & \partial Z_2(Px_{i-1}Py_{i-1})/\partial y & \cdots & \partial Z_n(Px_{i-1}Py_{i-1})/\partial y \\ \partial Z_1(x_iy_i)/\partial y & \partial Z_2(x_iy_i)/\partial y & \cdots\cdots & \partial Z_n(x_iy_i)/\partial y \end{bmatrix} \quad \mathbf{C} = \begin{bmatrix} C_1 \\ C_2 \\ C_3 \\ C_4 \\ C_5 \\ \vdots \\ C_{n-1} \\ C_n \end{bmatrix}$$

**Figure 5.12 A diagrammatic representation of the matrices described in equation 5.3.**

The relevant normalised Zernike polynomial functions are listed in tables 5.1 and 5.2 after being converted from table 1.1 to a Cartesian coordinate system (Schweigerling 2004).

| $Z_n^m$ | Polynomial (cartesian coordinates) |
|---|---|
| $Z_1^{-1}$ | 2 (y) |
| $Z_1^1$ | 2 (x) |
| $Z_2^{-2}$ | $\sqrt{6}$ (2xy) |
| $Z_2^0$ | $\sqrt{3}$ ($2x^2 + 2y^2 - 1$) |
| $Z_2^2$ | $\sqrt{6}$ ($x^2 - y^2$) |
| $Z_3^{-3}$ | $\sqrt{8}$ ($3x^2y - y^3$) |
| $Z_3^{-1}$ | $\sqrt{8}$ ($3x^2y + 3y^3 - 2y$) |
| $Z_3^1$ | $\sqrt{8}$ ($3x^3 + 3xy^2 - 2x$) |
| $Z_3^3$ | $\sqrt{8}$ ($x^3 - 3xy^2$) |
| $Z_4^{-4}$ | $\sqrt{10}$ ($4x^3y - 4xy^3$) |
| $Z_4^{-2}$ | $\sqrt{10}$ ($8x^3y + 8xy^3 - 6xy$) |
| $Z_4^0$ | $\sqrt{5}$ ($6x^4 + 12x^2y^2 + 6y^4 - 6x^2 - 6y^2 + 1$) |
| $Z_4^2$ | $\sqrt{10}$ ($4x^4 - 4y^4 - 3x^2 + 3y^2$) |
| $Z_4^4$ | $\sqrt{10}$ ($x^4 - 6x^2y^2 + y^4$) |
| $Z_5^{-5}$ | $\sqrt{12}$ ($5x^4y - 10x^2y^3 + y^5$) |
| $Z_5^{-3}$ | $\sqrt{12}$ ($15x^4y + 10x^2y^3 - 5y^5 - 12x^2y + 4y^3$) |
| $Z_5^{-1}$ | $\sqrt{12}$ ($10x^4y + 20x^2y^3 + 10y^5 - 12x^2y - 12y^3 + 3y$) |
| $Z_5^1$ | $\sqrt{12}$ ($10x^5 + 20x^3y^2 + 10xy^4 - 12x^3 - 12xy^2 + 3x$) |
| $Z_5^3$ | $\sqrt{12}$ ($5x^5 - 10x^3y^2 - 15xy^4 - 4x^3 + 12xy^2$) |
| $Z_5^5$ | $\sqrt{12}$ ($x^5 - 10x^3y^2 + 5xy^4$) |

**Table 5.1 List of Zernike polynomials in right-handed Cartesian form (OSA standard format)**

| $Z_n^m$ | $\partial Z/\partial x$ partial derivative | $\partial Z/\partial y$ partial derivative |
|---|---|---|
| $Z_1^{-1}$ | 0 | 2 |
| $Z_1^1$ | 2 | 0 |
| $Z_2^{-2}$ | $\sqrt{6}$ (2y) | $\sqrt{6}$ (2x) |
| $Z_2^0$ | $\sqrt{3}$ (4x) | $\sqrt{3}$ (4y) |
| $Z_2^2$ | $\sqrt{6}$ (2x) | $\sqrt{6}$ (-2y) |
| $Z_3^{-3}$ | $\sqrt{8}$ (6xy) | $\sqrt{8}$ ($3x^2 - 3y^2$) |
| $Z_3^{-1}$ | $\sqrt{8}$ (6xy) | $\sqrt{8}$ ($3x^2 + 9y^2 - 2$) |
| $Z_3^1$ | $\sqrt{8}$ ($9x^2 + 3y^2 - 2$) | $\sqrt{8}$ (6xy) |
| $Z_3^3$ | $\sqrt{8}$ ($3x^2 - 3y^2$) | $\sqrt{8}$ (–6xy) |
| $Z_4^{-4}$ | $\sqrt{10}$ ($12x^2y - 4y^3$) | $\sqrt{10}$ ($4x^3 - 12xy^2$) |
| $Z_4^{-2}$ | $\sqrt{10}$ ($24x^2y + 8y^3 - 6y$) | $\sqrt{10}$ ($8x^3 + 24xy^2 - 6x$) |
| $Z_4^0$ | $\sqrt{5}$ ($24x^3 + 24xy^2 - 12x$) | $\sqrt{5}$ ($24x^2y + 24y^3 - 12y$) |
| $Z_4^2$ | $\sqrt{10}$ ($16x^3 - 6x$) | $\sqrt{10}$ ($-16y^3 + 6y$) |
| $Z_4^4$ | $\sqrt{10}$ ($4x^3 - 12xy^2$) | $\sqrt{10}$ ($-12x^2y + 4y^3$) |
| $Z_5^{-5}$ | $\sqrt{12}$ ($20x^3y - 20xy^3$) | $\sqrt{12}$ ($5x^4 - 30x^2y^2 + 5y^4$) |
| $Z_5^{-3}$ | $\sqrt{12}$ ($60x^3y + 20xy^3 - 24xy$) | $\sqrt{12}$ ($15x^4 + 30x^2y^2 - 25y^4 - 12x^2 + 12y^2$) |
| $Z_5^{-1}$ | $\sqrt{12}$ ($40x^3y + 40xy^3 - 24xy$) | $\sqrt{12}$ ($10x^4 + 60x^2y^2 + 50y^4 - 12x^2 - 36y^2 + 3$) |
| $Z_5^1$ | $\sqrt{12}$ ($50x^4 + 60x^2y^2 + 10y^4 - 36x^2 - 12y^2 + 3$) | $\sqrt{12}$ ($40x^3y + 40xy^3 - 24xy$) |
| $Z_5^3$ | $\sqrt{12}$ ($25x^4 - 30x^2y^2 - 15y^4 - 12x^2 + 12y^2$) | $\sqrt{12}$ ($-20x^3y - 60xy^3 + 24xy$) |
| $Z_5^5$ | $\sqrt{12}$ ($5x^4 - 30x^2y^2 + 5y^4$) | $\sqrt{12}$ ($-20x^3y + 20xy^3$) |

**Table 5.2 List of partial derivatives of Zernike polynomials in right-handed Cartesian form (OSA standard format)**

Our software program fits all wavefront measurements with Zernike polynomials up to the $5^{th}$ order. The main factors influencing this decision were noise and aliasing considerations (see sections 3.4 and 3.6). It is possible to perform a F-test to optimise the aberration order that each wavefront measurement should be fitted to (Atchison and Scott 2002). However this approach creates difficulties for comparative studies and the statistical analysis of population studies. A similar difficulty would arise if we did not pharmacologically dilate the subject's pupil. Population and comparative studies require consistency in analysis and so all wavefronts are fitted to the same Zernike order and all pupils are pharmacologically dilated so they all can be analysed over a 6 mm diameter. For each wavefront measurement the pupil centre is determined from the alignment channel (image of the external eye) and then all subsequent analysis is limited to the subset of HS spots that correspond to the pupil size of interest.

Once the Zernike coefficients have been determined for each measurement the raw data is discarded (including the local slope values and the CCD images). The CCD output is displayed live to the operator during a measurement, however only the final image in a measurement series is held in computer memory. This is used as a representative image for the operator to perform a manual inspection and check. The software program automatically saves the key parameters of each measurement to the database. By electing to record the wavefront data in its analysed form, the database is faster to construct and requires far less space on the computer's hard drive. The database includes the examination details (e.g. subject name, date of birth, date of examination) the fitted Zernike coefficients, and various pupil parameters (e.g. pupil size, pupil centre coordinates, signal strength).

### 5.6 Data displays

One advantage of developing our own WFS rather than modifying a commercial instrument, is the freedom to choose the style and format of our data displays. Our software program displays data in various forms such as, the live CCD image with various overlays, histograms of CCD intensity levels, phase maps of the reconstructed wavefront, and bar graphs of the measured Zernike coefficients. The selected action (see section 5.1) determines whether the data displays will be refreshed in real time (action 4) or if they will only update after the complete series of measurements have been analysed (action 3). Our experimental WFS can capture data at speeds up to 10 Hz - computing speed rather than photon insufficiency is the limiting factor here.

Phase maps are common to most commercial WFSs and they are one of the primary display formats used by our WFS. The phase map is a useful learning tool for conceptualising the wavefront shape and for patient education. Phase maps give a general and quick impression of the wavefront characteristics, however they are open to misinterpretation and require a skilled observer to interpret them meaningfully, especially if a large dynamic range encountered requires a floating false-colour scale. Like most graphical representations of data, correct interpretation of results requires that the observer understands the scaling process.

For many research and clinical applications the Zernike coefficient values are a more useful, objective, and convenient data format. Our software program displays the Zernike coefficients in both a numerical and bar chart format. In a series of measurements the software program exports the Zernike coefficients with statistical information about the central tendencies and spread of values. Like most commercial

WFSs, our software program displays Zernike coefficients without any specific indication of the error associated with that specific value. In a series of measurements the standard deviation of each coefficient does give some indication of stability and spread of measurements, however this is a loose association as the true ocular aberrations themselves are not static over the measurement period of a few seconds. Attention is given to the correct use of significant figures by our software program and displays, however the Zernike coefficients are presented with no reference to their associated error. Future studies should investigate the accuracy of measurements performed with our WFSs and then software improvements should address the currently insufficient treatment of error analysis by at least displaying an estimate of the error associated with each wavefront measurement.

The bar chart display of Zernike coefficients created by our software program could be improved by including graphical indicators for the typical range of coefficient values for each Zernike mode in a normal population of eyes. The ZyWave 'time band' feature is an example of such a display. Currently our software program does not provide this feature but it is a relatively small job to include this capability in future software upgrades.

In some applications the operator may wish to convert the lower-order Zernike coefficients to a traditional refractive error format. Our software program provides this feature and converts the lower-order Zernike coefficients to an equivalent sphero-cylindrical refraction format (see section 2.17) using equations 5.8, 5.9, and 5.10 whose derivation is given by Brookes (2004). We can define;

$$\text{sphere (dioptres)} = \frac{4\sqrt{3}\alpha_4 - \sqrt{6}(\alpha_3 \sin 2\theta_0 + \alpha_5 \cos 2\theta_0)}{r^2} \quad , \tag{5.8}$$

$$\text{cylinder (dioptres)} = \frac{4\sqrt{3}\alpha_4 + \sqrt{6}(\alpha_3 \sin 2\theta_0 + \alpha_5 \cos 2\theta_0)}{r^2} \quad - \text{sphere} \quad , \tag{5.9}$$

$$\text{and} \quad \text{axis (degrees)} = \begin{cases} \theta_0 \\ \theta_0 + 180 \, , \end{cases} \tag{5.10}$$

where $\alpha_n$ are the Zernike coefficient values, $\theta_0$ is the stationary point of the astigmatic angle, and r is the pupil radius.

The complex interaction between multiple Zernike modes is not instinctively interpreted, especially when presented in a numerical format. The phase error (either positive or negative) for a certain Zernike coefficient may be neutralised across a large proportion of the pupil by the combined phase of several other modes, or alternatively, the combination of Zernike modes may exacerbate the phase error. The interactions between multiple modes are necessarily complex - we rely on them to describe a potentially very complicated surface. An ophthalmic clinician may prefer to interpret wavefront data as a single-value description: the *total wavefront RMS*. This condensed summary of data looses intricate details in the description of the wavefront, but most clinicians make use of this single-value descriptor because it is simpler to manage (LASIK leader 2002). As in all variance relationships, the total wavefront variance is equal to the sum of the individual variance values for each mode. The total wavefront RMS is equal to the square root of the sum of the squares of the individual Zernike coefficients. The calculation required to evaluate the total wavefront RMS is

straightforward because the definition of the Zernike modes has been contrived though the normalisation of the Zernike coefficients. Similarly, the Zernike coefficients of modes describing the lower-order aberrations may be used to generate a *lower-order wavefront RMS* value and the Zernike coefficients of modes describing the higher-order aberrations may be used to generate a *higher-order wavefront RMS* value. Our software program displays the total wavefront RMS, lower-order wavefront RMS, and the higher-order wavefront RMS, for each wavefront measurement.

In addition to the live CCD image, it is helpful for the examiner to receive real-time displays regarding key measurement parameters. If these parameters are displayed individually it forces the attention of the examiner to be divided across multiple parts of the screen. To address this issue the software program displays a multiple line-plot graph, which tracks in real-time, in a single graph, the key parameters of HS signal strength, pupil size, total wavefront RMS, higher-order RMS, and lower-order RMS for each accepted HS spot image. This single graph allows rapid analysis of trends for multiple parameters during a measurement series in a simpler and instinctive format than would be possible with five individual numeric displays.

# CHAPTER SIX

## Pilot studies of the experimental wavefront sensor

This chapter describes the outcomes of 3 pilot studies which examined the repeatability and the practical limits of the experimental WFS. The pilot studies helped to debug the software program and to develop a measurement protocol, ensuring that future experiments would run smoothly. Firstly a brief mention is given to the theoretical and simulated limitations of the experimental WFS.

### 6.1 Sources of noise and error

Ocular HS WFSs are prone to numerous sources of error (Neal *et al.* 2002). Depending on the application of the WFS, only some of these noise sources will be important. Some noise can be minimized with good optical design such as matching the peak of the quantum efficiency function of the CCD chip to the primary wavelength of the retinal beacon, or by using telecentric re-imaging of the HS spots.

Speckle noise in the HS spots, CCD non-uniformity, CCD read noise, pixelization, synch-jitter and CCD thermal noise all manifest as centroid determination errors (Neal *et al.* 2002). Centroid determination is considered independent of photon noise due to the relative abundance of photons available in ocular wavefront sensing applications (this is not the case in some astronomy applications). The use of a LED probing source was investigated during the optical design in an attempt to reduce speckle noise. Unfortunately with current technology levels this was not successful due to insufficient optical flux and a laser diode source was necessary. The quality of the CCD has direct bearing on the expected quantum efficiency, read noise, non-uniformity, and thermal noise. In regards to the practical operation of the experimental WFS, thermal noise is

considered nominal because the WFS is only expected to operate for brief periods and in a climate-controlled environment. Our software program partly compensates for hot pixels - excessively bright pixels caused by current leakage into the sensor well. The program subtracts a dark reference frame from the measurement frame and then any negative pixel values are set to zero before analysing the HS spot image. The centroiding algorithm itself has specific noise characteristics depending on the SNR it is operating under (Jiang *et al.* 2005).

Fitting errors are associated with the approximation that a wavefront can be discretely sampled and then described by a finite number of Zernike modes. Fitting errors manifest as spatial and temporal aliasing. Fitting the local slope data with Zernike coefficients is particularly sensitive to pupil centre determination error, and consequently subject alignment is crucial to accuracy of WFS measurements (Davies *et al.* 2003). This is a technique-dependent error (e.g. whether using the HS spots or an iris-edge detection process to determine the pupil centre) that causes mode-mixing, especially amongst the higher-order modes. Our optical design attempted to reduce the pupil centre determination error by introducing a simultaneous iris-edge detection process. The success or otherwise of this alternative technique has not been verified quantitatively due to time constraints.

Nearly all ocular HS WFS designs are prone to double-pass errors. However, an appropriate optical design of a small entrance pupil and a large exit pupil renders this effect almost negligible (Artal *et al.* 1995).

All of these errors occur in addition to the common alignment and focusing errors associated with subjective-control instruments. For further discussion of HS WFS noise and measurement error see Neal *et al.* (2002) and Tyson (1998).

### 6.2 Centroid determination - 1st pilot study

During the development stages of the centroiding program, computer simulations were performed to estimate its accuracy. A simulated point spread function (PSF) was created from an appropriately sized sinc function given the lenslet parameters, expected beam intensity, and retinal beacon wavelength. The PSF was shifted an arbitrary amount on the simulated CCD subfield grid (100% fill factor assumed), sampled discretely and then noise was added to represent the read noise of the CCD (12 electrons RMS). Photon noise and thermal noise were assumed insignificant and not modelled in the simulation. The centroiding program then estimated the shift in the location of the PSF. The simulation was successful in its main purpose - checking the centroiding software for bugs. A mean value for centroiding accuracy is necessary because it will vary systematically across HS spots due to geometry alignments/misalignments between the lenslet array and the CCD (Neal *et al.* 2002). The simulation estimated a mean centroiding accuracy of almost 0.25 microns across various alignments and misalignments of lenslet and CCD geometry, which corresponds to approximately 2% of a binned pixel width. This value is in good agreement with the theoretically-predicted value (Neal *et al.* 2002) and it is similar to the mean estimated centroid repeatability value determined from the 1st pilot study described below.

The 1st pilot study examined the centroid values obtained with repeated wavefront measurements of a plane mirror used in substitution for the eye. The mirror produces a

static plane wavefront, which allows the centroiding algorithm to be investigated in isolation. The plane mirror (λ/10 surface figure) used to generate the reference wavefront was retained in its position at the pupil plane (element B in fig. 4.1) following an optical alignment procedure. The laser power was also unchanged from the reduced power level used during reference wavefront generation. The software program was then modified to disable the iris-edge detector and to crop the HS spot image to a 6 mm pupil diameter, centred on the centre of the CCD frame (coincident with the optical axis). Twenty HS spot images were captured over approximately 2 seconds.

The mean shift in the HS spot centroids was 0.29 microns +/- 0.05 microns (one standard deviation). The low mean and standard deviation provide confidence in the repeatability of the centroiding algorithm. The centroid data was then allowed to proceed through the remainder of the software program to fit the wavefront with Zernike coefficients. The mean Zernike coefficients for all aberration modes from $2^{nd}$ to $5^{th}$ order were all less than 0.00 microns. This low value indicates the absence of systematic bias in these modes, at least in the middle of the linear range of operation. The standard deviation was also less than 0.00 microns for each aberration mode. Only limited conclusions regarding random noise in the centroid determination can be made from this standard deviation result. It is likely that vibration and misalignment effects were at a minimum because the study was performed immediately following an alignment procedure. Vibration and misalignment errors could be expected to be greater during use in a clinical environment and when performing measurements on real eyes.

The $1^{st}$ pilot study allowed a rudimentary investigation into the expected centroid determination repeatability in isolation from other noise sources. Other more

complicated sources of noise, such as pupil centre determination error, or subject alignment were not investigated due to time constraints. Future studies should endeavour to quantify the intrinsic aberration of the experimental WFS by comparing the centroids from the reference wavefront to a perfectly distributed geometric grid. The difference in reference HS spot locations compared to the geometric grid can be used to confirm that the intrinsic aberration of the WFS is minimal. It is important that the intrinsic aberration be low, because at the extremes of operation, if large intrinsic aberrations are combined onto the aberrations already present within the sensed wavefront, the system will eventually loose linearity. The principles of a HS WFS rely on assumptions that the aberrations in the wavefront measured are quite small, and vary smoothly across the pupil.

### 6.3 Development of experiment procedures - 2nd pilot study

A 2nd pilot study was performed on 10 healthy eyes (5 subjects) for the purpose of de-bugging software, improving future experiment designs, and to test the experimental WFS on real eyes. Basic experimental procedures were established prior to, and then refined throughout, the 2nd pilot study. These experimental procedures are described in the following section and were used in the subsequent 3rd pilot study (section 6.5) and experiments described in chapters 7 and 8, except where specifically noted otherwise. All experiments conducted as part of this thesis conform to the ethical guidelines and requirements of Dublin Institute of Technology.

Preliminarily the WFS was aligned and a CCD dark frame recorded. A reference HS spot image was recorded by positioning a plane mirror (surface figure $\lambda/10$) at the pupil plane (element B, fig. 4.1). The laser power at the eye was set to 1.2 microwatts and the exposure time of the CCD was set to 45 milliseconds.

The examiner briefly explained the purpose of the measurement and what the subject was likely to experience. No age limit was set by the subject selection criteria although young adult university students comprised the majority of volunteers in the 2nd and 3rd pilot studies and the experiments described in chapters 7 and 8. Subjects were examined to assess their suitability to safely undergo pupil dilation before participating. Subjects with ocular disease (including keratoconus) or history of ocular surgery (including refractive surgery) were excluded. Subjects with cataracts, media opacities, irregular pupil shapes, or dry eye were excluded due to their corrupting effects on HS spot image quality. To allow the pooling and comparison of individual results within a sample, subjects whose dilated pupil diameter was less than 6 mm were excluded. Due to optical design constraints, subjects with dilated pupil diameters greater than 9.5 mm and subjects with refractive errors outside the range of the WFS (–9.50 DS to +13.00 DS / – 4.75 DC for a 6 mm pupil) were also excluded.

After subject selection (which included examination by an optometrist to ensure the safe use of pharmacutical agents) and informed consent procedures, one drop of 1% Tropicamide was administered to each eye being measured. A 6 mm pupil diameter was selected as an appropriate value to measure wavefront aberrations over. Adequate time was allowed to achieve maximal pupil dilation - this typically occured after 30 minutes and a pupil diameter greater than 6 mm was verified by the examiner. The mydriatic effect was essential because aberration measurements of individual subjects are not equivalently comparable unless they are defined over the same pupil diameter (Schwiegerling 2002).

The decision to pharmacologically dilate the pupil raises various issues including how to define the pupil centre, which is known to move during dilation (Camellin *et al.* 2005). Pharmacological dilation can be less symmetric than natural scotopic-induced dilation (Yang and Wu 2007). It is known that spherical aberration increases with accommodation (Cheng *et al.* 2004). Therefore it is reasonable to expect cycloplegia itself (as distinct from mydriasis) may influence higher-order aberrations, especially over large pupil diameters and with pre-presbyopic subjects, although Yang and Wu (2007) found negligible effects on higher-order aberrations over 5 mm pupils. Aberration measurements through natural pupils are distinctly different to those measured through dilated pupils and they closer represent the optical performance of the eye for 'real world' circumstances.

All Zernike aberration coefficients presented in the experiments described in chapters 7 and 8 are referenced to a 6 mm pupil diameter. Current standards for reporting aberrations (Thibos *et al.* 2000) do not specify a standard pupil diameter. Most eyes can achieve a 6 mm pupil diameter with pharmacological dilation and so this restraint didn't unnecessarily limit the sample size of the group experiments presented in chapters 7 and 8. Aberration data for smaller pupil diameters can be obtained by performing various rescaling procedures or by masking the raw data in its HS spot form. These techniques are discussed by Howland and Howland (1977) and Neal *et al.* (2005). Extrapolation procedures for converting aberration coefficients beyond pupil diameters over which they were measured, are prone to error and inadvisable (Schwiegerling 2002). Tropicamide was chosen as the pharmacological agent because it provides a safe, relatively short duration, pupil dilation (Bartlett and Janus 2000). It also has moderate cycloplegic effects which help to stabilise the ocular aberrations and largely avoids

accommodation-induced aberration fluctuations. Sufficient cycloplegia was verified subjectively with blur of N6 print at 40 cm over habitual distance spectacles before wavefront measurements were performed. Results from the 2nd pilot study indicated that the mydryatic and cycloplegic effects were not consistently adequate for all subjects if a lower concentration of 0.5% Tropicamide was used (see figs. 6.12 and 6.13, section 6.4), and thus the refined experimental protocol specifically requires 1% concentration be used. A more robust cycloplegic effect is obtainable with other agents such as cyclopentolate and the population study by Thibos *et al.* (2002a) used this agent.

It is important to correct the subject's refractive error in the ingoing beam, even if this is only a partial correction such as a 'best sphere' corrrection. This is neccessarry to achieve a small retinal beacon and restrict the size of the HS spots to the diffraction limit. Maintining a low *HS spot size:subfield size* ratio limits cross-talk between neighbouring subfields. It is also important to remove gross refractive error in the outgoing beam to avoid saturating the WFS. The experimental WFS has a relatively large dynamic range for the first order aberrations ($Z_1^{-1}$, $Z_1^1$,), accordingly, global tip and tilt do not need to be removed optically before being sensed at the lenslet array in this application provided that cross-talk is still avoided. The Badal was set at the 'best sphere' value of the subject's refractive error. This primarily removes defocus $Z_2^0$ from the outgoing beam before it is sensed at the lenslet array. We considered passing the probing beam through the Badal to correct the 'best sphere' for the ingoing beam aswell, this process would act to reduce the size of the retinal beacon and improve HS spot image quality. However, this solution was not realised for fear of introducing multiple unwanted reflection problems. It was envisaged that the refractive error could be satisfactorily compensated for the ingoing beam by translating a lens (element R in

fig. 4.1) along the optical axis. The 2nd pilot study concluded this was not a practical solution in a clinical setting. The adjustment was too time consuming and prone to inducing misaligment. As one might expect, measurements with the focusing lens (element R in fig. 4.1) in its default position produced a clearer HS spot image for emmetropic subjects compared to ametropic subjects. This was especially evident when the 'best sphere' refractive error was greater than 2 diopters and emphasises the importance of maintaining a small retinal beacon in regard to image quality and image size of the HS spots.

During the 2nd pilot study an ad-hoc solution for correcting refractive error in the ingoing beam was used for some ametropic subjects. These subjects wore their habitual correction device (which included spectacles, rigid contact lenses and soft contact lenses) during measurements. A later experiment investigating the monochromatic aberrations over the central visual field (see chapter 8) initially had intended including aberration measurements performed in this way. However it was decided not to present any aberration results measured in this arrangement. The difficulty in correcting refractive errors with habitual devices is that the trial lenses/spectacles/contact lenses themselves contribute to the higher-order aberrations being sensed. This mixing of ocular aberrations and device aberrations occurs in other studies too, such as that by Thibos *et al.* (2002a), although these researchers took considerable efforts to minimise and to quantify these polluting effects. Additionally, the trial lenses and spectacle lenses produced severe reflection problems and rigid contact lenses caused difficulties for the iris-edge detection. Due to these difficulties, any future incorporation of habitual correction devices while performing aberration measurements with the experimental WFS should be considered carefully.

Each subject was aligned and positioned on the chin-rest and forehead-rest. The incorporation of a bite bar was avoided to make the WFS suitable for use in a clinical environment. Anecdotal experience from the 2nd pilot study suggests the stability of the wavefront aberration profiles is not adversely affected by the lack of a bite-bar. This assemment is supported quantatativley by the 3rd pilot study which demonstrated good levels of wavefront intra-measurement repeatability, suggesting that the intra-measurement movements of the eye during the 2 second (approximate) measurement period were insignificant for our application (see section 6.5).

To provide additional accommodation control, the fixation target was translated along the optical axis to produce a slightly 'fogged' target - an intentional myopic-type blur. This is a typical design feature of instruments attempting to relax accommodation. The subject was asked to fixate the laser in the central area of the fixation target, thereby aligning the subject's line of sight to the measurement axis. The examiner viewed a live display from the CCD and performed fine adjustments to subject alignment via the chin rest and stage which allows movement with 3 degrees of freedom. The examiner also assessed the HS spot quality and the correctness of the Badal setting. Any required adjustments to the Badal optometer, the spatial filter, or the ingoing beam location in the corneal plane were performed. These adjustments were typically aimed at improving HS image quality and avoiding unwanted corneal reflections. Due to non-uniformity in the laser beam, small changes in laser power at the eye occurred when the ingoing beam location was adjusted. Highly aberrated eyes required the diameter of the spatial filter to be increased slightly to prevent vignetting associated with a larger point spread function of the retinal beacon. The subject alignment was then re-checked and adjusted if necessary. The subject was asked to blink and then immediately following the blink, HS

spot images were captured. Aberration measurements were performed by the same examiner whenever possible to standardise image capturing, subject instructions, and subject alignment.

Twenty HS spot images were captured for each measurement over a typical duration of approximately 2 seconds. The Zernike coefficients from multiple images (20) were combined with the intention of improving accuracy albeit at the cost of temporal sensitivity. Spurious results from the 2nd pilot study suggested that if a fault occurred, it would typically last for a few frames within the series of 20 images (see fig. 6.3). As such, the use of *median* Zernike coefficient values, instead of *mean* values, was considered for the potential safe-guard it offered against intermittent spurious coefficient values. These sets of erratic coefficient values appeared to have two separate causes. Firstly, the inability of the software program to recognize a blink or partial blink. This category includes eyes whose upper eyelid partially obscured the edge of the dilated pupil even in the natural resting position. Secondly, erroneous performance of the iris-edge detection due either to physical obscuration of the iris-edge by the mask (i.e. poor subject alignment) or due to noise in the iris-edge detection algorithm. Although such corrupted data can be manually identified in review and discarded, it was preferred that this task be automated. The software program was modified to automatically remove data suffering severe corruption such as images captured during a blink or images with unsatisfactory detection of the iris edge. After discarding corrupt images the program immediately replaced these images with new exposures such that a full quota of 20 satisfactory images was always recorded for each measurement. This modification proved to be a significant operational improvement. After the software program was altered the safe-guard of using *median* coefficient values became

redundant and *mean* (not *median*) Zernike coefficient values were used in all subsequent data analysis. A manual review of the HS spot image quality, pupil edge detection, and subject alignment was retained in the experimental protocol as an extra assurity in verifying results. If the spot quality or subject alignment was poor the results were not used and the measurements were repeated. All measurements were taken in a dark room. Obscuration of the iris edge behind the mask is an operator-control error that was minimized with operator experience and also partially addressed by the software modifications.

Experience from the 2nd pilot study emphasized the importance of accurately setting the Badal optometer. The image quality of the HS spots can be unnecessarily degraded if the operator rushes this procedure and fails to set the Badal optometer accurately. An ancillary software program was created to provide the operator with magnitude and direction cues regarding any required adjustments to the Badal optometer. The program was designed to somewhat mimic the 'scan' function in the ZyWave, albeit with a non-motorised Badal adjustment. However, practical experience gained throughout the 2nd pilot study concluded the Badal setting could be achieved to a sufficient level of accuracy in a much faster way by simply using a subjective-focus technique with the spatial filter diaphragm (element O in fig. 4.1) acting as a focusing target. This technique was adopted as the Badal focussing procedure for the later 3rd pilot study and the experiments presented in chapters 7 and 8.

In accordance with laser safety procedures, the laser power at the eye was checked at regular periods with a powermeter. The laser power was checked before the start of each measurement session. Laser safety calculations are given in appendix B.

## 6.4 Key parameters analysed during the 2nd pilot study

The analysis of key parameters during the 2nd pilot study allowed faults in the experimental WFS to be identified and de-bugged. A small set of examples are presented here. Determining the pupil centre for each individual HS spot image as opposed to using a single representative value throughout an entire measurement series reduces the corrupting effects of fixational eye movements such as microsaccades and microtremor. Figs. 6.1 a) and b) show pupil centre tracking results for a subject over 10 series of measurements, each series consisting of 20 images. These plots of the pupil centre coordinates are representative of early results, which show an artificial limiting of the horizontal pupil centre to non-positive values. The data points in figs. 6.1 a) and b) can be seen to "stack up" along the y-axis. A software bug was responsible for this fault.

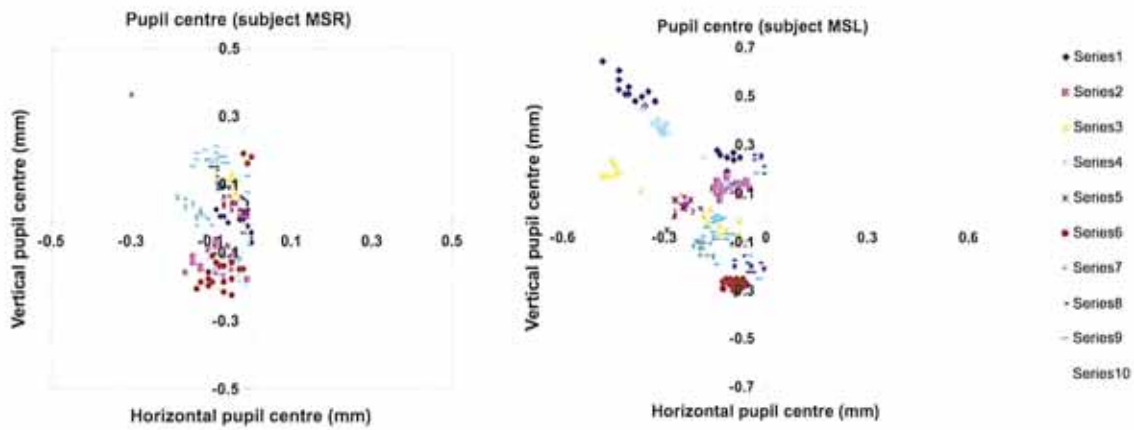


**Figure 6.1 Pupil centre tracking for early 2nd pilot study measurements on subject a) MSR and b) MSL.**

Figs. 6.2, 6.3 and 6.4 show pupil diameter tracking results for 3 subjects (respectively), over 10 series of measurements, each series consisting of 20 images. The pupil diameter plots in figs. 6.2 and 6.3 are representative of results produced early in the 2nd pilot study. Series 6 in fig. 6.2 shows an example of erroneous iris-edge detection occurring when the mask obscured the iris edge. This operator-control dependant error was more

likely to occur when the pupil size was at the extreme of the range of the WFS. Eyes with pupil diameters close to 6 mm (as is the case in fig. 6.2), or close to 9.5 mm are more difficult for the operator to align. This error is persistent and endures throughout the entire series. Anecdotally, borderline small pupils were significantly more common than borderline large pupils amongst our subjects. The frequency of this error was limited by use of a stronger mydriatic drug concentration (1% Tropicamide, rather than 0.5%), software modifications, and improving operator skill in subject alignment. This type of *series-persistent* error is distinct from the transient error evident in fig. 6.3. Series 2 in fig. 6.3 illustrates a temporary failure of the iris-edge detection algorithm, which returned to correct operation after two erroneous frames. Most likely this failure occurred due to a blink. The images were captured at approximately 8 Hz and a typical blink occurs over 260 milliseconds (Kaufman and Alm 2002), so this is a plausible event time scale. The occurrence of this error was greatly reduced by software modifications described in section 6.3, paragraph 9. Fig. 6.4 shows typical pupil diameter tracking results from the 2$^{nd}$ pilot study obtained after the software modifications had been made. If the data presented in fig. 6.4 is taken and each series is represented by its mean value, the standard deviation between measurements is 0.03 mm. Because the iris is not completely paralysed by 1% Tropicamide the value of 0.03 mm is not entirely a description of error - partially it reflects true fluctuations in the pupil diameter occurring between exposures.

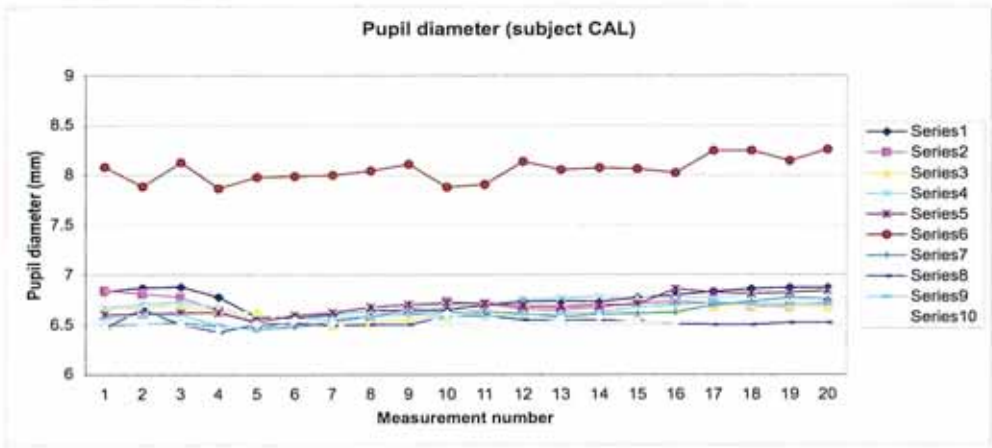


**Figure 6.2 Pupil diameter tracking for 2nd pilot study measurements on subject CAL.**

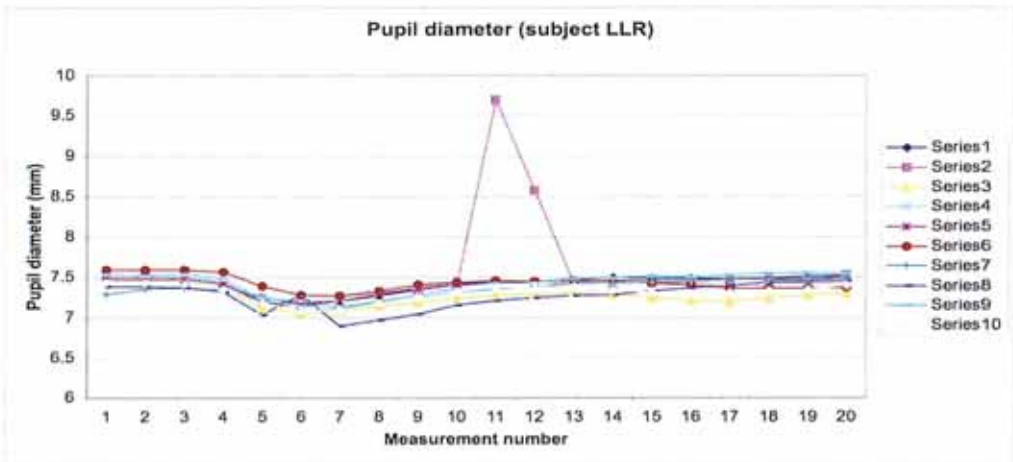


**Figure 6.3 Pupil diameter tracking for 2nd pilot study measurements on subject LLR.**

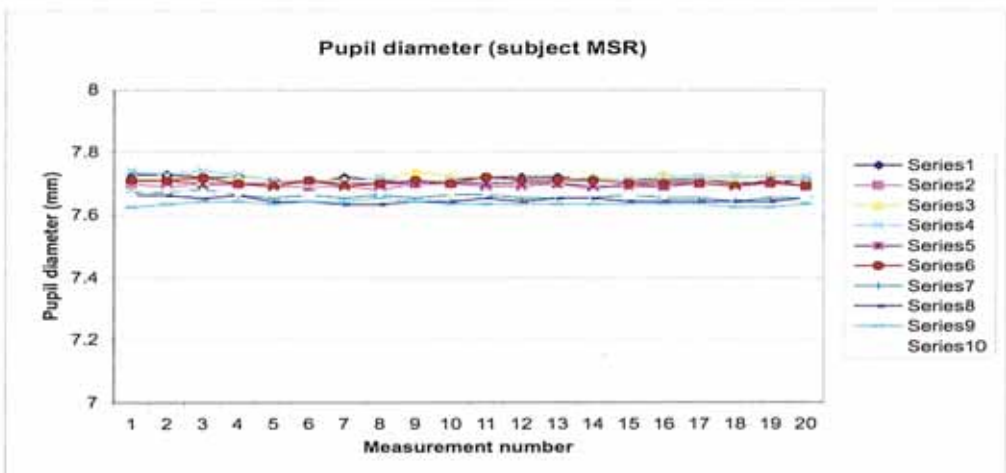


**Figure 6.4 Pupil diameter tracking for a typical subject after software improvements indicated by the 2nd pilot study had been applied.**

*Signal strength* is defined arbitrarily as the percentage of HS spots deemed acceptable by the software program with respect to the number of subapertures subtended by the pupil at the lenslet array. In this way, any subaperture whose centre falls within the pupil conjugate at the lenslet array is considered capable of producing a HS spot. Examples of signal strength for 2 subjects measured during the 2nd pilot study are shown in figs. 6.5 and 6.6 (respectively) over 10 series, each series consisting of 20 measurement frames. In both examples presented the signal strength is fairly consistent for all 10 series of measurements. However, subject ZSR in fig. 6.6 shows higher mean signal strength of 96% compared to 61% for subject PBL in fig. 6.5. The low signal strength observed in fig. 6.5 may be due to multiple reasons such as; a large number of HS spots being rejected due to CCD pixel saturation, low HS spot contrast, or HS spot encroachment toward its neighbouring subfield (cross-talk). However if any of these problems occur, the software program indicates the problem/s to the operator both before (while the software program is in stage 1) and during a measurement. If they had occurred it is likely that the operator would have addressed them by altering the CCD exposure time, altering the laser power, adjusting the Badal setting, adjusting the probing beam location, or adjusting the spatial filter as required. It is more likely that an alternative cause/s is responsible for the low signal strength. Anecdotal experience from the 2nd pilot study suggests that the persistent corruption of signal strength observed in fig. 6.5 and likewise for other ametropic subjects is related uncorrected refractive error in the probing beam. When more than approximately 2 diopters of 'best sphere' refractive error is uncorrected in the probing beam the retinal beacon deteriorates which produces dull and blurry HS spots. Similarly, poor signal strength occurs if the upper lid partially occludes the pupil in such a way that decreases the number of subapertures subtended by the wavefront without significantly disrupting the iris-edge detection. As

discussed in section 6.3 paragraph 5, the vast range of refractive error corrections required for the ingoing beam is a difficulty inherent to population studies and an issue that should be addressed in future instrument/experiment design modifications.

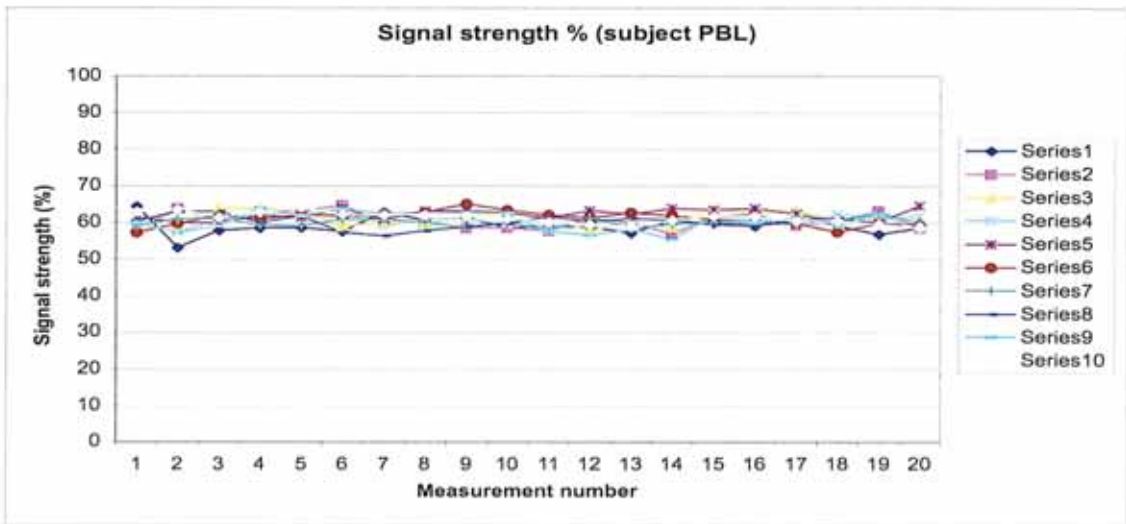


**Figure 6.5 Signal strength tracking for 2nd pilot study measurements of ametropic subject PBL.**

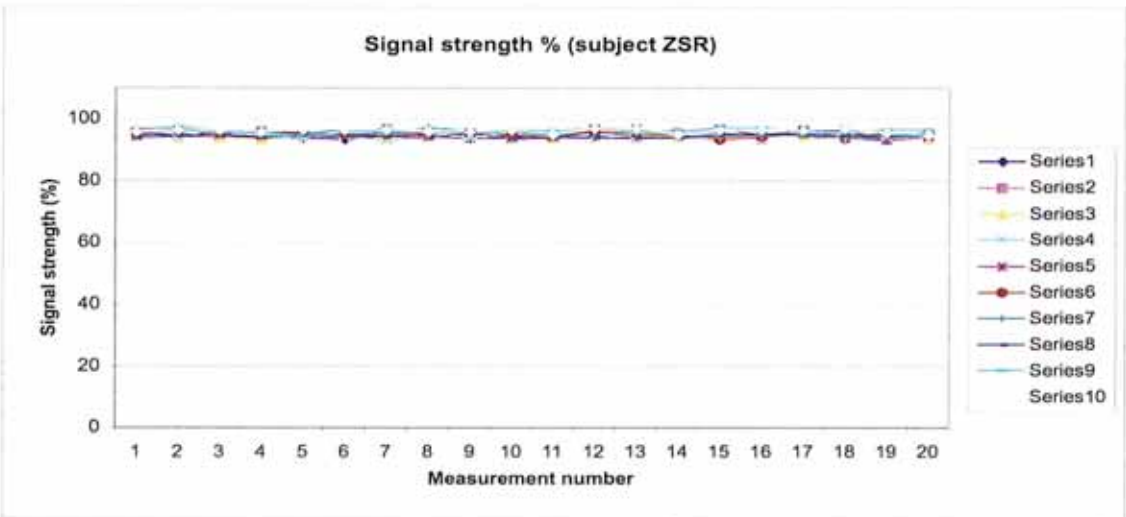


**Figure 6.6 Signal strength tracking for 2nd pilot study measurements of emmetropic subject ZSR.**

The aberration data from the 2nd pilot study is presented here although it is known to be unreliable due to the developmental and formative nature of the study. However the patterns displayed in the Zernike coefficient values were helpful in de-bugging and improving the WFS and to gauge a scale of inter-measurement variation we might expect in future experiments. As previously described, twenty HS images were captured

over approximately 2 seconds and the coefficient values were averaged to produce a single set of mean Zernike coefficients for each wavefront measurement. The subject rested momentarily before realignment and the process was then repeated a further 9 times to produce 10 series of measurements for all 5 subjects (10 eyes) participating in the 2nd pilot study. The highest standard deviation of any individual Zernike coefficient across a single series varied from 0.194 microns during the initial stages of the pilot study, to 0.048 microns during the later stages of the pilot study. The success of modifications to the software and experiment protocol during the 2nd pilot study is evident in this vast improvement in the stability of results. The maximum standard deviation value of 0.048 compares fairly to the 'time series' measurements performed by Brookes (2004) who found a typical repeatability of 0.02 microns for Zernike coefficients over a 6 mm pupil for normal eyes and without subject realignment. Mean Zernike coefficients measured over a single series are displayed in figs. 6.7, 6.8 and 6.9 for three typical eyes measured during the 2nd pilot study. The error bars represent +/- 1 standard deviation over each series of twenty images.

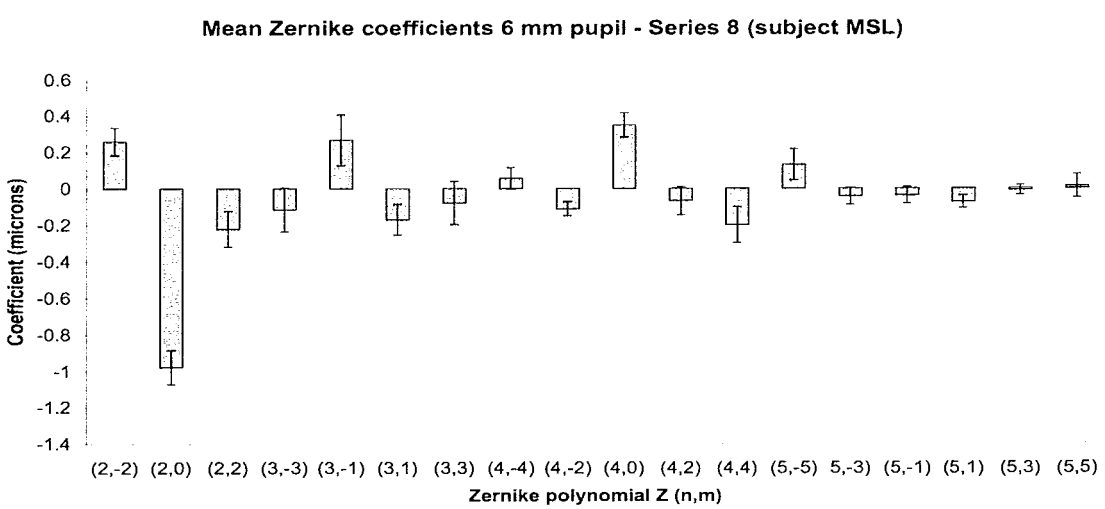


**Figure 6.7 Mean Zernike coefficient values over a 20 HS image series for a typical eye measured during the 2nd pilot study. Error bars represent +/- 1 standard deviation.**

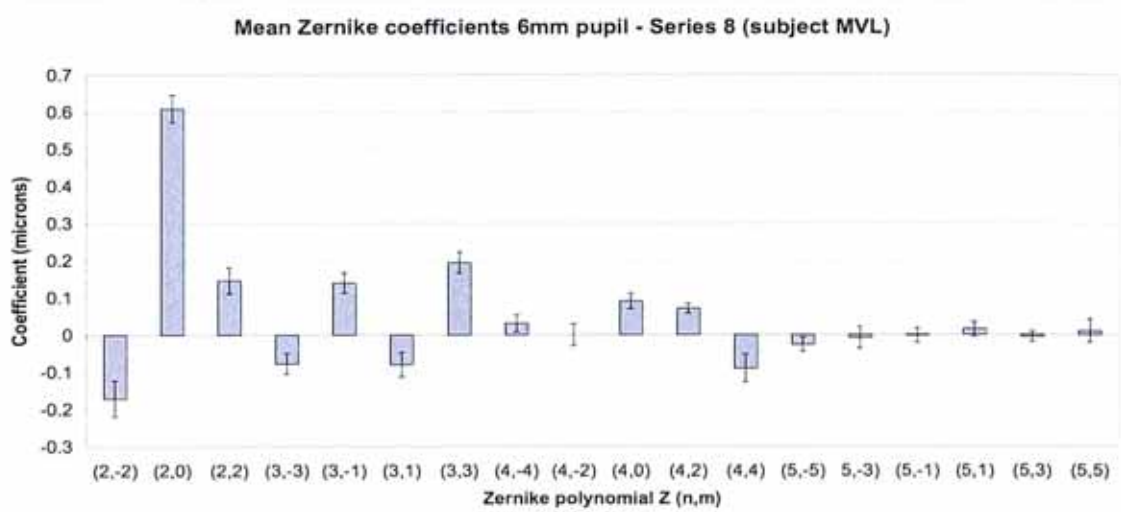


**Figure 6.8 Mean Zernike coefficient values over a 20 HS image series for a typical eye measured during the 2nd pilot study. Error bars represent +/- 1 standard deviation.**

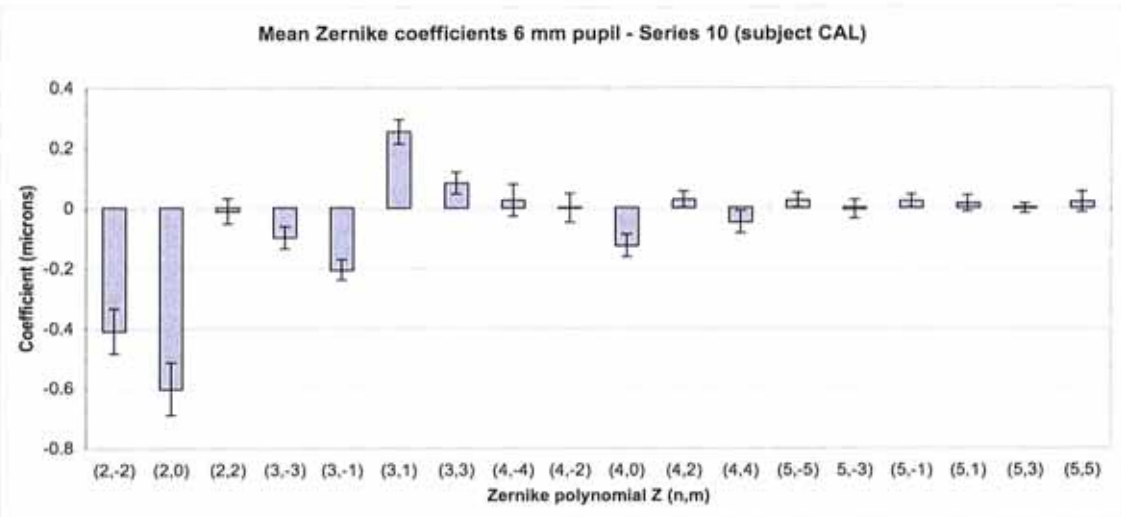


**Figure 6.9 Mean Zernike coefficient values over a 20 HS image series for a typical eye measured during the 2nd pilot study. Error bars represent +/- 1 standard deviation.**

Figs. 6.7 to 6.9 are typically representative of results collected during the 2nd pilot study. The general pattern of highly individual coefficient values along with a generalised decrease in coefficient magnitude as the aberration order increases are typical in the human eye (Thibos *et al.* 2002a). The magnitude of the standard deviation values, relative to the mean Zernike coefficient values, are acceptable and provided confidence that reasonably stable wavefront measurements were obtained. For 2nd to 4th order aberration modes the intra-subject variability observed was far less than inter-subject

variability (with each eye for each subject treated independently). This strengthens results and indicates that the main source of variability is population variation and not repeatability noise.

The standard deviation for each individual Zernike coefficient across the 10 series of measurements (with realignment procedures between each measurement series) varied from a maximum 0.699 microns during the early stages of the 2nd pilot study to a maximum of 0.054 microns during the late stages of the 2nd pilot study. This latter standard deviation value of 0.054 microns compares favourably with the repeatability of 0.05 microns to 0.08 microns reported by Brooks (2004) who also performed multiple measurements on real eyes over a 6 mm pupil with subject realignment procedures between each measurement. The standard deviation value of 0.054 microns provides a rudimentary indication of the repeatability level when subject re-alignment noise is incorporated into results. Mean Zernike coefficients measured over the 10 series (each series consisting of 20 HS images) are displayed in figs. 6.10 and 6.11 for two typical eyes (respectively) measured during the 2nd pilot study. The error bars represent +/- 1 standard deviation over the 10 measurement series. The patterns displayed support anecdotal conclusions that the subject alignment (and realignment) procedures used were suitable for our application and capable of producing a repeatability level quite similar to that achieved when wavefront measurements are recorded in rapid succession without realignment.

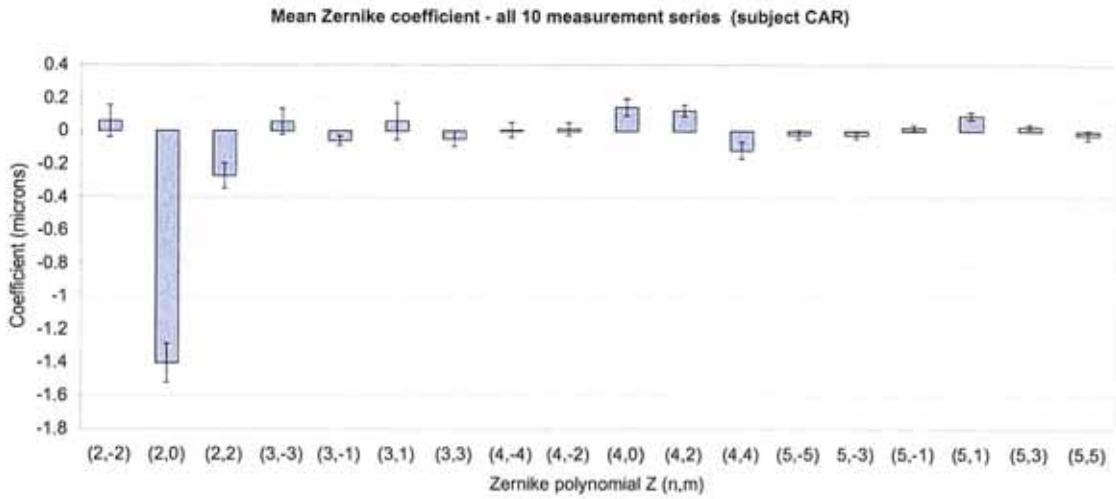


**Figure 6.10 Mean Zernike coefficient values over 10 measurement series for a typical eye during the 2nd pilot study. Error bars represent +/- 1 standard deviation.**

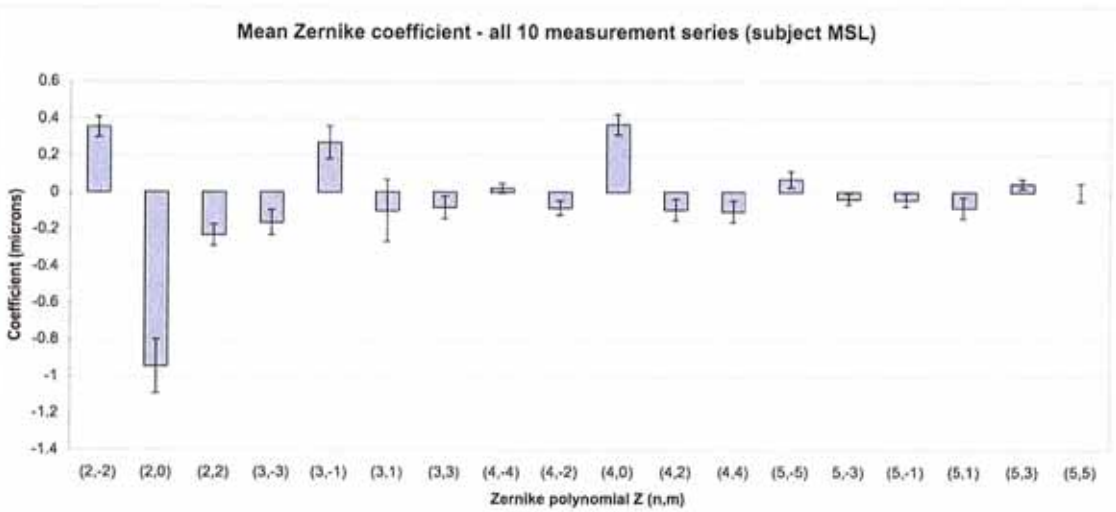


**Figure 6.11 Mean Zernike coefficient values over 10 measurement series for a typical eye during the 2nd pilot study. Error bars represent +/- 1 standard deviation.**

The most refined parameters produced by the experimental WFS are; total wavefront RMS, lower-order wavefront RMS, and higher-order wavefront RMS. Their correct and accurate determination relies on all of the preceding measurement processes. Examples of wavefront RMS values measured early during the 2nd pilot study are given in figs. 6.12 and 6.13. Fig. 6.12 shows dramatic fluctuation in the lower-order wavefront RMS and total wavefront RMS values consistent with accommodation fluctuation in the crystalline lens of the subject. Most likely this poor accommodation control was due to a combination of the low concentration (0.5%) Tropicamide used and an inadequate

amount of time allowed for the cycloplegic and mydriatic effects to manifest. Comparatively, fig. 6.13 shows fluctuation of a similar magnitude for the lower-order wavefront RMS (although the different y-axis scale may be initially deceiving), only late in the 2nd pilot study after modifications to the experimental procedure did results for wavefront RMS begin to stabilise as exemplified in fig. 6.14.

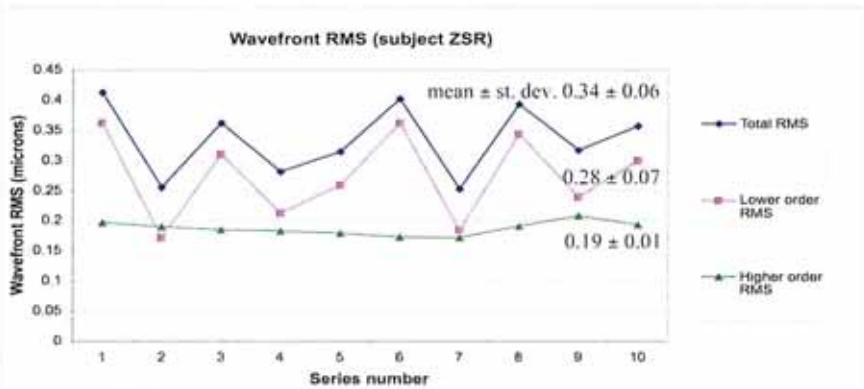


**Figure 6.12 Wavefront RMS tracking for early 2nd pilot study measurements on subject ZSR.**

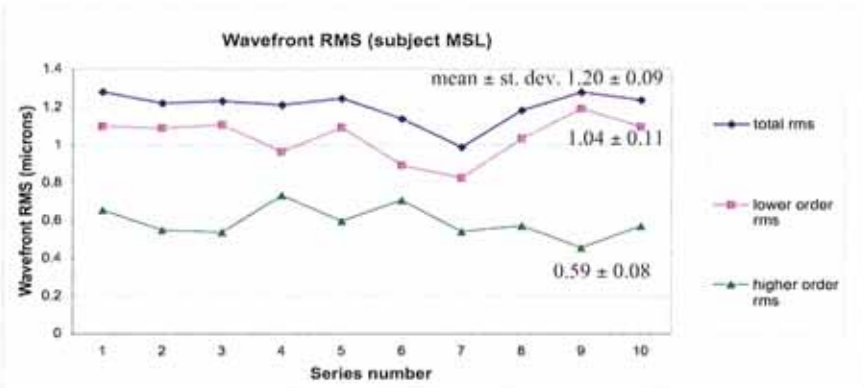


**Figure 6.13 Wavefront RMS tracking for early 2nd pilot study measurements on subject MSL.**

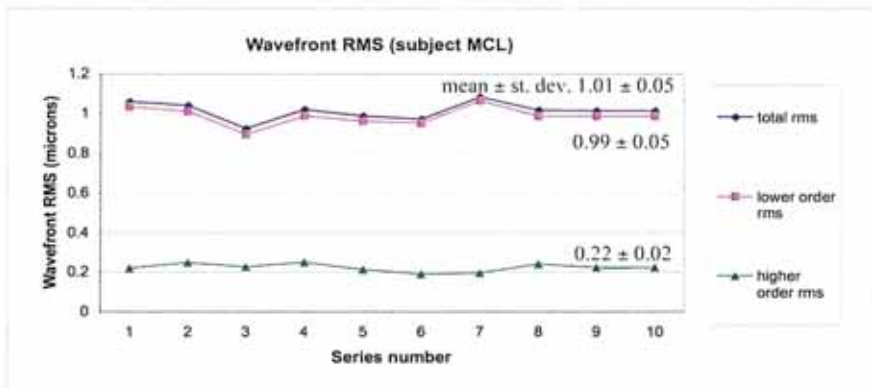


**Figure 6.14 Wavefront RMS tracking for later 2nd pilot study measurements on subject MCL.**

### 6.5 Repeatability of the experimental WFS and a commercial WFS - 3rd pilot study

An experienced observer from the subject group of the 2nd pilot study volunteered to participate in the 3rd pilot study, which investigated the short-term repeatability of the experimental WFS and the ZyWave WFS by Bausch and Lomb. Refined experiment procedures from the 2nd pilot study were followed and ten separate measurements were performed on the subject's left eye with each WFS. After each measurement the subject withdrew from the headrest and rested momentarily. All aberration results reported for the 3rd pilot study are in reference to a 6 mm pupil diameter and include the defocus $Z_2^0$ term. The highest standard deviation of any individual Zernike coefficient (2nd to 5th order) was 0.05 microns (experimental WFS) and 0.08 microns (ZyWave). The standard deviation of the total wavefront RMS (2nd to 5th order) was 0.11 microns (experimental WFS), and 0.13 microns (ZyWave). The standard deviation of the higher-order wavefront RMS (3rd to 5th order) was 0.05 microns (experimental WFS), and 0.07 microns (ZyWave). These results provide confidence in the repeatability of the experimental WFS, demonstrating results similar to those achieved by a commercial WFS.

The repeatability estimates of the 3rd pilot study have limited merit because the case study was only performed on one subject. As an adjunct to the 3rd pilot study, additional measurements were performed on a larger sample size (10 eyes) to further investigate the short-term repeatability of the ZyWave WFS. Three wavefront aberration measurements were performed on each eye using the ZyWave, with the subject momentarily withdrawing from the headrest between each measurement. The maximum intra-subject standard deviation of individual Zernike coefficients varied from 0.250 microns for the least repeatable subject, to 0.083 microns for the most repeatable

subject. This later mentioned subject was known to be an experienced observer and he agreed to participate in a medium-term repeatability study of the ZyWave. Again, the experimental procedures refined by the 2nd pilot study were followed and the subject's wavefront aberration was measured a further 12 times, over 11 days, at 4 different sittings. Three wavefront aberration measurements were performed at each sitting. The subject had a moderate myopic refractive error. The mean Zernike coefficients corresponding to a 6 mm pupil from this medium-term repeatability study are displayed in table 6.1 and fig. 6.15. Note that each measurement performed with the ZyWave is actually using a combination of the 'best' 3 HS spot images from a series of 5 HS spot images captured in succession. The criteria the ZyWave uses to select the 'best' 3 HS spot images is not available in the public domain.

The mean Zernike coefficients shown in table 6.1 and fig. 6.15 for the medium-term repeatability study are dominated by the $Z_2^0$ defocus mode. This could be expected because the subject has a moderate myopic refractive error, no ocular pathology, and no surgical history. Note the typical pattern of reducing coefficient values in the higher-orders, along with a dominance of $Z_4^0$ compared to other higher-order aberration modes. The wavefront measurements were performed over an eleven-day period and so the standard deviation values for the Zernike coefficients are expected to be greater than those reported from the short-term repeatability study. It is reasonable to assume that a biological system such as the eye is susceptible to a greater number of physiological processes capable of producing variations in wavefront aberrations over an eleven-day period compared to a period of a few minutes (Hofer *et al.* 2001). The standard deviation values reported in table 6.1 and fig. 6.15 represent true fluctuations of ocular aberrations in addition to instrumental noise.

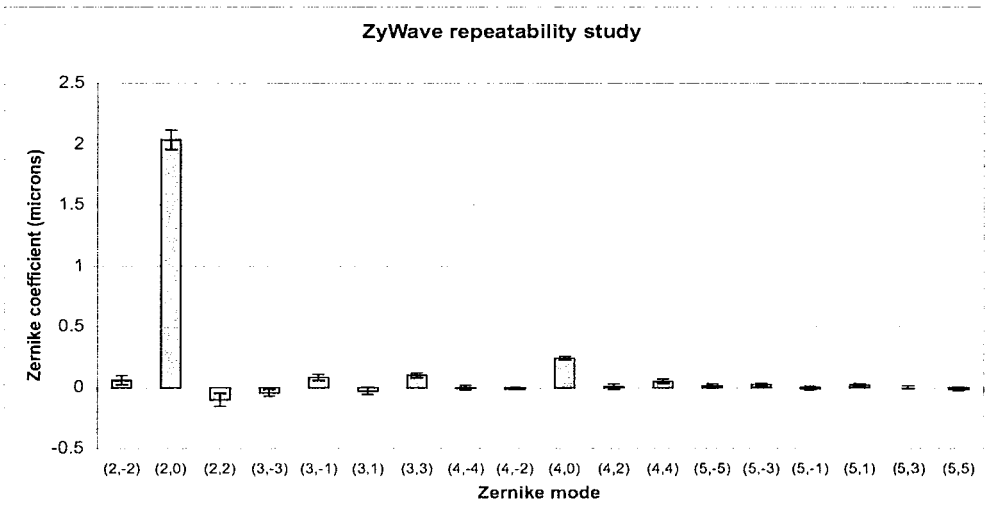


**Figure 6.15 Histogram of mean Zernike coefficients (microns) for the healthy right eye of subject ELR over a 6mm pupil. Error bars represent +/- 1 standard deviation.**

| $Z_n^m$ | Mean coefficient (microns) | Standard Deviation (microns) |
|---|---|---|
| $Z_2^{-2}$ | 0.059 | 0.037 |
| $Z_2^0$ | 2.034 | 0.080 |
| $Z_2^2$ | -0.101 | 0.054 |
| $Z_3^{-3}$ | -0.044 | 0.028 |
| $Z_3^{-1}$ | 0.083 | 0.025 |
| $Z_3^1$ | -0.028 | 0.029 |
| $Z_3^3$ | 0.099 | 0.019 |
| $Z_4^{-4}$ | -0.004 | 0.019 |
| $Z_4^{-2}$ | -0.011 | 0.008 |
| $Z_4^0$ | 0.240 | 0.016 |
| $Z_4^2$ | 0.004 | 0.023 |
| $Z_4^4$ | 0.048 | 0.019 |
| $Z_5^{-5}$ | 0.012 | 0.018 |
| $Z_5^{-3}$ | 0.022 | 0.012 |
| $Z_5^{-1}$ | -0.007 | 0.015 |
| $Z_5^1$ | 0.018 | 0.010 |
| $Z_5^3$ | 0.000 | 0.011 |
| $Z_5^5$ | -0.014 | 0.011 |

**Table 6.1 Mean Zernike coefficient values (microns) and standard deviation values for the healthy right eye of subject ELR over a 6 mm pupil.**

The individual Zernike coefficients from the medium-term repeatability study are shown in more detail in fig. 6.16 (2nd order), fig. 6.17 (3rd order), and fig. 6.18 (4th order). The coefficients for the 3rd and 4th order aberrations appear relatively stable over the eleven days, in absolute terms they are more repeatable than those of the 2nd order aberrations. However, the 3rd and 4th orders represent much smaller aberrations and so although the fluctuations in the coefficient values are typically less than 0.03 microns, the values of the coefficients themselves approach a similar magnitude. Results for the 5th order aberrations are not displayed graphically, although they continue this same trend observed from fig. 6.17 and 6.18. The Zernike coefficient values in figs. 6.16 to 6.18 show no distinctive pattern of fluctuation with respect to time or with respect to each other. The coefficient for $Z_4^0$ in fig. 6.18 is notably larger than fellow 4th order modes although generally it appears no more stable or unstable than fellow 4th order modes.

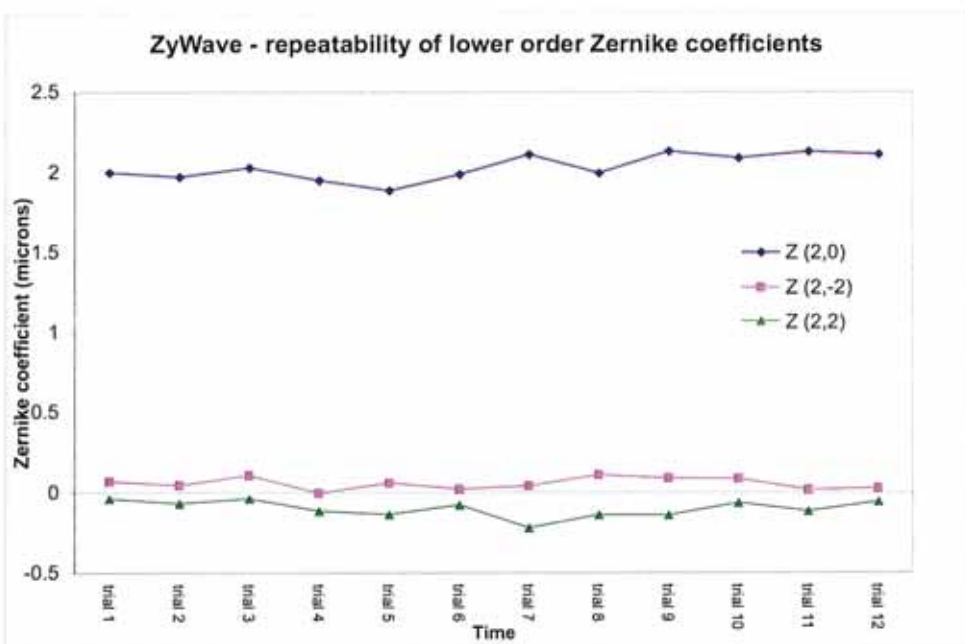


**Figure 6.16 Fluctuation of 2nd order aberrations for a normal healthy eye.**

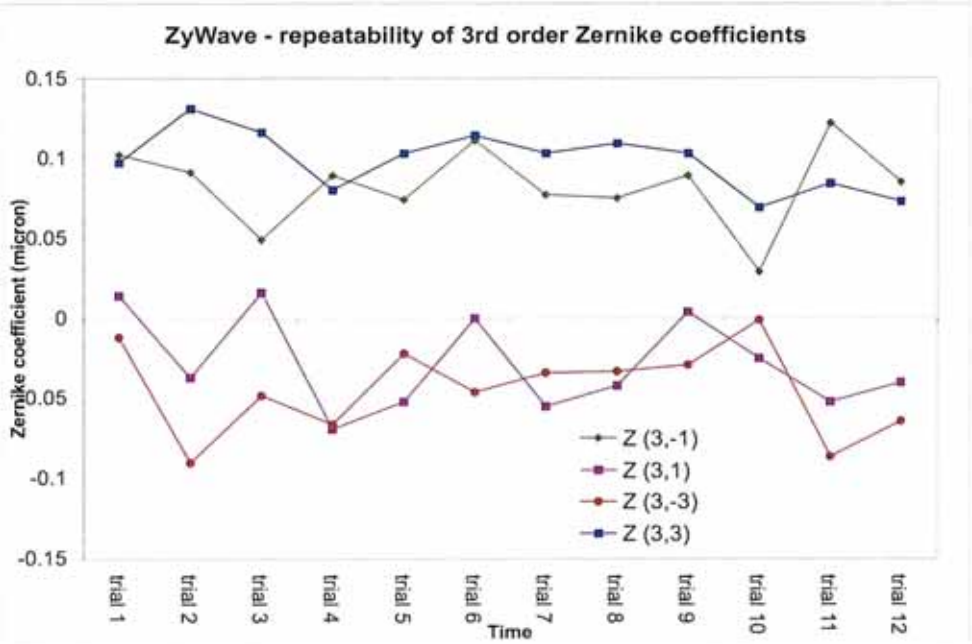


**Figure 6.17 Fluctuation of 3rd order aberrations for a normal healthy eye.**

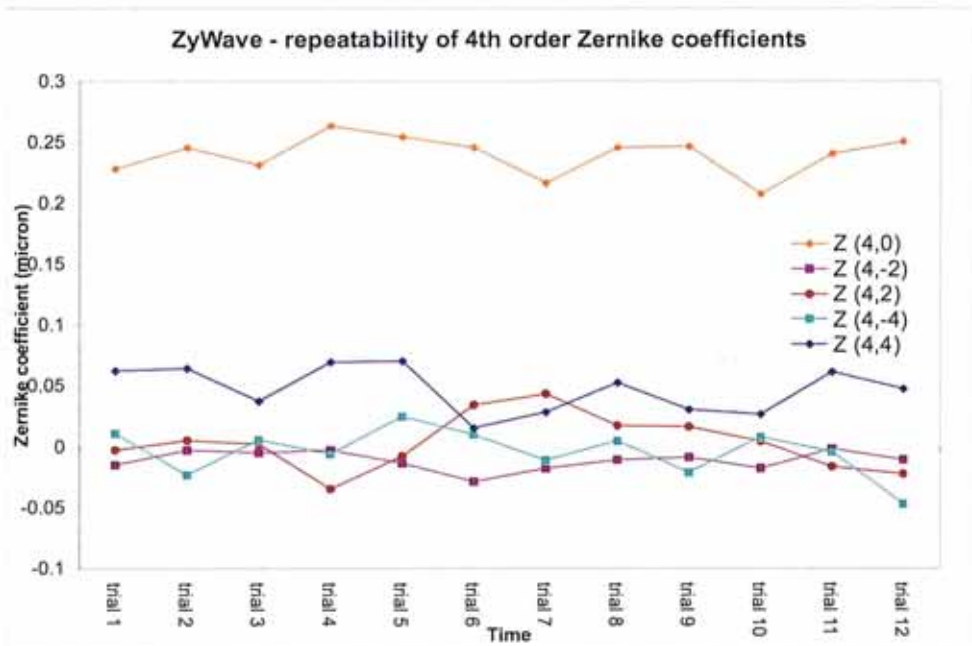


**Figure 6.18 Fluctuation of 4th order aberrations for a normal healthy eye.**

For subject ELR, table 6.1 shows that after term $Z_4^0$, typically the Zernike coefficient values for higher-order aberrations approach magnitudes between –0.1 microns and +0.1 microns. These compare similarly to the magnitude of standard deviation for the $Z_2^0$ defocus term (0.08 microns). The fluctuation of coefficients in table 6.1 and fig. 6.15 illustrate an underlying limitation that may become relevant to refractive surgery as customised wavefront ablation outcomes improve. Eventually if customised refractive

surgery is able to correct lower-order aberrations without exacerbating the higher-order aberrations beyond pre-operative values, the natural fluctuation of aberrations (principally due to the accommodation system) over many different time-scales will form a limit to the practical value of correcting higher-order modes in a typical pre-presbyopic eye.

During the medium-term repeatability study the wavefront aberration measurements were not performed at the same time of day for each sitting. Therefore, the Zernike coefficient values may indicate greater variation than if they had been measured at a consistent time for each sitting. It would be reasonable to expect that higher-order aberrations might exhibit a diurnal pattern. Numerous ocular parameters are known to fluctuate diurnally in the human eye (Stone *et al.* 2004), and aberrational changes occur on the scale of seconds, days, weeks and months in humans (Cheng *et al.* 2004, Hofer *et al.* 2001).

Like the short-term repeatability study, these medium-term repeatability results come from a case study on a single subject and so any conclusions drawn have limited merit. A different subject may demonstrate either reduced or greater repeatability. The drug used to dilate the pupil (Tropicamide 1%) does not provide a complete cycloplegic effect. As such, the accommodation reflex would have some influence on results, and not solely the 2$^{nd}$ order $Z_2^0$ defocus term. Higher-order aberrations of a cyclopleged eye are known to be different to those of a natural eye (Cheng *et al.* 2004). Plainis and colleagues (2005) confirmed the results of previous studies that spherical aberration $Z_4^0$ tends to shift to negative values with accommodation.

### 6.6 Outcomes from the pilot studies

The pilot studies verify the success of the experimental WFS in combining research-type features with a clinically-friendly instrument. The studies helped establish the operational limits of the experimental WFS. Experience gained from this first clinical test on real eyes provided insight into where the potential research strengths of the instrument lay and what minor modifications might best be adopted to correct minor design/operational oversights. The pilot studies highlighted the major restriction in aberration studies performed with the experimental WFS to date - until the Badal optometer is characterised the $Z_2^0$ defocus term is not comparable to any other published results.

Important aspects of the WFS design and the experimental procedure were altered as a result of the experience gained throughout the pilot studies. For example, up until that time the LED brightness required in both the alignment channel and the fixation channel had only been estimated by the optical design. The pilot studies confirmed that the illumination power selected was satisfactory. The probing laser brightness and the CCD exposure time requirements were also refined throughout the 2$^{nd}$ pilot study. The pilot studies also lead to an increase in reticule detail on the fixation target to improve subject alignment.

# CHAPTER SEVEN

## Comparison to a commercial wavefront sensor

This chapter describes an experiment conducted at the National University of Ireland, Galway, to examine agreement between the experimental WFS and the ZyWave WFS by Bausch and Lomb when measuring wavefront aberrations in normal human eyes. The general profile and magnitude of the phase maps produced by the two instruments are in good agreement. The similar values for Zernike coefficients also provide confidence in the performance of the experimental WFS. Although this comparison is not a robust calibration, it does provide an estimate of the relative accuracy of the experimental WFS.

### 7.1 Experiment procedure

This experiment was conducted according to procedures developed in section 6.3, and with the approval of the Dublin Institute of Technology Ethics Committee. Twelve volunteers (seven males and five females) were recruited and screened according to subject selection criteria developed in section 6.3. The subjects were instructed on the requirements of the experiment and risks involved. Some subjects elected to wear an occluder over the non-test eye during measurements. Measurements were performed on both eyes for nine subjects and only one eye for three of the subjects, giving a total of twenty-one eyes examined. The age of the subjects ranged from 20 years to 57 years, and the refractive errors ranged from +3.00 to -5.75 DS and from -0.25 DC to -1.75 DC. None of the subjects wore spectacle lenses or contact lenses during the experiment.

One drop of 1% Tropicamide was administered to each eye being measured and adequate time was allowed to achieve mydriasis (pupil dilation) and cycloplegia (loss of

accommodation). The laser power of our experimental WFS was 1.2 microwatts at the eye and the CCD exposure time was 45 milliseconds. The Badal optometer was positioned at the 'best sphere' value of the subject's refractive error to remove defocus from the sensing channel. Subjects were aligned with the WFS and positioned against the chin-rest and forehead-rest. Subjects were then asked to fixate the laser in the central area of the fixation target, thereby aligning the subject's line of sight to the measurement axis of the WFS. The examiner viewed the alignment channel image and made fine adjustments to the subject alignment. The subject was asked to blink and then immediately following the blink, HS spot images were captured. For each measurement, twenty images were captured over a typical duration of 2.5 seconds. All measurements were taken in a dark room. The examiner manually reviewed the image quality, pupil edge detection, and alignment of the subject. If the spot quality or subject alignment was poor, the results were not used and the measurement was repeated. A computer processed each image to determine the edge of the iris and the centroids of the HS spots. The local slope data was then used to fit the wavefront with Zernike polynomials up to the $5^{th}$ order by a least squares method over a 6 mm pupil by restricting the analysis of HS spots to a 3 mm radius from the determined pupil centre. The Zernike coefficients for each mode were then averaged to produce a single set of coefficients. All results from this experiment are reported for a 6 mm pupil diameter, according to accepted standards (Thibos *et al.* 2000), and with the defocus $Z_2^0$ term removed[8].

Immediately following measurements with the experimental WFS, subjects were aligned and measured with the ZyWave. For each measurement, the ZyWave captures five HS images and selects the 'best' three from which it generates a set of Zernike

[8] It was necessary to exclude the defocus term from analysis as the Badal optometer had not been characterised.

coefficients up to 5th order. For each subject, three successive measurements were performed with the ZyWave and then the Zernike coefficients for 6 mm pupil diameters were exported and converted to a standard format (Thibos *et al.* 2000). The Zernike coefficients for each mode were averaged to produce a single set of coefficients and the defocus $Z_2^0$ term was removed before comparing to results from the experimental WFS.

### 7.2 Results

From results for the entire group of 21 eyes, phase maps of eight typical eyes (2nd to 5th order) are shown in fig. 7.1. The general shape and magnitude of the phase maps produced by the two WFSs are in reasonable agreement and provide confidence that the experimental WFS measurements are comparable to those produced by a commercial WFS.

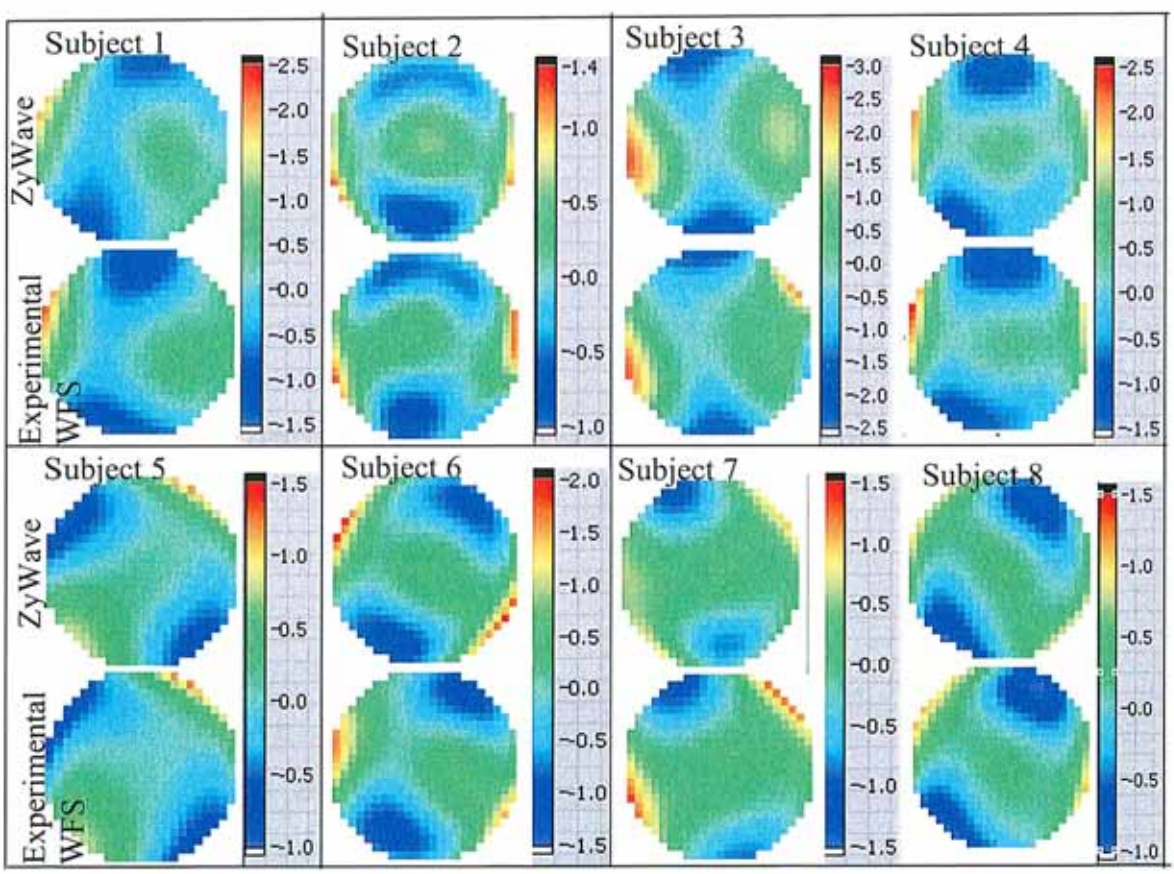


**Figure 7.1. Phase maps as measured by the ZyWave and the experimental WFS for eight eyes over a 6 mm pupil diameter. Defocus $Z_2^0$ has been removed from the analysis. The colour scales represent wavefront phase (microns) and are consistent within each pair of results.**

The Zernike coefficients measured by the ZyWave were subtracted from those measured by the experimental WFS to produce *residual Zernike coefficients* and *residual phase maps*. The random patterns and low amplitudes observed in the residual phase maps for the 21 eyes support the assertion that negligible systematic error or bias exists in results from the experimental WFS when compared to the ZyWave. Notwithstanding, the Zernike coefficients for some specific modes produced by the experimental WFS should be interpreted with discretion, as discussed shortly. Fig. 7.2 shows the residual phase maps of two typical eyes. The wavefront RMS values for subject 4 are 0.62 microns (ZyWave), compared to 0.70 microns (experimental WFS), and the residual RMS is 0.17 microns. If analysis is restricted to the higher-order modes ($3^{rd}$ to $5^{th}$ order) for subject 4, the wavefront RMS values are 0.35 microns (ZyWave), compared to 0.30 microns (experimental WFS), and the residual RMS is 0.11 microns. The wavefront RMS values for subject 8 are 0.43 microns (ZyWave), compared to 0.45 microns (experimental WFS), and the residual RMS is 0.14 microns. If analysis is restricted to the higher-order modes ($3^{rd}$ to $5^{th}$ order) for subject 8, the wavefront RMS values are 0.21 microns (ZyWave), compared to 0.21 microns (experimental WFS), and the residual RMS is 0.13 microns.

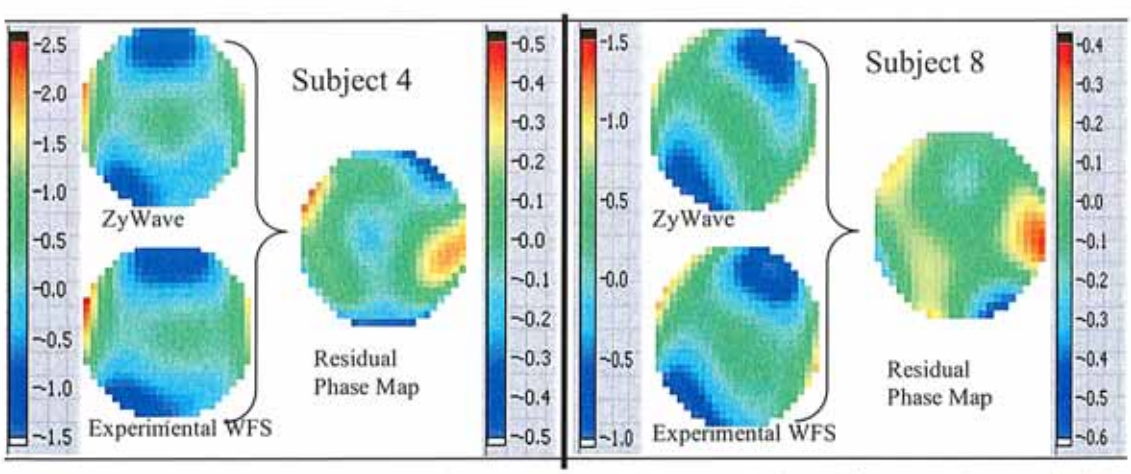


**Figure 7.2. Phase maps for subjects 4 and 8 over a 6 mm pupil diameter (defocus $Z_2^0$ removed from analysis) as measured by the ZyWave and the experimental WFS. The Zernike coefficients are subtracted from each other and the residual coefficients are used to reconstruct the residual phase map. The colour scales represent wavefront phase (microns) and are consistent for each pair of phase maps but reduced for the residual phase maps to allow detail to be discernable.**

For the entire group of 21 eyes, the residual wavefront RMS ($2^{nd}$ to $5^{th}$ order) was calculated for each individual eye and then group results were averaged, producing a mean residual RMS of 0.28 microns. If analysis is restricted to higher-order aberrations ($3^{rd}$ to $5^{th}$ order), the mean residual RMS is 0.22 microns. This residual higher-order RMS value may indicate differences in measurements between the two WFSs. However, when interpreting these results it is important to note that the measurements were performed on real eyes and therefore suffer a host of complicating factors, such as temporal fluctuations in aberrations, that are absent in validation studies presented by other authors using phase plates or calibrated lenses (Cheng *et al.* 2003).

If the higher-order ($3^{rd}$ to $5^{th}$ order) RMS values of the experimental WFS are compared to the ZyWave for individual eyes, the wavefront RMS is within ± 0.1 micron for over 80% of eyes examined in this experiment. This achieves agreement equal to the highest level observed by Liang *et al.* (2005) in their study comparing three commercial aberrometers (WaveScan, LADARWave and ZyWave), on 34 cyclopleged eyes. Liang *et al.* (2005) compared coma RMS, $Z_4^0$ spherical aberration, $3^{rd}$ order RMS and $4^{th}$ order RMS against results from all three WFSs. In these twelve comparisons, paired t-tests revealed p values of less than 0.01 in 9 out of twelve comparisons. However, only 38% of the absolute difference of higher-order aberrations RMS between the three instruments was within +/- 0.1 micron. In other comparison-validation studies, various levels of agreement have been reported. Moreno-Barriuso *et al.* (2001) reported an average standard deviation of Zernike coefficients within a given method was 0.07 microns for measurements on normal eyes. Whereas the average global standard deviation across techniques was 0.09 microns. Unfortunately, this study involved only three subjects and measurements were performed two years apart. It could be argued

that normal physiological aberration fluctuations were not well controlled over this relatively lengthy time. Salmon *et al.* (1998) comparing the HS method for measuring ocular aberrations with the SRR technique found between 0.1 and 0.3 microns RMS difference between the two techniques over a 5.6 mm pupil.

The mean residual Zernike coefficients of the 21 eyes are shown in Table 7.1 for a 6 mm pupil diameter. The mean residual coefficients for modes $Z_3^1$, $Z_4^0$, and $Z_4^4$, show a greater variation between the two instruments compared to their fellow modes (in each particular order) and may indicate a calibration difference in one or both of the WFSs. Measurements of these aberration modes from the experimental WFS should be interpreted with some discretion until a comprehensive calibration study is performed.

| $Z_n^m$ | $Z_2^{-2}$ | $Z_2^2$ | $Z_3^{-3}$ | $Z_3^{-1}$ | $Z_3^1$ | $Z_3^3$ | $Z_4^{-4}$ | $Z_4^{-2}$ | $Z_4^0$ |
|---|---|---|---|---|---|---|---|---|---|
| Mean residual coefficient (microns) | -0.04 | -0.08 | 0.01 | -0.04 | 0.10 | 0.00 | 0.00 | -0.02 | -0.09 |
| $Z_n^m$ | $Z_4^2$ | $Z_4^4$ | $Z_5^{-5}$ | $Z_5^{-3}$ | $Z_5^{-1}$ | $Z_5^1$ | $Z_5^3$ | $Z_5^5$ | |
| Mean residual coefficient (microns) | 0.00 | 0.03 | -0.01 | 0.01 | 0.01 | -0.01 | 0.00 | 0.00 | |

**Table 7.1. Mean residual Zernike coefficients of 21 eyes for a 6mm pupil diameter (defocus $Z_2^0$ removed).**

Differences between the measurements of each WFS can be attributed to various potential causes. Small subject-dependent variations of ocular aberrations are expected to occur between measurements obtained with the two WFSs due to temporal fluctuations in ocular aberrations. The fixation target used by the ZyWave (scene of Mt Fuji) could potentially cause variability in subject alignment during measurements and it is also possible that subjects didn't actually fixate on the optical axis of the ZyWave (anonymous reviewer 2007). These limitations coincide with the potential errors mentioned in section 6.1. Note that the ZyWave uses a laser source with wavelength 785 nm while the experimental WFS uses a 677 nm laser source. The variation of

wavefront aberrations with wavelength should not give any noticeable offset (except for defocus term) in view of the small wavelength difference (108 nm) and nearly stationary nature of high order aberrations in the near infrared region (Fernández *et al.* 2005, Llorente *et al.* 2003).

### 7.3 Discussion of the calibration task

Calibration and verification of an ocular WFS is a challenging task. Vision scientists have not developed an agreed, standard calibration technique, although Neal *et al.* (2002) have proposed a standardised methodology for measuring the precision and accuracy of a HS WFS. The lack of a gold-standard is pointed out by Salmon *et al.* (1998 p.2464)

> "lacking an absolute method for assessing the accuracy of measurements made by the Shack-Hartmann apparatus when it is used in human eyes……".

The task of calibration may encompass various metrics such as accuracy, repeatability, linearity and dynamic range. Ideally, the calibration procedure should avoid altering the optical configuration of the WFS when swapping from 'measurement mode' to 'calibration mode'. Measuring the wavefront aberration with and without whatever element (~ gold standard) is selected to generate a known wavefront aberration positioned in the pupil plane is a commonly used method. Any calibration technique must address the issue of confidence that can be put in the accuracy of the instrument or element being used as a gold-standard. For example, a calibration technique based on comparing the responses of a WFS and an interferometer (Campbell *et al.* 1999) is only accurate to the level of the interferometer.

Some scientists (Thibos *et al.* 2000) have proposed the production of standardised phase plates of known aberration statistics, which could then be distributed to research institutions for the purpose of acting as a gold-standard when calibrating WFSs. The wavefront aberration of the standardised phase plate could be determined by interferometry. At present, to the author's best knowledge, such plates are not available. Such plates are capable of producing high frequency aberration statistics representing atmospheric-like turbulence (Rhoadarmer and Angel 2001) but this is quite different to the task of representing ocular aberrations which are typically dominated by the lower orders.

A less expensive alternative to phase plates is a simple optical lens such as a positive powered doublet. Its profile could be measured with a stylus (contact) technology. With the known refractive index, surface profile and lens thickness, the aberrations generated by a proximal on-axis source could be calculated with some confidence (especially the lower-order aberrations). Alternatively the aberration profile of the doublet lens could be characterized by interferometry techniques. Zhou *et al.* (2004) configured a HS aberrometer to provide corneal topography and reflective corneal aberration measurements. They validated their WFS by comparing their results to theoretical values of calibrated aspheric surfaces. A similar validation technique using ray-tracing and model eyes is presented by Cheng *et al.* (2003). Laterally shifting the lens would also generate significant amounts of known $3^{rd}$ and $4^{th}$ order aberrations. This technique has been successful (Cox 2006) and is appealing because of the low cost of a simple doublet lens. The calibration lens could also form part of a simple artificial eye when combined with a micrometer stage and a black scattering screen to act as an artificial retina. By moving the screen along the optical axis, differing wavefront profiles would

be expected as determined from the interferometry or stylus profiling data. Alternatively, the doublet to screen distance may be fixed and the entire artificial eye translated along the optical axis. In this way, the experimental WFS is verified by examining the Zernike coefficients at various planes of propagation to ensure that the wavefront measurements are changing as expected.

Brooks (2004) describes the use of a spatial light modulator (SLM) to calibrate a HS WFS. One key advantage of using a SLM to calibrate an ocular WFS is that the SLM can rapidly change the aberration profile in the wavefront and test an instrument not only for spatial resolution and accuracy in sensing, but also it's temporal resolution and accuracy. This is an important advantage compared to static calibration procedures because ocular aberrations are known to fluctuate rapidly (Nirmaier *et al.* 2003). Calibrating the dynamic response of a WFS is especially advantageous if the WFS is operating in a closed-loop AO system. This issue is even more important in astronomy applications were the temporal constraints are typically more demanding. The SLM-calibration procedure described by Brooks (2004) allows each aberration mode to be examined either in isolation or in combination. With this technique it is not necessary to assume that higher-order modes are behaving well just because the lower-order modes are well calibrated. Another benefit of this technique is its 'completeness' in that it tests both the physical instrument and its software.

Assuming that one of the techniques described above has provided a suitable gold-standard - the next task in the calibration process is to decide on the appropriate data analysis. If the experimental Zernike coefficient data was simply plotted against the gold-standard Zernike coefficients and a linear regression analysis applied, the

correlation between the two techniques could be obtained. This type of analysis would reveal scaling errors between the experimental WFS and the gold-standard by departure from unity of the gradient of the fitted regression. The y-intercept would indicate any constant error in measurement between the experimental WFS and the gold-standard. When two methods of measurement are compared it is almost always wrong to present a scatter plot with correlation as a measure of agreement between the paired data. High correlation does not necessarily imply high agreement (Bland *et al.* 1986). Indeed large shifts in measurement scales (as expected in the eye when both lower-order and higher-order aberrations are measured) may leave the correlation coefficient unaltered. A better measure of agreement can be provided by plotting the difference against the mean for each pair of measurements. It would also be beneficial to display the overall mean difference bounded by the limits of agreement.

A statistical approach to examining the accuracy of a WFS against a gold standard measurement involves comparing each pair of Zernike coefficients using a paired comparison hypothesis test. The null hypothesis is that the experimental Zernike coefficient does equal that measured by the gold standard. The alternate hypothesis is that the experimental Zernike coefficient does not equal the Zernike coefficient of the gold standard. Assuming the experimental WFS is being tested against a gold standard using real eyes, each subject should be measured on both WFSs in a randomised order, at the same sitting, and the wavefronts should be fitted to an equal Zernike polynomial order such that the number of data points in each data set are equal. Cross-over techniques could also be used to block out and control the effects of temporal fluctuations in the ocular aberrations. If the aberration coefficients follow a normal distribution, a parametric test should be used in a statical comparison (such as a paired

t-test). The paired t-test seems a suitable choice as the data lends itself to be organised in pairs with a definite relationship. The paired-t test can be used to compare samples that are subjected to different conditions, provided the samples in each pair are identical otherwise. In this case, each different eye gives a different pair of data points. Each Zernike mode then has a t statistic and p-value. For this test to be valid the differences only need to be approximately normally distributed. Therefore it is not advisable to use a paired t-test in situations where there are extreme outliers.

### 7.5 Conclusions

This experiment provides confidence that the experimental WFS produces results comparable to those measured with a commercial WFS on normal eyes. It does not provide a robust calibration, although the opportunity was taken to discuss some of the issues that require consideration when planning a calibration experiment. Future experiments involving the experimental WFS should include a comprehensive characterisation of the Badal optometer. A simple characterisation procedure using trial lenses similar to that described by Webb *et al.* (2003) regarding the SRR would provide sufficient detail for the lower-order aberrations involved. More precise techniques (as discussed in section 7.3) would be required to calibrate the WFS response (repeatability and accuracy) in measuring higher-order aberrations.

# CHAPTER EIGHT

## A population study of the variation in monochromatic aberrations of the normal human eye over the central visual field

In this chapter, monochromatic aberrations of 60 normal eyes measured over the central field with the experimental WFS are presented. Aberration measurements were made on-axis and at 5 degree field angles in the nasal, inferior, temporal and superior semi-meridians. Particular attention is given to aberration distributions and possible strategies for aberration correction are discussed. It is hoped that this data will aid in the development of wide-field model eyes (Goncharov and Dainty 2007) and designs for multi-conjugate ocular adaptive optics systems to achieve wide-field high-resolution retinal imaging (Carroll *et al.* 2005). This experiment was conducted at the optometry clinic, Dublin Institute of Technology and at the applied optics laboratory, National University of Ireland, Galway.

### 8.1 Experiment rationale

Vision scientists consider it an important fundamental and clinical endeavor to accurately describe the higher-order monochromatic aberrations of the human eye. Ultimately having more experimental data one could better understand the origin of ocular aberrations and their significance to image formation on the retina. Due to the relatively recent development of HS WFSs for the human eye (Liang *et al.* 1994), there have been only a few population studies of normal eyes using this technology. A study by Thibos and colleagues (2002) is one of the largest in the literature, detailing the statistical variation of higher-order aberrations over a 6 mm pupil for 200 eyes. An earlier population study by Porter *et al.* (2001) describes the aberration structure of 218 normal human eyes for 5.7 mm pupils. More recently, Cheng *et al.* (2004) reported

aberration measurements for 74 eyes over a 5 mm pupil as part of their study of ocular aberrations and accommodation.

Regarding off-axis aberrations, work by Guirao and Artal (1999) has concentrated on off-axis refraction (describing lower-order aberrations) and the off-axis modulation transfer function. Currently there are few studies of off-axis ocular aberrations measured using HS technology. Lundström and colleagues (2005) presented results for off-axis aberration measurements at 20 degrees and 30 degrees eccentricities of the horizontal nasal visual field of 50 eyes using HS technology and other refraction techniques. However, most reports in this field are case studies performed with only a few subjects. A study by Navarro *et al.* (1998) showed off-axis optical quality of the eye for four subjects over 6.7 mm pupils. Atchison and Scott (2002), and Atchison *et al.* (2003 and 2004) presented results for off-axis aberration study in five eyes for 6 mm pupils. To enlarge the data available in this area it was decided to conduct an experiment examining the higher-order monochromatic aberrations in a population of normal healthy eyes over the central 10 degree field.

### 8.2 Experiment procedure

This experiment was conducted according to the procedures developed in section 6.3, and with the approval of the Ethics Committee of Dublin Institute of Technology. Thirty-two volunteers (14 males and 18 females) were recruited and screened according to subject selection criteria developed in section 6.3. The volunteers were instructed on the requirements of the experiment and risks involved. Measurements were performed on both eyes of twenty-eight subjects and only one eye for four subjects, giving a total of sixty eyes examined. The age of the subjects ranged from 12 years to 57 years (mean

25.7 years). The refractive errors of subjects ranged from +4.25 DS to -4.00 DS (mean -2.07 DS), and from -0.25 DC to -2.75 DC (mean -0.73 DC). Some subjects elected to wear an occluder over the non-test eye during measurements. None of the subjects wore spectacle lenses or contact lenses during the experiment.

One drop of 1% Tropicamide was administered to each eye being measured and adequate time was allowed to achieve mydriasis (pupil dilation) and cycloplegia (loss of accommodation). The laser power was set to 1.2 microwatts at the eye and the CCD exposure time was 45 milliseconds. The Badal optometer was positioned at the 'best sphere' value of the subject's refractive error to remove defocus from the sensing channel. Each subject was aligned with the WFS and positioned against the chin-rest and forehead-rest. The subject was asked to fixate the laser in the central area of the fixation target, thereby aligning the subject's line of sight to the measurement axis of the WFS. The examiner viewed the alignment channel image and made fine adjustments to the subject alignment. The subject was asked to blink and then immediately following the blink, HS spot images were captured. For each measurement, twenty images were captured over a typical duration of 2.5 seconds. All measurements were taken in a dark room. The examiner manually reviewed the image quality, iris-edge detection, and the subject alignment. If the spot quality, iris-edge detection, or subject alignment was poor, the results were not used and the measurement was repeated. A computer processed each image to determine the edge of the iris and the centroids of the HS spots. The local slope data was then used to fit the wavefront with Zernike polynomials up to the $5^{th}$ order by a least squares method over a 6 mm pupil by restricting the analysis of HS spots to a 3 mm radius from the determined pupil centre. The Zernike coefficients for each mode were then averaged to produce a single set of

mean coefficients which were used in all subsequent analysis. All results from this experiment are reported for a 6 mm pupil diameter, according to accepted standards (Thibos *et al.* 2000), and with defocus $Z_2^0$ removed.

On-axis aberration measurements were performed on all sixty eyes, and off-axis aberration measurements were also performed on thirty-one eyes. For off-axis measurements, subjects were asked to fixate a marker in the fixation target corresponding to a 5 degree field angle. The WFS was then realigned to the new pupil centre position. Twenty images were recorded over a typical duration of 2.5 seconds for each of the four field angles investigated; 5 degrees nasal field, 5 degrees superior field, 5 degrees temporal field, and 5 degrees inferior field.

### 8.3 Data analysis

Because we are primarily interested in higher-order aberrations, Zernike coefficients describing the first order aberrations of tip $Z_1^{-1}$ and tilt $Z_1^1$, and the second order defocus mode $Z_2^0$, were removed from the reconstructed wavefronts before commencing data analysis. For the majority of subjects, aberrations of fellow eyes were measured and bilateral symmetry as demonstrated in other studies (Thibos *et al.* 2002a) and (Porter *et al.* 2001) needs to be addressed. For certain modes bilateral symmetry of ocular aberrations results in a strong correlation between the fitted Zernike coefficients of fellow eyes. To compensate for this effect, prior to pooling Zernike coefficients for the group, all modes with an odd symmetry about the vertical axis for the left eye were converted to an equivalent set of coefficients for the right eye by a linear transform as described by Thibos *et al.* (2000).

Due to the relatively small angle (5 degrees) used for off-axis wavefront measurements, perspective elongation of the pupil shape (which becomes elliptical when observing at oblique angles) is considered negligible and no transform was applied to our data. Simulations indicated this source of error was insignificant compared to other noise sources in the iris-edge detection process. For larger angles that require a perspective elongation correction, a transform method of Zernike coefficients for elliptical pupils should be applied (Lundström and Unsbo 2007).

## 8.4 Results for on-axis wavefront measurements

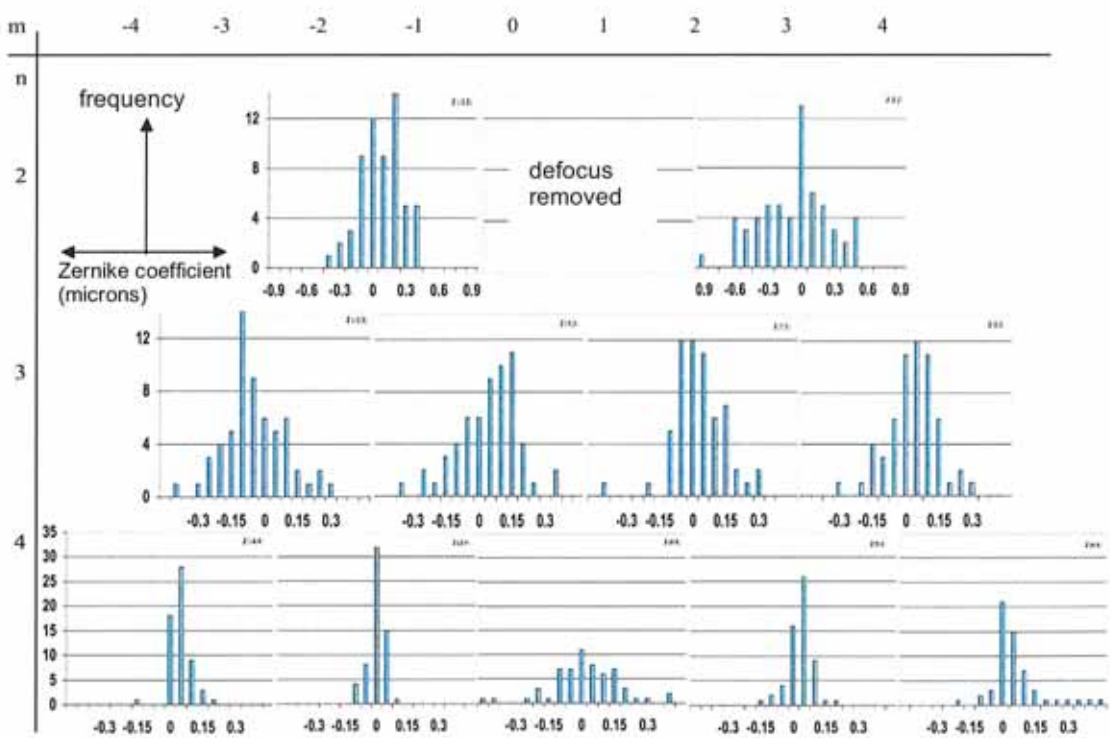


**Figure. 8.1 The distribution of the Zernike coefficients for on-axis measurements. Note that scales are only consistent within a particular aberration order. The scales on the x- and y- axes respectively are: (-1 to +1 microns, and 0 to 14) for 2nd order, (-0.5 to +0.5 microns, and 0 to 14) for 3rd order, and (-0.5 to +0.5 microns, and 0 to 35) for 4th order. The x-axis value refers to the middle value of that particular bin.**

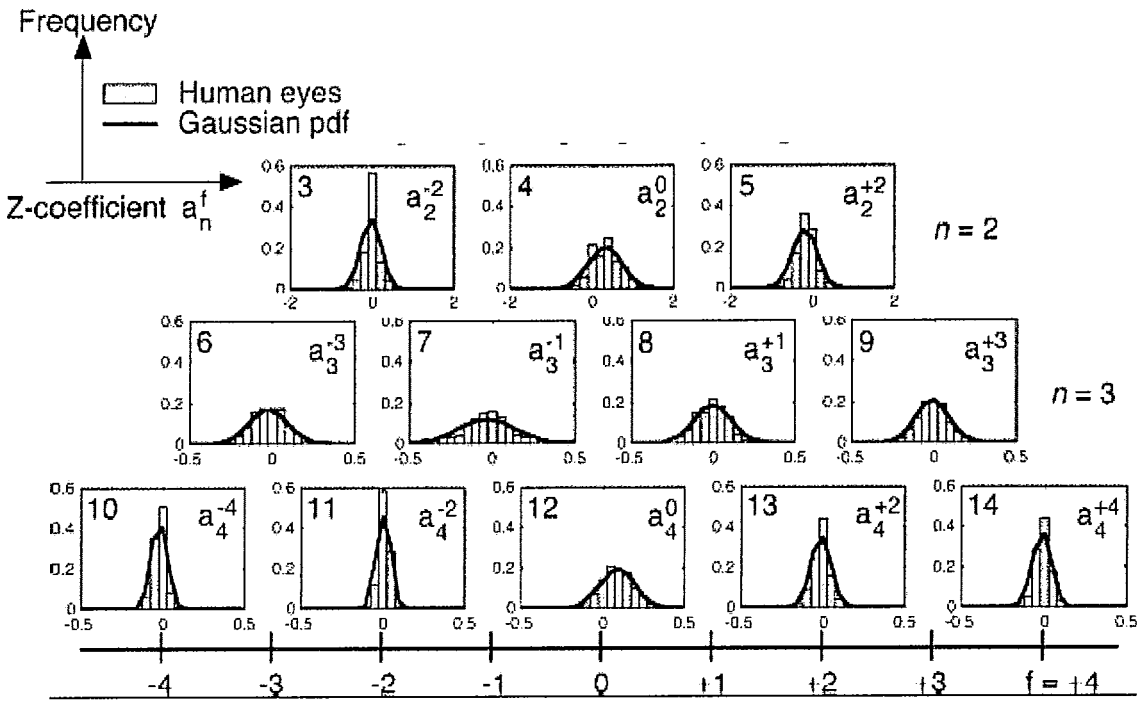


**Figure 8.2 The distribution of the Zernike coefficients adapted from a figure published in the population study of Thibos *et al.* (2002a). Note that scales are only consistent within a particular aberration order.**

The histogram distributions of Zernike coefficients for each mode are shown in fig. 8.1 for the 2nd to 4th orders for on-axis measurements. A high degree of individual variation in ocular aberrations is evident. Most aberration modes have a mean population coefficient value close to zero. However, due to biological variation it is unlikely that a subject would actually have a coefficient of exactly zero for a particular mode. It has been speculated by Thibos *et al.* (2002a) this might be evidence of the emmetropisation process extending to include higher-order aberrations (a claim supported by Brunette *et al.* 2003), or evidence of an evolutionary pressure towards aberration-free vision. The histograms in fig. 8.1 appear reasonably symmetric suggesting that they might be successfully fitted with Gaussian probability density functions. The histograms of 5th order aberration coefficients were also analyzed and they demonstrate similar trends, although these histograms are not shown. The magnitude of higher-order aberrations for any one subject was typically low compared to the dominant 2nd order aberrations. The

mean higher-order (3rd to 5th order) RMS wavefront error is 0.33 ± 0.17 microns. This compares similarly to the mean higher-order (3rd to 6th order) RMS wavefront error of 0.327 ± 0.13 microns reported by Salmon and van de Pol (2006). For a 6 mm pupil, 0.33 microns of defocus $Z_2^0$ approximately corresponds to 0.25 DS - the traditional level of significance for refractive error correction. This may be comparable to the amount of retinal image degradation produced by 0.33 microns of higher-order aberrations, assuming the MTF analysis of Guiro *et al.* (2002) can be extrapolated to infer a similar equivalency of retinal image blur would occur for the mean higher-order RMS value presented. The on-axis aberration results support general observations made by the larger studies of Porter *et al.* (2001) and Thibos *et al.* (2002a). For the sake of comparison, fig. 8.2 shows an extract of the population distributions of Zernike coefficients for the 2nd to 4th aberration modes published by Thibos *et al.* (2002a).

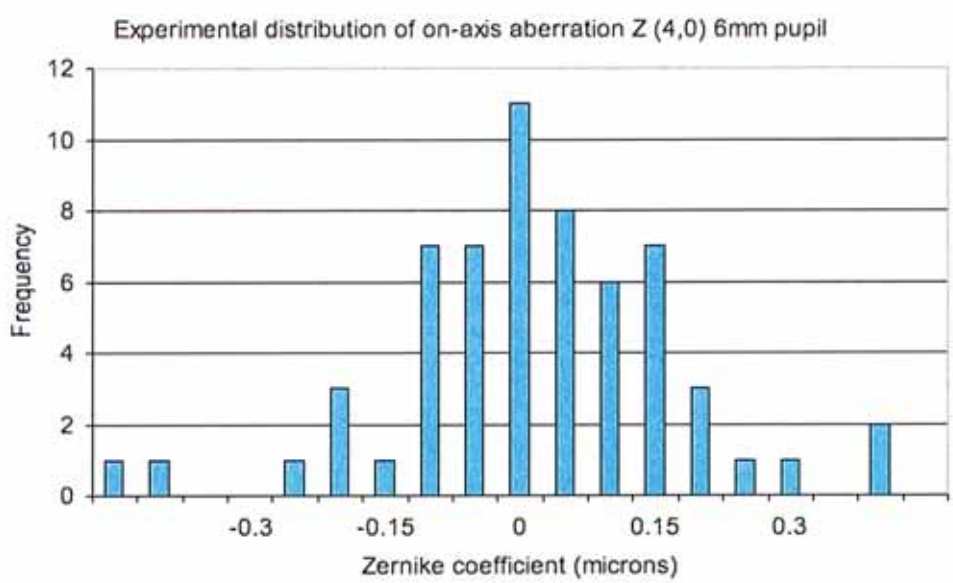


**Figure 8.3. Histogram displaying the distribution of spherical aberration for 60 eyes for 6 mm pupil. The x-axis value refers to the middle value of that particular bin.**

The distribution for spherical aberration $Z_4^0$ is shown in greater detail in fig. 8.3. The mean coefficient for spherical aberration $Z_4^0$ is 0.00 ± 0.16 microns. Findings in other studies (Thibos *et al.* 2002a, Porter *et al.* 2001, Cheng *et al.* 2004) show slightly positive values for the mean $Z_4^0$ coefficient. It is arguable whether the mean value presented here is a true description of a 'typical' eye. It could be argued that the result is biased due to the small sample size or due to the relatively young population selected (mean age 25.7 years). Experimental data by many authors (Calver *et al.* 1999, Smith *et al.* 2001, Alió *et al.* 2005, Amano *et al.* 2004) indicate that ocular spherical aberration gradually increases with age. It has also been suggested that the crystalline lens partly compensates the spherical aberration of the cornea (Artal and Guirao 1998, Artal *et al.* 2001). At a younger age this compensatory mechanism seems to be more efficient, leading to a lower amount of ocular spherical aberration (Artal *et al.* 2002).

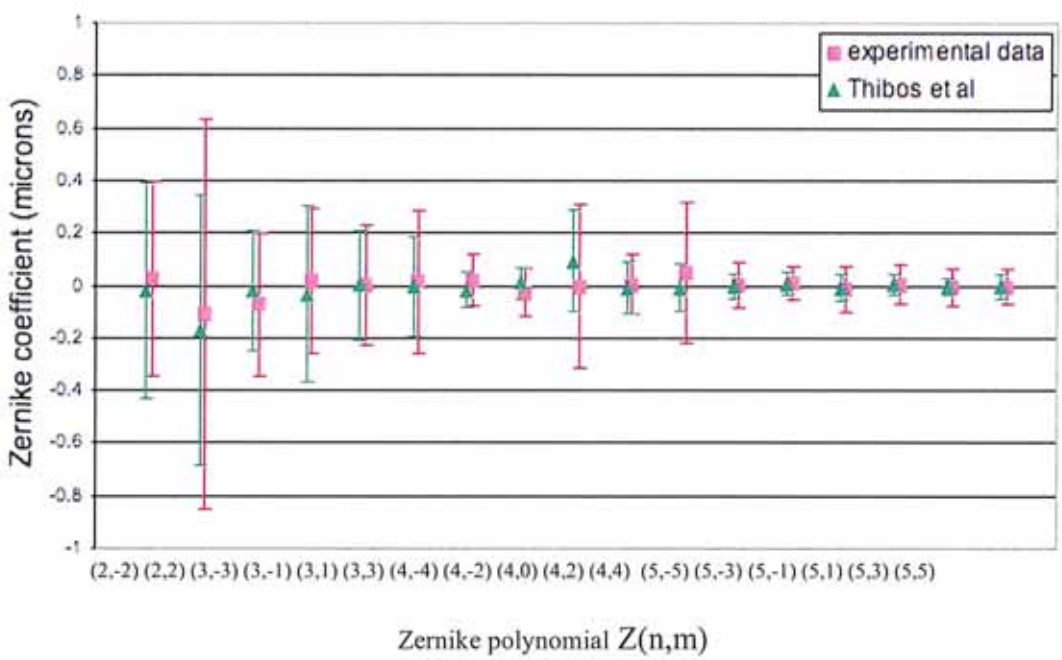


**Figure. 8.4 The statistical distribution of Zernike coefficients over 6 mm pupil diameters for modes up to the 5th order as measured by the experimental WFS and those estimated from Thibos *et al.* (2002a). The corresponding mean values are shown as square icons and triangle icons respectively. Error bars represent ± 2 standard deviations.**

The population distributions of Zernike coefficients display profiles similar to earlier studies (Thibos *et al.* 2002a, Porter *et al.* 2001, Cheng *et al.* 2004). Fig. 8.4 shows the statistical distribution of coefficients for the analysed Zernike modes for on-axis measurements compared against distributions estimated from Thibos *et al.* (2002a). The error bars represent ± 2 standard deviations. There appears to be reasonable agreement in the range and typical mean values expected in a population of normal healthy eyes. Both studies illustrate the general trend of a decreasing standard deviation of coefficient values as the aberration mode increases. This data provides an estimate on the range of coefficients one might expect in a population of normal young eyes.

Fig. 8.4 shows a slightly larger standard deviation in the experimental WFS data for modes $Z_2^{-2}$ and $Z_2^{2}$ compared to the data of Thibos *et al.* (2002a). This can be attributed to the fact that Thibos *et al.* (2002a) optimally corrected astigmatism with trial lenses, whereas our experimental procedure didn't. Other modes revealed more significant differences in the population ranges presented by this study and that of Thibos *et al.* (2002a). The standard deviation of the Zernike coefficient for secondary astigmatism $Z_4^{4}$ (fig. 8.3) appears atypically large when measured by the experimental WFS. Our study found a standard deviation of ± 0.13 microns for 6 mm pupil diameters. This suggests that secondary astigmatism $Z_4^{4}$ may have a relatively broad distribution, similar to spherical aberration $Z_4^{0}$, owing to high inter-subject variability. However, other studies such as Cheng *et al.* (2004), have found a smaller population standard deviation of ± 0.07 microns for mode $Z_4^{4}$ (estimated from Cheng *et al.* 2004) over a 5 mm pupil, and Thibos *et al.* (2002a) found a population standard deviation of only 0.05 (estimated from Thibos *et al.* 2002a) for a 6 mm pupil. Additionally, the ZyWave comparison experiment presented in chapter 7 indicated the coefficients of modes $Z_4^{0}$

and $Z_4^4$ produced by the experimental WFS may contain larger uncertainty. Therefore, this population statistic should be interpreted with some discretion.

## 8.5 Results for off-axis

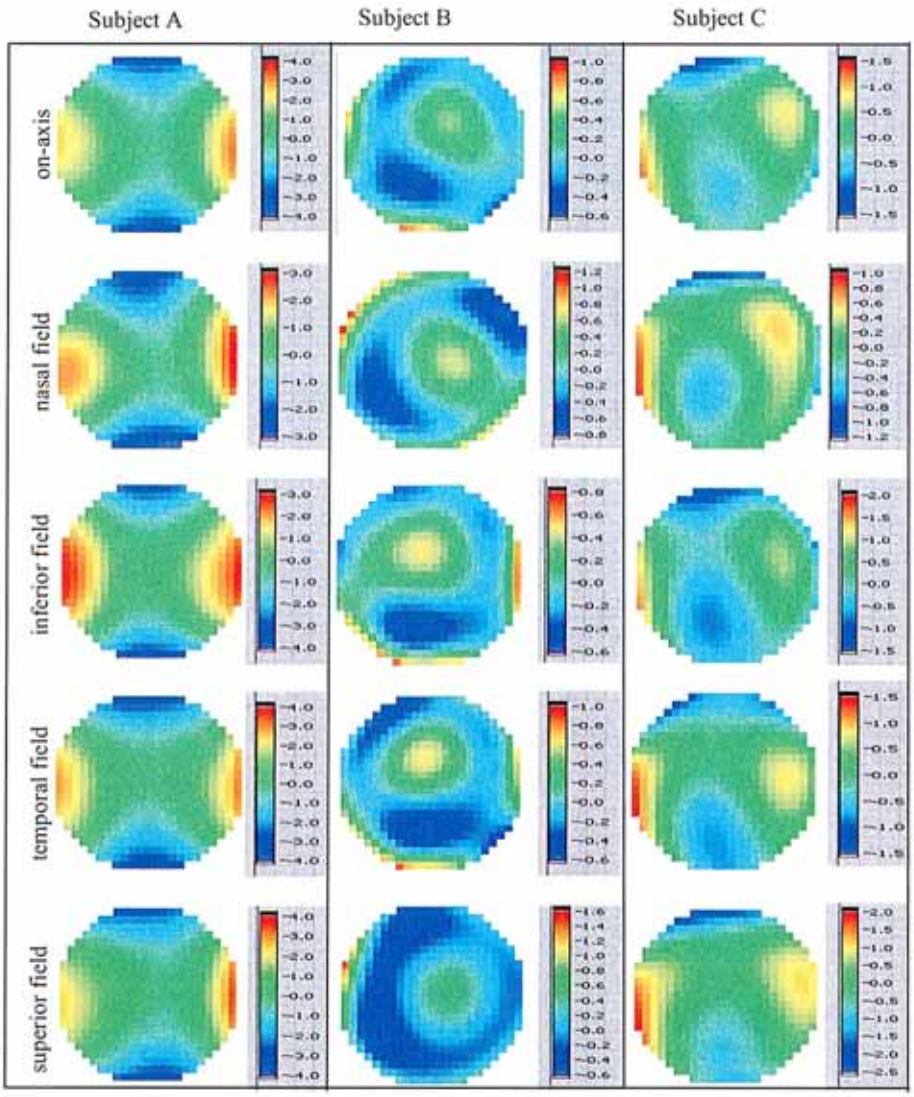


**Figure 8.5 Phase maps for three eyes of ocular aberrations over the central visual field for 6 mm pupils. Off-axis phase map are relative to 5 degree field angles. Note the colour scale is different between all phase maps due to the large variation in range between different field angles.**

It has been known for many years that ocular aberrations and image quality vary slowly over the central field (Jennings and Charman 1981). The lowest aberrations occur on, and centred symmetrically around, the optical axis rather than the visual axis (Jennings and Charman 1981). Examples of phase maps for on-axis and off-axis measurements are shown in fig. 8.5 for three typical eyes. All results are reported for 2$^{nd}$ to 5$^{th}$ order

with defocus $Z_2^0$ removed, over 6 mm pupils. For each eye the general wavefront shape appears relatively similar for measurements on-axis and at most field angles. However, the colour scales reveal significant variation in amplitude between the wavefronts. Astigmatism is expected to show the most significant variation with field angle, however, at relatively small angles of 5 degrees, these results illustrate considerable individual variation in the way ocular aberrations change across the central field. Astigmatism is not always the dominant field aberration to increase off-axis.

It is also worth noting in fig. 8.5 that references to the 'temporal field' may actually be better aligned to the optical axis of the eye than 'on-axis' measurements. This is because the optical axis of the eye is typically titled by about 5 degrees temporally with respect to the line of sight (although this value has significant individual variation) (Bradley and Thibos 1995). Note that the optical axis is defined as the line passing through or near the centres of rotation of the four optical surfaces of the eye, whereas the line of sight is defined as the axis connecting the fovea and the fixation target via the centre of the entrance pupil and exit pupil. The horizontal angular separation (angle alpha) between the line of sight and the optical axis varies from +17 degrees temporal to -2 degrees nasal (Bradley and Thibos 1995). Vertically, the line of sight and the optical axis are better aligned. The optical consequences of an individual's misalignment of the optical axis could be investigated in future experiments with the experimental WFS.

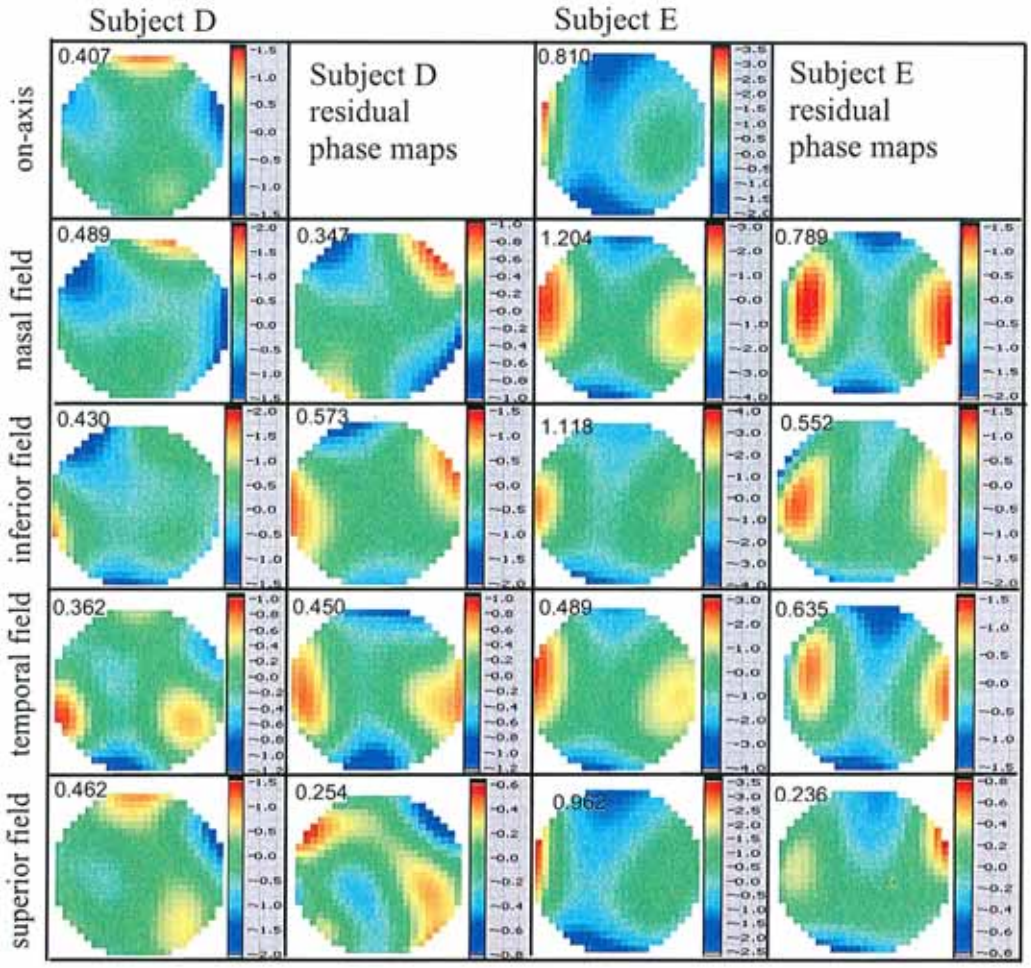


**Figure 8.6. On-axis, off-axis, and residual phase maps for 2 right eyes. All results presented over a 6 mm pupil diameter with defocus removed. The wavefront RMS (microns) is overlaid on each phase map. The residual phase map for each off-axis field angle is generated by subtracting Zernike coefficients for on-axis aberrations from Zernike coefficients for off-axis aberrations.**

*Residual wavefront* maps were generated for each field angle by subtracting the on-axis Zernike coefficients from those measured off-axis at the field angle. Fig. 8.6 displays on-axis, off-axis, and residual wavefront maps for 2 typical eyes. The results are reported for $2^{nd}$ to $5^{th}$ order, with defocus $Z_2^0$ removed, over 6 mm pupils. The wavefront RMS (defocus $Z_2^0$ removed) in microns is overlaid on each phase map and each residual phase map. In both of these eyes, the temporal field off-axis wavefront has a lower RMS than the on-axis wavefront, while all other off-axis wavefronts have a greater RMS than the on-axis wavefront. For these two eyes, results suggest that aberrations may be minimal at some small angle in the temporal visual field rather than

exactly on the line of sight. However, this is not necessarily a trend observed of all eyes. The lowest residual RMS value is found in the superior field for both eyes, although this is not a feature typical of all eyes. For these two eyes, when moving away from the line of sight, aberrations undergo the smallest change in the superior field direction compared to the other field directions investigated. It is important to note the large inter-subject variability we observed in the relationship between on-axis and off-axis aberrations for the 31 eyes investigated.

The tendencies displayed in fig. 8.6 are not necessarily universal, however, we shall use them to illustrate two possible scenarios for correcting aberrations in the eye. For subject D shown in fig. 8.6 (left-hand side), removing aberrations on-axis by means of a deformable mirror conjugated to the pupil would not improve field aberrations in the temporal and inferior fields, suggesting that a better correction over the entire field might be achieved by removing a common component that is averaged across the field. Considering the other example of subject E shown in fig. 8.6 (right-hand side), removing on-axis aberrations would also partially correct off-axis fields (except for the temporal field), as the aberrations are more uniform across the central field. It is evident that depending on the particular task, one could use different regimes for field correction. For example, the goal may be to provide a minimum average residual RMS aberration in a given field region, or the goal may be to attain a nearly uniform residual RMS aberration cross the central field. Bará and Navarro (2003) proposed an analytical method, which is based on the residual RMS eye aberrations, for optimal wide-field correction at the pupil.

The Zernike coefficients of the four field angles investigated were averaged for each of the 31 eyes and then were pooled to produce the statistical distribution of each aberration mode shown in fig. 8.7. The distribution of the mean off-axis aberrations is compared against the on-axis aberration distributions for 60 eyes (data also shown in fig. 8.4). The distributions appear very similar in range and mean values. This suggests that the correction of off-axis field aberrations by removing the wavefront component averaged across the field, one could employ a deformable mirror with a comparable stroke as required for the correction of on-axis aberrations.

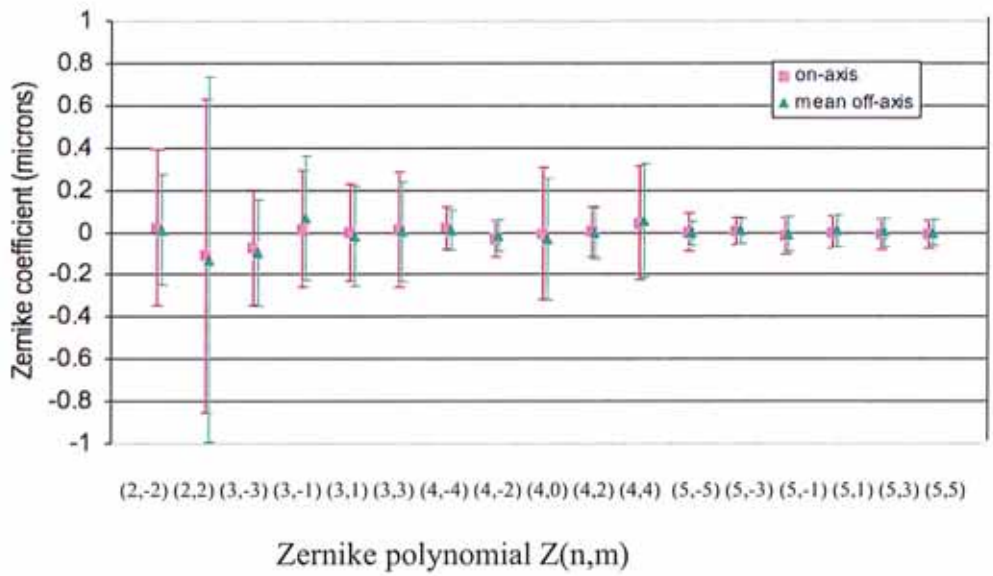


**Figure 8.7. The statistical distribution of Zernike coefficients measured on-axis compared to off-axis as measured by the experimental WFS for modes up to the 5$^{th}$ order. Mean values are represented by square and triangle icons. Error bars represent +/- 2 standard deviations.**

## 8.6 Discussion

The main rationale for this experiment was to model population statistics for monochromatic aberrations in the normal eye, with the view supporting development of wide-field model eyes and multi-conjugate adaptive optics (MCAO) in the eye. Traditional AO uses a corrective element conjugated to the pupil plane. Using additional corrective optics conjugated to some location away from the pupil could

enhance the correction of the field aberrations. This approach might be different from MCAO, which developed recently in astronomy to increase the field of view of ground-based telescopes. MCAO corrects for atmospheric turbulence, which can usually be approximated as a sequence of few discrete flat thin layers (phase screens). In contrast to the optical effects of atmospheric turbulence, the optical structure of the eye has intrinsic field aberrations as any other non-perfect imaging system. The nature of these field aberrations is quite different, for example the crystalline lens with its distributed structure of refractive index introduces aberrations continuously unlike a thin phase screens. The field dependence of low order terms and their significance to image formation are different from the aberrations caused by atmospheric turbulence. This means that correction of ocular aberrations over extended field of view might require a larger number of corrective elements positioned at different optical conjugates than the two deformable mirrors typically used in MCAO for astronomical telescopes. The recent work of Bedggood *et al.* (2006) confirms the limitation of MCAO approach.

## 8.7 Conclusions

This experiment took advantage of some of the unique features of the experimental WFS and verifies its success in combining research type features with a clinically friendly instrument. The experiment provided a real-life clinical test of the operational capabilities of our experimental WFS. The experience and feedback gained has provided insight into where the potential research strengths of the instrument design lie. The experiment produced population data regarding monochromatic aberrations over the central field of normal eyes. It is intended to use these results for developing subject-specific wide field schematic eye models incorporating a gradient index lens (Goncharov and Dainty 2007). It is hoped that this statistical data would aid future

designs for multi-directional ocular adaptive optics systems to achieve widefield high resolution retinal images.

# CHAPTER NINE

## Summary of work done and findings

This chapter summarises the work done in fulfilling the requirements of a masters of philosophy (by research) degree. The primary goal of this work was to measure and characterise monochromatic aberrations in the normal human eye. We aimed to develop a HS WFS that offered unique advantages compared to other designs. How the work fits into vision science is discussed and proposals for future investigations in the field are given.

### 9.1 Thesis work

Our initial task was to design a HS WFS that combined the flexibility of features typical in a research instrument with clinically-friendly features more typical of a commercial instrument. The design was finalised and the project progressed to construction. The mechanical, electronic, and optical components were successfully combined to produce a versatile ocular HS WFS. The WFS boasts advantages of simultaneous pupil centre determination, off-axis capability, realtime data displays, and efficient lenslet sampling orientation. Original software was developed for the WFS and provides a user-friendly interface suitable for a clinical setting. Three small pilot studies allowed the experimental WFS to be tested on real eyes and the repeatability of measurements to be investigated. The instrument is compact and transportable, allowing it to be readily transported between two separate experiments conducted at Galway and Dublin. The 1$^{st}$ experiment compared agreement between the experimental WFS and the ZyWave WFS when measuring monochromatic aberrations on 21 normal eyes. The 2$^{nd}$ experiment investigated the variation in monochromatic aberrations over the central field. Wavefront aberrations were measured on-axis for 60 eyes and 31 of these eyes were

also measured at off-axis field angles in the four principal semi-meridians. The results were used to produce a statistical model of the population distribution of ocular aberrations. The design of the experimental WFS has been published (Sheehan *et al.* 2005) and presented at conferences (Sheehan *et al.* 2005, 2006). The results of the 1st and 2nd experiments have been published in a peer-reviewed journal (Sheehan *et al.* 2007).

### 9.2 Proposed future WFS modifications

As with any instrument development, hindsight has revealed a number of possible design alterations that would enhance the instrument's capabilities. One example of a possible software modification is to incorporate a subject-focus detector in the alignment channel. This could be in the form of a spatial frequency detector which indicates to the operator when the iris-edge is in good focus and may reduce examiner error in judging when the instrument is at the correct working distance from the subject (correct pupil conjugation). The potential to improve software features is seemingly endless. However, the current software program is already performing at a satisfactory level, it is completely de-bugged, and presents a very user-friendly GUI. I think it is more constructive (and more interesting) to discuss possible optical design modifications as described below. Firstly, modifications that require relatively small reconfigurations of the optical design are suggested, followed by two suggested modifications that would require major reconfiguration of the design.

Although the optical design of the experimental WFS produced satisfactory results, the lack of refractive error correction for the ingoing beam significantly affected HS spot quality for some subjects measured due to deterioration of the retinal beacon. Future

modifications should endeavour to allow refractive error compensation in the ingoing laser beam, whilst still avoiding polluting the sensing pass with either back-reflections or foreign correction device (eg trial lenses) aberrations (see section 4.3).

The experimental WFS would benefit from a minor adjustment to the magnification of the sensing and alignment channels. If reconfigured, the maximum range of measurable pupil diameters could be increased above 9.5 mm to a more inclusive limit for a population of pharmacologically dilated pupils. The relevant conflicting considerations and limitations have already been discussed (see section 5.1).

Other suggested small modifications include; motorising the positioning mechanism of the Badal stage to speed up the measurement process, modifying the headrest to include a nasal stabiliser as well as the existing forehead-rest and chin-rest to improve subject stability, and replacing the parallel plate beamsplitter at element D fig 4.1 with an optical wedge to avoid ghosting of the fixation target (see section 4.2 p.119).

The first suggested major design reconfiguration is to incorporate a binocular capability into our WFS. The rationale for this proposal follows. Monocular first order aberrations of tip and tilt simply represent a transverse shift in the image plane and they are meaningless in most vision science experiments except for AO systems which typically correct tip and tilt aberrations with gimbal mirrors when imaging the retina. However, these first order aberrations could provide useful clinical information if measured in a relative (binocular) manner. They represent an associated phoria measurement which is a routine measurement performed at most initial optometric consultations. A binocular WFS offers a clinical advantage compared to traditional monocular autorefractors – by

using a calibration between the binocular channels, the first order aberrations of the subject can be measured. With a major modification, our experimental WFS could incorporate a binocular sensing channel. Once constructed, a clinical study of the first order aberrations could be compared to traditional measurements of phoria. Binocular WFSs have been constructed by some researchers such as Mihashi *et al.* (2006) and thus far have been mainly used to study accommodation and vergence relationships with higher-order aberrations (Neal no date). The clinical advantages and potential of a binocular WFS haven't yet been realised by commercial WFS manufacturers – a gap exists in the market to demonstrate the clinical relevance of 1$^{st}$ order aberration measurements in the eye.

The second suggested major design reconfiguration is to incorporate a chromatic aberration measurement ability into our WFS. This could be confined to second order defocus measurement only (longitudinal chromatic aberration). This is a very promising adaptation to the instrument design and if the wavefront data was combined with the tri-luminance efficiency curves, a much more practical measurement of visual performance could be achieved. To my knowledge this would be the first such manipulation of HS data. Marcos *et al.* (1999) discuss this topic and the adaptation of HS sensors to study chromatic effects in the eye. Such a project would not be trivial, especially if a capability to measure transverse chromatic aberration was attempted. The reconfiguration would possibly require staggered collimation of the probing beams, converting the Badal optometer arrangement to concave mirrors, and avoiding the use of re-imaging lenses to prevent chromatic alignment problems within the instrument. An alternative method for separating the sensing wavelengths from the fixation target wavelengths may also be required.

## 9.3 Proposed future work and research

There are many research areas where WFSs have the potential to add valuable information to vision science. A relatively basic task that should have priority for our WFS is characterisation of the Badal optometer. Until the Badal is characterised, results from our experimental WFS regarding the defocus term are not accurately known and can't be compared to other published results. Once the Badal characterisation is complete, other more interesting research work can begin. The projects suggested below are designed to take advantage of the unique capabilities the experimental WFS.

The iris-edge detection technique used by our experimental WFS to determine the pupil parameters should be investigated and compared to the traditional technique of using HS spots to estimate the pupil parameters. Primarily this work requires a software modification so that both techniques could execute simultaneously for wavefront measurements on real or artificial eyes. This is a unique opportunity to verify what we hope will prove to be a superior technique for HS WFS pupil centre determination - particularly under challenging situations such as poor HS spot quality. The accuracy of these techniques is important for wavefront sensing which is particularly sensitive to the pupil centre determination.

Hofer *et al.* 2001 and Diaz-Santana *et al.* (2003) have performed investigations into temporal fluctuations of higher-order aberrations in the eye. Our experimental WFS could be used to examine various research subtopics regarding temporal changes in aberrations including; optical quality degradations in the inter-blink period, healing following ocular surgery (especially relevant are refractive surgery techniques intended to minimise higher-order aberrations such as customised ablation patterns and new flap-

generation techniques), aberrations and contact lens movement associated with the blink process.

One of our original design aims was to explore the possibility of replacing the typical laser source of a WFS with a LED. LED sources have potential advantages over laser diode and SLD sources such as reduced image speckle and lower costs. The main reason we were unsuccessful in implementing a LED source was due to the insuffucient optical flux through a small pupil (first pass) whilst still maintaining a retinal beacon size below the diffraction limit of the lenslets. If a larger entrance pupil was allowable for the first pass, adequate optical flux might be achievable and a reasonable signal return from the retinal reflection might be possible. So the question arises - how large can we make the entrance pupil of the first pass? HS WFSs used in measuring ocular aberrations typically pass a wavefront through the eye twice before it is sensed. This first pass through the eye uses a small entrance pupil and is assumed to impart negligable phase structure onto the wavefront compared to the second pass which allows the outgoing beam to travel through a large exit pupil (Artal *et al.* 1995). Future experiments with our experimental WFS could examine over what range of entrance and exit pupil sizes ratios does the double pass approximation remain valid for. If a larger entrance pupil is allowable for the first pass, sufficient optical flux might be achievable with current commercially avaliable LEDs and the results could have implications for future WFS designs which may prefer to use a LED source to create the probing beam.

Currently our experimental WFS is being used by Alexander Goncharov and Maciej Nowakowski to collect further data regarding off-axis aberrations in the normal eye.

This collaboration has developed *subject-specific* model eyes through a reverse ray-tracing and optimisation technique seeded from the parameters of a generic model eye (Goncharov *et al.* 2007). It is hoped this work will aid in the development of wide-field MCAO in the eye. MCAO for the eye aims to increase the field of view over which aberrations are sensed and corrected. Future retinal imaging with AO will most likely require larger diffraction-limited fields as well as eccentric diffraction-limited imaging at locations such as the optic nerve head (which typically inserts to the globe at approximately 15 degree eccentricity). If the contrast issue can be solved, other retinal structures apart from the blood vessels and the photoreceptors will be able to be imaged with MCAO systems and the technique will play a significant role in pathology detection and monitoring. This is in addition to the uses wavefront sensing is likely to facilitate as a routine adjunct to traditional clinical eye examinations. WFS has potential to be used as a screening technique for early detection of lenticular and corneal irregularities (such as Forme Fruste Keratoconus). If MCAO can provide an increase in the diffraction-limited field size for retinal imaging (currently ocular AO systems with flood-illuminated single image capture systems achieve diffraction limited imaging over approximately 20 arc minutes) it will reduce the need to montage several images together to create a suitable image size.

Wide field AO may be a more achievable goal in the eye compared to astronomy due to the relatively slow evolution of wavefront aberrations in the eye and the abundance of photons available for wavefront sensing. Bară and Navarro (2002) pose some of the related design questions and approaches for ocular MCAO. For example, determination of the optimal conjugation for the correction device (typically a deformable mirror), or determining the stroke requirement and number of actuators that the correction device

requires. Another design question is - how many modes would require correction in a MCAO system to achieve the diffraction limit across a specified pupil diameter and across a specified field angle for a typical eye? Thibos *et al.* (2002) found the 14 largest modes had to be removed to achieve the diffraction limit for a 6mm pupil in a standard single-conjugate AO system. Off-axis wavefront sensing is associated with a large increase in astigmatism and MCAO systems attempting to image the peripheral retina would most likely require a dedicated astigmatism correction device such as rotating cross-cylinder lenses in addition to the defocus correction device. However, to answer these design questions regarding MCAO systems with quantitative detail to support our reasoning, more research regarding off-axis aberrations in the typical eye is required.

The design of our experimental WFS provides off-axis sensing capability and we have already taken the opportunity to research typical wavefront aberrations encountered off-axis (see chapter 9). Further research regarding the typical off-axis aberrations in the human eye is likely to be helpful in designing and constructing future MCAO system for the eye. Multiconjugate compensation to enlarge the field of view of AO systems (MCAO) will most likely would require widefield wavefront measurement, multiple wavefront correction devices, and development of multi-conjugate processing algorithms (Tyson 1998). These predictions can equally be applied to both astronomy (Rigaut *et al.* 2000) and vision science. Neal and Copland (2003) present a design for a tomographic WFS using a scanning mirror conjugate to probe the pupil plane to probe the eye in a multidirectional manner. The sensing beam is then de-scanned by the same mirror before continuing on to the sampling element. Development and construction of MCAO systems for the eye is likely to occur in the near future.

## 9.4 Conclusions

As WFSs continue to become more familiar in the clinical setting, clinicians need to become increasingly knowledgeable regarding their principles of operation. WFSs will become more common within primary eye-care practices as the instrument purchase costs reduce, as refractive surgery volume increases, customised contact lens technology develops, and as AO instrumentation for the eye develops. Novel WFS design innovations (such as those explored in this work) are helping to produce versatile and improved devices. Features such as transportability and adaptability offer significant advantages in both the clinical and research settings. The continued development of ocular wavefront sensing technology is of great benefit to patients, clinicians, and researchers.

## Bibliography


Alonso M. (1948). A simple proof of Malus' theorem in geometrical optics. *Am. J. Physics*. **16**, 462-463.

Alonso M., Finn E.J. (1992). Physics. Harlow: Pearson Education Limited.

Alió J.L., Schimchak P., Negri H.P., Montés-Micó R. (2005). Crystalline lens optical dysfunction through aging. *Ophthalmol.* **112**, 2022-2029.

Amano S., Amano Y., Yamagami S., Miyai T., Miyata K., Samejima T., Oshika T. (2004). Age-related changes in corneal and ocular higher-order wavefront aberrations. *Am. J. Ophthalmol.* **137**, 988-992.

Anonymous reviewer. (2007). Private communications regarding manuscript submitted for publication in Optic Express. April - May 2007.

Artal P., Berrio E., Guirao A., Piers P. (2002). Contribution of the cornea and internal surfaces to the change of ocular aberrations. *J. Opt. Soc. Am. A.* **19**, 137-143.

Artal P., Chen L., Fernandez E.J., Singer B., Manzanera S., Williams D.R. (2003). Adaptive optics for vision: the eye's adaptation to point spread function. *J. Refract. Surg.* **19:5**, 585-587.

Artal P., Guirao A. (1998). Contributions of the cornea and the lens to the aberrations of the human eye. *Opt. Lett.* **23**, 1713-1715.

Artal P., Guirao A., Berrio E., Williams D.R. (2001). Compensation of corneal aberrations by the internal optics in the human eye. *J. Vis.* **1:1**, 1-8.

Artal P., Marcos S., Navarro R., Williams D.R. (1995). Odd aberrations and double-pass measurements of retinal image quality. *J. Opt. Soc. Am. A.* **12:2**, 195-201.

Artal P., Navarro R. (1994). Modulation Transfer Function as a function of pupil diameter, *J. Opt. Soc. Am. A.* **11**, 246-249.

Atchison D.A. (2005). Recent advances in measurement of monochromatic aberrations of human eyes. *Clin. Exp. Optom.* **88:1**, 5-27.

Atchison D.A. (2004). Anterior corneal and internal contributions to peripheral aberrations of human eyes. *J. Opt. Soc. Am. A.* **21**, 335-359.

Atchison D.A., Scott D.H. (2002). Monochromatic aberrations of human eyes in the horizontal visual field. *J. Opt. Soc. Am. A.* **19:11**, 2180-2183.

Atchison D.A., Scott D.H., Charman W.N. (2003). Hartmann-Shack technique and refraction across the horizontal visual field. *J. Opt. Soc. Am. A.* **20:6**, 965-973.

Atchison D.A., Smith G. (2000). Optics of the human eye. Melbourne: Butterworth-Heinemann.

Bará S. (2003). Measuring eye aberrations with Hartmann-Shack wavefront sensors: Should the irradiance distribution across the eye pupil be taken into account? *J. Opt. Soc. Am. A.* **20:12**, 2237-2245.

Bará S., Navarro R. (2003). Wide-field compensation of monochromatic eye aberrations: expected performance and design trade-offs. *J. Opt. Soc. Am. A.* **20:1**, 1-10.

Barbur J.L., Chisholm C.M., Harlow A.J. (1999). Effects of increased scattered light on visual performance. In *Non-invasive assessment of the visual system (Technical digest series)*. **1**, 6-9. Washington: Optical Society of America.

Barrett H.H., Dainty C., and Lara D. (2007). Maximum-likelihood methods in wavefront sensing: stochastic models and likelihood functions. *J. Opt. Soc. Am. A.* **24:2**, 391-414.

Bartlett J.D., Janus S.D. (2000). Clinical ocular pharmacology ($4^{th}$ edition). London: Butterworth-Heinemann.

Bartsch D.U., Zhu L., Sun P.C., Fainman S., Freeman W.R. (2002). Retinal imaging with a low-cost micromachined membrane deformable mirror. *J. Biomed Opt.* **7:3**, 451-456.

Bedggood P.A., Ashman R., Smith G., Metha A.B. (2006). Multiconjugate adaptive optics applied to an anatomically accurate human eye model. *Opt. Express*. **14**, 8019-8030.

Bland J.M, Altman D.G. (1986). Stastistical methods for assessing agreement between two methods of clinical measurement. *Lancet*. **1**, 307-310.

Born M., Wolf E. (1980). Principles of optics: Electomagnetic theory of propogation, interference and diffraction of light (6th edition). Oxford: Pergamon Press. Chapter 13.

Booth M.J., Neil M.A.A., Juskaitis R., Wilson T. (2002). Adaptive aberration correction in a confocal microscope. *Proc. Natl. Acad. Sci. USA*. **99:9**, 5788-5792.

Bradley A., Thibos L.N. (1995a). Modeling off-axis vision - I: the optical effects of decentering visual targets or the eye's entrance pupil. In Peli E. (Ed.). Vision models for target detection and resolution. Singapore: World Scientific Press. pp. 313-337.

Bradley A., Thibos L.N. (1995b). How to measure chromatic aberration and locate useful reference axes of the human eye. Presented at the Optical Society of America meeting. Portland, September 1995. Retrieved 29th October 2007 from: http://www.opt.indiana.edu/people/faculty/thibos/ABLNTOSA95/slide01.html

Brooks J. (2004). A compact Shack-Hartmann wavefront sensor for the eye. PhD thesis, Imperial College of Science Technology and Medicine, London.

Brunette I., Bueno J.M., Parent M., Hamam H., Simonet P. (2003). Monochromatic aberrations as a function of age, from childhood to advanced age. *Invest. Ophthalmol. Vis. Sci.* **44:12**, 5438-5446.

Calver R.I., Cox M.J., Elliott D.B. (1999). Effect of aging on the monochromatic aberrations of the human eye. *J. Opt. Soc. Am. A.* **16**, 2069-2078.

Camellin M., Gambino F., Casaro S. (2005) Measurement of the spatial shift in the pupil centre. *J. Cat. Ref. Surg.*, **31:9**, 1719-1721.

Campbell E.W., Bauman B.J., Sweider D.R., Olivier S.S. (1999). High-accuracy calibration of an adaptive optics system using a phase shifting diffraction

interferometer. Presented at SPIE's 44th Annual meeting of the international symposium on optical science, engineering, and instrumentation. Denver, July 1999. Retrieved 29th October 2007 from: http://www.llnl.gov /tid/lof/documents/pdf/236017.pdf

Campbell F.W., Green D.G. (1965). Optical and retinal factors affecting visual resolution. *J. Physiol. (Lond.)*, **181**, 576-593.

Carpenter R.H.S. (2000). Eye movements. Retrieved 16th July 2006 from: http://www.cai.cam.ac.uk/people/rhsc/oculo.html

Carroll J., Gray D.C., Roorda A., Williams D.R. (2005). Recent advances in retinal imaging with adaptive optics. *Optics and Photonics News*. **16:1**, 36-42.

Carroll J., Neitz M., Hofer H., Neitz J., Williams D.R. (2004). Functional photoreceptor loss revealed with adaptive optics: An alternate cause of colour blindness. *Proc. Natl. Acad. Sci. USA*. **101:22**, 8461-8466.

Catlin D. (2004). Private communication regarding Hartmann-Shack autoretinoscope design and evaluation. 10th December 2004.

Charman W.N. (1991). Wavefront aberrations of the eye: a review. *Optom. Vis. Sci.* **68**, 574–583.

Charman W.N. (2004). Wavefront technology. In Naroo S.A. (Ed.), Refractive surgery: A guide to assessment and management. Edinburgh: Butterworth Heinmann. pp.65-75.

Charman W.N., Heron G. (1988). Fluctuations in accommodation: a review. *Ophthalmic Physiol. Opt.* **8**, 153-164.

Cheng H., Barnett J.K., Vilupuru A.S., Marsack J.D., Kasthurirangan S., Applegate R.A., Roorda A., (2004). A population study on changes in wave aberrations with accommodation, *J. Vis.* **4**, 272-280.

Cheng X., Himebaugh N.L., Kollbaum P.S., Thibos L.N., Bradley A. (2003). Validation of a clinical Shack-Hartmann aberrometer. *Optom. Vis. Sci.* **80**, 587-595.

Christou J.C., Roorda A., Williams D.R. (2004). Deconvolution of adaptive optics retinal images. *J. Opt. Soc. Am. A*. **21:8**, 1393-1401.

Collins M., Davis B., Wood J. (1995). Microfluctuations of steady-state accommodation and the cardiopulmonary system. *Vis. Res.***35**, 2491-2502.

Commission Internationale de l'Eclairage. (1970). International lighting vocabulary (3rd Edition). Paris: Retrieved on 18th August 2007 from: http://www.handprint.com/HP/WCL/IMG/psf.gif

Coster D. (2002). Cornea - Fundamentals of clinical ophthalmology. London: BMJ Books.

Cox I., Lagana M. (2004). Feasibility of wavefront customised contact lenses. In Krueger R.R., Applegate R.A., MacRae S.M. (Eds.), Wavefront customised visual correction. Thorofare: Slack Inc. pp. 279-284.

Cox M.J. Personal communication. 2006.

Cox M.J., Atchison D.A., Scott D.H. (2003). Scatter and its implications for the measurement of optical image quality in human eyes. *Optom. Vis. Sci.* **80:1**, 58-68.

Cui C., Lakshminarayanan V. (1998). Choice of reference axis in ocular wave-front aberration measurement. *J. Opt. Soc. Am. A*. **15:9**, 2488-2496.

Dainty C. (2001). Imaging: lecture notes. London: Imperial College of Science Technology and Medicine.

Dave T. (2004a). Automated refraction – design and applications. *Optometry Today*. June, p.28-32.

Dave T. (2004b). Wavefront aberrometry – current theories and concepts. *Optometry Today*. November, p.41-45.

Davies N., Diaz-Santana L., Lara-Saucedo D. (2003). Repeatability of ocular wavefront measurement. *Optom. Vis. Sci.*, **80:2**, 142-150.

Delori F.C., Pflibsen K.P. (1989). Spectral reflectance of the human ocular fundus. *App. Opt.* **28:6**, 1061-1077.

Diaz Santana Haro L. Wavefront sensing in the human eye with a Shack-Hartmann sensor. (2000). Ph.D. thesis, Imperial College of Science Technology and Medicine, London.

Diaz Santana L., Dainty J.C. (1999). Single-pass measurements of the wave-front aberrations of the human eye by use of retinal lipofuscin autofluorescence. *Opt. Lett.* **24**, 61-63.

Diaz-Santana L., Dainty J.C. (2001). Effects of retinal scattering in the ocular double-pass process. *J. Opt. Soc. Am. A.*, **18:7**, 1437-1444.

Diaz-Santana L., Davies N., Lara-Saucedo D. (2002). Accuracy of wavefront measurement and the potential effect of erroneous custom corneal correction on the modulation transfer function. *Ophthalmic and Physiological Optics*. **22:6**, 573-573

Diaz Santana L., Torti C., Munro I., Glasson P., Dainty C. (2003). Benefit of higher closed-loop bandwidths in ocular adaptive optics. *Opt. Exp.* **11**, 2597-2605.

Ditchburn R.W. (1980). The function of small saccades. *Vis. Res.* **20**, 271-272.

Doble N., Williams D.R. (2004). The application of MEMS technology for adaptive optics in vision science. *IEEE J. Sel. Top. Quantum Electronics.* **10:3**, 629-635.

Doble N., Yoon G., Chen L., Bierden P., Singer B., Olivier S., Williams D.R. (2002). Use of a microelectromechanical mirror for adaptive optics in the human eye. *Opt. Lett.* **27:17**, 1537-1539.

Dubra A., Paterson C., Dainty C. (2004). Study of the tear topography dynamics using a lateral shearing interferometer. *Opt. Exp.* **12:25**, 6278-6288.

European Committee for Electrotechnical Standardization (2001). Safety of laser products – user's guide. *IEC 60825-1:1993/A2:2001*, 69-93, Dublin: National Standards Authority of Ireland.

European Southern Observatory (2003) Curvature sensing – how does it work. European Organisation for Astronomical Research in the Southern Hemisphere webpage. Retrieved on 18th August 2007 from: www.eso.org/~rdorn/ CCID35/how.html

Fercher A.F., Drexler W., Hitzenberger C.K., Lasser T. (2003). Optical coherence tomography – principles and applications. *Rep. Prog. Phys.* **66**, 239-303.

Fernández E., Unterhuber A., Prieto P., Hermann B., Drexler W., Artal P. (2005). Ocular aberrations as a function of wavelength in the near infrared measured with a femtosecond laser. *Opt. Exp.* **13:2**, 400-409.

Fowles G.R. (1989). Introduction to modern optics (2nd edition). New York: Dover.

Freeman M.H., Hull C.C. (2003). Optics (11th edition). Edinburgh: Butterworth Heinemann.

Ginis H.S., Plainis S., Pallikaris A. (2004). Variability of wavefront aberration measurements in small pupil sizes using a clinical Shack-Hartmann aberrometer. *BMC Ophthalmol.* **4:1**.

Goncharov A.V., Dainty C. (2007). Wide-field schematic eye model with gradient-index lens. *J. Opt. Soc. Am. A.* **24:8**, 2157-2174.

Goncharov A.V., Nowakowski M., Sheehan M.T., Dainty C.J. (2007). Reconstruction of the optical system of the human eye with reverse ray-tracing. Accepted for publication in Optics Express 2007.

Goodman J.W. (2005). Introduction to Fourier optics (3rd edition). Greenwood village: Roberts and company publishers.

Gray D.C., Merigan W., Wolfing J.I., Gee B.P., Porter J., Dubra A., Twietmeyer T.H., Ahmad K., Tumbar R., Reinholz F., Williams D.R. (2006). In vivo fluorescence imaging of primate retinal ganglion cells and retinal pigment epithelial cells. *Opt. Exp.* **14:16**, 7144-7158.

Guirao A., Artal P. (1999). Off-axis monochromatic aberrations estimated from double pass measurements in the human eye. *Vis. Res.* **39**, 207-217.

Guirao A., Porter J., Williams D.R., Cox I.G. (2002). Calculated impact of higher-order monochromatic aberrations on retinal image quality in a population of human eyes. *J. Opt. Soc. Am. A.* **19:1**, 1-9.

Guzowski M., Wang J.J., Rochtchina E., Rose K.A., Mitchell P. (2003). Five-year refractive changes in an older population: the Blue Mountains Eye Study. *Ophthalmology.* **110:7**, 1364-1370.

Hampson K.M., Munro I., Paterson C., Dainty C. (2005). Weak correlation between the aberration dynamics of the human eye and the cardiopulmonary system, *J. Opt. Soc. Am. A.* **22**, 1241-1250.

Hardy J.W. (1998) Adaptive optics for astronomical telescopes. Oxford: Oxford University Press.

Hean Pui B., Hayes-Gill B., Clark M., Somekh M., See C., Piéri J., Morgan S.P., Ng. A. (2002). The design and characterisation of an optical VLSI processor for real time centroid detection. *Analog Int. Cir. Sig. Proc.* **32:1**, 67-75.

Heath J.W., Young B. (2000). Wheater's functional histology (4th edition). Edinburgh: Churchill Livingstone.

Hecht E. (1987). Optics (2nd edition). Reading: Addison-Wesley.

Heisterkamp A., Mamom T., Kermani O., Drommer W., Welling H., Ertmer W., Lubatschowski H. (2003). Intrastromal refractive surgery with ultra short laser pulses: in vivo study on the rabbit eye. *Graefes Arch. Clin. Exp. Ophthalmol.* **241:6**, 511-517.

Hennelly M.L., Barbur J.L., Edgar D.F., Woodward E.G. (1997). The light scattering characteristics of the eye. *Ophthalmic and Physiological Optics* **17**, 171.

Hofer H., Artal P., Singer B., Aragón J.L., Williams D.R. (2001). Dynamics of the eye's wave aberration. *J. Opt. Soc. Am. A*, **18:3**, 497-506.

Hofer H., Williams D.R. (2002). The eye's mechanisms for autocalibration. *Optics and Photonics news.* **13:1**, 34-39.

Howarth P.A., Zhang X.X., Bradley A., Still D.L., Thibos L.N. (1988). Does the chromatic aberration of the eye vary with age? *J. Opt. Soc. Am. A.* **5:12**, 2087-2092.

Howland B. (1960). Use of crossed cylinder lens in photographic lens evaluation. *Applied Optics.* **7**, 1587-1588.

Howland H.C., Howland B. (1977). A subjective method for the measurement of monochromatic aberrations of the eye. *J. Opt. Soc. Am.* **67**, 1508–1518.

Ivanoff A. (1956). About the spherical aberration of the eye. *J. Opt. Soc. Am. A*, **46**. 901-903.

Jennings J.A.M., Charman W.N. (1981). Off-axis image quality in the human eye. *Vis. Res.* **21**, 445-455.

Jenny R. (2000). Fundamentals of optics. Translated by Kittelberger S. Graz: Technical University of Graz.

Jiang Z., Gong S., Dai Y. (2005). Monte-Carlo analysis of centroid detected accuracy for wavefront sensor. *Opt. Laser Tech.* **37:7**, 541-546.

Kanski J.J. (2003). Clinical ophthalmology – a systematic approach (5th edition). Edinburgh: Butterworth Heinemann.

Kanski J.J, Milewski S.A. (2002). Diseases of the macula - a practical approach. London: Mosby.

Kaufman P.L., Alm A. (Eds.) (2002). Adler's physiology of the eye (10th edition). London: Elsevier Science Health.

Ke C., Yi X., Xu Z., Lai J. (2005). Monolithic integration technology between microlens arrays and infrared charge coupled devices. *Opt. Laser Tech.* **37**, 239-243.

Konno S., Akiba J., Yoshida A. (2001). Retinal thickness measurements with optical coherence tomography and the scanning retinal thickness analyzer. *Retina.* **21:1**, 57-61.

Korb D.R. (Ed.). (2002). The tear film - structure, function and clinical examination. Oxford: Butterworth-Heinemann.

Krieglstein G.K., Jonescu-Cuypers C.P., Severin M., Vobig M.A. (2000). Atlas of Ophthalmology. Berlin: Springer-Verlag.

Laser Sight Centers. (2002). Lasik leader. Issue 8.

Li X., Jiang W., Gonglewski J.D., Vorontsov M.A., Gruneisen M.T., Restaino S.R., Tyson R.A. (2002). Comparing zonal reconstruction algorithms and modal reconstruction algorithms in adaptive optics system. In Gonglewski J.D. (Ed.), High-resolution wavefront control: methods, devices, and applications IV: SPIE conference proceedings. **4825**, pp.121-130.

Liang C.L., Juo S.H., Chang C.J. (2005). Comparison of higher order wavefront aberrations with three aberrometers. *J. Cataract Refract. Surg.* **31**. 2153-2156.

Liang J., Williams D.R, Miller D.T. (1997). Supernormal vision and high-resolution retinal imaging through adaptive optics. *J. Opt. Soc. Am.* **14**, 2884-2892.

Liang J., Grimm B., Goelz S., Bille J.F. (1994). Objective measurements of wave aberrations of the human eye with the use of a Hartmann-Shack wave-front sensor. *J. Opt. Soc. Am. A.* **11:7**, 1949-1957.

Lipson S.G., Lipson H.L, Tannhauser D.S. (1995). Optical physics (3rd edition). Cambridge: The press syndicate of the University of Cambridge.

Llorente L., Díaz-Santana L., Lara-Saucedo D., Marcos S. (2003). Aberrations of the human eye in visible and near infrared illumination. *Optom. Vis. Sci.* **80**, 26-35.

Lundström L., Gustafsson J., Svensson I., Unsbo P. (2005). Assessment of objective and subjective eccentric refraction, *Optom. Vis. Sci.* **82**, 298-306.

Lundström L., Unsbo P. (2004). Unwrapping HS images from highly aberrated eyes using an iterative B-spline based extrapolation method. *Optom. Vis. Sci.*, **81**, 383-388.

Lundström L., Unsbo P. (2007). Transformation of Zernike coefficients: scaled, translated, and rotated wavefronts with circular and elliptical pupils. *J. Opt. Soc. Am. A.* **24**, 569-577.

Malacara D. (Ed.) (1992). Optical shop testing (2nd edition). New York: John Wiley and Sons. pp.456-473.

Marcos S. (2003) Image quality of the human eye. *International Ophthalmology Clinics*. **2:43**, 43-62.

Marcos S., Barbero S., Llorente L., Merayo-Lloves J. (2001). Optical response to LASIK surgery for myopia from total and corneal aberration measurements. *Invest. Ophthalmol. Vis. Sci.* **42:13**, 3349-3356.

Marcos S., Burns S.A., Moreno-Barriuso E., Navarro R. (1999). A new approach to the study of ocular chromatic aberrations, *Vis. Res.* **39**, 4309–4323.

Marcos S., Diaz-Santana L., Llorente L., Dainty C. (2002). Ocular aberrations with ray tracing and Shack-Hartmann wavefront sensors: Does polarization play a role? *J. Opt. Soc. Am. A.* **19:6**, 1063-1072.

Martinez-Conde S., Macknik S.L., Hubel D.H. (2004). The role of fixational eye movements in visual perception. *Nature*. **5**, 229-240.

McKendrick A.M., Brennan N.A. (1996). Distribution of astigmatism in the adult population. *J. Opt. Soc. Am. A.* **13:2**, 206-214.

McLellan J.S., Marcos S., Burns S.A. (2001). Age-related changes in monochromatic wave aberrations of the human eye. *Invest. Ophthalmol. Vis. Sci.* **42:6**, 1390-1395.

McLellan J.S., Prieto P.M., Marcos S., Burns S. (2006). Effects of interactions among wave aberrations on optical image quality. *Vis. Res.* **46**, 3009-3016.

McGuire P.C., Sandler D.G., Lloyd-Hart M., Rhoadarmer T.A. (1999). Adaptive optics: Neural network wavefront sensing, reconstruction and prediction. In Clark J.W., Lindenau T., Ristig M.L. (Eds.), Lecture notes in physics: Scientific applications of

neural nets: Proceedings of the WE-Heraeus seminar. Heidelberg: Springer-Verlag. pp.1-38.

Molebny V.V., Pallikaris I.G., Naoumidis L.P., Chyzh I.H., Molebny S.V., Sokurenko V.M. (1997). Retina ray-tracing technique for eye-refraction mapping. *Proc SPIE*. **2971**, 175-183.

Moreno-Barriuso E., Marcos S., Navarro R., Burns S.A. (2001). Comparing laser ray tracing, spatially resolved refractometer and Hartmann-Shack sensor to measure the ocular wave aberration. *Opt. Vis. Sci.* **78**, 152-156.

Muller R.A., Buffington A. (1974). Real-time correction of atmospherically degraded telescope images through image sharpening. *J. Opt. Soc. Am.* **64:9**, 1200-1210.

National Research Council. (1985). Emergent techniques for assessment of visual performance. Washington: The National Academies Press.

Navarro R., Losada M.A. (1997). Aberrations and relative efficiency of light pencils in the living human eye. *Optom. Vis. Sci.* **74**, 540-547.

Navarro R., Moreno E., Dorronsoro C. (1998). Monochromatic aberrations and point-spread functions of the human eye across the visual field. *J. Opt. Soc. Am. A.* **15**, 2522-2529.

Neal D.R., Baer C.D., Topa D.M. (2005). Errors in Zernike transformations and non-modal reconstruction methods. *J. Refract. Surg.* **21:5**, 558-562.

Neal D.R., Copland R.J. (2003). Tomographic wavefront analysis system and method of mapping an optical system, United States Patent Application Publication, US2003/0038921 A1. Retrieved on 17th July 2005 from: http://www.freepatentsonline.com/EP1367935.html

Neal D.R., Copland J., Neal D. (2002) Shack-Hartmann wavefront sensor precision and accuracy. In Duparré A., Singh B. (Eds.), Advanced characterization techniques for optical, semiconductor, and data storage components. *Proc. SPIE.* Bellingham: SPIE press. **4779**, 148-160.

Neal D.R., Schwiegerling J. (2005). Historical development of the Shack-Hartmann wavefront sensor. In Harvey J.E., Hooker R.B. (Eds.), Legends in applied optics Bellingham: SPIE press. pp.132-139.

Neil M.A.A., Booth M.J., Wilson T. (2000). Closed-loop aberration correction by use of a modal Zernike wave-front sensor. *Opt. Lett.* **25:15**, 1083-1085.

Nirmaier T., Pudasaini G., Bille J. (2003). Very fast wave-front measurements at the human eye with a custom CMOS based Hartmann-Shack sensor, *Opt. Exp.* **11:21**, 2704-2716.

Noll R. (1976). Zernike polynomials and atmospheric turbulence. *J. Opt. Soc. Am.* **66:3**, 207-211.

Pulaski P. (2003) Making the trade. *SPIE oe magazine.* May 2003 p.40

Piers P.A., Fernandez E.J., Manzanera S., Norrby S., Artal P. (2004). Adaptive optics simulation of intraocular lenses with modified spherical aberration. *Invest. Ophthalmol. Vis. Sci.* **45:12**, 4601-4610.

Plainis S., Ginis H.S., Pallikaris A. (2005). The effect of ocular aberrations on steady-state errors of accommodative response. *J. Vis.* **5:5**, 466-477.

Platt B.C., Shack R. (2001). History and principles of Shack-Hartmann wavefront sensing. *J. Refract. Surg.* **17**, 573-577.

Porter J., Guirao A., Cox I.G., Williams D.R. (2001). The human eye's monochromatic aberrations in a large population. *J. Opt. Soc. Am. A.* **18:8**, 1793–1803.

Prasada S., Torgersen T.C., Pauca V.P., Plemmons R.J., Van Der Gracht J. (2003). Engineering the pupil phase to improve image quality. In Rahman Z., Schowengerdt R., Reichenbach S. (Eds.), Visual information processing XII: *Proc SPIE.* Bellingham: SPIE press. **5108**, pp.1-12.

Preece S.J., Claridge E. (2002). Monte Carlo modeling of the spectral reflectance of the human eye. *Phys. Med. Biol.* **47**, 2863-2877.

Prieto P.M., Vargas-Martín F., McLellan J.S., Burns S.A. (2002) Effect of the polarization on ocular wave aberration measurements. *J. Opt. Soc. Am. A.* **19:4**, 809-814.

Remington L.A. (2005). Clinical anatomy of the visual system (2nd edition). St. Louis: Butterworth-Heinemann Elsevier. p181

Rhoadarmer T.A., Angel J.R.P. (2001). Low-cost, broadband static phase plate for generating atmosphericlike turbulence. *Appl. Opt.* **40:18**, 2946-2955.

Rigaut F.J., Ellerbroek B.L., Flicker R. (2000). Principles, limitations and performance of multi-conjugate adaptive optics. In Wizinowich P.L. (Ed.) Adaptive optical systems technology. *Proc SPIE.* Bellingham: SPIE press. **4007:2**, 1022-1031.

Rolland J. (2006). Fundamental laws - chapter 2: The vectorial expression of refraction/reflection laws. Retrieved 23 April, 2006 from: http://oda.creol.ucf.edu/OSE5203/Chap2-1-Fund-laws.ppt#13

Roorda A. (2005). Making the most of AO for vision science. *Proc. CfAO summer school for adaptive optics.* Santa Cruz: Center for Adaptive Optics. pp.1-15.

Roorda A., Williams D.R. (1999). The arrangement of the three cone classes in the living human eye. *Nature.* **397**, 520-522.

Salmon T.O., Thibos L.N., Bradley A. (1998). Comparison of the eye's wave-front aberration measured psychophysically and with the Shack-Hartmann wave-front sensor. *J. Opt. Soc. Am. A.* **15:9**, 2457-2465.

Salmon T.O., Thibos L.N. (2002). Videokeratoscope-line-of-sight misalignment and its effect on measurements of corneal and internal ocular aberrations. *J. Opt. Soc. Am. A.* **19:4**, 657-669.

Salmon T.O., van de Pol C. (2006). Normal-eye Zernike coefficients and RMS wavefront errors. *J. Cataract Refract. Surg.* **32**, 1064-1074.

Schäfer B., Mann K. (2002). Determination of beam parameters and coherence properties of laser radiation by use of an extended Hartmann-Shack wave-front sensor. *Appl. Opt.* **41:15**, 2809-2817.

Schwiegerling J. (2004). Fieldguide to visual and ophthalmic optics. Bellingham: SPIE press.

Schwiegerling J. (2004). Gaussian weighting of ocular wave-front measurements. *J. Opt. Soc. Am. A.* **21:11**, 2065-2072.

Schwiegerling J. (2002). Scaling Zernike expansion coefficients to different pupil sizes. *J. Opt. Soc. Am. A.* **19:10**, 1937-1945.

Serway R.A., Jewett J.W. (2004). Physics for scientists and engineers, with modern physics (6th edition). Belmont: Thomson-Brooks Cole.

Shirai T. (2002). Liquid-crystal adaptive optics based feedback interferometry for high resolution retinal imaging. *Appl. Opt.* **41:19,** 4013-4023.

Sheehan M.T., Goncharov A.V., Dainty J.C. (2005). Design of a versatile clinical aberrometer, In Mazuray L., Wartmann R. (Eds.) Optical Design and Engineering II, *Proc. SPIE* **5962,** 59620M.

Sheehan M.T., Goncharov A.V., O'Dwyer V., Toal V., Dainty J.C., (2006). A population study of on-axis and off-axis ocular aberrations, Oral presentation. ICO Topical Meeting on *Optoinformatics and Information Photonics.* St Petersberg. September 2006.

Sheehan M.T., Goncharov A.V., O'Dwyer V.M., Toal V., Dainty C. (2007). A population study of the variation in monochromatic aberrations of the normal human eye over the central visual field. *Opt. Exp.* **15:12**, 7367-7380.

Simmers A.J., Gray L.S., Wilkins A.J. (2001). The influence of tinted lenses upon ocular accommodation. *Vis. Res.* **41:9**, 1229-1238.

Smirnov M.S. (1961). Measurement of the wave aberration of the human eye. *Biofizika* **6**, 687–703.

Smith G., Cox M.J., Calver R., Garner L.F. (2001). The spherical aberration of the crystalline lens of the human eye. *Vis. Res.* **41**, 235-243.

Smolek M.K., Klyce S.D. (2003). Zernike polynomial fitting fails to represent all visually significant corneal aberrations. *Invest. Ophthalmol. Vis. Sci.* **44:11**, 4676-4681.

Southwell W.H. (1980). Wave-front estimation from wave-front slope measurements. *J. Opt. Soc. Am.* **70**, 998-1006.

Spiricon Inc. (2004). Hartmann wavefront analyser tutorial. Logan: Spiricon Inc.

Steinhübel W. (2007). i.Scription™: A new experience in vision. Press release dated 26 January 2007. Retrieved on 30th October 2007 from: http://www.vision.zeiss.com/C1256FBA0032FCC7/allBySubject/Press1

Stone R.A., Quinn G.E., Francis E.L., Ying G., Flitcroft D.I., Parekh P., Brown J., Orlow J., Schmid G. (2004). Diurnal axial length fluctuations in human eyes. *Invest. Ophthalmol. Vis. Sci.* **45**, 63-70.

Tanabe T., Miyata K., Samejima T., Hirohara Y., Mihashi T., Oshika T. (2004). Influence of wavefront aberration and corneal subepithelial haze on low-contrast visual acuity after photorefractive keratectomy. *Am. J. Ophthalmol.* **138:4**, 620-624.

Tasman W., Jaeger E.A. (Eds.). (2001). The Wills eye hospital atlas of clinical ophthalmology (2nd edition). Philadelphia: Lippincott Williams and Wilkins.

Thibos L.N., Applegate R.A., Schwiegerling J.T., Webb R. (2000). Standards for reporting the optical aberrations of eyes. In Lakahminarayanan V. (Ed.), Vision Science and its Applications, OSA Technical Digest, **35**, paper SuC1.

Thibos L.N., Cheng X., Bradley A. (2003). Design principles and limitations of wavefront-guided contact lenses. *Eye Contact Lens.* **29:1**, S167. Retrieved on 30th October 2007 from: http://research.opt.indiana.edu/library/waveGuidedLens/waveGuidedLens.html

Thibos L.N., Hong X., Bradley A., Applegate R.A. (2004). Accuracy and precision of objective refraction from wavefront aberrations. *J. Vis.* **4**, 329-351.

Thibos L.N., Hong X., Bradley A., Cheng X. (2002). Statistical variation of aberration structure and image quality in a normal population of healthy eyes. *J. Opt. Soc. Am. A.* **19**, 2329-2348.

Thibos L.N., Wheeler W., Horner D. (1997). Power vectors: an application of Fourier analysis to the description and statistic analysis of refractive error. *Optom. Vis. Sci.* **74**, 367-375.

Tunnacliffe A.H. (1993). Introduction to visual optics (4th edition). Canterbury: The Association of British Dispensing Opticians.

Tyson R.K. (1998). Principles of adaptive optics. London: Academic Press.

van Blockland G.J., van Norren D. (1986). Intensity and polarisation of scattered light at small angles from the human fovea. *Vis. Res.* **26**, 485-494.

Vdovin G., Loktev M., Simonov A., Kijko V., Volkov S. (2005). Adaptive correction of human-eye aberrations in a subjective feedback loop. *Opt. Lett.* **30:7**, 795-797.

Vdovin G., Loktev M. (2003). On the possibility of intraocular adaptive optics. *Opt. Exp.* **11:7**, 810-817.

Williams D.R., Artal P., Navarro R., McMahon M.J., Brainard D.H. (1996). Off-axis optical quality and retinal sampling in the human eye. *Vis. Res.* **36:8**, 1103-1114.

Wakefield K. (1994). Bennett's ophthalmic prescription work (3rd edition). Oxford: Butterworth-Heinemann.

Walsh G., Charman W.N., Howland H.C. (1984). Objective technique for the determination of monochromatic aberrations of the human eye. *J. Opt. Soc. Am. A.* **1**, 987–992.

Webb R.H., Penney C.M., Sobiech J., Staver P.R., Burns S.A. (2003). SSR (spatially resolved refractometer): a null-seeking aberrometer. *Appl. Opt.* **42:4**, 736-744.

Webb R., Penney C.M., Thompson K. (1992). Measurement of ocular local wavefront distortion with a spatially resolved refractometer. *Appl. Opt.* **31**, 3678-3686.

Welford W.T. (1989). Aberrations of optical systems. Bristol: Adam Hilger.

Yang Z., Du S. (1999). Histological measurement of human retinal thickness. *J. Tongji Med. Univ.* **19:3**, 246-8.

Yoon G. (2006). Customised vision correction laboratory. Retrieved 2 October, 2005 from: http://www.cvs.rochester.edu/yoonlab/wavefront.htm.

Zhou F., Hong X., Miller D.T., Thibos L.N., Bradley A. (2004). Validation of a combined corneal topographer and aberrometer based on Shack-Hartmann wavefront sensing. *J. Opt. Soc. Am. A.* **21:5**, 683-696.

## Appendix A

### Technical specifications for various instrument components

**The lenslet array**.

190 microns pitch, 10 mm focal length, square geometry.

Diffraction limit of lenslets: 78 microns (84 microns in the CCD plane), which corresponds to 3.2 x 3.2 binned pixels.

Sensor range: +/- 2.2 D (6mm pupil).

Source power: 1.2 microwatts at the eye

**The CCD camera.**The Pixel Fly QE is a small, electronically cooled CCD camera. It is front-surface illuminated, and does not offer region of interest, on-chip gain, or image intensifying features.

Readout rate: 23 frames/second (at 2 x 2 binning).

Integration time: 10 microseconds to 10 seconds.

Range: 12 bits (65dB).

Size: 39 x 39x 68 mm.

Readout noise: 12 e rms.

Chip: Sony icx285al progressive scan interline.

Pixel size: 6.45 microns x 6.45 microns.

Fill factor: 70%.

Number of pixels: 1390x1024 pixels.

The HS spots occupy 21 x 21 sub apertures of 16 x 16 binned pixels = 4.33mm x 4.33mm.

## Appendix B

## Laser safety calculations

The accessible emission limit (AEL) rates the laser device as class 3B and therefore various safety mechanisms must be adhered to (p193-195). The wavelength of laser diode is 677 nm, therefore the device must comply with safety limitations of maximum permissible exposure (MPE) to the cornea concerning retinal thermal hazard. The device is exempt from safety restrictions concerning the retinal photochemical hazard because this restriction only applies to wavelengths between 400 nm and 600 nm.

Emitting diameter of laser diode is 3 microns.

Focal length of collimating lens is 4.5 mm.

Angle of acceptance ($\gamma$) is .0336 milliradians.

Angular subtense ($\alpha$) $\alpha_{minimum}$ = 1.5 milliradians and $\alpha_{maximum}$ = 100 milliradians

$\alpha$ = 0.334mrad therefore $\alpha < \alpha_{minimum}$ , $\alpha << \gamma$ , and $C_6 = 1$

$T_2$ = 10 seconds for $\alpha < \alpha_{minimum}$ , therefore $t > T_2$ so we must use t = 30 000 seconds.

The standard pupil diameter is 7 mm, $\gamma_{pupil}$ 110 milliradians , MPE = 10 Watts/$m^2$ .

The standard pupil area is 3.848 x $10^{-5}m^2$, therefore the MPE = 384 microwatts.

Our WFS creates a beam intensity of 3.5 microwatts at the eye, so we are operating below the safety limit by a factor of about 100.

Reference: Safety of Laser products – European standard, CEI 60825-1 (also amendment A1 and A2), European committee for electrotechnical standardization, Brussels, 2001

## List of publications

Sheehan M.T., Goncharov A.V., Dainty C. (2005). Design of a versatile clinical aberrometer. In Mazuray L., Wartmann R. (Eds). Optical Design and Engineering II. *Proc. SPIE* **5962,** 59620M.

Sheehan M.T., Goncharov A.V., O'Dwyer V.M., Toal V., Dainty C. (2007). A population study of the variation in monochromatic aberrations of the normal human eye over the central visual field. *Opt. Exp.* **15:12**, 7367-7380.

Goncharov A.V., Nowakowski M., Sheehan M.T., Dainty C. (2007) Reconstruction of the optical system of the human eye with reverse ray-tracing. *J. Opt. Soc. Am.* Accepted Optics Express 2007